

Electronic Thesis and Dissertation Repository

---

2-10-2023 10:00 AM

## Late Neoproterozoic to middle Paleoproterozoic geology of Devon and Ellesmere islands, Canadian Arctic

Joshua P. Laughton, *The University of Western Ontario*

Supervisor: Osinski, Gordon R., *The University of Western Ontario*

A thesis submitted in partial fulfillment of the requirements for the Doctor of Philosophy degree in Geology

© Joshua P. Laughton 2023

Follow this and additional works at: <https://ir.lib.uwo.ca/etd>



Part of the [Geology Commons](#)

---

### Recommended Citation

Laughton, Joshua P., "Late Neoproterozoic to middle Paleoproterozoic geology of Devon and Ellesmere islands, Canadian Arctic" (2023). *Electronic Thesis and Dissertation Repository*. 9219.  
<https://ir.lib.uwo.ca/etd/9219>

This Dissertation/Thesis is brought to you for free and open access by Scholarship@Western. It has been accepted for inclusion in Electronic Thesis and Dissertation Repository by an authorized administrator of Scholarship@Western. For more information, please contact [wlsadmin@uwo.ca](mailto:wlsadmin@uwo.ca).

## Abstract

The northernmost exposure of the Laurentian shield in Canada outcrops on Devon and Ellesmere islands within the Canadian Arctic Archipelago. Due to the remote location, the basement rocks of these islands have received little attention. From this study, zircon crystallization ages demonstrate that Devon Island is underlain by a late Neoproterozoic terrane comprising orthogneisses emplaced at ca. 2.55–2.51 Ga and an interleaved metasedimentary sequence deposited at ca.  $\geq 2.47$  Ga. On northern Devon Island, younger metasedimentary sequence(s) were deposited at ca. 2.2–1.9 Ga and intruded by ca. 2.01–1.95 Ga granitoids. Devon and Ellesmere islands experienced widespread metamorphic activity associated with the Thelon orogeny between ca. 1.95–1.87 Ga, peaking at ca. 1.91 Ga. Minimum peak temperatures of metamorphism are estimated at ca.  $>800$  °C throughout Devon and Ellesmere islands and the first documented sapphirine + quartz assemblage in the Devon and Ellesmere islands area is diagnostic evidence of ultrahigh temperature conditions ( $>900$  °C). The abundance of spinel + quartz (ca.  $\geq 940$  °C) metasedimentary rocks on Ellesmere Island likely provides further evidence of widespread ultrahigh temperature conditions. Peak pressures of ca. 1.9 Ga metamorphism are estimated at ca. 9 kbar on southern Devon Island and ca. 6–7.5 kbar for northern Devon and Ellesmere islands. Earlier, poorly constrained metamorphic events are recorded at ca. 2.54, 2.47 and 2.30 Ga, possibly associated with pulses of the Arrowsmith orogeny. The late Neoproterozoic Devon terrane potentially extends to the southwest on Boothia Peninsula and to the northeast in the Prudhoe Land area of northwestern Greenland. The juvenile middle Paleoproterozoic rocks of northern Devon and Ellesmere islands represent a northern extension of the Thelon tectonic zone, which we term the Ellesmere tectonic zone.

## Keywords

Devon Island, Ellesmere Island, Nunavut, Canadian Arctic, Rae craton, Precambrian, Neoproterozoic, Paleoproterozoic, granulite, ultrahigh temperature, monazite, zircon, geochronology, petrochronology, phase equilibrium modelling.

## Summary for Lay Audience

The Canadian shield is exposed from southern Ontario to the northern reaches of the Canadian Arctic Archipelago in Nunavut. The Canadian shield is made up of metamorphic rocks that are one to four billion years old and are separated into several geologic provinces that have been merged through plate tectonic processes over billions of years.

This study focuses on the northernmost shield rocks in Canada, which are exposed on Devon and Ellesmere islands in the Canadian Arctic Archipelago. Due to the remote location and the mostly absent human population of these islands, the shield rocks have received minimal previous research compared to other areas of the Canadian shield. To expand our knowledge of the multi-billion-year geologic history of these islands, we use rock dating and pressure–temperature modelling techniques to determine when these rocks were formed, when they were involved in metamorphic events, and what pressures and temperatures they experienced during these metamorphic events.

Results demonstrate that the shield rocks on Devon Island were formed around 2.5 billion years ago, while the shield rocks on Ellesmere and some on northern Devon Island were formed around 2.1 to 1.9 billion years ago during the merging of geologic provinces. This merging of geologic provinces would have caused the formation of a mountain range and the underlying rocks were subjected to metamorphism with temperatures reaching  $>800$  °C. The discovery of a rock containing the minerals sapphirine + quartz, which only form together at very high temperatures, suggests that temperatures of metamorphism were locally  $>900$  °C.

Comparing the shield rocks on Devon and Ellesmere islands to other shield rocks in the area suggests that the shield rocks on Boothia Peninsula and northwestern Greenland may share the same multi-billion-year geologic history as Devon and Ellesmere islands.

## Co-Authorship Statement

Chapter 1. Literature review of information relevant to this thesis was collected and written by Joshua Laughton. Comments and editing were provided by Gordon Osinski.

Chapter 2. Fieldwork conducted by Joshua Laughton and Gordon Osinski. Sample analysis and writing by Joshua Laughton. Comments and editing were provided by Gordon Osinski and Chris Yakymchuk. This chapter has been published in *Precambrian Research*: Laughton, J., Osinski, G. R., & Yakymchuk, C. (2022). Late Neoproterozoic HT–UHT metamorphism on southern Devon Island, Canadian Arctic. *Precambrian Research*, 377, 106718.

Chapter 3. Fieldwork conducted by Gordon Osinski and Michael Zanetti. Sample analysis and writing by Joshua Laughton. Comments and editing were provided by Gordon Osinski. This chapter is in preparation for submission to the *Canadian Journal of Earth Sciences*: Late Neoproterozoic terrane and juvenile Paleoproterozoic rocks on northern Devon Island, Canadian Arctic. *Canadian Journal of Earth Sciences*, (in prep).

Chapter 4. Fieldwork conducted by Thomas Frisch and their field members. Sample analysis and writing by Joshua Laughton. Comments and editing were provided by Gordon Osinski. This chapter is in preparation for journal submission.

Chapter 5. Summary and conclusions of this thesis were written by Joshua Laughton. Comments and editing were provided by Gordon Osinski.

## Acknowledgments

First, thank you to Gordon Osinski for an incredible Ph.D. (and B.Sc.) experience over the past six years and thank you for saving us from curious polar bears. Chris Yakymchuk, thank you for your generous assistance in the realm of metamorphic petrology. Marc Beauchamp, thank you for the many, many, many hours of microprobe assistance and teachings. Thank you to the Geological Survey of Canada, especially Danielle Regis and Mary Sanborn-Barrie for the ongoing discussions regarding all things about late Neoproterozoic terranes. Thomas Frisch, thank you for the continued guidance in navigating the geology of Devon and Ellesmere islands. Most of all, to my parents, Brian and Cherie, and my grandparents James, Marjorie, Louis, and Bernice, thank you for everything.

# Table of Contents

Abstract.....	ii
Summary for Lay Audience.....	iv
Co-Authorship Statement.....	v
Acknowledgments.....	vi
Table of Contents.....	vii
List of Tables.....	xi
List of Figures.....	xii
List of Appendices.....	xix
Chapter 1.....	1
1 Literature review and thesis overview.....	1
1.1 Introduction.....	1
1.2 Archean–Paleoproterozoic geology of the Canadian Arctic and northern Greenland.....	2
1.2.1 Rae craton.....	2
1.2.2 Paleoproterozoic orogenesis.....	3
1.2.3 Late Neoproterozoic terrane.....	5
1.3 Archean–Paleoproterozoic geology of Devon and Ellesmere islands.....	7
1.3.1 Previous work.....	8
1.3.2 Structure and lithology.....	11
1.3.3 Geochronology.....	12
1.3.4 Metamorphism.....	13
1.4 Thesis overview.....	14
1.5 Sample overview.....	15
1.6 References.....	16
Chapter 2.....	25

2	Late Neoproterozoic terrane and Paleoproterozoic HT–UHT metamorphism on southern Devon Island, Canadian Arctic .....	25
2.1	Introduction.....	25
2.2	Geological setting .....	28
2.3	Field observations, petrography and geochemistry .....	29
2.3.1	Clinopyroxene–garnet quartzofeldspathic gneiss .....	31
2.3.2	Orthopyroxene quartzofeldspathic gneiss.....	34
2.3.3	Rutile–garnet metasedimentary rocks and leucogranite .....	34
2.3.4	Two-pyroxene metabasite.....	36
2.3.5	Biotite granite gneiss.....	36
2.4	Phase equilibrium modelling .....	36
2.5	LA-ICP-MS zircon geochronology.....	42
2.6	EPMA monazite petrochronology .....	47
2.7	Discussion.....	51
2.7.1	Late Neoproterozoic Devon Island terrane and Paleoproterozoic metamorphism.....	51
2.7.2	<i>P–T</i> conditions of Thelon–Inglefield metamorphism.....	54
2.7.3	2.5–1.9 Ga tectonics along the western Rae craton margin.....	56
2.8	Conclusions.....	57
2.9	References.....	57
	Chapter 3.....	66
3	Late Neoproterozoic terrane and juvenile Paleoproterozoic rocks on northern Devon Island, Canadian Arctic .....	66
3.1	Introduction.....	66
3.2	Geological setting .....	67
3.3	Sample descriptions and petrography .....	69
3.4	Methodology.....	74



3.4.1	LA-ICP-MS zircon dating.....	74
3.4.2	EPMA monazite dating.....	75
3.4.3	Phase equilibrium modelling .....	75
3.5	LA-ICP-MS zircon dating.....	77
3.6	EPMA monazite dating.....	80
3.7	Phase equilibrium modelling .....	84
3.8	Discussion.....	86
3.8.1	Late Neoproterozoic terrane with Paleoproterozoic metasedimentary rocks and plutonics on northern Devon Island .....	86
3.8.2	Paleoproterozoic metamorphism of northern Devon Island .....	87
3.8.3	Regional Neoproterozoic–Paleoproterozoic correlations .....	89
3.9	Conclusions.....	91
3.10	References.....	91
Chapter 4	.....	97
4	Paleoproterozoic metamorphism of the Ellesmere tectonic zone, Canadian Arctic ....	97
4.1	Introduction.....	97
4.2	Geological setting .....	98
4.3	Sample descriptions and petrography .....	101
4.4	Methodology .....	105
4.5	Results.....	108
4.6	Discussion.....	114
4.6.1	Metamorphism within the Ellesmere tectonic zone.....	114
4.6.2	Metamorphism across the Taltson–Thelon–Ellesmere–Inglefield orogenic zone.....	116
4.7	Conclusions.....	117
4.8	References.....	117
Chapter 5	.....	124

5	Tectonic summary and conclusions .....	124
5.1	Late Neoproterozoic and middle Paleoproterozoic geology of Devon and Ellesmere islands .....	124
5.2	Neoproterozoic–Paleoproterozoic tectonics in the Canadian Arctic and northwestern Greenland .....	126
5.3	Future work .....	128
5.4	References .....	129
	Appendices .....	132
A.1	Sample locations .....	132
A.2	Southern Devon Island mineral chemistry methodology .....	132
A.3	Southern Devon Island whole-rock chemistry .....	134
A.4	LA-ICP-MS zircon data .....	137
A.5	EPMA monazite data .....	147
A.6	Composition–temperature modelling .....	164
A.7	References .....	169
	Curriculum Vitae .....	170

## List of Tables

Table 2.1. Representative mineral assemblages of the major lithologies. Minerals are ordered from highest to lowest model abundance on average. Mineral abbreviations follow Whitney and Evans (2010). .....	30
Table 2.2. Bulk rock compositions (mol.%) used for phase equilibrium modelling. TS: bulk composition from thin section analysis. WR: bulk composition from whole-rock chemical analysis. $X_{\text{Fe}^{3+}} = \text{O}(\text{Fe}_2\text{O}_3)/\text{FeO} \cdot 2$ . .....	39
Table 3.1. Bulk-rock compositions (mol.%) of metapelite and metabasite samples used for phase equilibrium modelling. $X_{\text{Fe}^{3+}} = \text{O}(\text{Fe}_2\text{O}_3)/\text{FeO} \cdot 2$ . .....	84
Table 4.1. Bulk-rock compositions (mol.%) of migmatitic paragneiss samples from the Ellesmere tectonic zone used for phase equilibrium modelling. $X_{\text{Fe}^{3+}} = \text{O}(\text{Fe}_2\text{O}_3)/\text{FeO} \cdot 2$ . $X_{\text{Mg}} = \text{MgO}/(\text{MgO}+\text{FeO})$ . .....	107

## List of Figures

- Figure 1.1. Simplified geological map of Laurentia (modified from St-Onge et al., 2009). D, Devon Island; E, Ellesmere Island; B, Boothia Peninsula; S, Somerset Island; P, Prudhoe Land and Inglefield Land. .... 1
- Figure 1.2. Simplified geological map of the Rae craton and surrounding Precambrian geology in northern Canada (modified from Drayson et al., 2022). Devon and Ellesmere islands are outside of the mapping area, north of Baffin Island. SI: Somerset Island; BP: Boothia Peninsula; QM: Queen Maud..... 3
- Figure 1.3. Present day extent and metamorphic facies of the 2.5–2.35 Ga Arrowsmith orogen along the western flank of the Rae craton and associated terranes (modified from Berman et al., 2013). Tmz: Taltson magmatic zone; Thelon tz: Thelon tectonic zone; BP: Boothia Peninsula; QM: Queen Maud..... 4
- Figure 1.4. Maps of the Archean–Paleoproterozoic geology on (a) Boothia Peninsula and Somerset Island (from Regis and Sanborn-Barrie, 2022), and (b) the Prudhoe Land and Inglefield Land area of northwestern Greenland (modified from Nutman et al., 2008)..... 7
- Figure 1.5. Areas covered by previous fieldwork on Devon and Ellesmere islands. The exposure of crystalline basement rocks is in red. Frisch (1988) and Harrison (1984) covered the entire region. .... 9
- Figure 1.6. Crystalline basement map of Devon and Ellesmere islands. Geology modified after Frisch (1984, 1988)..... 11
- Figure 2.1. (a) Geological setting of the northern Laurentian shield, highlighting the Rae craton and associated terranes. Map adapted after Davis et al. (2021), Nutman et al. (2008), and Sanborn-Barrie et al. (2019). The extent of ca. 2.5–2.4 Ga rocks on Devon Island and in Prudhoe Land is not well constrained, thus representing approximate boundaries. The dashed black line represents the easternmost extent of Arrowsmith metamorphism proposed by Berman et al. (2013). (b) Precambrian basement exposed on Devon and Ellesmere islands highlighting previously published zircon (z) and monazite (m) (Th)–U–Pb ages from Frisch (1988), Frisch and Hunt (1988), Schärer and Deutsch (1990) and Gilotti et al. (2018). At the

Haughton impact structure on western Devon Island, the Precambrian basement is exposed as clasts within impact melt rocks (e.g., Metzler et al., 1988). ..... 26

Figure 2.2. Geologic map of the Precambrian geology in the Dundas Harbour area (Talluruti) of southern Devon Island. Sample numbers are displayed for those discussed in the text..... 30

Figure 2.3. Field photos of the major lithologies on southern Devon Island. (a) Overview of the mapping area facing northwest above Johnson Bay. Field of view is ~3-km. Clinopyroxene–garnet quartzofeldspathic gneiss (cpx-grt qg) outcrops along the coast of Johnson Bay, underlying rutile–garnet metasedimentary rocks and leucogranite (rt-grt ms/lg) and orthopyroxene quartzofeldspathic gneiss (opx qg). (b) Clinopyroxene–garnet quartzofeldspathic gneiss with white plagioclase augen and subordinate pink K-feldspar augen. (c) Clinopyroxene–garnet quartzofeldspathic gneiss showing a feldspar-dominant leucosome and garnet–clinopyroxene dominant melanosome. A large (~3 cm) clinopyroxene porphyroblast is in the centre of the image. (d) Orthopyroxene quartzofeldspathic gneiss with a two-feldspar augen texture. (e) Rutile–garnet metapelite lens within rutile–garnet leucogranite. (k) Two-pyroxene metabasite with tonalitic leucosome. (l) Flattened biotite granite gneiss. .... 32

Figure 2.4. Photomicrographs of the major lithologies on southern Devon Island. (a) Clinopyroxene–garnet quartzofeldspathic gneiss with garnet and clinopyroxene around quartz ribbons and a feldspar matrix. (b) Feldspar-absent, clinopyroxene, garnet, and quartz melanocratic lens within clinopyroxene–garnet quartzofeldspathic gneiss. (c) Orthopyroxene quartzofeldspathic gneiss with orthopyroxene around a quartz ribbon, lesser hornblende and biotite, and a feldspar matrix. (d) Orthopyroxene quartzofeldspathic gneiss with garnet and clinopyroxene in the equilibrium assemblage. (e) Rutile–garnet metapelite with minor biotite and sillimanite, and a quartz–feldspar matrix. (f) Backscattered electron image showing rutile replacing ilmenite in a rutile–garnet metapelite. Rutile forms a rim around the ilmenite core, both of which are affected by post-peak metamorphic alteration. (g) Sapphirine–quartz assemblage from an outcrop of rutile–garnet metasedimentary rocks. The centered sapphirine grain is surrounded by plagioclase and quartz. A symplectic cordierite–quartz intergrowth above the sapphirine is replacing garnet. (h) Two-pyroxene metabasite with a granoblastic

texture of plagioclase, orthopyroxene and clinopyroxene. (i) Biotite granite gneiss with quartz ribbons and flattened polycrystalline feldspar augen..... 33

Figure 2.5. (a) Whole-rock ASI [molar  $\text{Al}_2\text{O}_3/(\text{CaO}+\text{Na}_2\text{O}+\text{K}_2\text{O})$ ] versus  $X_{\text{Mg}}$  [molar  $\text{MgO}/(\text{MgO}+\text{FeO})$ ]. (b) Whole-rock primitive mantle normalized rare-earth element profiles with primitive mantle values from McDonough and Sun (1995). ..... 35

Figure 2.6. Phase maps of thin sections used for phase equilibrium modelling. Phase proportions for each sample are listed in the inset table. .... 38

Figure 2.7. Suprasolidus  $P$ – $T$  isochemical phase diagrams. Inferred peak metamorphic assemblage fields are bolded. Isolines are shown as red or blue dashed lines, only within the inferred peak metamorphic assemblage fields. Isolines are bolded for the closest modelled proportions to the observed mineral modes and compositions. One-oxide normalized mol.% is approximately equivalent to vol.%.  $g(z) = \text{Ca}/[\text{Fe}+\text{Mg}+\text{Ca}(+\text{Mn})]$ ;  $pl(\text{ca}) = \text{Ca}/(\text{Ca}+\text{Na}+\text{K})$ . Grossular proportions for (f) are  $g(z) = 0.05$  across the entire garnet and rutile stability field. The unmodeled fields represent subsolidus  $P$ – $T$  space. Mineral abbreviations follow the activity-composition models used. .... 41

Figure 2.8. Zircon U–Pb Tera-Wasserburg concordia diagrams and representative zircon imagery (CL and BSE). UI: upper intercept date; LI: lower intercept date; C: concordia date; WM:  $^{207}\text{Pb}/^{206}\text{Pb}$  weighted mean date. 25  $\mu\text{m}$  analysis spots are shown for scale on zircon imagery. Individual zircon dates are ordered relative to spot analysis location. All U–Pb zircon results, including core and rim analysis locations, are in presented in Appendix A.4. .... 44

Figure 2.9. Monazite locations in thin section, yttrium concentration maps, and total Th–U–Pb age probability density diagrams separated into relatively low versus high yttrium domains. Thin sections are shown as RGB (Al–Ca–Mg) element maps. A small amount of the quartz represented in black is other Al, Ca, and Mg deficient phases such as ilmenite, magnetite, or zircon. The top of sample 3245 is a late pegmatite, not part of the biotite diorite. Monazite numbers correspond to monazite spot numbers reported in Appendix A.5. .... 49

Figure 2.10. Summary of pressure–temperature–time results. (a) Probability density diagram of all (Th)–U–Pb zircon and monazite ages. Major peaks are at ca. 2.5 and 1.9 Ga, with lesser peaks between ca. 2.3–2.1 Ga. (b)  $P$ – $T$  diagram displaying the overlapping peak stability fields

of the pyroxene quartzofeldspathic gneisses (3237, 3240, 3257) and two-pyroxene metabasites (3238, 3239), and the peak stability field for the rutile–garnet metapelite (3301). The black lines show the kyanite–sillimanite boundary and reactions of rutile-bearing metapelites from White et al. (2014a) in the KFMASHTO system with K-feldspar, quartz and melt in excess. The dashed grey line represents a possible clockwise  $P$ – $T$  path associated with HT–UHT Thelon–Inglefield metamorphism. The proposed path does not cross orthopyroxene forming reactions, as orthopyroxene was not observed in the metasedimentary rocks, but does cross the sill + bi to g + cd + ilm + ru + liq reaction upon cooling, forming the cordierite–quartz symplectites observed in the sapphirine–quartz sample (3294). ..... 53

Figure 3.1. (a) Map of northern Laurentia highlighting the Rae craton and other relevant Archean–Paleoproterozoic units. Modified after Chapter 2 and Regis and Sanborn-Barrie (2022). (b) Map of Devon and Ellesmere islands displaying all previously published (Th)–U–Pb zircon (z) and monazite (m) ages from the crystalline basement rocks. Modified after Chapter 2..... 67

Figure 3.2. Map of eastern Devon Island displaying the locations of samples used in this study. Geology of the crystalline basement is after Frisch (1984)..... 70

Figure 3.3. Field photographs of the crystalline basement on northern Devon Island. (a) Migmatitic hornblende–biotite orthogneiss (HAU-16-1453A) intruded by a post-kinematic biotite granite dike (HAU-16-1453C) south of Sverdrup Inlet. Footprints are present in the bottom of the image for scale. (b) Migmatitic sillimanite–cordierite–biotite paragneiss (HAU-16-1179) south of Sverdrup Inlet. (c) Garnet–biotite–cordierite metapelite (HMP-00-216A) from an iron-stained outcrop of the migmatitic paragneiss south of Sverdrup Inlet. (d) Orthopyroxene–biotite granodiorite gneiss (ED-TL-4) with granite intrusions southeast of Truelove Inlet. The field of view for this image ~3 m. (e) Quartzite (HAU-16-1034B) with minor K-feldspar and sillimanite south of Brae Bay. (f) K-feldspar megacrystic granite (ED-EG-2) on the eastern end of Brae Bay. .... 72

Figure 3.4. Photomicrographs of the crystalline basement on northern Devon Island. (a) Migmatitic hornblende–biotite orthogneiss HAU-16-1453A. (b) Migmatitic sillimanite–cordierite–biotite paragneiss HAU-16-1179. (c) Garnet–biotite–cordierite metapelite HMP-00-216A. (d) Cordierite replacing garnet in sample HMP-00-216. (e) Hornblende–

clinopyroxene–orthopyroxene metabasite HMP-00-213. (f) Thin quartz films around feldspar and pyroxene in metabasite HMP-00-213 indicating possible partial melting. (g) Biotite–sillimanite–garnet metapelite HAU-10-026. (h) Biotite–orthopyroxene metabasite ED-C-2. (i) Thin quartz films around feldspar and pyroxene in metabasite ED-C-2 indicating possible partial melting. PPL: plane polarized light image. XPL: Crossed polarized light image. BSE: backscattered electron image. Mineral abbreviations from Whitney and Evans (2010). ..... 73

Figure 3.5. Thin section phase maps of metapelite samples used for phase equilibrium modelling and EPMA monazite dating. .... 77

Figure 3.6. Wetherill concordia diagrams and representative CL imagery of metaigneous LA-ICP-MS zircon dating results. Errors reported in  $2\sigma$ . .... 78

Figure 3.7. Wetherill concordia diagrams, representative CL imagery, and histograms/probability density diagrams of metasedimentary LA-ICP-MS zircon dating results. Errors reported in  $2\sigma$ . .... 80

Figure 3.8. Histograms/probability density diagrams of metaigneous EPMA monazite dating results. Errors reported in  $2\sigma$ . .... 82

Figure 3.9. (a–b) Histograms/probability density diagrams of metasedimentary EPMA monazite dating results. Probability density diagrams are separated by relative Y content in monazite. Errors reported in  $2\sigma$ . (c)  $Y_2O_3$  vs. monazite age (Ma) plot. The yttrium content has a general high–low–high trend, starting with high Y monazite growth before garnet stability, low Y monazite growth during garnet stability (peak metamorphism) and high Y monazite growth during garnet breakdown. .... 83

Figure 3.10. Suprasolidus P–T models for two metapelite (a–b) and two metabasite (c–d) samples. The inferred peak stability fields are outlined in red. Mineral abbreviations follow the a–x models used and field shading corresponds to relative variance. .... 85

Figure 4.1. Simplified map of north-central Laurentia highlighting the extent of the ca. 2.0–1.9 Ga Taltson, Thelon, Ellesmere, and Inglefield orogenic zones merging Archean cratons (modified after Caswell et al., 2021 and St-Onge et al., 2009). E, Ellesmere Island; D, Devon Island; BP, Boothia Peninsula; QM, Queen Maud. .... 98



Figure 4.2. Simplified geological map of the southeastern Ellesmere Island crystalline basement showing the locations of paragneiss samples used in this study and zircon (z) and monazite (m) ages of metagneous rocks from Frisch (1988), Frisch and Hunt (1988) and Gilotti et al. (2018). Geology is modified after Frisch (1984a) and Frisch (1984b)..... 100

Figure 4.3. Plane polarized light photomicrographs of spinel-bearing migmatitic paragneiss from the Ellesmere tectonic zone. (a) Sample FS-77-143 showing a garnet rim surrounded by cordierite, spinel, biotite and sillimanite. Quartz is observed in direct contact with spinel. (b) Sample FS-77-268 showing a centred lenticular garnet with quartz inclusions. Spinel is in contact with biotite and is almost completely mantled by quartz. (c) Sample FSM-77-214 showing garnet nearby discrete spinel grains mantled by cordierite. A large quartz grain is centred between the spinel and garnet. (d) Sample FSM-77-218-1 showing spinel and cordierite symplectic intergrowths along garnet rims. Quartz is observed nearby spinel but not in direct contact. (e) Sample FSM-77-273-4 showing a melanocratic layer of sillimanite, cordierite, spinel and iron oxides between coarse quartz and feldspar grains. Spinel and cordierite symplectic intergrowths mantle sillimanite, and more discrete spinel is observed near iron oxides. (f) Sample FSM-77-307 showing a garnet with biotite inclusions. Spinel is present as symplectic intergrowths with cordierite, and as discrete grains within sillimanite and mantled by a cordierite film. Quartz is nearby but not observed in direct contact with spinel. Mineral abbreviations from Whitney and Evans (2010)..... 102

Figure 4.4. Phase maps of four migmatitic paragneiss thin sections from the Ellesmere tectonic zone. (a) FS-77-268 is mostly leucocratic and more strongly sheared compared to the other samples. Lenticular garnets contain quartz inclusions and have thin trails of sillimanite and spinel. (b) FSM-77-218-1 shows a leucocratic K-feldspar and quartz dominated layer on the left, and a melanocratic plagioclase dominated layer on the right. Large (1–2 cm) garnets with spinel and sillimanite mostly concentrated along garnet rims. Within the leucocratic portion of the sample, spinel is present near quartz but not in direct contact. Garnet contains numerous inclusions of biotite, sillimanite, and quartz. (c) Sample FSM-77-273-4 mostly comprises leucocratic layers of coarse quartz, K-feldspar and plagioclase, possibly representing melt pseudomorphs. Between the leucocratic layers is a melanocratic layer of garnet, cordierite, sillimanite, biotite, spinel, ilmenite and magnetite. (d) FSM-77-307 shows an abundance of cordierite in the matrix, along with quartz, K-feldspar and plagioclase. These garnets also

contain many inclusions of biotite, sillimanite, and quartz. Spinel is mostly associated with sillimanite, cordierite and ilmenite. .... 104

Figure 4.5. Suprasolidus P–T diagrams of peak metamorphic paragneiss compositions inferring spinel-absent peak metamorphic conditions. The inferred garnet–sillimanite–cordierite–biotite peak assemblages are outlined in red. H<sub>2</sub>O content was adjusted to intersect the inferred peak assemblages with the solidus at ca. 6 kbar. Stability field shading corresponds to variance with darker shading corresponding to lower variance. .... 109

Figure 4.6. Suprasolidus P–T diagrams of peak metamorphic paragneiss compositions inferring spinel-bearing peak metamorphic conditions. Spinel-bearing stability fields without orthopyroxene or sapphirine are outlined in red. H<sub>2</sub>O content was adjusted to intersect the spinel stability field with the solidus at ca. 6 kbar. .... 110

Figure 4.7. Suprasolidus P–T diagrams of melt reintegrated paragneiss compositions which are roughly representative of protolith (pre-anatexis) compositions. The stability limits of garnet, cordierite and spinel are outlined in red, blue and green respectively. The solidus for each model is minimally saturated with H<sub>2</sub>O at ca. 6 kbar. .... 112

Figure 4.8. (a) P–T diagram summarizing the phase equilibrium modelling results and possible P–T paths of metamorphism. The extents of cordierite–garnet–sillimanite–biotite stability fields from Figure 4.5 and spinel-bearing stability fields without orthopyroxene or sapphirine from Figure 4.6 are shaded in dark grey. The boundaries of the solidus, garnet, cordierite, and spinel stability using the melt-reintegrated compositions from Figure 4.7 are shaded in light grey, red, blue, and green respectively. (b) Modebox showing the change in phase proportions during an isobaric closed system (no melt loss) prograde path of metamorphism at 6 kbar. Modal proportions are based on the melt-reintegrated protolith composition of sample FSM-77-218-1. .... 113

Figure 5.1. Simplified summary of possible ca. 2.5–1.9 Ga tectonic events involving the formation and metamorphism of the crystalline basement on Devon and Ellesmere islands. .... 125

## List of Appendices

Appendix 1. List of Devon and Ellesmere islands samples used in this thesis. ....	132
Appendix 2. Whole-rock major chemistry (wt.%) of southern Devon Island samples. b.d., below detection. ....	134
Appendix 3: Whole-rock trace chemistry (ppm) of southern Devon Island samples. ....	135
Appendix 4. LA-ICP-MS zircon dating results of southern Devon Island samples. c: core; r: rim; h: homogenous. Discordancy = $(^{206}\text{Pb}/^{238}\text{U Age} / ^{207}\text{Pb}/^{206}\text{Pb Age} - 1) * 100$ . ....	137
Appendix 5. LA-ICP-MS zircon dating results of northern Devon Island samples. Discordancy = $(^{206}\text{Pb}/^{238}\text{U Age} / ^{207}\text{Pb}/^{206}\text{Pb Age} - 1) * 100$ . ....	143
Appendix 6. EPMA monazite dating results of southern Devon Island samples. c: core; r: rim; ir: inner rim; or: outer rim; n: no obvious domain morphology. b.d., below detection. ....	147
Appendix 7. Monazite age vs. $\text{Y}_2\text{O}_3$ , $\text{ThO}_2$ , $\text{CaO}$ , and $\text{SiO}_2$ for southern Devon Island samples. Oxide abundances are in wt.%. 3245: biotite diorite, 3248: biotite granite gneiss, 3301: rutile-garnet metapelite, 3351: biotite granite gneiss. ....	157
Appendix 8. EPMA monazite dating results of northern Devon Island samples. ....	158
Appendix 9. Bulk-rock compositions (mol.%) for $\text{H}_2\text{O-T}$ modelling of metapelite and metabasite samples from northern Devon Island. $X_{\text{Fe}^{3+}} = \text{O}(\text{Fe}_2\text{O}_3)/\text{FeO} * 2$ . ....	164
Appendix 10. $\text{H}_2\text{O-T}$ models for two metapelite (a-b) and two metabasite (c-d) northern Devon Island samples. The proportion of $\text{H}_2\text{O}$ selected for P-T modelling is shown as a dashed red line. Mineral abbreviations follow the a-x models used, and field shading corresponds to relative variance. ....	165
Appendix 11. Bulk-rock compositions (mol.%) for $\text{H}_2\text{O-T}$ and melt-T modelling of migmatitic paragneiss samples from the Ellesmere tectonic zone. $X_{\text{Fe}^{3+}} = \text{O}(\text{Fe}_2\text{O}_3)/\text{FeO} * 2$ . $X_{\text{Mg}} = \text{MgO}/(\text{MgO} + \text{FeO})$ . ....	166

Appendix 12. H<sub>2</sub>O–T models for migmatitic paragneiss samples from the Ellesmere tectonic zone. The proportion of H<sub>2</sub>O selected for P–T modelling of garnet–sillimanite–cordierite–biotite peak assemblages is shown as a dashed blue line. The proportion of H<sub>2</sub>O selected for P–T modelling of spinel + quartz peak assemblages is shown as a dashed red line. The solidus is bolded and suprasolidus stability fields are shaded in darker grey. Mineral abbreviations follow the a–x models used..... 167

Appendix 13. Melt–T models for migmatitic paragneiss samples from the Ellesmere tectonic zone. The proportion of melt selected for melt-reintegrated protolith P–T modelling of is shown as a dashed red line. The solidus is bolded and suprasolidus stability fields are shaded in darker grey. Mineral abbreviations follow the a–x models used. .... 168

## Chapter 1

### 1 Literature review and thesis overview

#### 1.1 Introduction

The core of Laurentia is composed of Archean cratons separated by various Proterozoic orogens (Fig. 1.1, e.g., Hoffman, 1988; Whitmeyer and Karlstrom, 2007). The most northerly of these Archean cratons is the Rae craton, part of the Churchill Province, which extends from northern Alberta in central Canada to eastern Greenland. The western margin of the Rae craton is separated from the Slave craton by the Paleoproterozoic Thelon tectonic zone (e.g., Gibb and Thomas, 1977; Davis et al., 2021). Traditionally, the northernmost extent of the Rae craton and Thelon tectonic zone, thus the northernmost extent of the Laurentian shield, have been interpreted to outcrop on Devon and Ellesmere islands in the Canadian Arctic Archipelago (e.g., Hoffman, 1989; St-Onge et al., 2009).

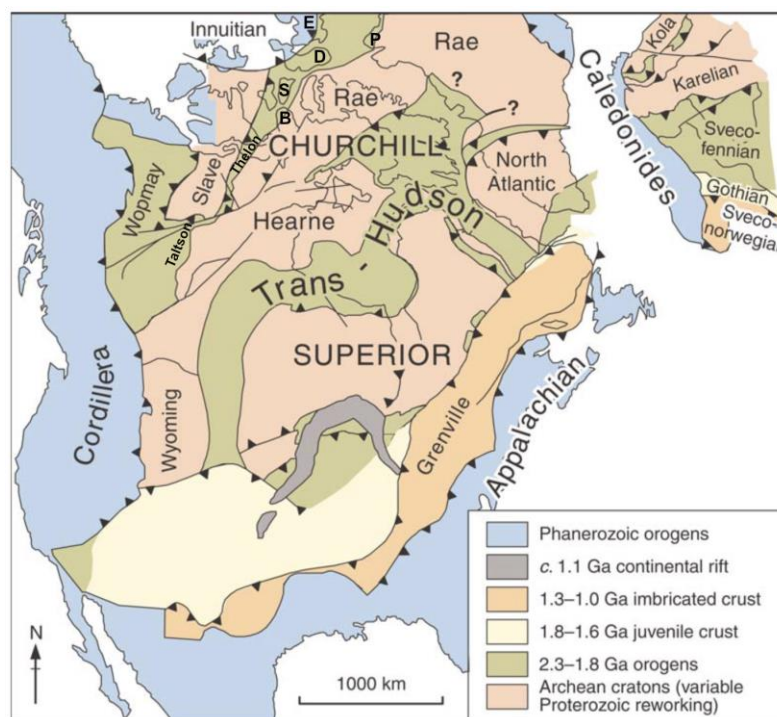


**Figure 1.1. Simplified geological map of Laurentia (modified from St-Onge et al., 2009). D, Devon Island; E, Ellesmere Island; B, Boothia Peninsula; S, Somerset Island; P, Prudhoe Land and Inglefield Land.**

As may be expected from such a remote area, the shield rocks of Devon and southern Ellesmere islands have received relatively little attention. Previous work in the region is mostly limited to helicopter- or dog-sled-based reconnaissance studies conducted by the Geological Survey of Canada in the 1950s to 1980s (e.g., Roots, 1963a; Christie, 1978; Frisch, 1988). Since then, studies of the Rae craton and associated geology south of Devon and Ellesmere islands have considerably updated the regional tectonometamorphic history (e.g., Hoffman, 1988; Schultz et al., 2007; Nutman et al., 2008; Berman et al., 2013; Davis et al., 2021), leading researchers to extrapolate how Devon and Ellesmere islands were involved in the Archean–Paleoproterozoic assembly of Laurentia (Fig. 1.1b, e.g., St-Onge et al., 2009; Berman et al., 2013; Harrison and St-Onge, 2023). This thesis aims to determine the timing of crust formation and conditions of subsequent tectonometamorphic events on Devon and Ellesmere islands to establish their Archean–Paleoproterozoic history, clarifying their role in the assembly of Laurentia.

## 1.2 Archean–Paleoproterozoic geology of the Canadian Arctic and northern Greenland

### 1.2.1 Rae craton

The Archean Rae craton is bounded to the south with the Hearne craton by the Snowbird tectonic zone and to the west with the Slave craton and Buffalo Head terrane by the Thelon tectonic zone and Taltson magmatic zone, respectively (Fig. 1.2, e.g., Hoffman, 1988). It is dominated by amphibolite- to granulite-facies Meso-Neoarchean (ca. 2.9–2.6 Ga) continental crust (e.g., Skulski et al., 2003; Hinchey et al., 2011; Pehrsson et al., 2014; Skulski et al., 2018) interleaved with Neoarchean (ca. 2.7 Ga) supracrustal rocks (e.g., Pehrsson et al., 2013; Sanborn-Barrie et al., 2014) and intruded by abundant Neoarchean (ca. 2.6 Ga) granitoids (e.g., Hinchey et al., 2011; Peterson et al., 2015). The Archean cratonic crust is unconformably overlain by a Paleoproterozoic (ca. 2.3–1.9 Ga) sedimentary cover sequence (Rainbird et al., 2010) and intruded by pulses of Paleoproterozoic magmatism, including the ca. 2.49–2.46 Ga Queen Maud granitoids (Schultz et al., 2007; Davis et al., 2014), ca. 2.32–2.29 Ga Arrowsmith granitoids (Hartlaub et al., 2007), 1.84–1.82 Ga Trans-Hudson granitoids and ca. 1.76–1.75 Ga Nueltin granite (Peterson et al., 2002).

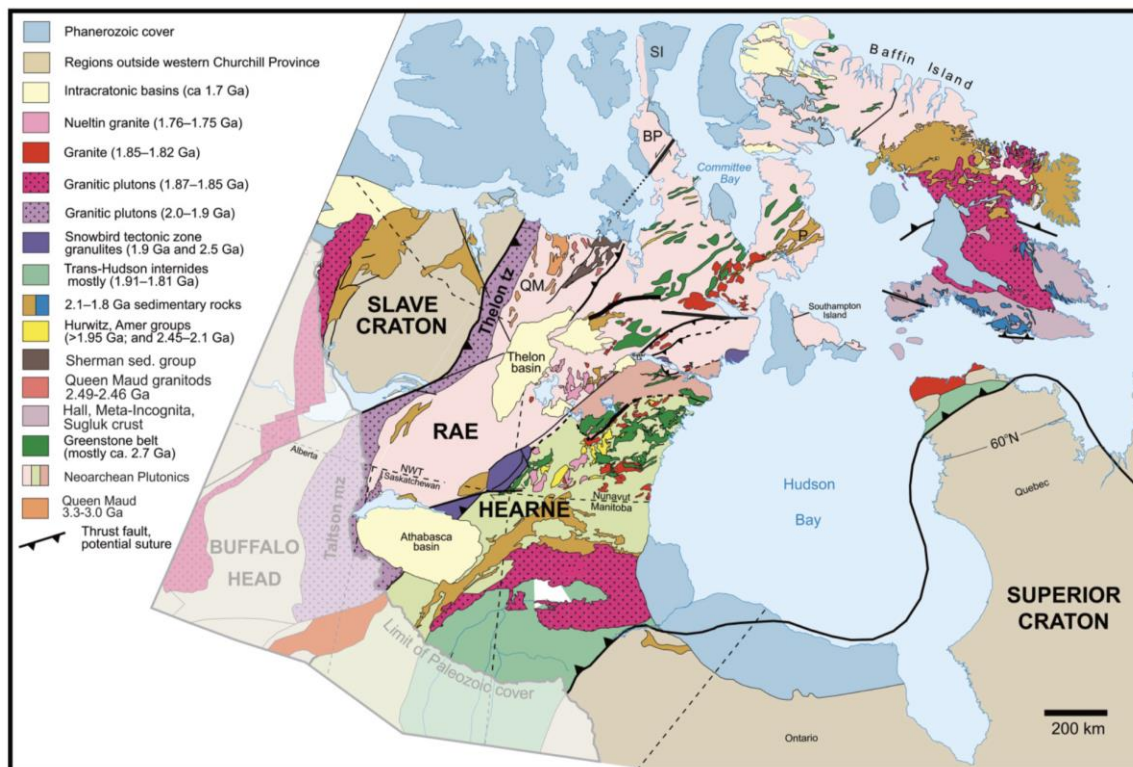


**Figure 1.2. Simplified geological map of the Rae craton and surrounding Precambrian geology in northern Canada (modified from Drayson et al., 2022). Devon and Ellesmere islands are outside of the mapping area, north of Baffin Island. SI: Somerset Island; BP: Boothia Peninsula; QM: Queen Maud.**

### 1.2.2 Paleoproterozoic orogenesis

The western margin of the Rae craton was reworked during the Paleoproterozoic by the Arrowsmith orogeny (2.5–2.35 Ga) (Berman et al., 2005; Berman et al., 2013) and Taltson–Thelon orogenies (2.0–1.9 Ga) (e.g., Gibb and Thomas, 1977; Card et al., 2014). Proposed by Berman et al. (2005), the Arrowsmith orogeny was a 2.5–2.35 Ga continental collisional event along the western margin of the Rae craton. This orogenic zone runs southeast-northwest from northern Alberta to potentially as far north as Devon Island (Fig. 1.3, Berman et al., 2013). Globally this orogeny is a significant event as it occurred during a period of tectonic quiescence (e.g., Condie et al., 2009). The Arrowsmith orogeny is proposed as an Andean-type accretionary margin suggested to have started with a ca. 2.5–2.4 Ga magmatic arc with east-dipping subduction below the western flank of the Rae

craton and transitioning to a ca. 2.4–2.35 Ga collisional orogeny (Berman et al., 2005; Berman et al., 2010). The northwestern Rae craton experienced episodic, high-grade metamorphism between ca. 2.54 and 2.35 Ga, with granitoid magmatism between ca. 2.5 and 2.46 Ga (Berman et al., 2013; Schultz et al., 2007). In the southwestern Rae craton, high-grade metamorphism occurred between ca. 2.47 and 2.28 Ga, with granitoid magmatism between ca. 2.32 and 2.29 Ga (Hartlaub et al., 2007; Berman et al., 2013). Metamorphic facies range from greenschist to granulite, but primarily reached amphibolite to granulite facies metamorphism with peak pressure–temperature conditions of ca. 7 kbar and 800 °C (Berman et al., 2013).

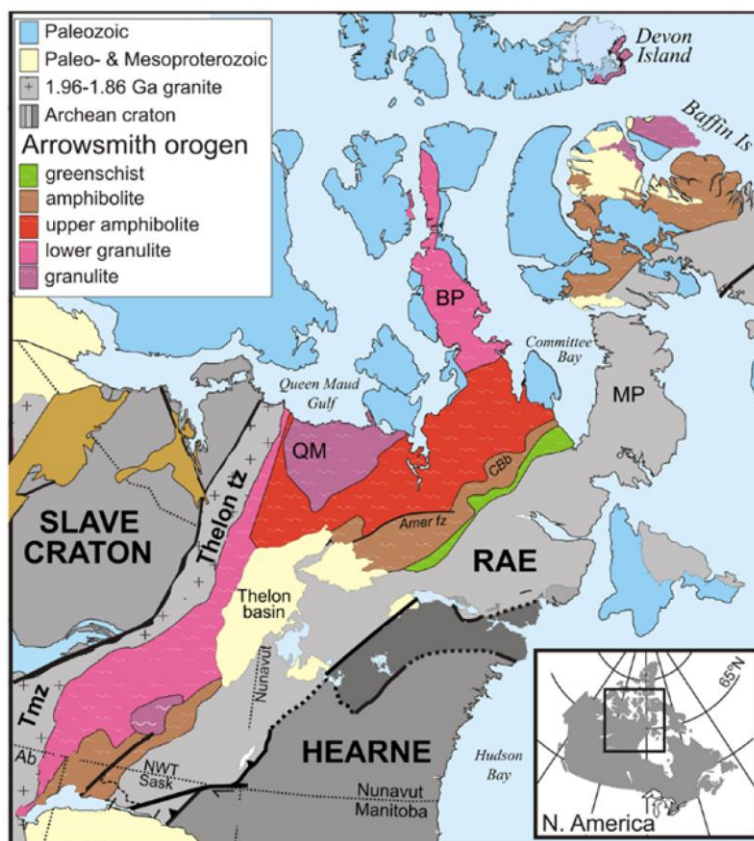


**Figure 1.3. Present day extent and metamorphic facies of the 2.5–2.35 Ga Arrowsmith orogen along the western flank of the Rae craton and associated terranes (modified from Berman et al., 2013). Tmz: Taltson magmatic zone; Thelon tz: Thelon tectonic zone; BP: Boothia Peninsula; QM: Queen Maud.**



The younger ca. 2.0–1.9 Ga Taltson and Thelon orogenies formed in response to the convergence of the western Rae craton with the Buffalo Head terrane and Slave craton respectively. The collision of these domains produced juvenile plutonic arcs, which are represented by the Taltson magmatic zone and Thelon tectonic zone respectively (Fig. 1.2) and are separated by the Great Slave Lake shear zone. Plutonic rocks of the Taltson magmatic zone include a phase of ca. 1.99–1.60 Ga granitoids and later ca. 1.94–1.93 Ga granitoids (Bostock et al., 1987; McDonough et al., 2000). Plutonic rocks of the Thelon tectonic zone include a phase of ca. 2.07–1.95 Ga granitoids, later ca. 1.91 Ga peraluminous leucogranite, and ca. 1.90–1.88 Ga high-Zr granites (van Breemen et al., 1987; Davis et al., 2013; Davis et al., 2014; Whalen, 2018; Berman et al., 2018). The Thelon tectonic zone also includes clastic metasedimentary rocks deposited before (< 2.09 Ga) and after (ca. 1.95–1.91 Ga) the main phase of Thelon plutonism (Davis et al., 2021), for which some comparable metasedimentary rocks are also found within the Taltson magmatic zone (e.g., Bostock and van Breemen, 1994). Peak metamorphism of the Thelon orogeny occurred at ca. 1.92–1.89 Ga during tectonic thickening (Berman et al., 2018), reaching amphibolite to granulite facies within the Thelon tectonic zone and adjacent domains (e.g., Davis et al., 2013; Kitsul et al., 2000; Frisch and Hunt, 1993; Tersmette, 2012). A similar timeframe of metamorphism has been shown for the Taltson orogeny (e.g., McDonough et al., 2000), with evidence of reaching ultrahigh temperature conditions within the Taltson magmatic zone (> 900 °C, e.g., Chacko et al., 1994; Grover et al., 1997). Exposure of the Thelon tectonic zone ends on the Canadian mainland west of Queen Maud (Fig. 1.2), however, it has been suggested to continue northward below the sedimentary cover on Prince of Wales Island, and possibly exposed again on Ellesmere and/or Devon islands (Gilotti et al., 2018), as well as northwestern Greenland (Nutman et al., 2008; Sanborn-Barrie et al., 2017).

### 1.2.3 Late Neoproterozoic terrane

Along the western and northern margins of the Rae craton, on both sides of Devon and Ellesmere islands, are areas historically considered to be part of the ca. 2.9–2.6 Ga Rae cratonic crust but have recently been revealed as younger late Neoproterozoic to early Paleoproterozoic rocks (ca. 2.55–2.45 Ga, e.g., Schultz et al., 2007; Nutman et al., 2008;

Sanborn-Barrie et al., 2019; Cloutier et al., 2021; Regis et al., 2022; Regis and Sanborn-Barrie, 2022). Along the western margin of the Rae craton, southwest of Devon and Ellesmere islands, a recent geological mapping project of Boothia Peninsula and Somerset Island by the Geological Survey of Canada has shown that ca. 2.56–2.51 Ga quartz monzonite and tonalite-trondhjemite-granodiorite dominate the exposed basement rocks of Boothia Peninsula and part of Somerset Island (Fig. 1.4a, Sanborn-Barrie et al., 2018; Sanborn-Barrie et al., 2019; Regis and Sanborn-Barrie, 2022). These are overlain by a ca. 2.5 Ga clastic metasedimentary sequence and cut by ca. 2.49–2.48 Ga intermediate to mafic plutonics (Regis and Sanborn-Barrie, 2022). Early metamorphism and deformation of this late Neoproterozoic terrane is suggested at ca. 2.44 Ga and ca. 2.39–2.37 Ga, potentially during two stages of the Arrowsmith orogeny, with peak metamorphic conditions of ca. 5–7 kbar and 750–850 °C (Sanborn-Barrie and Regis, 2020). The northwestern part of Boothia Peninsula and Somerset Island are dominated by a younger clastic-carbonate metasedimentary sequence with ca. 2.02–1.97 Ga detritus suggested to have been derived from the Thelon magmatic arc (Sanborn-Barrie and Regis, 2020). Multistage metamorphism associated with the Thelon orogeny is recorded between ca. 1.94–1.91 Ga with granulite facies to ultrahigh temperature conditions (Sanborn-Barrie and Regis, 2020; Kitsul et al., 2000; Frisch and Hunt, 1993). The Neoproterozoic terrane on Boothia Peninsula is suggested to extend further southwest along the western Rae craton, to the Sherman domain in the Queen Maud area (Regis and Sanborn-Barrie, 2022; Schultz et al., 2007), and potentially to the Nonacho basement complex (Regis et al., 2022) and Zemplak domain in the southwest Rae craton area (Cloutier et al., 2021).

Along the northern margin of the Rae craton, east of Devon and Ellesmere islands, another possible occurrence of late Neoproterozoic rocks is exposed in the Prudhoe Land area of northwestern Greenland (Fig. 1.4b, Nutman et al., 2008; Dawes et al., 1988). Here, orthogneisses of the Thule mixed gneiss-complex have poorly constrained late Neoproterozoic crystallization ages of ca. 2.60–2.50 Ga (Nutman et al., 2008). Younger orthogneisses of the Prudhoe Land granulite complex have crystallization ages of ca. 1.99 Ga (Nutman et al., 2008), like the plutonics of the Thelon tectonic zone. To the north in Inglefield Land, the Etah group metasedimentary sequence was deposited between ca. 1.98–1.92 Ga with predominantly ca. 2.00–1.98 Ga detritus (Nutman et al., 2008). These are intruded by

granitoids of the Etah metaigneous complex, representing a younger, ca. 1.95–1.92 Ga plutonic suite (Nutman et al., 2008). Metamorphic ages for the Prudhoe Land and Inglefield Land basement rocks are in the range of ca. 1.92–1.90 Ga (Nutman et al., 2008).

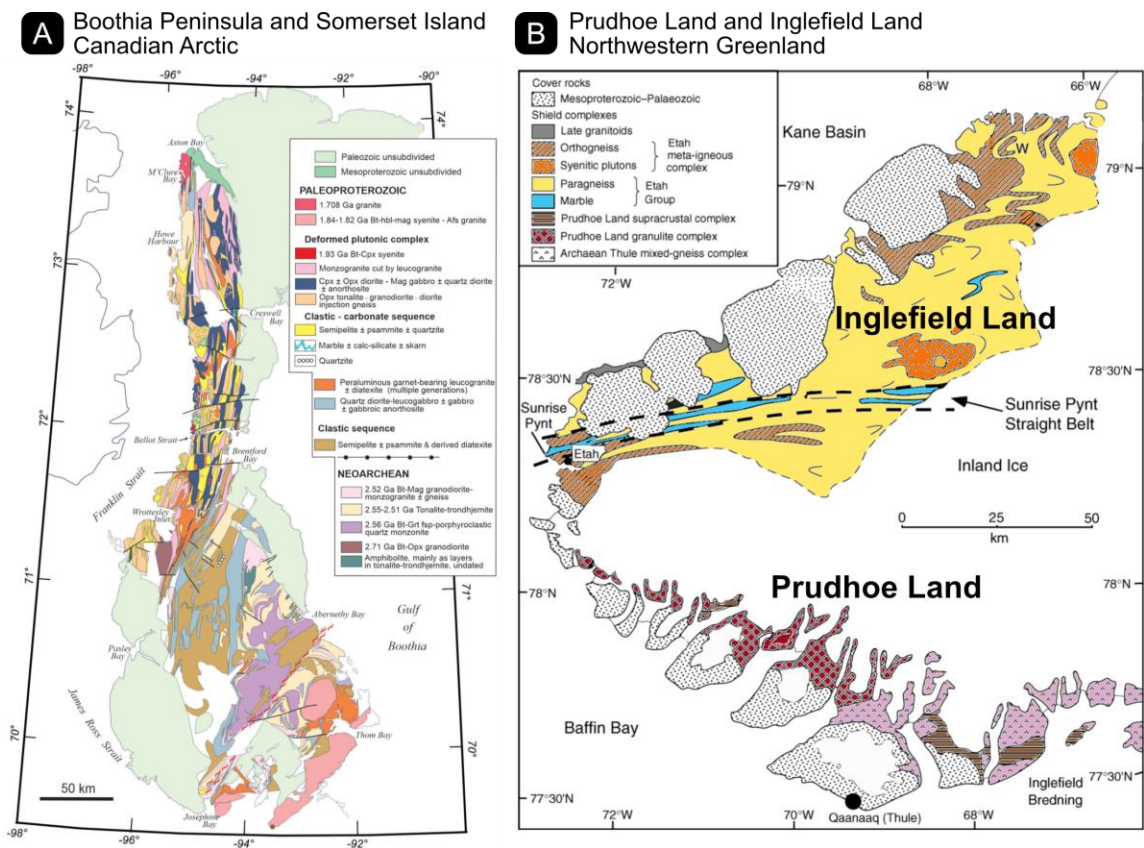


**Figure 1.4. Maps of the Archean–Paleoproterozoic geology on (a) Boothia Peninsula and Somerset Island (from Regis and Sanborn-Barrie, 2022), and (b) the Prudhoe Land and Inglefield Land area of northwestern Greenland (modified from Nutman et al., 2008).**

### 1.3 Archean–Paleoproterozoic geology of Devon and Ellesmere islands

Between the late Neoproterozoic terrane and middle Paleoproterozoic rocks of Boothia Peninsula and Somerset Island and possibly similar rocks in northwestern Greenland, are the crystalline basement rocks of Devon and Ellesmere islands (Fig. 1.1). To improve the tectonometamorphic Archean–Paleoproterozoic history of the Canadian Arctic and

northern Greenland, the extensions and metamorphic histories of late Neoproterozoic terranes, juvenile Paleoproterozoic orogenic zones and/or Rae cratonic crust on Devon and Ellesmere islands must be established.

### 1.3.1 Previous work

Positioned in the remote northern reaches of the Canadian Arctic Archipelago, the Devon and Ellesmere islands region was subject to early geographic exploration in the 18<sup>th</sup>, 19<sup>th</sup>, and early 20<sup>th</sup> centuries, primarily related to navigating the famed “Northwest Passage” and the race to the North Pole. During these historic excursions, some brief geologic observations were made along the coasts of Devon and Ellesmere islands, which are summarized in Dawes and Christie (1982) and Christie and Dawes (1991). Highlights of these early observations include finding evidence of granulite facies metamorphism and identifying marble intruded by granitoids on Ellesmere Island by geologists Per Schei and Albert P. Low respectively (Dawes and Christie, 1982; Frisch, 1988).

Formal geologic exploration in the Devon and Ellesmere islands region by the Geological Survey of Canada began in 1955 during “Operation Franklin” which included two accounts of the crystalline basement by E.F. Roots (Fig. 1.5). The first account details a small area on the southern coast of Ellesmere Island, between South Cape and Baad Fjord (Roots, 1963a), and the other describes the area between Cape Sparbo and Truelove Inlet on northern Devon Island (Roots, 1963b). Roots (1963a) and Roots (1963b) described these rocks predominantly as metasedimentary gneisses of Archean or Proterozoic age.

In 1961 and 1962, R.L. Christie traversed the coast of southeastern Ellesmere Island by dog-sled to establish the first regional geologic map of southern Ellesmere Island; showing the distribution of Precambrian basement rocks along the coast of Ellesmere Island (Fig. 1.5; Christie, 1962a; Christie, 1962b). Following this, Christie conducted a similar reconnaissance mission on Devon Island in 1968 and 1969 (Fig. 1.5; Christie, 1978). Altogether providing the first regional overview and descriptions of the Precambrian basement of Devon and Ellesmere islands, most notably highlighting the structural differences between the two islands; as well as, the abundance of shear fabrics in the region, especially on Devon Island.

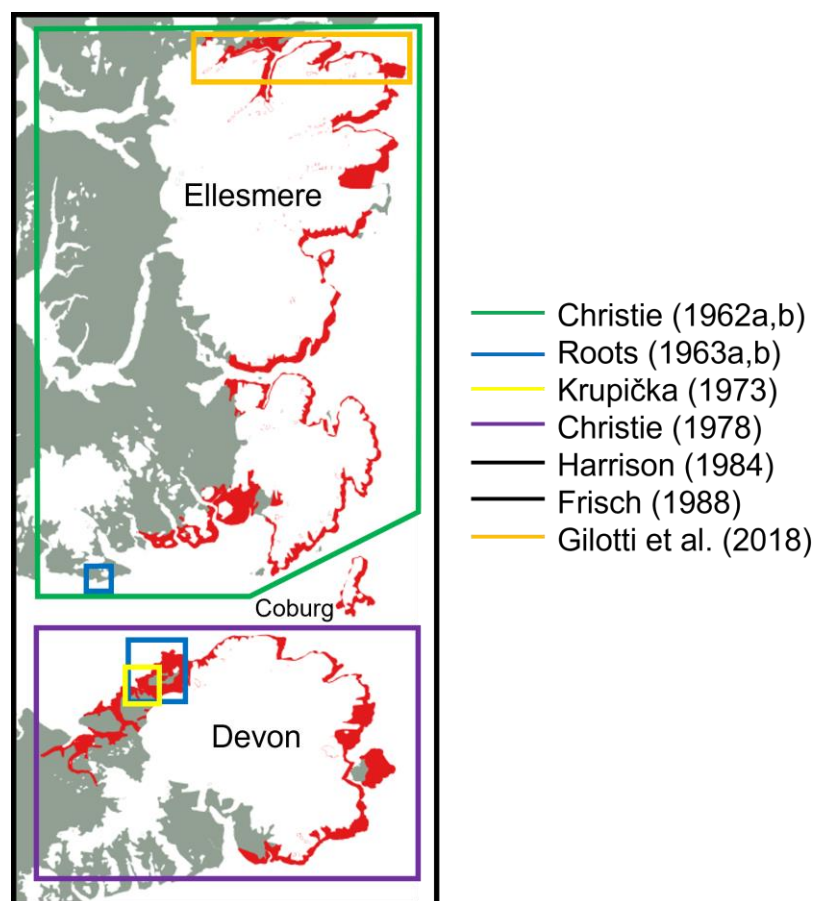


**Figure 1.5. Areas covered by previous fieldwork on Devon and Ellesmere islands. The exposure of crystalline basement rocks is in red. Frisch (1988) and Harrison (1984) covered the entire region.**

In 1971, J. Krupička studied the Precambrian basement in the Truelove area of northern Devon Island (Fig. 1.5; Krupička, 1973). The rocks at Truelove were described as granulite facies orthopyroxene gneisses grading into retrograded amphibolite facies gneisses. Krupička (1973) also identified abundant mylonitic rocks in the area.

The most expansive study of the Devon and Ellesmere islands crystalline basement to date was led by Thomas Frisch between 1977 and 1984 (Fig. 1.5). Frisch's preliminary findings were published in Geological Survey of Canada reports (Frisch et al., 1978; Frisch, 1979; Frisch, 1981; Frisch, 1983), along with a final cumulative memoir (Frisch, 1988) and geochronology report (Frisch and Hunt, 1988). Frisch (1988) provides detailed rock descriptions, whole-rock chemistry, mineral chemistry and thermobarometry estimates,

while Frisch (1988) and Frisch and Hunt (1988) reported the first U–Pb zircon and monazite ages for Devon and Ellesmere islands. Frisch also produced three geological maps (scale 1:250,000) which are the most detailed for these islands to date: Frisch (1984a) covers central Ellesmere Island, Frisch (1984b) covers southern Ellesmere Island and Frisch (1984c) covers Devon Island. Frisch (1988) also described the Precambrian rocks on Coburg Island for the first time. Even though this geological exploration mission was on a reconnaissance level, Frisch (1988) noted that the “coverage of Devon Island is even less detailed than the rest of the map area”.

At the same time as fieldwork led by Frisch, Petro-Canada also conducted a reconnaissance study across Devon, Ellesmere and Coburg islands in 1982 and 1983 after hearing reports of gossans and malachite stainings by Frisch (1983) and Frisch et al. (1978) (Fig. 1.5; Gibbons, 1985). Results from this study are reported in Harrison (1984) and Gibbons (1985). Petro-Canada’s prospecting permits were soon after resigned after no deposits of economic value were located.

After the early 1980’s the next research mission conducted on Devon or Ellesmere islands was led by J.A. Gilotti in 2014, who published new U–Pb zircon ages from the northernmost crystalline basement rocks of southern Ellesmere Island (Fig. 1.5; Gilotti et al., 2018); while  $^{40}\text{Ar}/^{39}\text{Ar}$  dating of shear zones from the same area was later published by Caswell et al. (2021).

Finally, indirect research of the Devon Island crystalline basement has been conducted by studying Precambrian clasts within the impact melt rocks of the Haughton impact structure on western Devon Island (Fig. 1.5). Here, Metzler et al. (1988) provided petrographic descriptions and whole-rock compositions of the Precambrian clasts, while Schärer and Deutsch (1990) and Erickson et al. (2021) published (Th)–U–Pb monazite and zircon ages, as well as, whole-rock Nd model ages by Schärer and Deutsch (1990).

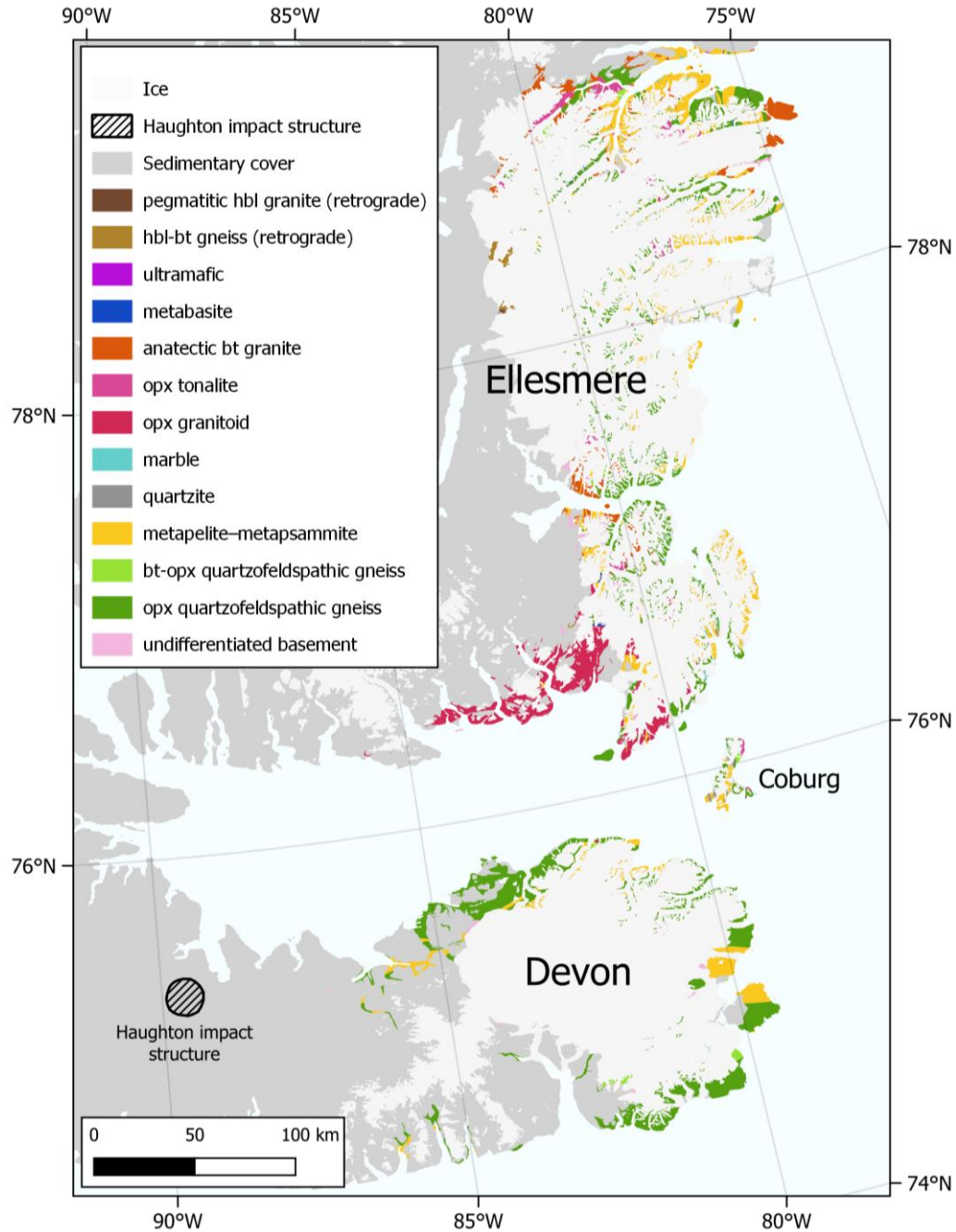


**Figure 1.6. Crystalline basement map of Devon and Ellesmere islands. Geology modified after Frisch (1984, 1988).**

### 1.3.2 Structure and lithology

Underlying the Paleozoic sedimentary strata of the Arctic Platform (e.g., Thorsteinsson and Mayr, 1987) the predominantly granulite facies crystalline basement of eastern Devon and southeastern Ellesmere islands is exposed along the rugged coastal margins and nunataks

of the Devon Ice Cap and Prince of Wales icefield (Fig. 1.6). Within Jones Sound, between Devon and Ellesmere islands, the crystalline basement is also exposed on Coburg Island. On Devon Island the regional gneissic fabric trends east-west, while on Ellesmere and Coburg islands it trends north-south (Christie, 1978; Frisch, 1988). The gneissic fabric generally runs parallel to lithologic contacts and dips steeply throughout the entire region (Christie, 1978; Frisch, 1988). At least three folding events were recognized by Frisch (1988). Two early stages of isoclinal folding resulted in intense flattening with fold axes parallel to the gneissic fabric. This was followed by a later period of broad, open folding, with fold axes mostly trending northwest. Devon Island appears to have experienced greater deformational strain relative to Ellesmere Island, based on the abundance of shear zones and augen gneisses reported from Devon Island (Christie, 1978; Harrison, 1984; Frisch, 1988).

On Devon Island, most of the crystalline basement has been mapped as orthopyroxene granitic to tonalitic quartzofeldspathic gneiss (Frisch, 1984c). These orthopyroxene gneisses are interleaved with metasedimentary rocks, most of which are described as migmatitic garnet–sillimanite–cordierite metapelite to metapsammite (Frisch, 1988), with lesser quartzite and rare marble occurrences (Harrison, 1984). Similar lithologies outcrop on Ellesmere Island, with a few notable differences; massive orthopyroxene granitoids are abundant on Ellesmere Island, especially in the southern and western basement exposures; and marble is more common within metasedimentary outcrops (Frisch, 1984a, Frisch, 1984b; Frisch, 1988).

### 1.3.3 Geochronology

Previous radiometric age dating of the Devon and Ellesmere islands crystalline basement is relatively limited (Frisch, 1988; Frisch and Hunt, 1988; Hegner and Jackson, 1990; Schärer and Deutsch, 1990; Gilotti et al., 2018; Caswell, 2018; Erickson et al., 2021). The oldest ages in the area are from orthopyroxene quartzofeldspathic gneisses on southern Devon Island, which give ca. 2.52 and >2.43 Ga zircon minimum crystallization ages (Frisch, 1988; Frisch and Hunt, 1988). These are comparable to the late Neoproterozoic terrane ages along the western Rae craton (e.g., Boothia Peninsula, Regis and Sanborn-Barrie, 2022). Zircon dating of shocked basement clasts within the impact melt rocks of the



Haughton impact structure have yielded zircon ages as old as ca. 2.50 Ga (Erickson et al., 2021; Schärer and Deutsch, 1990); however, these are from oscillatory zoned grains in metasedimentary gneisses and thus may represent detrital ages, not an Archean protolith age.

On Ellesmere Island, dating of orthopyroxene quartzofeldspathic gneisses and granitoids revealed ages at ca. 2.01–1.91 Ga (Frisch, 1988; Frisch and Hunt, 1988; Gilotti et al., 2018). The zircon ages between ca. 2.01–1.96 Ga are interpreted as crystallization ages, which strongly correlates with crystallization ages from the Thelon tectonic zone (e.g., Berman et al., 2018). Monazite ages on Ellesmere and northern Devon islands, as well as a younger population of zircon ages from anatectic granites fall between ca. 1.96–1.90 Ga (Frisch, 1988; Frisch and Hunt, 1988; Schärer and Deutsch, 1990; Gilotti et al., 2018; Erickson et al., 2021), suggestive of widespread metamorphism in the area.

Whole-rock Nd model ages from southern and northern Devon Island rocks range between ca. 2.7–2.1 Ga (Hegner and Jackson, 1990; Schärer and Deutsch, 1990), which suggests late Neoproterozoic rocks could be exposed on both coasts of Devon Island. Whole-rock Nd model ages from Ellesmere Island yield a restricted age range between ca. 2.1–2.0 Ga (Hegner and Jackson, 1990), suggesting that Ellesmere Island represents a juvenile Paleoproterozoic arc with no Archean material. Whole-rock Nd model ages from Coburg Island fall between ca. 2.7–2.1 Ga (Hegner and Jackson, 1990), suggestive of late Neoproterozoic crust like Devon Island; however, the north-south structural fabric and abundance of marble have more in common with the juvenile Ellesmere Island rocks.

#### 1.3.4 Metamorphism

The dominance of granulite facies assemblages and widespread migmatitic rocks throughout Devon and Ellesmere islands (e.g., Krupička, 1973; Harrison, 1984; Frisch, 1988), suggests high temperature suprasolidus metamorphic conditions were dominant during one or more metamorphic events in the region. Quantitative pressure–temperature constraints of metamorphism are limited to classical thermobarometry estimates reported by Frisch (1988). Temperature estimates are primarily based on Fe–Mg exchange thermometers (e.g., garnet–cordierite, garnet–pyroxene, two-pyroxene), giving results in

the range of ca. 500–750 °C (Frisch, 1988). Since Fe–Mg exchange geothermometry of granulites is highly susceptible to Fe–Mg diffusion upon retrogression (e.g., Frost and Chacko, 1989), these temperature estimates are suggested to largely reflect decompression and cooling conditions, rather than peak metamorphism (Frisch, 1988). Geobarometry estimates of metamorphic pressure conditions are at ca. 5–7 kbar (Frisch, 1988), and are generally higher on Devon Island compared to Ellesmere Island (Frisch, 1988).

## 1.4 Thesis overview

This thesis is focused on studying the geology and tectonometamorphic evolution of Devon and Ellesmere islands in the Canadian Arctic Archipelago; aiming to significantly expand on the limited previous research in this remote area of the Laurentian Shield. Chapters 2–4 are divided by geographic region with Chapter 2 on southern Devon Island, Chapter 3 on northern Devon Island and Chapter 4 on Ellesmere Island. Chapter 5 provides a summary and conclusions to the newfound results of the Devon and Ellesmere islands crystalline basement.

Chapter 2 presents zircon and monazite chronology and metamorphic pressure–temperature constraints for southern Devon Island. Results demonstrate that southern Devon Island is a late Neoproterozoic (ca. 2.55–2.47 Ga) terrane composed of lower to middle crustal, granulite facies rocks with evidence of anatexis and pervasive solid-state ductile deformation. Igneous protoliths were emplaced between ca. 2.55–2.51 Ga and a clastic sedimentary sequence was deposited at ca.  $\geq 2.47$  Ga. Early, poorly constrained metamorphic events are recorded at ca. 2.54, 2.47 and 2.30 Ga, possibly associated with pulses of the Arrowsmith orogeny (ca. 2.5–2.3 Ga). The area was later reworked by high temperature to ultrahigh temperature metamorphism at ca. 1.91 Ga during with the Thelon–Inglefield orogeny; with peak pressure–temperature conditions of ca. 9 kbar and  $>850$  °C. The discovery of a sapphirine–quartz assemblage is a first for the Devon Island area and is diagnostic evidence of ultrahigh temperature conditions within the Thelon–Inglefield orogenic zone.

Chapter 3 presents zircon and monazite chronology and metamorphic pressure–temperature constraints for northern Devon Island. Results demonstrate that ca. 2.55 Ga

late Neoproterozoic terrane extends to northern Devon Island. This terrane is interleaved with middle Paleoproterozoic metasedimentary sequence(s) consisting of ca. 2.2–1.9 Ga metapelite–metapsammite and ca. 2.1–1.9 Ga quartzite. Zircon dating of granite–granodiorite gneisses demonstrate that ca. 2.01–1.95 Ga plutonics are present on northern Devon Island, likely representing a northern extension of the Thelon tectonic zone. Monazite dating shows that widespread Thelon–Inglefield metamorphism peaked at ca. 1.91 Ga, the same as southern Devon Island. Thelon–Inglefield metamorphism attained peak pressure–temperature conditions of ca. 6.5–7.5 kbar and 800–870 °C, lower than southern Devon Island, suggestive of a shallower exhumed crustal level relative to southern Devon Island.

Chapter 4 presents phase equilibrium modelling based pressure–temperature constraints for granulite facies metamorphism of Ellesmere Island. Migmatitic paragneiss assemblages comprise garnet, sillimanite, cordierite and biotite which suggest peak metamorphic conditions between ca. 5–7 kbar and 750–860 °C. The common presence of spinel + quartz bearing assemblages suggest ultrahigh temperature metamorphic conditions of ca. 5–6.5 kbar and  $\geq 940$  °C. These results contribute to the expanding evidence of ultrahigh temperature conditions associated with ca. 2.0–1.9 Ga orogenesis in the region.

Chapter 5 summarizes and concludes Chapters 2–4, discussing the late Neoproterozoic to middle Paleoproterozoic evolution of Devon and Ellesmere islands, correlations to the regional Neoproterozoic–Paleoproterozoic geology and suggestions for future studies, based on the newfound results of this thesis.

## 1.5 Sample overview

This thesis utilizes a large collection of rock samples from Devon and Ellesmere islands, collected over many field expeditions between 1977 and 2018. Chapter 2 uses a selection of samples collected by Joshua Laughton and Gordon Osinski during a field season in 2018 at the Dundas Harbour area of southern Devon Island. Chapter 3 uses samples collected across northern Devon Island by Gordon Osinski in 2000, 2010 and 2016, and by Michael Zanetti in 2017. Chapter 4 uses samples from Ellesmere Island which were loaned from the Geological Survey of Canada, Ottawa and originally collected by Thomas Frisch and

their field members between 1977–1978. Description and discussion of some of Thomas Frisch's samples used in this thesis are reported in Frisch (1988) and Frisch and Hunt (1988). The geographic locations for all samples used in this thesis are listed in Appendix A.1.

## 1.6 References

- Berman, R. G., Davis, W. J., & Pehrsson, S. (2007). Collisional Snowbird tectonic zone resurrected: Growth of Laurentia during the 1.9 Ga accretionary phase of the Hudsonian orogeny. *Geology*, 35(10), 911–914.
- Berman, R. G., Davis, W. J., Whalen, J. B., Taylor, B. E., McMartin, I., Mccurdy, M. W., Mitchell, R. K., Ma, S., Coyle, M., Roberts, B., & Craven, J. A. (2018). Report of activities for the GEM-2 Chantrey-Thelon activity: Thelon tectonic zone project, Nunavut (pp. 1–22). Geological Survey of Canada.
- Berman, R. G., Pehrsson, S., Davis, W. J., Ryan, J. J., Qui, H., & Ashton, K. E. (2013). The Arrowsmith orogeny: Geochronological and thermobarometric constraints on its extent and tectonic setting in the Rae craton, with implications for pre-Nuna supercontinent reconstruction. *Precambrian Research*, 232, 44–69.
- Berman, R. G., Sanborn-Barrie, M., Rayner, N., Carson, C., Sandeman, H. A., & Skulski, T. (2010). Petrological and in situ SHRIMP geochronological constraints on the tectonometamorphic evolution of the Committee Bay belt, Rae Province, Nunavut. *Precambrian Research*, 181(1-4), 1–20.
- Berman, R. G., Sanborn-Barrie, M., Stern, R. A., & Carson, C. J. (2005). Tectonometamorphism at ca. 2.35 and 1.85 Ga in the Rae domain, western Churchill Province, Nunavut, Canada: Insights from structural, metamorphic and in situ geochronological analysis of the southwestern Committee Bay Belt. In *Canadian Mineralogist* (Vol. 43, Issue 1, pp. 409–442).

- Bostock, H. H., & van Breemen, O. (1994). Ages of detrital and metamorphic zircons and monazites from a pre-Taltson magmatic zone basin at the western margin of Rae Province. *Canadian Journal of Earth Sciences*, 31(8), 1353–1364.
- Bostock, H.H., van Breemen, O., Loveridge, W.D. (1987). Proterozoic geochronology in the Taltson Magmatic Zone, N.W.T. In: *Radiogenic Age and Isotopic Studies*, Report 1. Geological Survey of Canada, Paper 87-2, pp. 73–80.
- Card, C. D., Bethune, K. M., Davis, W. J., Rayner, N., & Ashton, K. E. (2014). The case for a distinct Taltson orogeny: Evidence from northwest Saskatchewan, Canada. *Precambrian Research*, 255, 245–265.
- Caswell, B., Gilotti, J. A., Webb, L. E., McClelland, W. C., Kościńska, K., Piepjohn, K., & von Gosen, W. (2021).  $^{40}\text{Ar}/^{39}\text{Ar}$  dating of Paleoproterozoic shear zones in the Ellesmere–Devon crystalline terrane, Nunavut, Canadian Arctic. *Canadian Journal of Earth Sciences*, 58, 1073–1084.
- Chacko, T., Creaser, R. A., & Poon, D. (1994). Spinel+quartz granites and associated metasedimentary enclaves from the Taltson magmatic zone. Alberta, Canada: a view into a root zone of a high temperature S-type granite batholith. *Mineralogical Magazine A*, 58, 161–162.
- Christie, R. L. (1962a). Geology, Alexandra Fiord, Ellesmere Island, District of Franklin [Map].
- Christie, R. L. (1962b). Geology, Southeast Ellesmere Island, District of Franklin [Map].
- Christie, R. L. (1978). A structural reconnaissance of Eastern Devon Island, Arctic Archipelago. Geological Survey of Canada, Open File 537, 1–63.
- Christie, R. L., & Dawes, P. R. (1991). Geographic and Geological Exploration. In H. P. Trettin (Ed.), *Geology of the Inuitian Orogen and Arctic Platform of Canada and Greenland*. Geological Society of America.

- Cloutier, M. A., Bethune, K. M., Ashton, K. E., & Deane, J. M. K. (2021). U-Pb geochronology, geochemistry, and isotopic composition of granitoids across the Nolan-Zemlak domain boundary in the SW Rae craton, Laurentia: Evidence for a late Neoproterozoic suture reworked during Arrowsmith orogen. *Precambrian Research*, 362, 106303.
- Condie, K. C., Belousova, E., Griffin, W. L., & Sircombe, K. N. (2009). Granitoid events in space and time: constraints from igneous and detrital zircon age spectra. *Gondwana Research*, 15(3-4), 228-242.
- Davis, W. J., Berman, R. G., & MacKinnon, A. (2013). U-Pb geochronology of archival rock samples from the Queen Maud Block, Thelon Tectonic Zone and Rae Craton, Kitikmeot region, Nunavut, Canada (Geological Survey of Canada, Open File, Vol. 7409). Natural Resources Canada.
- Davis, W. J., Berman, R. G., Nadeau, L., & Percival, J. (2014). U-Pb zircon geochronology of a transect across the Thelon Tectonic Zone, Queen Maud region, and adjacent Rae Craton, Kitikmeot region, Nunavut, Canada (Geological Survey of Canada, Open File, Vol. 7652). Natural Resources Canada.
- Davis, W. J., Sanborn-Barrie, M., Berman, R. G., & Pehrsson, S. (2021). Timing and provenance of Paleoproterozoic supracrustal rocks in the central Thelon tectonic zone, Canada: implications for the tectonic evolution of western Laurentia from ca. 2.1 to 1.9 Ga. *Canadian Journal of Earth Sciences*, 58, 378–395.
- Dawes, P. R., & Christie, R. L. (1982). History of exploration and geology in the Nares Strait region. In: Dawes, P. R., & Kerr, J. W., Nares Strait and the drift of Greenland: a conflict in plate tectonics. *Meddelelser om Grønland, Geoscience* 8, 19–36.
- Dawes, P. R., Larsen, O., & Kalsbeek, F. (1988). Archean and Proterozoic crust in North-West Greenland: evidence from Rb-Sr whole-rock age determinations. *Canadian Journal of Earth Sciences*, 25(9), 1365–1373.

- Drayson, D., Camacho, A., Sanborn-Barrie, M., Regis, D., Larson, K. P., Osinchuk, A., & DuFrane, S. A. (2022). Deformation history and tectonic significance of the Sanagak Lake shear zone, Boothia Peninsula, Nunavut. *Canadian Journal of Earth Sciences*.
- Erickson, T. M., Kirkland, C. L., Jourdan, F., Schmieder, M., Hartnady, M. I. H., Cox, M. A., & Timms, N. E. (2021). Resolving the age of the Haughton impact structure using coupled  $^{40}\text{Ar}/^{39}\text{Ar}$  and U-Pb geochronology. *Geochimica et Cosmochimica Acta*, 304, 68–82.
- Frisch, T. (1979). Reconnaissance studies of the Precambrian crystalline basement on Devon Island, District of Franklin. *Geological Survey of Canada, Paper, 79-1A*, 113–114.
- Frisch, T. (1981). Further Reconnaissance Mapping of the Precambrian Shield on Devon Island, District of Franklin. *Geological Survey of Canada, Paper, 81-1A*, 31–32.
- Frisch, T. (1983). Reconnaissance geology of the Precambrian Shield of Ellesmere, Devon and Coburg Islands, Arctic Archipelago: a preliminary account. *Geological Survey of Canada, Paper, 82-10*, 1–11.
- Frisch, T. (1984a). Geology, Prince of Wales Mountains, District of Franklin, Northwest Territories. *Geological Survey of Canada, Map, 1572*.
- Frisch, T. (1984b). Geology, Makinson Inlet, District of Franklin, Northwest Territories. *Geological Survey of Canada, Map, 1573*.
- Frisch, T. (1984c). Geology, Devon Ice Cap, District of Franklin, Northwest Territories. *Geological Survey of Canada, Map, 1574*.
- Frisch, T. (1988). Reconnaissance geology of the Precambrian shield of Ellesmere, Devon and Coburg Islands, Canadian Arctic Archipelago. *Bulletin Geological Survey of Canada, Memoir 409*, 102 p.

- Frisch, T., & Hunt, P. A. (1988). U-Pb zircon and monazite ages from the Precambrian Shield of Ellesmere and Devon islands, Arctic Archipelago. *Bulletin Geological Survey of Canada*, Paper 88-2, 117–125.
- Frisch, T., & Hunt, P. A. (1993). Reconnaissance U-Pb geochronology of the crystalline core of the Boothia Uplift, District of Franklin, Northwest Territories. *Geological Survey of Canada*, Paper, 93-2, 3–22.
- Frisch, T., Morgan, W. C., Dunning, G. R. (1978). Reconnaissance geology of the Precambrian shield on Ellesmere and Coburg islands, Canadian Arctic Archipelago. *Geological Survey of Canada*, 78-1A, 135–138.
- Frost, B. R., & Chacko, T. (1989). The Granulite Uncertainty Principle: Limitations on Thermobarometry in Granulites. *The Journal of Geology*, 97(4), 435–450.
- Gibb, R. A., & Thomas, M. D. (1977). The Thelon front: A cryptic suture in the Canadian shield? *Tectonophysics*, 38(3-4), 211–222.
- Gibbins, W.A. (1985). Arctic Islands Region; in *Mineral Industry Report 1982-1983, Northwest Territories*, ed. J. A. Brophy; Department of Indian Affairs and Northern Development, Ottawa, 95-155.
- Gilotti, J. A., McClelland, W. C., Piepjohn, K., & von Gosen, W. (2018). U–Pb geochronology of Paleoproterozoic gneiss from southeastern Ellesmere Island: implications for displacement estimates on the Wegener fault. *Arktos*, 4(1), 12.
- Grover, T. W., Pattison, D. R. M., McDonough, M. R., & McNicoll, V. J. (1997). Tectonometamorphic evolution of the southern Taltson magmatic zone and associated shear zones, northeastern Alberta. *Canadian Mineralogist*, 35(5), 1051–1067.
- Harrison, J. C. (1984). Eastern Ellesmere, Coburg and eastern Devon islands mineral inventory, NTS 29G, 38F and G, 39B, C, D, E, F, G and H, 48E and H, District of Franklin, N.W.T. Northwest Territories Mineral Assessment report no. 81743, 1-125.



- Hartlaub, R. P., Heaman, L. M., Chacko, T., & Ashton, K. E. (2007). Circa 2.3-Ga magmatism of the Arrowsmith orogeny, Uranium City region, western Churchill craton, Canada. *The Journal of Geology*, 115(2), 181-195.
- Hegner, E., & Jackson, G. D. (1990). Nd isotopic constraints on Late Archean and Early Proterozoic crust formation in Baffin and Ellesmere islands, northern Labrador and Ungava Peninsula, eastern Canada. *Eos, Transactions, American Geophysical Union*, 71, 1689.
- Hinchey, A. M., Davis, W. J., Ryan, J. J., Nadeau, L. (2011). Neoproterozoic high-potassium granites of the Boothia mainland area, Rae domain, Churchill Province: U-Pb zircon and Sm-Nd whole rock isotopic constraints 1. *Canadian Journal of Earth Sciences*, 48, 247–279.
- Hoffman, P. (1988). United plates of America, the birth of a craton: Early Proterozoic assembly and growth of Laurentia. *Annual Review of Earth and Planetary Sciences*, 16(1), 543–603.
- Hoffman, P. F., Bally, A. W., & Palmer, A. R. (1989). Precambrian geology and tectonic history of North America. *The geology of North America—an overview*, 447-512.
- Kitsul, V. I., Glebovitsky, V. A., Vapnik, Y. A., & Frisch, T. (2000). Gneisses from the granulite terrane of the central Boothia Uplift, Arctic Canada. *Canadian Mineralogist*, 38, 443–454.
- Krupička, J. (1973). Granulite facies rocks on northeastern Devon Island, Arctic Archipelago. *Geological Survey of Canada, Paper*, 73-8, 1–41.
- McDonough, M. R., McNicoll, V. J., Schetselaar, E. M., & Grover, T. W. (2000). Geochronological and kinematic constraints on crustal shortening and escape in a two-sided oblique-slip collisional and magmatic orogen, Paleoproterozoic Taltson magmatic zone, northeastern Alberta. *Canadian Journal of Earth Sciences*, 37(11), 1549–1573.

- Metzler, A., Ostertag, R., Redeker, H.-J., & Stöffler, D. (1988). Composition of the crystalline basement and shock metamorphism of crystalline and sedimentary target rocks at the Houghton impact crater, Devon Island, Canada. *Meteoritics*, 23(3), 197–207.
- Nutman, A. P., Dawes, P. R., Kalsbeek, F., & Hamilton, M. A. (2008). Palaeoproterozoic and Archaean gneiss complexes in northern Greenland: Palaeoproterozoic terrane assembly in the High Arctic. *Precambrian Research*, 161(3-4), 419–451.
- Pehrsson, S. J., Berman, R. G., & Davis, W. J. (2013). Paleoproterozoic orogenesis during Nuna aggregation: A case study of reworking of the Rae craton, Woodburn Lake, Nunavut. *Precambrian Research*, 232, 167–188.  
<https://doi.org/10.1016/j.precamres.2013.02.010>
- Pehrsson, S. J., Currie, M., Ashton, K. E., Harper, C. T., Paul, D., Pana, D., Berman, R. G., Bostock, H., Corkery, T., Jefferson, C. W., & Tella, S. (2014). Bedrock geology compilation and regional synthesis of south Rae and parts of Hearne domains, Churchill Province, Northwest Territories, Saskatchewan, Nunavut, Manitoba and Alberta [Map]. Natural Resources Canada. <https://doi.org/10.4095/292232>
- Peterson, T. D., Van Breemen, O., Sandeman, H., & Cousens, B. (2002). Proterozoic (1.85–1.75 Ga) igneous suites of the Western Churchill Province: granitoid and ultrapotassic magmatism in a reworked Archean hinterland. *Precambrian Research*, 119(1), 73–100.
- Rainbird, R. H., Davis, W. J., Pehrsson, S. J., Wodicka, N., Rayner, N., & Skulski, T. (2010). Early Paleoproterozoic supracrustal assemblages of the Rae domain, Nunavut, Canada: Intracratonic basin development during supercontinent break-up and assembly. *Precambrian Research*, 181(1), 167–186.
- Regis, D., Canam, R., & Martel, E. (2022). U-Pb geochronological results from the Nonacho Lake area (NTS 75-F), Northwest Territories (Geological Survey of Canada, Open File, Vol. 8880). Natural Resources Canada.

- Regis, D., & Sanborn-Barrie, M. (2022). Delimiting the extent of “Boothia terrane” crust, Nunavut: new U-Pb geochronological results (No. 978-0-660-45346-0; Geological Survey of Canada, Open File, Vol. 8917). Natural Resources Canada.
- Roots, E. F. (1963a). Cape Sparbo area. Geological Survey of Canada, Memoir, 320, 189-194.
- Roots, E. F. (1963b). Crystalline rocks west of South Cape. Geological Survey of Canada, Memoir, 320, 275-283.
- Sanborn-Barrie, M., Davis, W. J., Berman, R. G., Rayner, N., Skulski, T., & Sandeman, H. (2014). Neoproterozoic continental crust formation and Paleoproterozoic deformation of the central Rae craton, Committee Bay belt, Nunavut. *Canadian Journal of Earth Sciences*, 51(6), 635–667.
- Sanborn-Barrie, M., and Regis, R. (2020). 2.56–1.87 Ga evolution of the Rae cratonic margin: micro- to macro-scale constraints from Boothia Peninsula-Somerset Island, Nunavut, Geoconvention Abstracts.
- Sanborn-Barrie, M., Regis, D., & Ford, A. (2019). Integrated geoscience of the Northwest Passage, Nunavut; GEM-2 Boothia Peninsula-Somerset Island project, report of activities 2018. Geological Survey of Canada, Open File, 8557.
- Sanborn-Barrie, M., Regis, D., Ford, A., Osinchuk, A., & Drayson, D. (2018). Report of activities for the GEM-2 Boothia Peninsula-Somerset Island Project: integrated geoscience of the Northwest Passage, Nunavut. Geological Survey of Canada, Open File, 8339.
- Sanborn-Barrie, M., Thrane, K., Wodicka, N., & Rayner, N. (2017). The Laurentia – West Greenland connection at 1.9 Ga: New insights from the Rinkian fold belt. *Gondwana Research*, 51, 289–309.
- Schärer, U., & Deutsch, A. (1990). Isotope systematics and shock-wave metamorphism: II. U–Pb and Rb–Sr in naturally shocked rocks: the Houghton Impact Structure, Canada. *Geochimica et Cosmochimica Acta*, 54, 3435–3447.

- Schultz, M. E. J., Chacko, T., Heaman, L. M., Sandeman, H. A., Simonetti, A., & Creaser, R. A. (2007). Queen Maud block: A newly recognized Paleoproterozoic (2.4–2.5 Ga) terrane in northwest Laurentia. *Geology*, 35(8), 707.
- Skulski, T., Sandeman, H., Sanborn-Barrie, M., MacHattie, T., Young, M., Carson, C., Berman, R., Brown, J., Rayner, N., Panagapko, D., Byrne, D., & Deyell, C. (2003). Bedrock geology of the Ellice Hills map area and new constraints on the regional geology of the Committee Bay area, Nunavut. Geological Survey of Canada, Current Research, 2003-C22, 1–11.
- St-Onge, M. R., Van Gool, J. M., Garde, A., & Scott, D. J. (2009). Correlation of Archaean and Palaeoproterozoic units between northeastern Canada and western Greenland: constraining the pre-collisional upper plate accretionary history of the Trans-Hudson orogen. Geological Society, London, Special Publications, 318(1), 193–235.
- Thorsteinsson, R., & Mayr, U. (1987). The sedimentary rocks of Devon Island, Canadian Arctic Archipelago. Geological Survey of Canada, Memoir, 411, 1–182.
- van Breemen, O., Thompson, P. H., Hunt, P. A., & Culshaw, N. (1987). U-Pb zircon and monazite geochronology from the northern Thelon Tectonic Zone, District of Mackenzie. Radiogenic Age and Isotopic Studies, Report, 1, 87–82.
- Whalen, J. B., Berman, R. G., Davis, W. J., Sanborn-Barrie, M., & Nadeau, L. (2018). Bedrock geochemistry of the central Thelon Tectonic Zone, Nunavut (Geological Survey of Canada, Open File, Vol. 8234). Natural Resources Canada.
- Whitmeyer, S. J., & Karlstrom, K. E. (2007). Tectonic model for the Proterozoic growth of North America. *Geosphere*, 3(4), 220–259.

## Chapter 2

# 2 Late Neoproterozoic terrane and Paleoproterozoic HT–UHT metamorphism on southern Devon Island, Canadian Arctic

## 2.1 Introduction

The Laurentian shield constitutes the largest expanse of Precambrian rocks currently exposed on the Earth's surface. The north-central section of the Laurentian shield is dominated by the Archean Rae craton, primarily comprising amphibolite to granulite facies, Meso-Neoproterozoic ( $\geq 2.6$  Ga) plutonics and ca. 2.7–2.6 Ga supracrustal belts, intruded by Paleoproterozoic granitoids (Fig. 2.1a; e.g., Hoffman, 1988; Peterson et al., 2002; Berman et al., 2005; Hartlaub et al., 2007; Sanborn-Barrie et al., 2014). Along the western margin of the Rae craton are some younger, late Neoproterozoic (ca. 2.5–2.4 Ga) domains, including the eastern Queen Maud Block (Schultz et al., 2007; Davis et al., 2014) and Boothia Peninsula (Frisch and Hunt, 1993; Sanborn-Barrie et al., 2019) in the Canadian Arctic, and Prudhoe Land (Nutman et al., 2008) in northwestern Greenland. The Rae craton is separated from the Archean Slave craton to the west by the Thelon tectonic zone, a 50–100 km wide, Paleoproterozoic accretionary arc (Gibb and Thomas, 1977; Hoffman, 1988), comprising ca. 2.07–1.96 Ga plutonics (van Breemen et al., 1987; Berman et al., 2018) and subordinate ca. 2.09–1.91 Ga supracrustal rocks (Davis et al., 2021) bordered by the reworked margins of the Rae and Slave cratons. Continuations of the Thelon tectonic zone to the south and north are marked by the Taltson magmatic zone (e.g., Card et al., 2014) and Inglefield Mobile Belt (Nutman et al., 2008), respectively. The formation of these Paleoproterozoic arcs (Thelon, Taltson, Inglefield) is commonly attributed to collisional events between the Rae craton and the Slave craton, Buffalo Head terrane, and other intervening terranes (Hoffman, 1988). This caused widespread ca. 2.0–1.9 Ga upper-amphibolite to granulite facies metamorphism (e.g., Frisch and Hunt, 1993; Grover et al., 1996; Nutman et al., 2008), locally reaching ultrahigh temperature (UHT) conditions in the Taltson magmatic zone (Farquhar et al., 1996), and possibly in the Thelon tectonic zone and flanking domains (Kitsul et al., 2000). Earlier, more cryptic metamorphism along the western Rae craton has been attributed to the 2.5–2.3 Ga Arrowsmith orogeny (Berman et al., 2005), reaching peak metamorphic conditions of  $\sim 7$  kbar and 800 °C (Berman et al.,

2013). The Arrowsmith orogeny has been proposed as an Andean-type accretionary margin along the western margin of the Rae craton colliding with unknown continental block(s), the origin and history of which is currently debated (Berman et al., 2013).

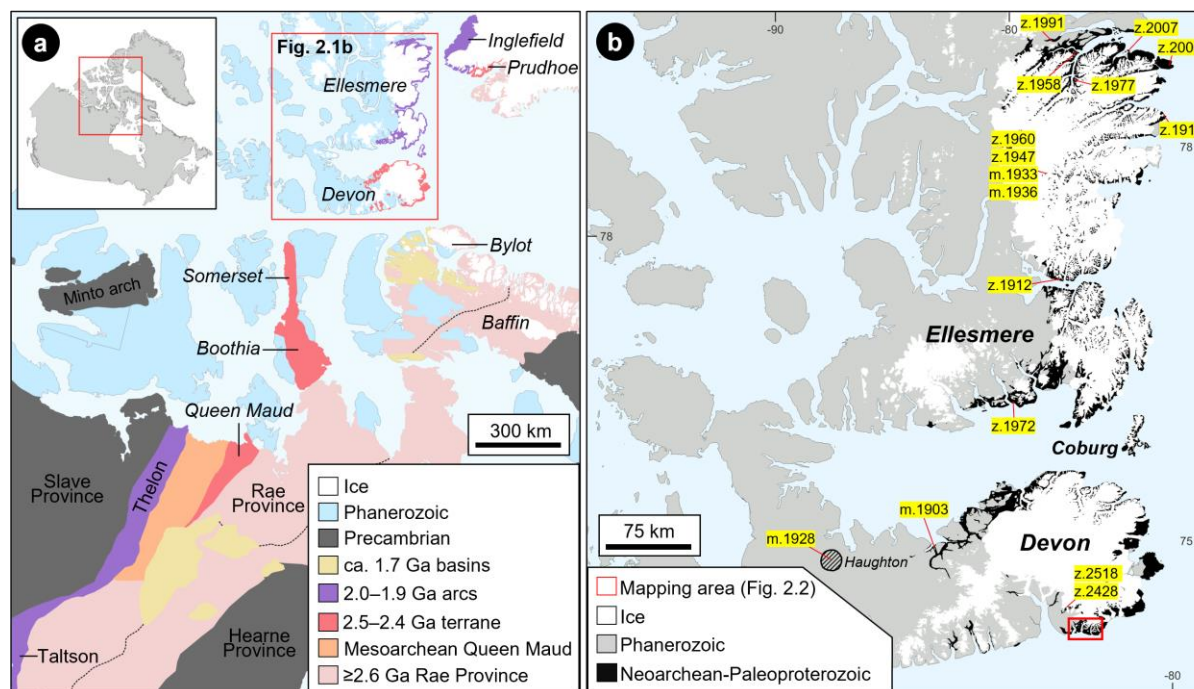


**Figure 2.1. (a) Geological setting of the northern Laurentian shield, highlighting the Rae craton and associated terranes. Map adapted after Davis et al. (2021), Nutman et al. (2008), and Sanborn-Barrie et al. (2019). The extent of ca. 2.5–2.4 Ga rocks on Devon Island and in Prudhoe Land is not well constrained, thus representing approximate boundaries. The dashed black line represents the easternmost extent of Arrowsmith metamorphism proposed by Berman et al. (2013). (b) Precambrian basement exposed on Devon and Ellesmere islands highlighting previously published zircon (z) and monazite (m) (Th)–U–Pb ages from Frisch (1988), Frisch and Hunt (1988), Schärer and Deutsch (1990) and Gilotti et al. (2018). At the Haughton impact structure on western Devon Island, the Precambrian basement is exposed as clasts within impact melt rocks (e.g., Metzler et al., 1988).**

The northernmost exposure of Laurentian shield rocks in Canada are on eastern Devon and southern Ellesmere islands, within the Canadian Arctic Archipelago (Fig. 2.1b). Limited previous research in this remote area suggests that southern and possibly northern Devon

Island is a late Neoproterozoic (ca. 2.5 Ga) terrane (Frisch, 1988; Frisch and Hunt, 1988; Hegner and Jackson, 1990; Schärer and Deutsch, 1990), whereas Ellesmere Island is a middle Paleoproterozoic (ca. 2.0–1.9 Ga) terrane (Frisch, 1988; Frisch and Hunt, 1988; Gilotti et al., 2018); both absent of  $\geq 2.6$  Ga Rae craton material. Devon and Ellesmere islands were reworked by at least one metamorphic event; ca. 1.9 Ga granulite facies metamorphism (Frisch, 1988; Frisch and Hunt, 1988), attributed to the Thelon–Inglefield orogeny (c.f. Gilotti et al., 2018; Caswell et al., 2021). Whereas the similarly aged Taltson and Thelon orogenies have been differentiated in the southern Rae domain (Card et al., 2014), there is currently insufficient aeromagnetic and geochronologic data available to discriminate between Thelon and Inglefield events in the Canadian Arctic Archipelago and northern Greenland. Thus, herein we refer to ca. 2.0–1.9 Ga ages from Devon and Ellesmere islands as Thelon–Inglefield. Pressure–temperature (P–T) constraints of Thelon–Inglefield metamorphism on Devon and Ellesmere islands have been previously estimated at 3–7 kbar and 500–750 °C (Frisch, 1988), but these are likely to reflect decompression and cooling conditions, rather than peak P–T conditions. Confirming the age of the oldest crust exposed on Devon and Ellesmere islands would help define the extent of the Rae craton and associated terranes in this poorly understood region the Laurentian shield. In addition, determining the peak P–T conditions of granulite facies metamorphism would give insight into the poorly constrained metamorphic conditions of the Thelon–Inglefield orogeny in this region.

In this contribution, we use in-situ zircon and monazite (Th)–U–Pb chronology on samples collected from southern Devon Island (Fig. 2.1b) to investigate whether the earliest crust-forming event in the Devon and Ellesmere islands region is late Neoproterozoic (ca. 2.5 Ga) or of  $\geq 2.6$  Ga Rae craton affinity. We also use zircon and monazite chronology to determine the timing of metamorphic events and phase equilibrium modelling to determine the peak P–T conditions of granulite facies metamorphism. Zircon and monazite results confirm southern Devon Island is a late Neoproterozoic terrane (ca. 2.55–2.47 Ga) – with no  $\geq 2.6$  Ga Rae craton material – reworked by granulite facies metamorphism at ca. 1.91 Ga during the Thelon–Inglefield orogeny and possibly earlier (ca. 2.54, 2.47 Ga, 2.30 Ga) during the Arrowsmith orogeny. Peak P–T conditions of ca. 1.91 Ga granulite facies metamorphism are estimated at ca. 9 kbar and  $>850$  °C, and the first sapphirine–quartz assemblage

discovered in the Canadian Arctic provides diagnostic evidence of local UHT metamorphism during the Thelon–Inglefield orogeny.

## 2.2 Geological setting

The Precambrian basement of eastern Devon and southern Ellesmere islands comprises granulite facies rocks with local amphibolite facies retrograde metamorphism (Frisch, 1988), which are overlain by Neoproterozoic and younger strata to the west and north (e.g., Thorsteinsson and Mayr, 1987). On Devon Island the regional gneissic fabric strikes east-west while on Ellesmere Island it strikes north-south, both fabrics are generally parallel to lithologic contacts and dip steeply throughout the region (Christie, 1967; Christie, 1978; Frisch, 1988). Three periods of folding have been recognized (Frisch, 1988): two earlier periods of isoclinal folding resulted in intense flattening with fold axes parallel to the gneissic fabric and a later period of broad, open folding, with fold axes primarily trending northwest. Higher deformational strain on Devon Island relative to Ellesmere Island is suggested by the greater abundance of shear zones and augen gneisses reported on Devon Island (Christie, 1978; Harrison, 1984; Frisch, 1988). The major rock types recognized on Devon and Ellesmere islands by Frisch (1988) include orthopyroxene-bearing quartzofeldspathic gneisses; metasedimentary rocks consisting of metapelite to metapsammite garnet–sillimanite–cordierite gneisses, quartzite, and marble; and coeval and younger granitoids. Compared to Ellesmere Island, marble is scarce on Devon Island, confined to minor occurrences in the northeast (Harrison, 1984; Frisch, 1988), suggesting the presence of more than one sedimentary sequence. Similarly, major bodies of granitoids are abundant on Ellesmere Island but have not been documented on Devon Island (Frisch, 1988).

On Ellesmere Island, Paleoproterozoic (2.01–1.91 Ga) zircon and monazite ages have been reported from the orthopyroxene-bearing gneisses and granitoids (Frisch, 1988; Frisch and Hunt, 1988, Gilotti et al., 2018). A population of zircon ages between ca. 2.01–1.96 Ga are magmatic protolith ages, comparable to the magmatic ages from the Thelon tectonic zone (ca. 2.07–1.96 Ga; van Breemen et al., 1987; Berman et al., 2018), and a younger population of ages between ca. 1.96–1.91 Ga from anatectic granites and monazite represent the timing of granulite facies metamorphism attributed to the Thelon–Inglefield



orogeny (c.f. Gilotti et al., 2018; Caswell et al., 2021). Whole-rock Nd model ages from Ellesmere Island of 2.1–2.0 Ga (Hegner and Jackson, 1990), further signify that Ellesmere Island is a juvenile Paleoproterozoic arc terrane. On northern Devon Island, Paleoproterozoic (1.93 Ga, 1.90 Ga; Schärer and Deutsch, 1990) monazite ages also suggest Thelon–Inglefield metamorphism, while late Neoproterozoic to early Paleoproterozoic (2.52 Ga, 2.43 Ga; Frisch, 1988; Frisch and Hunt, 1988) magmatic ages on southern Devon Island suggest an older Archean protolith, at least for southern Devon Island. Whole-rock Nd model ages from both northern and southern Devon Island have been reported in the range of 2.7–2.1 Ga (Hegner and Jackson, 1990; Schärer and Deutsch, 1990), suggesting Archean material could extend up to northern Devon Island.

Granulite facies assemblages and the presence of migmatites and anatectic granites throughout Devon and Ellesmere islands (Krupička, 1973; Harrison, 1984; Frisch, 1988), suggest high-temperature suprasolidus metamorphic conditions were widespread during the Thelon–Inglefield orogeny. P–T estimates of Thelon–Inglefield metamorphism on Devon and Ellesmere islands, primarily based on garnet–cordierite, garnet–pyroxene, and two-pyroxene thermobarometry, are in the range of 3–7 kbar and 500–750 °C (Frisch, 1988), reflecting decompression and cooling conditions, rather than peak metamorphism.

### 2.3 Field observations, petrography and geochemistry

Approximately 20-km south of the previously reported late Neoproterozoic ages (Fig. 2.1b), a 30-km section of the southern Devon Island coast, in the Dundas Harbour area (Talluruti), was mapped and sampled in summer 2018. A new geological map of the area is presented in Figure 2.2. Mineral assemblages of the major lithologies in our mapping area are summarized in Table 2.1. Representative samples were selected for whole-rock and mineral chemistry analysis. Whole-rock compositions were determined at ALS Laboratories (Sudbury) with the CCP-PKG01 analysis package. Major and trace elements were analyzed by inductively coupled plasma atomic emission spectroscopy (ICP-AES) and inductively coupled plasma mass spectrometer (ICP-MS) respectively. Mineral compositions were determined using a JEOL JXA-8530F field-emission electron microprobe at the Earth and Planetary Materials Analysis Laboratory, University of Western Ontario, Canada. Further details of the mineral chemistry analysis are provided in

Appendix A.2. Whole-rock chemistry results are presented in Appendix A.3 and are summarized below.

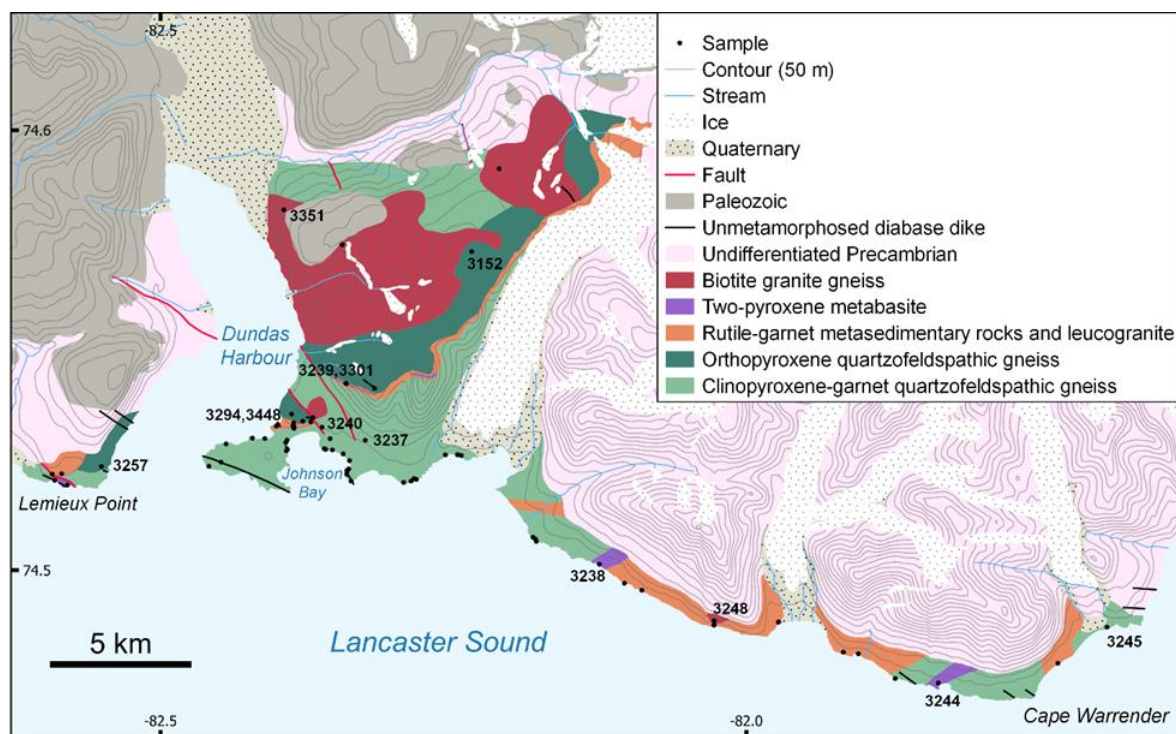


**Figure 2.2.** Geologic map of the Precambrian geology in the Dundas Harbour area (Talluruti) of southern Devon Island. Sample numbers are displayed for those discussed in the text.

**Table 2.1.** Representative mineral assemblages of the major lithologies. Minerals are ordered from highest to lowest model abundance on average. Mineral abbreviations follow Whitney and Evans (2010).

Rock type	Assemblage
cpx-grt quartzofeldspathic gneiss	pl+kfs+qz+grt+cpx+ap+ilm( $\pm$ hbl $\pm$ bt $\pm$ mag)
opx quartzofeldspathic gneiss	pl+kfs+qz+opx+ap+ilm( $\pm$ hbl $\pm$ bt $\pm$ mag $\pm$ cpx $\pm$ grt)
rt-grt metasedimentary rocks	pl+kfs+grt+qz+rt+ilm( $\pm$ bt $\pm$ mag $\pm$ sil $\pm$ spr $\pm$ spl $\pm$ crd)
rt-grt leucogranite	pl+kfs+qz+grt+rt+ilm ( $\pm$ bt $\pm$ mag)
two-px metabasite	pl+cpx+opx ( $\pm$ hbl $\pm$ bt $\pm$ qz $\pm$ ilm $\pm$ mag $\pm$ ap)
bt granite gneiss	kfs+qz+pl+ilm+mag ( $\pm$ bt $\pm$ opx $\pm$ ap)

The gneissic foliation in this area of southern Devon Island is generally parallel to lithological contacts, on average striking southwest at 230° and dipping northwest at 30°, with minor local variations. Intense ductile deformation is apparent from predominant feldspar augen and quartz ribbon textures observed throughout all units; the former defining a penetrative lineation in most outcrops, trending and dipping parallel to dip of the gneissic foliation.

### 2.3.1 Clinopyroxene–garnet quartzofeldspathic gneiss

The most abundant unit in the mapping area is a garnet– and clinopyroxene–bearing quartzofeldspathic gneiss with a two-feldspar (plagioclase and subordinate K-feldspar) augen texture (Figs. 2.3a–b, 2.4a). Plagioclase augen are composed of recrystallized polycrystalline grains, although some of the larger augen have relict monocrystalline cores surrounded by recrystallized rims of plagioclase and K-feldspar. Plagioclase compositions are generally homogenous with an average anorthite content of An<sub>0.38</sub>, but some larger augen cores are zoned with anorthite content increasing inward up to An<sub>0.52</sub>, suggestive of an igneous protolith. K-feldspar augen are all polycrystalline aggregates composed of smaller grains, compared to plagioclase; and between the feldspar augen are plastically deformed, polycrystalline quartz ribbons. Garnet porphyroclasts are located within the recrystallized rims of feldspar augen and exhibit a narrow compositional range with diagnostically high grossular (0.20–0.23) and low pyrope (0.07–0.11) contents, with no major elemental zoning. Hedenbergite clinopyroxene (Morimoto, 1988) (Fs<sub>0.26–0.30</sub>, En<sub>0.25–0.28</sub>, Wo<sub>0.45–0.46</sub>) outlines the perimeter of quartz ribbons and has a low sodium content (0.028–0.038 cpfu for 6 oxygen). Varying amounts (~0–3 vol.%) of hornblende and subordinate biotite are present in most outcrops but appear to be replaced by and lesser to clinopyroxene in most instances. Minor phases include ilmenite with lesser magnetite, relatively abundant apatite (1–2 vol.%), zircon and allanite. Melanocratic, feldspar-absent layers composed of garnet, clinopyroxene, and quartz assemblages were observed in most outcrops (Figs. 2.3c, 2.4b). These layers are adjacent to feldspar and quartz dominated leucocratic layers, suggestive of partial melting within the clinopyroxene–garnet quartzofeldspathic gneiss.

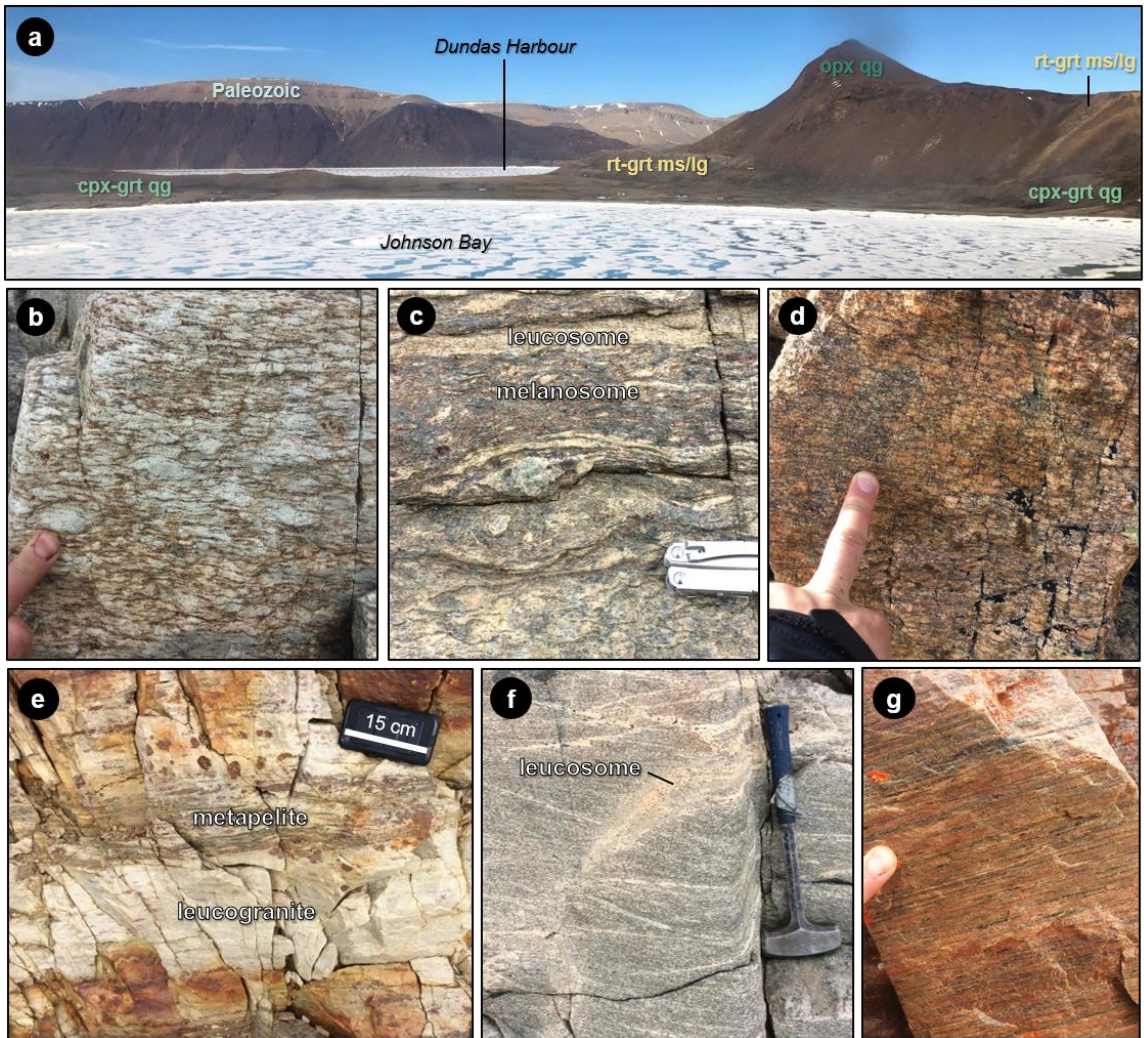


**Figure 2.3.** Field photos of the major lithologies on southern Devon Island. (a) Overview of the mapping area facing northwest above Johnson Bay. Field of view is ~3-km. Clinopyroxene–garnet quartzofeldspathic gneiss (cpx-grt qq) outcrops along the coast of Johnson Bay, underlying rutile–garnet metasedimentary rocks and leucogranite (rt-grt ms/lg) and orthopyroxene quartzofeldspathic gneiss (opx qq). (b) Clinopyroxene–garnet quartzofeldspathic gneiss with white plagioclase augen and subordinate pink K-feldspar augen. (c) Clinopyroxene–garnet quartzofeldspathic gneiss showing a feldspar-dominant leucosome and garnet–clinopyroxene dominant melanosome. A large (~3 cm) clinopyroxene porphyroclast is in the centre of the image. (d) Orthopyroxene quartzofeldspathic gneiss with a two-feldspar augen

texture. (e) Rutile–garnet metapelite lens within rutile–garnet leucogranite. (k) Two-pyroxene metabasite with tonalitic leucosome. (l) Flattened biotite granite gneiss.

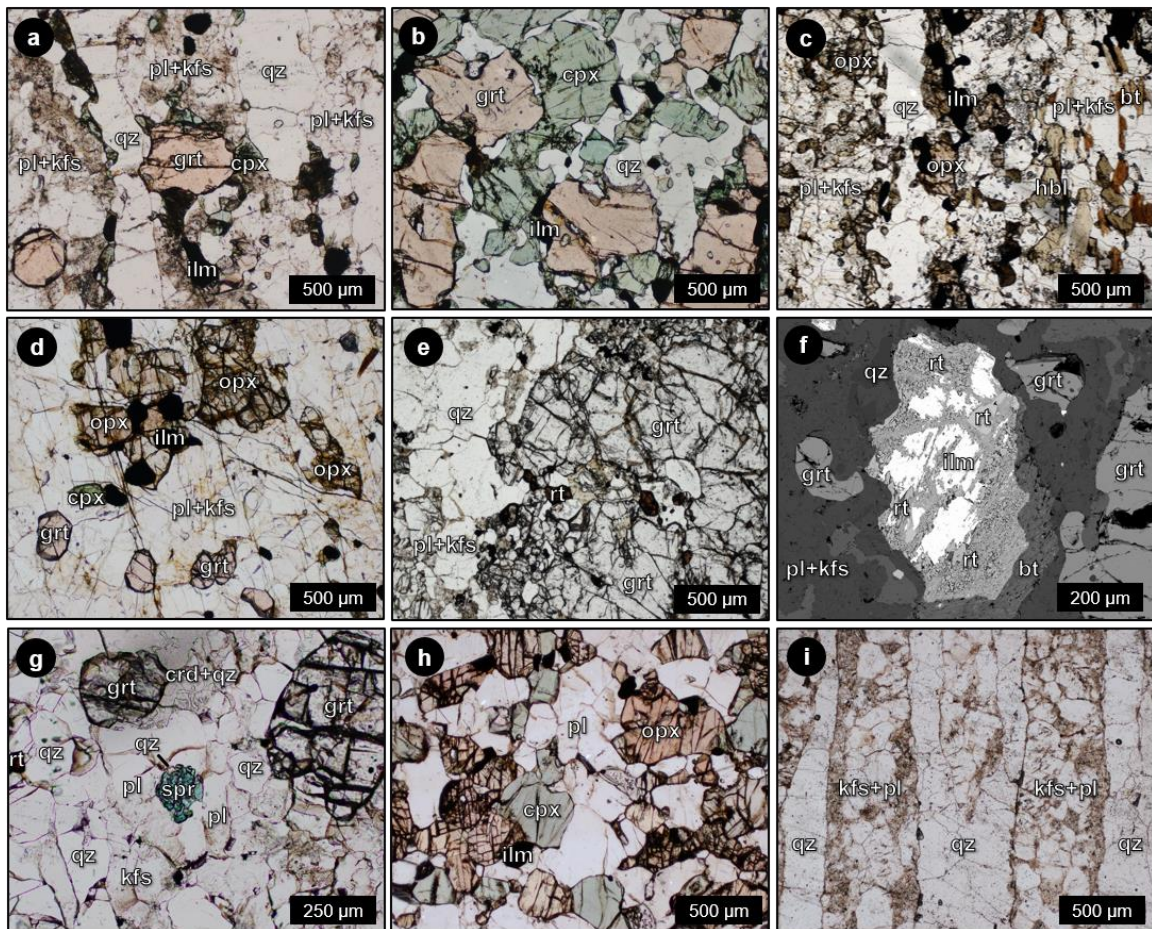


**Figure 2.4. Photomicrographs of the major lithologies on southern Devon Island. (a)** Clinopyroxene–garnet quartzofeldspathic gneiss with garnet and clinopyroxene around quartz ribbons and a feldspar matrix. **(b)** Feldspar-absent, clinopyroxene, garnet, and quartz melanocratic lens within clinopyroxene–garnet quartzofeldspathic gneiss. **(c)** Orthopyroxene quartzofeldspathic gneiss with orthopyroxene around a quartz ribbon, lesser hornblende and biotite, and a feldspar matrix. **(d)** Orthopyroxene quartzofeldspathic gneiss with garnet and clinopyroxene in the equilibrium assemblage. **(e)** Rutile–garnet metapelite with minor biotite and sillimanite, and a quartz–feldspar matrix. **(f)** Backscattered electron image showing rutile replacing ilmenite in a rutile–garnet metapelite. Rutile forms a rim around the ilmenite core, both of which are affected by post-peak metamorphic alteration. **(g)**

**Sapphirine–quartz assemblage from an outcrop of rutile–garnet metasedimentary rocks. The centered sapphirine grain is surrounded by plagioclase and quartz. A symplectic cordierite–quartz intergrowth above the sapphirine is replacing garnet. (h) Two-pyroxene metabasite with a granoblastic texture of plagioclase, orthopyroxene and clinopyroxene. (i) Biotite granite gneiss with quartz ribbons and flattened polycrystalline feldspar augen.**

### 2.3.2 Orthopyroxene quartzofeldspathic gneiss

Structurally overlying the clinopyroxene–garnet quartzofeldspathic gneiss, are darker-coloured, orthopyroxene-bearing quartzofeldspathic gneisses with the same two-feldspar augen texture (Figs. 2.3d, 2.4c). The main difference between pyroxene quartzofeldspathic gneiss variants is the presence of orthopyroxene over garnet and clinopyroxene. Orthopyroxene is ferrosilite ( $\text{Fs}_{0.52}$ ,  $\text{En}_{0.46-0.47}$ ,  $\text{Wo}_{0.01}$ ), with low aluminum content [ $y(\text{opx}) = 0.01-0.03$ ;  $y(\text{opx}) = \text{Al}-(2\text{-Si})$ ]; and plagioclase is more anorthite-rich ( $\text{An}_{0.42}$ ) compared to clinopyroxene–garnet quartzofeldspathic gneiss. This unit also includes an increase in hornblende and biotite modal abundances and a decrease in quartz. Only one sample (3257), collected from the western shore of Dundas Harbour, contains an orthopyroxene (10 vol.%), clinopyroxene (1 vol.%) and garnet (1 vol.%) assemblage (Fig. 2.4d).

Both variants of pyroxene quartzofeldspathic gneisses are metaluminous and display similar REE profiles with moderate HREE values ( $\text{Gd}_N/\text{Yb}_N = 2.6-3.6$ ) relative to the other units (Fig. 2.5). The main geochemical difference between the two variants is a more mafic composition for orthopyroxene quartzofeldspathic gneiss ( $X_{\text{Mg}} = 0.29-0.47$ ) compared to clinopyroxene–garnet quartzofeldspathic gneiss ( $X_{\text{Mg}} = 0.21-0.22$ ).

### 2.3.3 Rutile–garnet metasedimentary rocks and leucogranite

Structurally above and below the pyroxene quartzofeldspathic gneisses is rusty-weathered rutile– and garnet–bearing anatectic metapelite to metapsammite (Figs. 2.3e, 2.4e). Partial melting of these metasedimentary rocks is apparent by concordant layers of bright-white rutile– and garnet–bearing leucogranite, which are deformed and parallel to the foliation of the host metasedimentary rocks. Metasedimentary assemblages are dominated by plagioclase ( $\text{An}_{0.30-0.40}$ ) with subordinate K-feldspar and quartz, up to 50 vol.% garnet and

consistently around 1–2 vol.% rutile, with minor ilmenite, biotite, magnetite, sillimanite, or spinel. Leucogranite assemblages are similar, but with an increase in leucocratic minerals, lesser garnet, rutile, iron-oxides, and little to no biotite or sillimanite. For both units, rutile commonly replaces larger grains of ilmenite (Fig. 2.4f). Garnet has low grossular (0.03–0.12) and high pyrope (0.29–0.36) contents, with minor grossular zoning from core (0.03) to rim (0.05) in larger grains. Rutile–garnet metasedimentary rocks and leucogranite are both peraluminous, but metasedimentary rocks are enriched in HREE ( $Gd_N/Yb_N = 1.0$ ) relative to leucogranite ( $Gd_N/Yb_N = 0.3$ ), likely due to differing garnet modes.

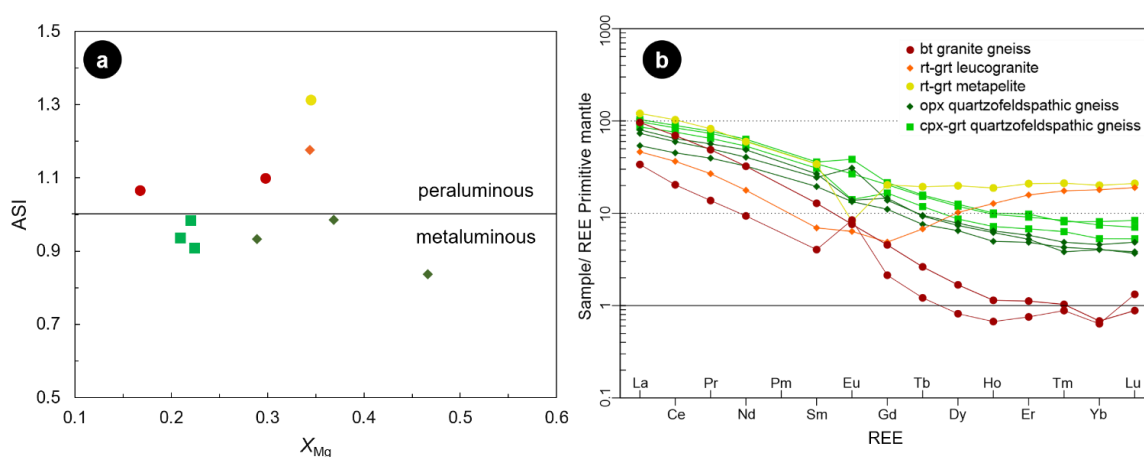


**Figure 2.5. (a) Whole-rock ASI [molar  $Al_2O_3/(CaO+Na_2O+K_2O)$ ] versus  $X_{Mg}$  [molar  $MgO/(MgO+FeO)$ ]. (b) Whole-rock primitive mantle normalized rare-earth element profiles with primitive mantle values from McDonough and Sun (1995).**

Sapphirine was observed in one rutile–garnet metapelite sample (3294), with a diagnostic UHT assemblage (e.g., Kelsey and Hand, 2015) of quartz, K-feldspar, plagioclase, garnet, sillimanite, rutile, sapphirine, spinel, and ilmenite. Quartz makes up ~20 vol.% of the sample, with sapphirine and spinel making up ~1 vol.%. Sapphirine and quartz are commonly separated by plagioclase, but direct contact was observed in at least one instance (Fig. 2.4g). Sapphirine has  $x(spr)$  [ $Fe^{2+}/(Fe^{2+}+Mg^{2+})$ ] values between 0.21–0.22; and reduced  $f(spr)$  ( $Fe^{3+}$  cpfu) values between 0.09–0.14 for 20 oxygen. This sample also contains cordierite–quartz symplectic intergrowths after garnet (Fig. 2.4g), which is the only occurrence of cordierite in our mapping area.

### 2.3.4 Two-pyroxene metabasite

Commonly nearby rutile–garnet metasedimentary rocks are enclaves, thin concordant layers, or larger bodies of dark-grey two-pyroxene metabasite (Figs. 2.3f, 2.4h), representative of supracrustal metavolcanics or metaplutonic sills. Concordant layers or enclaves of two-pyroxene metabasite within rutile–garnet metasedimentary rocks typically have a granoblastic texture (Fig. 2.6c), while some of the larger bodies exhibit a weak augen texture (Fig. 2.6b). Partial melting of the two-pyroxene metabasite is evident by varying degrees of leucosome development in outcrop (Fig. 2.3f). Plagioclase ( $An_{0.41-0.89}$ ), clinopyroxene ( $Fs_{0.12-0.20}$ ,  $En_{0.35-0.41}$ ,  $Wo_{0.45-0.48}$ ) and orthopyroxene ( $Fe_{0.31-0.47}$ ,  $En_{0.52-0.68}$ ,  $Wo_{0.00-0.01}$ ) make up the majority of the metabasite assemblages. Hornblende and subordinate biotite are present in varying amounts (~0–10 vol.%) but are always subordinate to pyroxene. Minor quartz is present in some outcrops but is typically absent and garnet is absent from all two-pyroxene metabasite outcrops observed. Minor ilmenite, magnetite, zircon, and apatite are also present.

### 2.3.5 Biotite granite gneiss

Strongly flattened, pinkish-red, peraluminous biotite monzogranite to syenogranite gneisses outcrop predominantly within the pyroxene quartzofeldspathic gneisses east of Dundas Harbour (Figs. 2.3g, 2.4i). No direct contact relationships with the pyroxene quartzofeldspathic gneisses were observed in outcrop but possible intrusive contacts were observed in float rocks with orthopyroxene quartzofeldspathic gneiss. Mineral assemblages are dominantly composed of K-feldspar, quartz, and plagioclase, with minor biotite or lesser orthopyroxene. Minor phases also included ilmenite, magnetite, zircon, and monazite.

## 2.4 Phase equilibrium modelling

Phase equilibrium modelling was performed to determine the peak P–T conditions of metamorphism. Pyroxene quartzofeldspathic gneiss and two-pyroxene metabasite assemblages were modelled in the 10-component  $Na_2O$ - $CaO$ - $K_2O$ - $FeO$ - $MgO$ - $Al_2O_3$ - $SiO_2$ - $H_2O$ - $TiO_2$ - $Fe_2O_3$  (NCKFMASHTO) chemical system using the activity-composition models of Green et al. (2016) and a rutile–garnet metapelite assemblage was modelled in



the 11-component MnO-Na<sub>2</sub>O-CaO-K<sub>2</sub>O-FeO-MgO-Al<sub>2</sub>O<sub>3</sub>-SiO<sub>2</sub>-H<sub>2</sub>O-TiO<sub>2</sub>-Fe<sub>2</sub>O<sub>3</sub> (MnNCKFMASHTO) chemical system using the activity-composition models of White et al. (2014a) and White et al. (2014b). All were modelled using the internally consistent thermodynamic database (ds62) of Holland and Powell (2011) and the THERMOCALC 3.50 software package (Powell and Holland, 1988).

Bulk rock compositions were determined by thin section analysis using mineral chemistry and modes for samples: 3237, 3238, 3239 and 3301 (Fig. 2.6), and by whole-rock chemical analysis for samples 3240 and 3257 (Table 2.2). Mineral modes were estimated by element map analysis using the XMapTools 3.4.1 software program (Lanari et al., 2014). All minerals were included in the bulk rock composition estimation except for apatite. H<sub>2</sub>O was estimated assuming stoichiometric proportions within each hydrous phase (biotite, hornblende), and ferric iron was estimated by charge-balance calculations (e.g., Droop, 1987). For the pyroxene quartzofeldspathic gneisses modelled with whole-rock compositions (3240, 3257), the same H<sub>2</sub>O and ferric iron proportions were used from the comparable pyroxene quartzofeldspathic gneiss (3237) composition determined by thin section analysis. For clinopyroxene–garnet quartzofeldspathic gneiss 3240, the H<sub>2</sub>O content was increased to 0.25 mol.% to compensate for additional hornblende and biotite observed in thin section.

Suprasolidus isochemical phase diagrams in the P–T space of 4–12 kbar and 700–1000 °C respectively, are presented in Figure 2.7. Clinopyroxene–garnet quartzofeldspathic gneiss 3237 has a peak metamorphic assemblage of garnet, clinopyroxene, plagioclase, K-feldspar, quartz, ilmenite, and melt (Fig. 2.6a). The minor amount (0.5 vol.%) of hornblende in the sample is assumed to have formed during the cooling path and thus is not included in the peak assemblage. This peak stability field is predicted at >820–785 °C with increasing pressure (Fig. 2.7a). The absence of orthopyroxene constrains the minimum pressure to >7.6 kbar, whereas the absence of titanite or rutile constrains the maximum pressure to ca. <11 kbar. Garnet is predicted at pressures >5.7–8.9 kbar with increasing temperature. Garnet and clinopyroxene isomodes nearly reproduce the observed assemblages (6 and 5 vol.% respectively) in the lower pressure and higher temperature portion of the peak field.

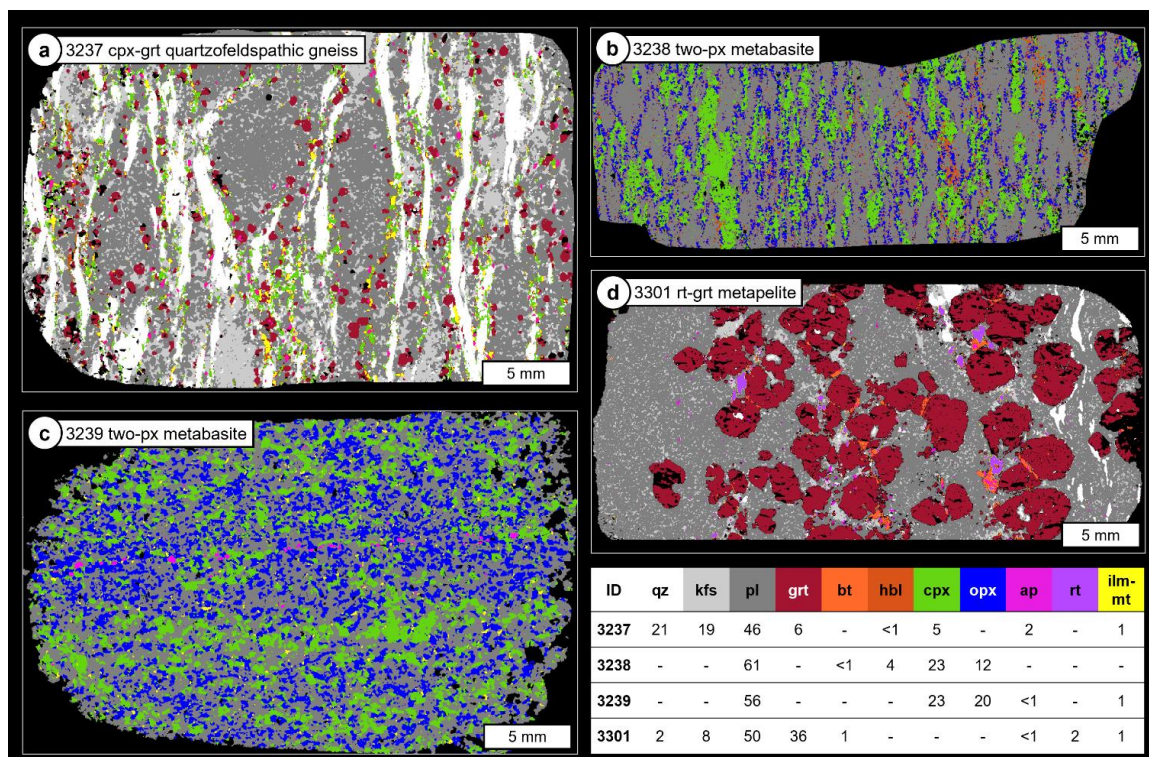


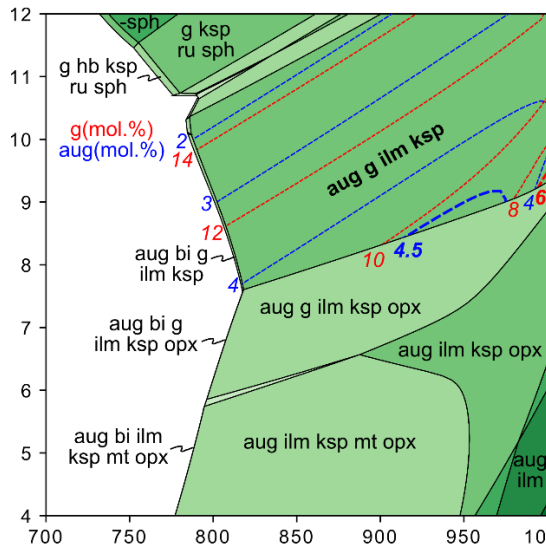
**Figure 2.6. Phase maps of thin sections used for phase equilibrium modelling. Phase proportions for each sample are listed in the inset table.**

Two-pyroxene metabasite 3238 has a peak assemblage of clinopyroxene, orthopyroxene, hornblende, plagioclase, and melt (Fig. 2.6b). The minor amount (<0.1 vol.%) of biotite and quartz present in thin section are assumed to be retrograde or relict prograde phases, or possible melt crystallization in the case of quartz. The stability field for this assemblage, plus <0.1 mol.% of rutile, is predicted at >890 °C and <10 kbar (Fig. 2.7b). Below ca. 8 kbar ilmenite replaces rutile however, neither oxide is present in this sample. Above 10 kbar, garnet becomes stable, but was not observed in any two-pyroxene metabasite outcrops. Orthopyroxene isomodes closely model the 12 vol.% orthopyroxene observed in the sample, favoring the higher pressure and lower temperature portion of the rutile-bearing field. Clinopyroxene modes are higher than observed (23 vol.%), which has been shown for other metabasites modelled with the Green et al. (2016) models (e.g., Forshaw et al., 2019).

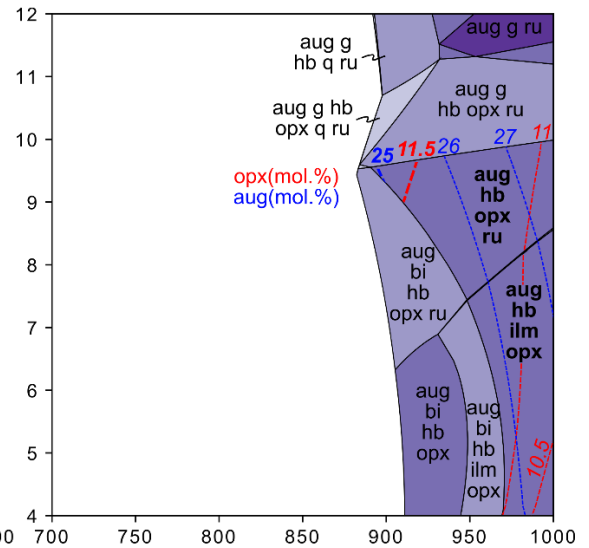
**Table 2.2. Bulk rock compositions (mol.%) used for phase equilibrium modelling. TS: bulk composition from thin section analysis. WR: bulk composition from whole-rock chemical analysis.  $X_{\text{Fe}^{3+}} = \text{O}(\text{Fe}_2\text{O}_3)/\text{FeO} \cdot 2$ .**

Sample	Rock type	Method	H <sub>2</sub> O	SiO <sub>2</sub>	Al <sub>2</sub> O <sub>3</sub>	CaO	MgO	FeO	K <sub>2</sub> O	Na <sub>2</sub> O	TiO <sub>2</sub>	MnO	O	$X_{\text{Fe}^{3+}}$
3237	cpx-grt gneiss	TS	0.02	70.12	10.69	6.11	1.27	5.34	1.95	3.29	0.89	-	0.32	0.12
3238	two-px metabasite	TS	0.51	52.35	12.05	15.81	11.81	4.78	0.22	1.97	0.17	-	0.35	0.15
3239	two-px metabasite	TS	0.01	52.57	10.23	14.06	11.35	8.92	0.06	1.90	0.60	-	0.31	0.07
3240	cpx-grt gneiss	WR	0.25	69.67	10.18	4.94	1.76	5.97	2.33	3.60	0.95	-	0.35	0.12
3257	cpx-grt-opx gneiss	WR	0.02	68.73	9.64	5.07	3.08	6.82	2.09	3.17	0.99	-	0.40	0.12
3301	rt-grt metapelite	TS	0.18	55.18	14.40	4.37	7.15	12.63	0.85	3.45	1.48	0.24	0.07	0.01

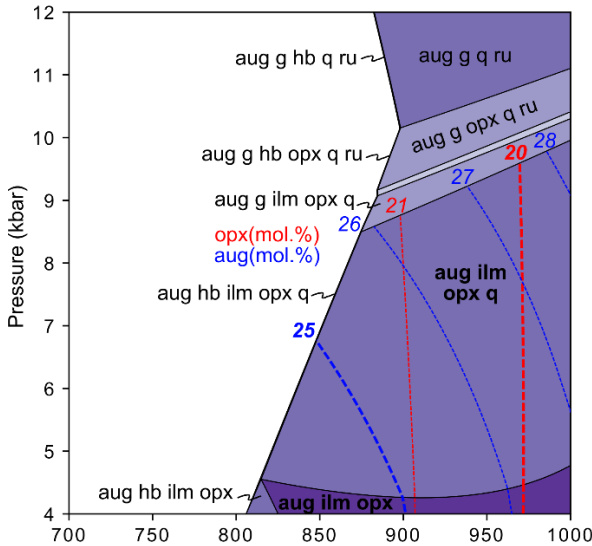
(a) 3237 cpx-grt quartzofeldspathic gneiss (+L +pl +q)



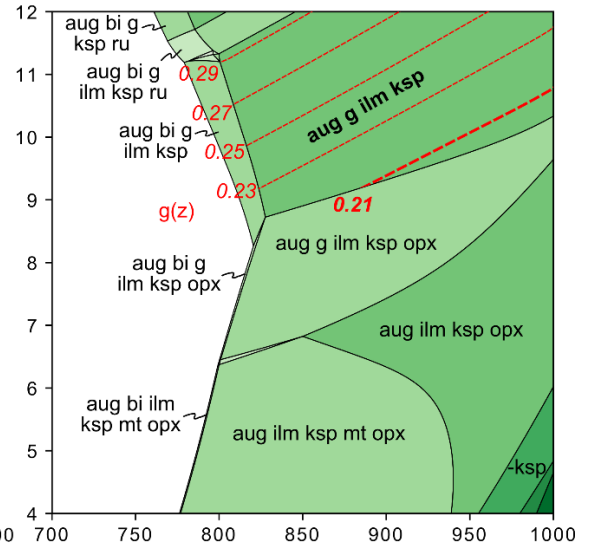
(b) 3238 two-px metabasite (+L +pl)



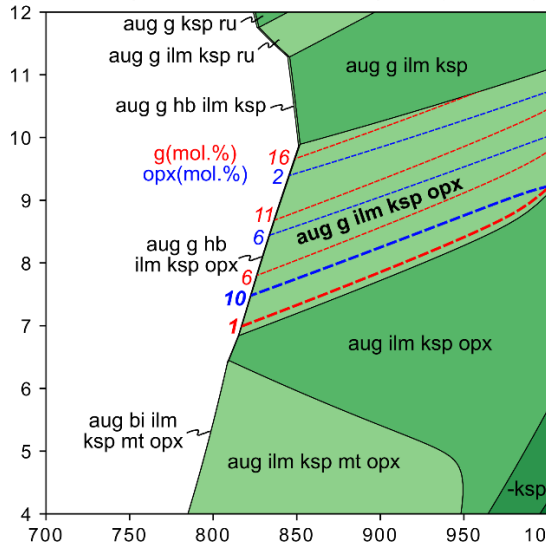
(c) 3239 two-px metabasite (+L +pl)



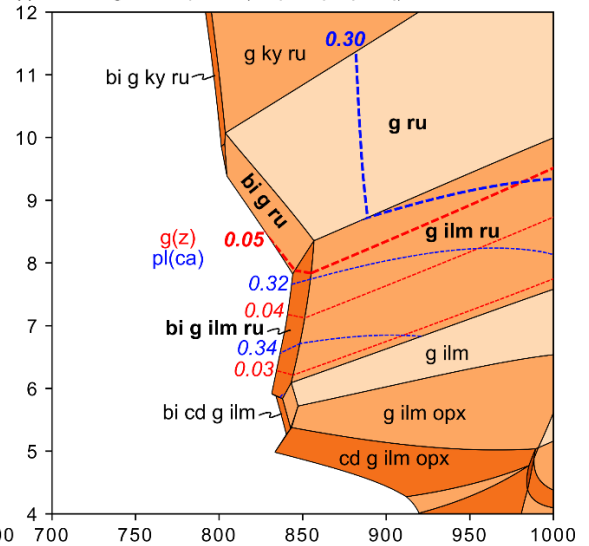
(d) 3240 cpx-grt quartzofeldspathic gneiss (+L +pl +q)



(e) 3257 cpx-grt-opx quartzofeldspathic gneiss (+L +pl +q)



(f) 3301 rt-grt metapelite (+liq +ksp +pl +q)



Temperature (°C)

**Figure 2.7. Suprasolidus  $P$ – $T$  isochemical phase diagrams. Inferred peak metamorphic assemblage fields are bolded. Isolines are shown as red or blue dashed lines, only within the inferred peak metamorphic assemblage fields. Isolines are bolded for the closest modelled proportions to the observed mineral modes and compositions. One-oxide normalized mol.% is approximately equivalent to vol.%.  $g(z) = \text{Ca}/[\text{Fe}+\text{Mg}+\text{Ca}(+\text{Mn})]$ ;  $pl(\text{ca}) = \text{Ca}/(\text{Ca}+\text{Na}+\text{K})$ . Grossular proportions for (f) are  $g(z) = 0.05$  across the entire garnet and rutile stability field. The unmodeled fields represent subsolidus  $P$ – $T$  space. Mineral abbreviations follow the activity-composition models used.**

The second two-pyroxene metabasite (3239) has a peak assemblage of orthopyroxene, clinopyroxene, plagioclase, ilmenite, and melt (Fig. 2.6c). Hornblende, biotite, and quartz are absent from the sample; the only other phase being a minor layer of apatite. The stability field for the peak assemblage, plus <0.1 vol.% of quartz, is predicted at >815 °C and <8.5–10 kbar with increasing temperature (Fig. 2.7c). The absence of garnet and rutile defines the maximum pressure limit. The essentially anhydrous bulk rock composition used for modelling (0.01 mol.% H<sub>2</sub>O) allowed for minor quartz stability down to ca. 4.5 kbar and >1000 °C even though it is not observed in thin section. The observed 20 mol.% of orthopyroxene is modelled at ca. 975 °C. Clinopyroxene modes are again higher than the observed mode (23 mol.%) throughout the entire peak stability fields.

The second clinopyroxene–garnet quartzofeldspathic gneiss (3240) has the same peak assemblage of garnet, clinopyroxene, plagioclase, K-feldspar, quartz, ilmenite, and melt. This sample contains more biotite and hornblende (~2 vol.% total) but both are still interpreted as retrograde phases. The stability field for the peak assemblage is predicted at >830–800 °C with increasing pressure (Fig. 2.7d). The absence of orthopyroxene constrains the minimum pressure to >8.7 kbar, whereas the absence of rutile constrains the maximum pressure to ca. <11.5 kbar. If biotite is assumed to be involved in the peak assemblage,  $P$ – $T$  constraints are reduced to 8.3–11.3 kbar and 780–830 °C. Garnet is predicted at pressures >6.4–9.7 kbar with increasing temperature. Grossular isopleths model the observed garnet composition [ $g(z) = 0.21$ ] in the lower pressure and higher temperature portion (ca. <10.5 kbar, >900 °C) of the peak stability field.

The clinopyroxene– and garnet–bearing orthopyroxene quartzofeldspathic gneiss (3257) has a peak assemblage of orthopyroxene, garnet, clinopyroxene, plagioclase, K-feldspar, quartz, ilmenite, and melt. The stability field for this peak assemblage is predicted at >820–850 °C with increasing pressure (Fig. 2.7e). The presence of coexisting orthopyroxene, clinopyroxene, and garnet constrains the pressure to <9.9–11.1 kbar and >6.9–9.1 kbar with increasing temperature. Garnet is predicted at pressures >6.9–9.1 kbar with increasing temperature. The observed thin section assemblage containing 1 vol.% garnet and 10 vol.% orthopyroxene favours the lower pressure portion (ca. 7–9 kbar) of the peak stability field. For all three quartzofeldspathic gneiss samples (3237, 3240, 3257), magnetite is not predicted in the inferred peak stability fields as it is restricted to pressures <7 kbar, within garnet absent and orthopyroxene present fields.

Rutile–garnet metapelite 3301 has a peak assemblage of garnet, plagioclase, K-feldspar, quartz, rutile, and melt (Fig. 2.6d). The 1 mol.% of biotite in this sample is interpreted as relict prograde grains that have been shielded by the large garnet grains. The 1 mol.% of ilmenite occurs as relict cores that have been replaced by rutile and are not interpreted as part of the peak assemblage (Fig. 2.4f). The stability field for the peak assemblage is predicted at >8.4 kbar and >800 °C (Fig. 2.7f). If ilmenite is included in the peak assemblage, this changes the modelled pressure constraints to >6 kbar and ca. <9 kbar. Garnet isopleths model the observed grossular ratios [ $g(z) = 0.05$ ] across the entire garnet–rutile stability field and plagioclase isopleths model the observed anorthite proportions [ $pl(ca) = 0.30$ ] at 8.5–11 kbar and ca. 900 °C. The intersection of the observed grossular and anorthite proportions is at 9.3 kbar and 980 °C in the garnet + rutile + ilmenite field.

## 2.5 LA-ICP-MS zircon geochronology

In-situ U–Pb zircon geochronology was performed to determine the age of protolith emplacement and granulite facies metamorphism. All zircon  $\geq 25$   $\mu\text{m}$  were imaged with cathodoluminescence (CL) and backscattered electron (BSE) imaging on a JEOL JXA-8530F field-emission electron microprobe at the Earth and Planetary Materials Analysis Laboratory, University of Western Ontario. Analytical conditions included a 50 nA beam current, 1  $\mu\text{m}$  beam diameter and 0.2 msec dwell time. U–Pb zircon geochronology was conducted at the Metal Isotope Geochemistry Laboratory, University of Waterloo using a

Photon Machines Analyte G2 laser ablation system in combination with an Agilent 8800 triple quadrupole ICP-MS. A 25  $\mu\text{m}$  diameter laser spot size operating at 7 Hz and with an energy (measured at the sample surface) of 4  $\text{J}/\text{cm}^2$  was used for all analyses. Prior to analysis, 2 pre-ablation shots (40  $\mu\text{m}$  laser diameter) were used to remove surface contamination. This was followed by a 30 s gas background measurement and then 30 s of ablation. Ablated aerosol was carried to the ICP-MS using  $\sim 1.1$  L/min He carrier gas in a Helix ablation cell and mixed with  $\sim 1.1$  L/min argon makeup gas added in a mixing bulb after the cell. The following masses were analyzed (integration times in ms):  $^{238}\text{U}$  (20 ms),  $^{232}\text{Th}$  (10 ms),  $^{207}\text{Pb}$  (70 ms),  $^{206}\text{Pb}$  (30 ms) and  $^{88}\text{Sr}$  (10 ms) in single collector mode.

One to five spots were analyzed on each zircon depending on the size and zoning complexity of the grain. Several reference materials were analyzed to correct for instrumental and downhole fractionation every 5–6 analyses of unknowns; primary reference materials included 91500 (Wiedenbeck et al., 1995) for relatively low-U analyses and Plešovice (Slama et al., 2008) for relatively high-U analyses. Data were processed in Iolite (v3.6) using the U–Pb geochronology 4 data reduction scheme (Paton et al., 2011). Secondary reference materials included Temora 2, which yielded a weighted mean  $^{206}\text{Pb}/^{238}\text{U}$  age of  $419 \pm 2$  Ma (2s;  $n = 10$ ) that is slightly higher than the accepted age of 417 Ma (Black et al., 2004). An additional secondary zircon reference material (R33) yielded an age of  $^{206}\text{Pb}/^{238}\text{U}$  age  $415 \pm 2$  Ma (2s;  $n = 10$ ), which is slightly lower than the accepted age of 419 Ma (Black et al., 2004). All isotopic ratios and calculated ages are reported with a  $2\sigma$  error at the 95% confidence level. Concordia plots and weighted mean ages were calculated with IsoplotR (Vermeesch, 2018). The results of zircon geochronology are presented in Figure 2.8 and Appendix A.4.

All 130 zircon analyses across the six samples yield a continuous array of  $^{207}\text{Pb}/^{206}\text{Pb}$  dates from ca. 2.60 to 1.77 Ga. A discordia line with all 130 analyses yields poorly-constrained upper and lower intercept dates of  $2516 \pm 10$  Ma and  $1832 \pm 13$  Ma (MSWD = 9.6) respectively. Th/U ratios range between 0.06 to 2.31, with majority of analyses between 0.15–1.50.

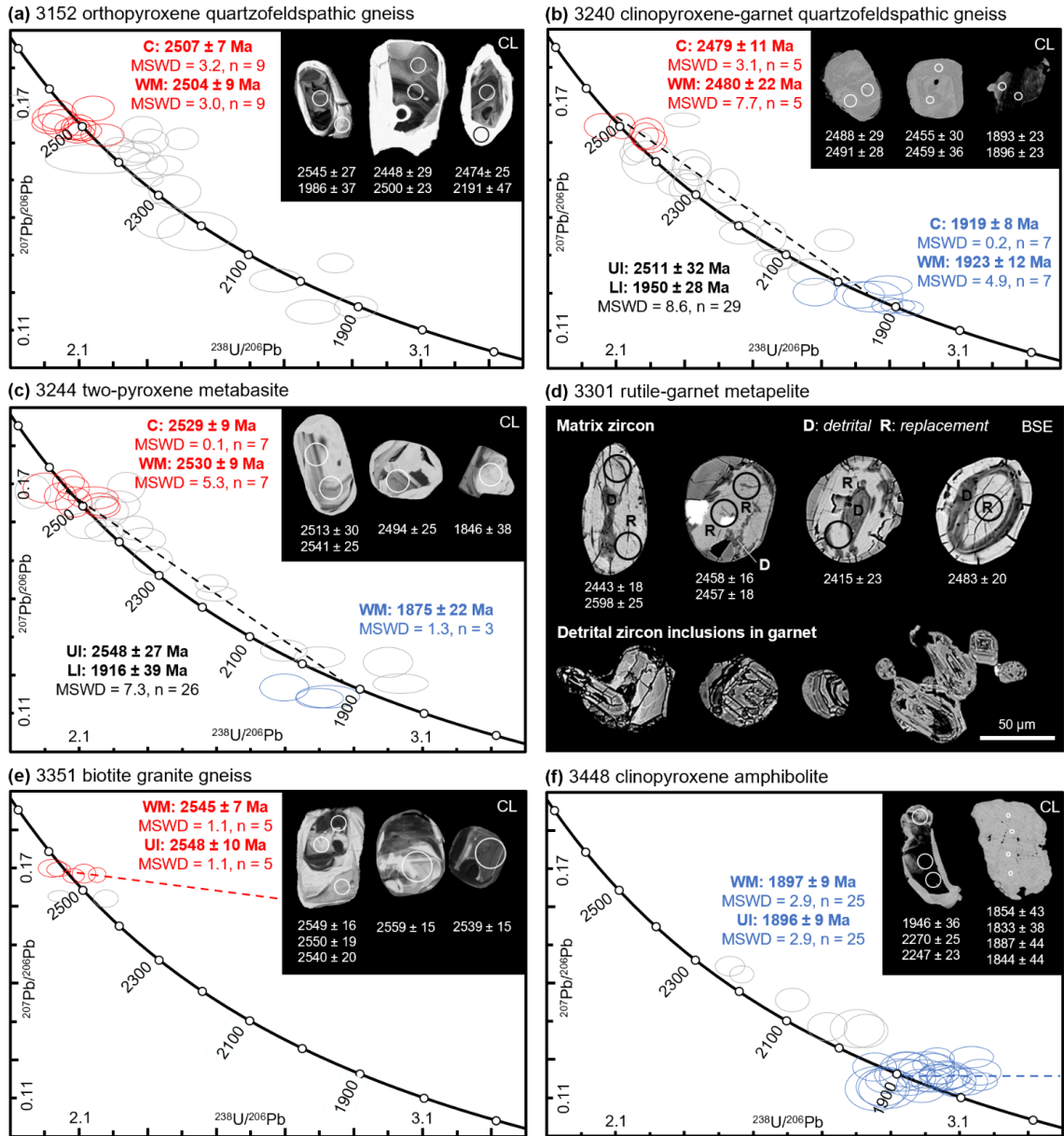


**Figure 2.8. Zircon U–Pb Tera-Wasserburg concordia diagrams and representative zircon imagery (CL and BSE). UI: upper intercept date; LI: lower intercept date; C: concordia date; WM:  $^{207}\text{Pb}/^{206}\text{Pb}$  weighted mean date. 25 μm analysis spots are shown for scale on zircon imagery. Individual zircon dates are ordered relative to spot analysis location. All U–Pb zircon results, including core and rim analysis locations, are in presented in Appendix A.4.**



Orthopyroxene quartzofeldspathic gneiss 3152 has a mineral assemblage of plagioclase, K-feldspar, orthopyroxene, quartz, hornblende, biotite, apatite, ilmenite, and magnetite. Zircon is 40–200  $\mu\text{m}$  in diameter, round to prismatic with dark CL oscillatory zoned cores and bright recrystallized rims. Twenty-nine analyses across nineteen zircon yield a mostly continuous array of  $^{207}\text{Pb}/^{206}\text{Pb}$  dates in the range of ca. 2.55–1.87 Ga (Fig. 2.8a). A population of nine of the oldest oscillatory zoned core analyses that are  $\leq 3\%$  discordant yield a concordia date of  $2507 \pm 7$  Ma (MSWD = 3.2) and  $^{207}\text{Pb}/^{206}\text{Pb}$  weighted mean of  $2504 \pm 9$  Ma (MSWD = 3.0). The three youngest analyses, from recrystallized rims mantled on ca. 2.5 Ga cores, have  $^{207}\text{Pb}/^{206}\text{Pb}$  dates between ca. 1.99 and 1.87 Ga.

Clinopyroxene–garnet quartzofeldspathic gneiss 3240 has a mineral assemblage of plagioclase, K-feldspar, quartz, garnet, clinopyroxene, hornblende, biotite, apatite, ilmenite, and magnetite. Zircon is 40–300  $\mu\text{m}$  in diameter, round and mostly homogeneously bright under CL with a few dark CL rims on some grains. Twenty-nine analyses across twenty zircon yield a continuous array of  $^{207}\text{Pb}/^{206}\text{Pb}$  dates in the range of ca. 2.52–1.89 Ga. All analyses define a discordia array with upper and lower intercepts at  $2511 \pm 32$  Ma and  $1950 \pm 28$  Ma (MSWD = 8.6), respectively (Fig. 2.8b). A population of five of the oldest core analyses that are  $\leq 1\%$  discordant yield concordia and  $^{207}\text{Pb}/^{206}\text{Pb}$  weighted mean dates of  $2479 \pm 11$  Ma (MSWD = 3.1) and  $2480 \pm 22$  Ma (MSWD = 7.7), respectively. Seven of the youngest analyses, with  $^{207}\text{Pb}/^{206}\text{Pb}$  dates between ca. 1.97–1.89 Ga, are mostly from dark CL domains and yield concordia and  $^{207}\text{Pb}/^{206}\text{Pb}$  weighted mean dates of  $1919 \pm 8$  Ma (MSWD = 0.2) and  $1923 \pm 12$  Ma (MSWD = 4.9), respectively.

Two-pyroxene metabasite 3244 has a mineral assemblage of plagioclase, orthopyroxene, clinopyroxene, quartz, apatite, magnetite, and ilmenite. Zircon is 50–150  $\mu\text{m}$  in diameter, prismatic to round, with dark, oscillatory zoned cores, and bright, recrystallized metamorphic rims in CL. Twenty-six analyses from sixteen zircon yield  $^{207}\text{Pb}/^{206}\text{Pb}$  dates in the range of ca. 2.55–1.85 Ga. All analyses define a discordia array with upper and lower intercepts at  $2548 \pm 27$  Ma and  $1916 \pm 39$  Ma (MSWD = 7.3) respectively (Fig. 2.8c). A population of seven of the oldest oscillatory zoned cores, that are  $\leq 3\%$  discordant, yield concordia and  $^{207}\text{Pb}/^{206}\text{Pb}$  weighted mean dates of  $2529 \pm 9$  Ma (MSWD = 0.1) and  $2530 \pm 9$  Ma (MSWD = 5.3), respectively. The three youngest analyses are from small ( $\sim 50$   $\mu\text{m}$ )

neoblastic or wholly recrystallized metamorphic zircon which have  $^{207}\text{Pb}/^{206}\text{Pb}$  dates between ca. 1.88–1.85 Ga, with a weighted mean of  $1875 \pm 22$  Ma (MSWD = 1.3).

Rutile–garnet metapelite 3301 has a mineral assemblage of plagioclase, garnet, K-feldspar, quartz, rutile, biotite, and ilmenite. Zircon is 25–100  $\mu\text{m}$  in diameter, round, and typically has dark, oscillatory zoned detrital cores, and bright, recrystallized rims in CL. BSE images reveal complex replacement textures with dark BSE oscillatory zoned cores irregularly recrystallized by homogenous, bright BSE domains (Fig. 2.8d). Notably, the replacement textures are only present in matrix zircon. All zircon within garnet show no evidence of replacement domains, suggesting the zircon replacement event occurred post garnet growth. Eight analyses from six matrix zircon yield  $^{207}\text{Pb}/^{206}\text{Pb}$  dates in the range of ca. 2.60–2.16 Ga. Three near concordant analyses ( $\leq 2\%$ ) from recrystallized cores yield concordia and  $^{207}\text{Pb}/^{206}\text{Pb}$  weighted mean dates of  $2473 \pm 9$  Ma (MSWD = 4.2) and  $2469 \pm 10$  Ma (MSWD = 3.1), respectively.

Biotite granite gneiss 3351 has a mineral assemblage of K-feldspar, quartz, plagioclase, biotite, apatite, ilmenite, and magnetite. Zircon is generally 40–50  $\mu\text{m}$  in diameter, and has complex dark CL cores with thin, bright, recrystallized metamorphic rims. Seven analyses across five zircon yield  $^{207}\text{Pb}/^{206}\text{Pb}$  dates in the range of ca. 2.55–2.47 Ga. Five of the analyses define a discordia array with upper intercept date of  $2548 \pm 10$  Ma (MSWD = 0.5) and a geologically meaningless lower intercept date of ca. 600 Ma (Fig. 2.8e). The same five analyses yield a  $^{207}\text{Pb}/^{206}\text{Pb}$  weighted mean date of  $2545 \pm 7$  Ma (MSWD = 1.1).

Sample 3448 was collected from a clinopyroxene amphibolite layer, parallel to the host orthopyroxene quartzofeldspathic gneiss. The mineral assemblage includes plagioclase, hornblende, biotite, clinopyroxene, ilmenite, magnetite, and apatite. Majority of the zircon is between 50–150  $\mu\text{m}$  in diameter, with a few anomalously large (up to 1200  $\mu\text{m}$ ) grains associated with a band of coarse ilmenite and magnetite. The large zircon are amorphous and bright in CL displaying little to no zonation. Thirty-one analyses from fourteen zircon yield  $^{207}\text{Pb}/^{206}\text{Pb}$  dates in the range of ca. 2.27–1.77 Ga (Fig. 2.8f). Six older, discordant analyses with  $^{207}\text{Pb}/^{206}\text{Pb}$  dates in the range of ca. 2.27–2.03 Ga suggest a late Neoproterozoic or early Paleoproterozoic protolith like the previous samples. The remaining twenty-five

analyses have  $^{207}\text{Pb}/^{206}\text{Pb}$  dates between ca. 1.95–1.77 Ga, with a combined weighted mean date of  $1897 \pm 9$  Ma (MSWD = 2.9). Setting a discordia anchor at 0 Ma, these twenty-five analyses yield an upper intercept date of  $1896 \pm 9$  Ma (MSWD = 2.9).

## 2.6 EPMA monazite petrochronology

In-situ total Th–U–Pb electron probe micro-analysis (EPMA) monazite dating was performed to determine the timing of metamorphic events. Chemical trends in monazite (e.g., Y, Th) and their petrographic context are used to link time with specific rock-forming reactions (garnet growth/breakdown, presence of melt) (e.g., Williams et al., 2017). With the same electron microprobe previously mentioned, we used a monazite dating procedure as follows: Monazite was located with full thin section maps of Ce. Element maps of Y, Th, U and Pb were produced for all or majority of the monazite grains  $>10$   $\mu\text{m}$ . Monazite maps were processed simultaneously for semi-quantitative correlation across different grains (e.g., Williams et al., 2006). Wavelength dispersive spectroscopy (WDS) spot measurements were made based on monazite chemical domains observed from element maps. Analytical conditions for WDS spot analysis included a 120 nA beam current with a 3  $\mu\text{m}$  beam diameter. U and Pb had a dwell time of 200 s plus 100 s on background (two-point), while Th and Y had a dwell time of 100 s and 50 s on background (two-point). Dates were calculated using the monazite age equation from Montel et al. (1996). Monazite consistency standards GSC-3345 ( $^{207}\text{Pb}/^{206}\text{Pb}$  = ca. 1821 Ma) and GSC-8153 ( $^{206}\text{Pb}/^{238}\text{U}$  = ca. 512 Ma) were utilized throughout the analytical session, achieving weighted mean dates of  $1846 \pm 20$  Ma (MSWD = 1.1,  $n = 7$ ) and  $512 \pm 16$  Ma (MSWD = 0.9,  $n = 7$ ) respectively. The results of monazite chemical dating are presented in Figure 2.9 and Appendix A.5.

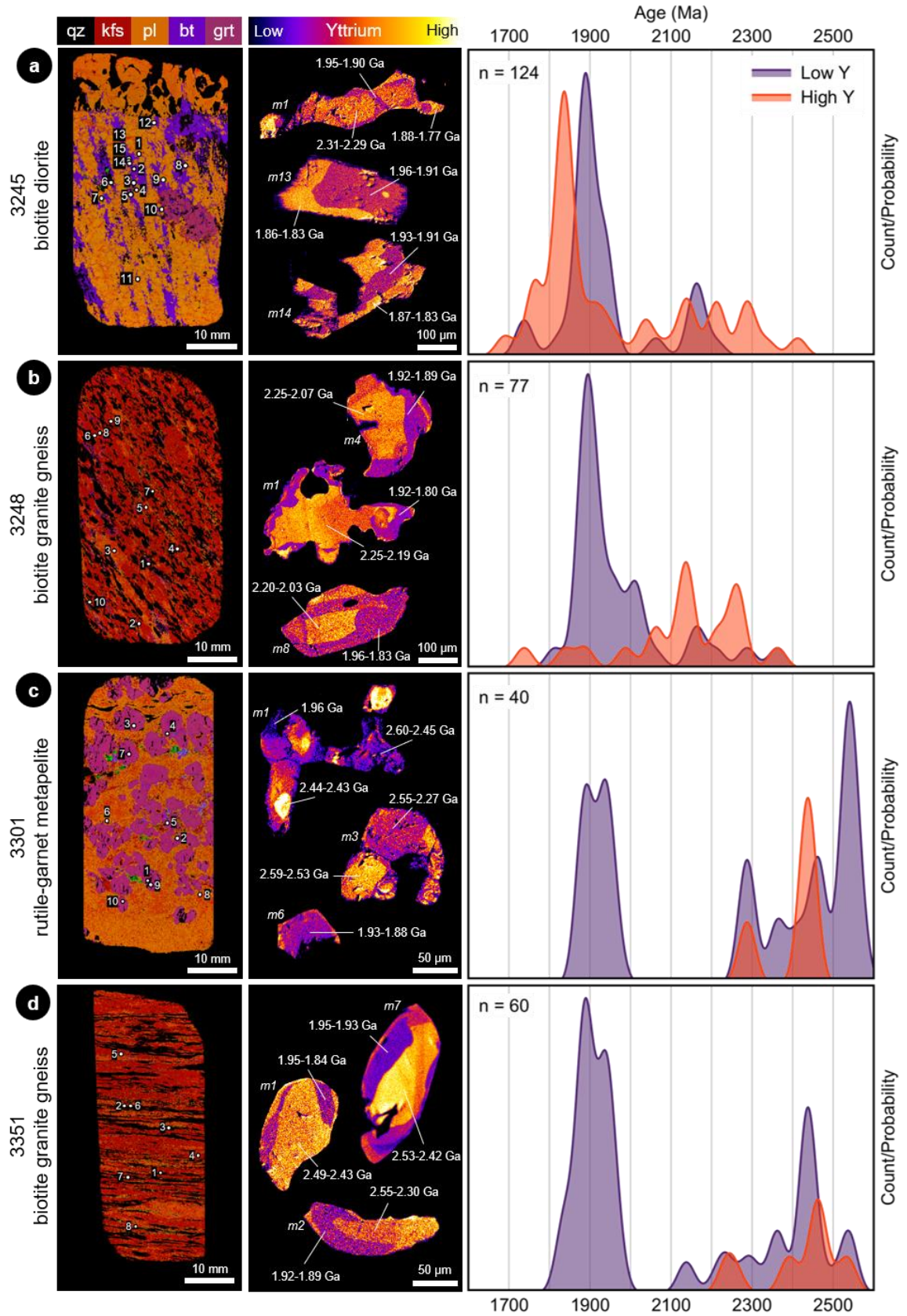


**Figure 2.9. Monazite locations in thin section, yttrium concentration maps, and total Th–U–Pb age probability density diagrams separated into relatively low versus high yttrium domains. Thin sections are shown as RGB (Al-Ca-Mg) element maps. A small amount of the quartz represented in black is other Al, Ca, and Mg deficient phases such as ilmenite, magnetite, or zircon. The top of sample 3245 is a late pegmatite, not part of the biotite diorite. Monazite numbers correspond to monazite spot numbers reported in Appendix A.5.**

Dismissing four outlier dates, the remaining 297 monazite analyses across all four samples yield a continuous array of dates between ca. 2.60–1.69 Ga, with the largest population of analyses near ca. 1.9 Ga. Sample 3245 is from a small outcrop of biotite diorite within clinopyroxene–garnet quartzofeldspathic gneiss. There is one large (5 mm) garnet in thin section which is evidently broken-down with amorphous grain boundaries (Fig. 2.9a). All monazite is located within the plagioclase–biotite matrix, never within the garnet. This sample contains the largest monazite grains, up to 600  $\mu\text{m}$  in length, with an average length of 250  $\mu\text{m}$ . Monazite is parallel to foliation and elongated, suggesting at least partial growth during the most recent regional contraction event. One hundred and twenty analyses across fifteen monazite yield dates in a semi-continuous range of ca. 2.33–1.69 Ga. Six of the oldest analyses from cores of high Y and Th yield a weighted mean date of  $2299 \pm 12$  Ma (MSWD = 2.2). Four analyses from thin inner rims with low Y and high Th, mantling ca. 2.30 Ga cores, yield a weighted mean date of  $2182 \pm 10$  Ma (MSWD = 3.2). Thirteen analyses with dates between ca. 2.18–2.04 Ga yield a rough weighted mean of  $2122 \pm 8$  Ma (MSWD = 10.7) but are from cores of moderate Y and Th that are morphologically similar to the older ca. 2.30 Ga cores, and thus could be older grains which have experienced Pb loss or other open-system behavior. Thirty-five analyses from low Y and Ca, and highly variable Th, Si, P, and Sm neoblastic cores or resorbed inner rims mantling ca. 2.30 Ga cores have a continuous array of dates between ca. 1.96–1.87 Ga and result in a weighted mean date of  $1905 \pm 4$  Ma (MSWD = 2.9). Around ca. 1.87 Ga there is a notable transition to high Y, Ca, P, and Sm, and low Th and Si monazite growth as outer rims mantling ca. 1.90 Ga inner rims or rims on ca. 1.90 Ga cores. Monazite of this domain give a continuous array of dates, primarily between ca. 1.87–1.79 Ga; thirty-two of these analyses yield a weighted mean of  $1830 \pm 6$  Ma (MSWD = 2.0).

Biotite granite gneiss 3238 is primarily composed of K-feldspar and quartz with subordinate mafic layers of plagioclase and biotite (Fig. 2.9b). Monazite is 100 to 400  $\mu\text{m}$  in length and is subparallel to parallel to the gneissic foliation. Seventy-four analyses across nine monazite yield dates in a continuous range of ca. 2.29–1.80 Ga. Nine of the oldest analyses from cores of high Y and low Th yield a weighted mean of  $2247 \pm 13$  Ma (MSWD = 2.0). Four analyses from cores of low Y, which may represent a distinct growth event, like biotite diorite 3245, yield a weighted mean date of  $2191 \pm 18$  Ma (MSWD = 0.8). Thirty-six analyses from low Y, high Th rims mantling ca. 2.30–2.10 Ga cores range between ca. 1.97–1.87 Ga, with a weighted mean of  $1909 \pm 5$  Ma (MSWD = 4.3).

In addition to zircon geochronology, monazite petrochronology was performed on rutile–garnet metapelite 3301. Monazite is relatively small, in the range of 40 to 150  $\mu\text{m}$  in length with no distinct preferred orientation. Nine monazites were analyzed, six are garnet inclusions, one is partially enclosed by garnet (#2), and two are within the feldspar matrix (#6, #8) (Fig. 2.9c). Forty analyses across all nine monazite yield dates in the range of ca. 2.60–1.88 Ga with a large gap between ca. 2.27–1.96 Ga. The older population of monazite with dates between ca. 2.60–2.27 Ga show complex zoning patterns that are difficult to correlate with age. The thirteen oldest analyses are from low Y, high Th, Ca, and Si cores with dates ranging between ca. 2.60–2.49 Ga, and yield a rough weighted mean date of  $2544 \pm 6$  Ma (MSWD = 9.3). Nine high Y analyses, generally from inner rims, yield a weighted mean date of  $2453 \pm 8$  Ma (MSWD = 2.4). The last monazite peak for the older population of monazite is represented by four analyses which yield a weighted mean date of  $2282 \pm 10$  Ma (MSWD = 0.6). The two monazites analyzed in the feldspar matrix are homogeneous with low Y and Th contents; together, along with analyses of low Y, moderate Th rims from monazite partially enclosed in garnet yield younger dates between ca. 1.96–1.88 Ga, with a weighted mean of  $1922 \pm 10$  Ma (MSWD = 2.7, n = 10).

Biotite granite gneiss 3351 was also analyzed by monazite petrochronology in addition to zircon geochronology. Monazite is 60 to 250  $\mu\text{m}$  in length, parallel to the gneissic foliation, and mostly located along quartz ribbons (Fig. 2.9d). Fifty-nine analyses from eight monazite yield dates in the range of ca. 2.55–1.83 Ga with a gap between ca. 2.22–1.96 Ga. Five analyses from high Y cores yield a weighted mean of  $2491 \pm 13$  Ma (MSWD =

3.9). Eight analyses from slightly younger low Y cores yield a weighted mean of  $2431 \pm 9$  Ma (MSWD = 0.5). A continuous array of analyses from low Y rims and small neoblastic cores give dates between ca. 1.96–1.83 Ga, with a rough weighted mean of  $1910 \pm 5$  Ma (MSWD = 5.9, n = 30).

## 2.7 Discussion

### 2.7.1 Late Neoproterozoic Devon Island terrane and Paleoproterozoic metamorphism

Determining the age of the oldest crust in the Devon and Ellesmere islands area is critical for confining the extent of the  $\geq 2.6$  Ga Rae craton and associated late Neoproterozoic and Paleoproterozoic domains in the northern Laurentian shield. The major units outcropping in our mapping area of southern Devon Island are clinopyroxene–garnet quartzofeldspathic gneiss, orthopyroxene quartzofeldspathic gneiss, rutile–garnet metasedimentary rocks and leucogranite, two-pyroxene metabasite, and biotite granite gneiss (Fig. 2.2). The interleaving structural relationship of the rutile–garnet metasedimentary rocks with the pyroxene quartzofeldspathic gneisses and two-pyroxene metabasite (Figs. 2.2, 2.3a) suggests southeastern Devon Island is composed of supracrustal crust with mixed igneous and sedimentary protoliths.

Zircon and monazite chronology confirm a late Neoproterozoic to middle Paleoproterozoic history for southern Devon Island, ranging from ca. 2.55 to 1.80 Ga (Fig. 2.10a), with no evidence of  $\geq 2.6$  Ga Rae craton material. Oscillatory zoned zircon cores from orthopyroxene quartzofeldspathic gneiss (3152), two-pyroxene metabasite (3244), and biotite granite gneiss (3351) suggest magmatic emplacement between ca. 2.55–2.51 Ga (Figs. 2.8a, 2.8c, 2.8e). Clinopyroxene–garnet quartzofeldspathic gneiss (3240) has homogenous ca. 2.48 Ga zircon cores, suggesting early Paleoproterozoic metamorphism following late Neoproterozoic emplacement (Fig. 2.8b). Rutile–garnet metasedimentary rocks comprise ca. 2.47 Ga recrystallized zircon domains replacing oscillatory zoned detrital zircon (Fig. 2.8d), providing evidence of early Paleoproterozoic metamorphism, and restricting sedimentary deposition on southern Devon Island to  $\geq 2.47$  Ga. Additionally, early Paleoproterozoic metamorphism is supported by ca. 2.45 Ga monazite ages from high

Y domains in rutile–garnet metasedimentary rocks (3301) and high Y to low Y monazite cores in biotite granite gneiss (3351) (Figs. 2.9c–d). The late Neoproterozoic (ca. 2.6–2.5 Ga) monazite analyses from rutile–garnet metasedimentary rocks (3301) and biotite granite gneiss (3351), could be indicative of an even earlier metamorphic event (ca. 2.54 Ga), around the time of protolith formation, but these analyses could not be linked to specific monazite growth domains to justify this interpretation. Either of these early metamorphic events (ca. 2.47 Ga, 2.54 Ga) could be linked to metamorphism during the initial phase of the Arrowsmith orogeny (2.54–2.45 Ga; Berman et al., 2013).

Between the major zircon and monazite growth events at 2.5 and 1.9 Ga are more ambiguous ages (Fig. 2.10a). The oldest monazite populations from the biotite diorite (3245) and biotite granite gneiss (3248), as well as a small peak in monazite growth from rutile–garnet metasedimentary rocks (3301), suggest metamorphism around ca. 2.3 Ga (Figs. 2.9a–c). This is supported by a few concordant to near concordant zircon analyses from the pyroxene quartzofeldspathic gneisses (3152; 3240) with dates around ca. 2.33–2.25 Ga (Figs. 2.8a–b). However, due to the potential discordancy of chemical monazite ages and the mobility of Pb in zircon during high-temperature metamorphism (especially at UHT conditions; c.f. Whitehouse et al., 2014), the ages between the major the 2.5 Ga and 1.9 Ga growth events cannot be conclusively attributed to specific events.

Thelon–Inglefield metamorphism is undoubtedly represented on southern Devon Island as most of the monazite analyses, and a significant portion of the zircon analyses, are in the range of ca. 1.95–1.85 Ga (Fig. 2.10a). Monazite analyses from all four samples have significant peaks between ca. 1.95–1.87 Ga (Fig. 2.9), corresponding to low Y and highly variable Th domains. Combined, these monazite domains yield a weighted mean age of 1.91 Ga ( $n = 122$ ), which we interpret as the timing of peak granulite facies metamorphism and anatexis associated with the Thelon–Inglefield orogeny. The low Y content suggests garnet was stable at this time and the highly variable Th and Si content suggests melt was present (e.g., Dumond et al., 2015). Disappearance of variable Th and Si monazite domains at ca. 1.87 Ga for all samples (Fig. 2.9), suggests melt was crystallized or extracted between 1.91–1.87 Ga. The youngest populations of zircon analyses, mostly from rims on ca. 2.5



Ga cores, yield weighted mean dates between ca. 1.92–1.87 Ga (Figs. 2.8b, 2.8c, 2.8f), further supporting Thelon–Inglefield metamorphism at ca. 1.91 Ga.

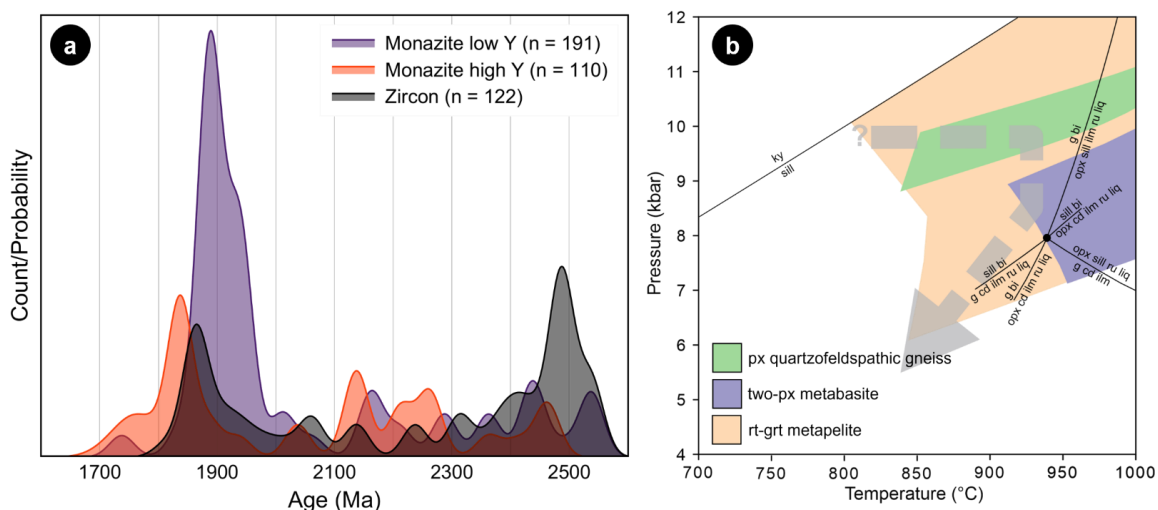


**Figure 2.10. Summary of pressure–temperature–time results. (a) Probability density diagram of all (Th)–U–Pb zircon and monazite ages. Major peaks are at ca. 2.5 and 1.9 Ga, with lesser peaks between ca. 2.3– 2.1 Ga. (b)  $P$ – $T$  diagram displaying the overlapping peak stability fields of the pyroxene quartzofeldspathic gneisses (3237, 3240, 3257) and two-pyroxene metabasites (3238, 3239), and the peak stability field for the rutile–garnet metapelite (3301). The black lines show the kyanite–sillimanite boundary and reactions of rutile-bearing metapelites from White et al. (2014a) in the KFMASHTO system with K-feldspar, quartz and melt in excess. The dashed grey line represents a possible clockwise  $P$ – $T$  path associated with HT–UHT Thelon–Inglefield metamorphism. The proposed path does not cross orthopyroxene forming reactions, as orthopyroxene was not observed in the metasedimentary rocks, but does cross the sill + bi to g + cd + ilm + ru + liq reaction upon cooling, forming the cordierite–quartz symplectites observed in the sapphirine–quartz sample (3294).**

Following peak Thelon–Inglefield metamorphism, the biotite diorite sample (3245) is the only to preserve a younger population of monazite ages, showing a distinct transition to high Y, low Th and Si monazite at ca. 1.87 Ga (Fig. 2.9a). These analyses from monazite rims, with dates in the range of ca. 1.87–1.79 Ga on ca. 1.90 Ga cores, suggest growth during garnet breakdown and after melt extraction. This age range overlaps with the ca.

1.87–1.84 Ga  $^{40}\text{Ar}/^{39}\text{Ar}$  age of ductile shearing documented for the northernmost Paleoproterozoic rocks on Ellesmere Island (Caswell et al., 2021); suggesting deformation was widespread across Devon and Ellesmere islands, following peak Thelon–Inglefield metamorphism. Deformation after anatexis is consistent with our field observations on southern Devon Island, given the foliation of the leucogranite within metasedimentary rocks (Fig. 2.3e), and the pervasive, presumably solid-state ductile deformation exemplified by feldspar augen and quartz ribbon textures (Figs. 2.3b, 2.3d, 2.6a–b). The biotite diorite (3245) was likely the only sample to preserve this younger monazite growth due to the abundance of biotite, thus a higher bulk rock H<sub>2</sub>O content, giving rise to dissolution-precipitation reactions during deformation (e.g., Oriolo et al., 2018), while the other samples are essentially anhydrous (Figs. 2.9b–d).

### 2.7.2 *P–T* conditions of Thelon–Inglefield metamorphism

Having confirmed ca. 1.91 Ga granulite facies metamorphism on southern Devon Island, we are able to evaluate the poorly constrained peak *P–T* conditions of Thelon–Inglefield metamorphism in northern Laurentia. Importantly, our discovery of a sapphirine–quartz assemblage on southern Devon Island is diagnostic of UHT metamorphism (>900 °C; e.g., Kelsey and Hand, 2015) along the flank of the Thelon–Inglefield arc. This is the first discovery of a sapphirine–quartz assemblage in the Devon Island area and represents the northernmost UHT occurrence on Earth (c.f. Kelsey and Hand, 2015). The low ferric iron content of sapphirine and bulk rock estimations ( $X_{\text{Fe}^{3+}} = 0.01–0.15$ ) are a further indication of UHT conditions since high ferric iron ratios are known to expand the stability of sapphirine to lower temperatures (e.g., Wheller and Powell, 2014). This is the second occurrence of sapphirine reported from Devon and Ellesmere islands; the other being a sapphirine–cordierite–orthopyroxene gneiss from northeastern Devon Island (Frisch, 1988). However, the absence of quartz from the northeastern Devon Island sample is not diagnostic evidence of UHT metamorphism (e.g., Kelsey and Hand, 2015).

Phase equilibrium modelling results are also indicative of HT–UHT conditions on southern Devon Island, with the majority of the interpreted peak stability fields overlapping at ca. 9 kbar and >850 °C (Fig. 2.10b), near or within the UHT regime. By rock type, the overlap of the pyroxene quartzofeldspathic gneiss stability fields suggest peak *P–T* conditions

around 9–11 kbar and  $>840$  °C; two-pyroxene metabasite suggest pressures  $<10$  kbar and temperatures  $>900$  °C; and rutile–garnet metapelite suggests conditions between ca. 6–11 kbar and  $>800$  °C. Additionally, modelled isolines generally favour P–T conditions at ca. 9 kbar and  $\geq 900$  °C (Fig. 2.7). Relatively low H<sub>2</sub>O proportions were used for modelling (due to the low modes of hydrous minerals), resulting in high solidus temperatures (775–900 °C), consequently increasing the peak temperature estimates. If more H<sub>2</sub>O is added to the bulk rock composition, this would move the solidus to lower temperatures, lowering the peak temperature estimates. Nevertheless, temperatures  $<850$  °C are not appropriate for sapphirine–quartz assemblages (e.g., Kelsey and Hand, 2015).

Pressure–temperature–time paths regarding the evolution of Thelon–Inglefield metamorphism are difficult to constrain with our samples as there are few examples of microstructures indicative of the prograde or retrograde P–T evolution. Petrographic analysis shows rutile replacing the rims of large ilmenite grains in rutile–garnet metasedimentary rocks (Fig. 2.4f), suggesting an increase in pressure (counterclockwise P–T path), transitioning from ilmenite-dominant P–T space to rutile-dominant P–T space as shown by phase equilibrium modelling (Fig. 2.7f). However, ilmenite and rutile stability fields can be significantly altered depending on ferric iron estimations (e.g., Diener and Powell, 2010) and changes in oxygen fugacity during a protracted P–T evolution (e.g., Yakymchuk et al., 2019), so this is not conclusive evidence of a counterclockwise path. An alternative P–T trajectory is a clockwise path; this would likely result in the near-peak cooling stage crossing the orthopyroxene-in boundaries modelled for the clinopyroxene–garnet quartzofeldspathic gneisses (Figs. 2.7a, 2.7d), and given the HT–UHT conditions, some orthopyroxene growth would be expected, but was not observed. The sapphirine–quartz sample (3294) contains cordierite–quartz symplectites that are inferred to be the product of garnet breakdown (Fig. 2.4g), and similar cordierite after garnet reactions have been previously documented on Devon and Ellesmere islands (Frisch, 1988). This requires decompression at (ultra)high temperatures (e.g., Kelsey and Hand, 2015) and suggests a clockwise P–T evolution for this sample; as has been previously suggested for Devon and Ellesmere islands (Frisch, 1988). Although cryptic and based on microstructures (cordierite after garnet) from a single sample, we favor a clockwise P–T path during Thelon–Inglefield metamorphism on southern Devon Island (Fig. 2.10b), but we acknowledge that this is

tentative and requires additional samples that contain mineral assemblages and microtextures amenable to detailed P–T path reconstructions.

### 2.7.3 2.5–1.9 Ga tectonics along the western Rae craton margin

Based on our results and previous studies (Frisch, 1988; Frisch and Hunt, 1988; Gilotti et al., 2018), there is no evidence of  $\geq 2.6$  Ga Rae craton material on Devon and Ellesmere islands. Instead, the oldest crust is the ca. 2.55–2.47 Ga late Neoproterozoic supracrustal terrane studied here on southern Devon Island (cf., Frisch, 1988; Frisch and Hunt, 1988), which likely accreted onto the western margin of the Rae craton. Based on published data, it appears that this late Neoproterozoic terrane does not extend to Ellesmere Island (Frisch, 1988; Frisch and Hunt, 1988; Gilotti et al., 2018), which is likely a northern extension of the Thelon–Inglefield arc. There is some evidence that this late Neoproterozoic crust extends to northern Devon Island (c.f. Schärer and Deutsch, 1990; Hegner and Jackson, 1990), but this remains to be fully constrained.

Elsewhere along the western margin of the Rae craton, further extensions of late Neoproterozoic domains have been recognized on Boothia Peninsula and Somerset Island (Frisch and Hunt, 1993; Sanborn-Barrie et al., 2019), the eastern Queen Maud Block (Schultz et al., 2007; Davis et al., 2014), and Prudhoe Land (Nutman et al., 2008) (Fig. 2.1a). In the Boothia-Somerset area, ca. 2.56–2.5 Ga magmatic ages and ca. 2.51–2.49 Ga sedimentary deposition ages (Sanborn-Barrie et al., 2019; Regis et al., 2019) suggest cogenetic formation with Devon Island. Furthermore, thermobarometry estimates of ca. 1.94–1.92 Ga Thelon–Inglefield metamorphism (Frisch and Hunt, 1993) in the Boothia-Somerset area are locally as high as 8.7 kbar and 960 °C (Kitsul et al., 2000), comparable to southern Devon Island. This terrane may continue further south, into the eastern Queen Maud Block, where ca. 2.52–2.47 Ga magmatic ages have been reported (Schultz et al., 2007; Davis et al., 2014) between Mesoproterozoic rocks of the western Queen Maud Block and  $\geq 2.6$  Ga Rae craton rocks (Fig. 2.1a), but was not reworked by Thelon–Inglefield metamorphism (Schultz et al., 2007). Late Neoproterozoic extensions northeast of Devon Island may be represented in the Prudhoe Land area of northwestern Greenland, which comprises orthogneisses of the Thule mixed-gneiss complex with magmatic zircon ages in the range of ca. 2.60–2.23 Ga (Nutman et al., 2008). Thelon–Inglefield metamorphic ages

for Prudhoe Land are in the range of ca. 1.92–1.90 Ga (Nutman et al., 2008); but limited quantitative P–T constraints are available for comparison with Devon Island (e.g., Garde et al., 1984).

These correlations along the western margin of the Rae craton suggest a possible shared late Neoproterozoic to middle Paleoproterozoic history between Devon Island, Boothia Peninsula, the eastern Queen Maud Block, and the Prudhoe Land area. A late Neoproterozoic to early Paleoproterozoic tectonic front involving these domains could represent a coherent tectonic block(s) involved in the onset of the Arrowsmith orogeny while later Thelon–Inglefield metamorphism reworked most of these domains, locally reaching UHT metamorphic conditions along the flank of juvenile magmatic arc rocks (e.g., Ellesmere Island), possibly in a back-arc tectonic setting.

## 2.8 Conclusions

This contribution, in combination with earlier reconnaissance work, establishes southern Devon Island as a late Neoproterozoic terrane composed of lower to middle crustal, granulite facies rocks displaying evidence of partial melting and pervasive solid-state ductile deformation. Igneous protoliths (biotite granite gneiss, two-pyroxene metabasite, pyroxene quartzofeldspathic gneiss) were emplaced between ca. 2.55–2.51 Ga and sedimentary protoliths (rutile–garnet metasedimentary rocks) were deposited ca.  $\geq 2.47$  Ga. Earlier, poorly constrained metamorphic events are recorded at ca. 2.54, 2.47 and 2.30 Ga, possibly associated with pulses of the Arrowsmith orogeny. This terrane was later reworked at ca. 1.91 Ga during with the Thelon–Inglefield orogeny; with peak P–T conditions of ca. 9 kbar and  $>850$  °C, resulting in anatexis, followed by significant ductile deformation. The discovery of a sapphirine–quartz assemblage gives clear indication that local UHT conditions were obtained within Thelon–Inglefield orogenic domain, likewise to the UHT conditions in the Taltson magmatic zone further south.

## 2.9 References

Berman, R. G., Sanborn-Barrie, M., Stern, R. A., & Carson, C. J. (2005).  
Tectonometamorphism at ca. 2.35 and 1.85 Ga in the Rae domain, western Churchill

- Province, Nunavut, Canada: insights from structural, metamorphic and in situ geochronological analysis of the southwestern Committee Bay Belt. *Canadian Mineralogist*, 43(1), 409–442.
- Berman, R. G., Pehrsson, S., Davis, W. J., Ryan, J. J., Qui, H., & Ashton, K. E. (2013). The Arrowsmith orogeny: Geochronological and thermobarometric constraints on its extent and tectonic setting in the Rae craton, with implications for pre-Nuna supercontinent reconstruction. *Precambrian Research*, 232, 44–69.
- Berman, R. G., Davis, W. J., Sanborn-Barrie, M., Whalen, J. B., Taylor, B. E., McMartin, I., McCurdy, M. W., Mitchell, R. K., Ma, S., Coyle, M., Roberts, B., & Craven, J. A. (2018). Report of activities for the GEM-2 Chantrey-Thelon activity: Thelon Tectonic Zone project, Nunavut (Geological Survey of Canada, Open File, Vol. 8372). Natural Resources Canada.
- Black, L. P., Kamo, S. L., Allen, C. M., Davis, D. W., Aleinikoff, J. N., Valley, J. W., Mundil, R., Campbell, I. H., Korsch, R. J., Williams, I. S., & Foudoulis, C. (2004). Improved  $^{206}\text{Pb}/^{238}\text{U}$  microprobe geochronology by the monitoring of a trace-element-related matrix effect; SHRIMP, ID-TIMS, ELA-ICP-MS and oxygen isotope documentation for a series of zircon standards. *Chemical Geology*, 205(1-2), 115–140.
- Card, C. D., Bethune, K. M., Davis, W. J., Rayner, N., & Ashton, K. E. (2014). The case for a distinct Taltson orogeny: Evidence from northwest Saskatchewan, Canada. *Precambrian Research*, 255, 245–265.
- Caswell, B., Gilotti, J.A., Webb, L.E., McClelland, W.C., Kościńska, K., Piepjohn, K., von Gosen, W. (2021).  $^{40}\text{Ar}/^{39}\text{Ar}$  dating of Paleoproterozoic shear zones in the Ellesmere–Devon crystalline terrane, Nunavut, Canadian Arctic. *Canadian Journal of Earth Sciences*.
- Christie, R. L. (1967). Bache Peninsula, Ellesmere Island, Arctic Archipelago. Geological Survey of Canada, Memoir, 347, 1–63.

- Christie, R. L. (1978). A structural reconnaissance of eastern Devon Island, Arctic Archipelago Geological Survey of Canada, Open File, 537.
- Davis, W. J., Berman, R. G., Nadeau, L., & Percival, J. (2014). U-Pb zircon geochronology of a transect across the Thelon Tectonic Zone, Queen Maud region, and adjacent Rae Craton, Kitikmeot region, Nunavut, Canada. Geological Survey of Canada, Open File, 7652.
- Davis, W. J., Sanborn-Barrie, M., Berman, R. G., & Pehrsson, S. (2021). Timing and provenance of Paleoproterozoic supracrustal rocks in the central Thelon tectonic zone, Canada: implications for the tectonic evolution of western Laurentia from ca. 2.1 to 1.9 Ga. In *Canadian Journal of Earth Sciences* (pp. 1–18).
- Diener, J. F. A., & Powell, R. (2010). Influence of ferric iron on the stability of mineral assemblages. *Journal of Metamorphic Geology*, 28(6), 599–613.
- Droop, G. T. R. (1987). A general equation for estimating Fe<sup>3+</sup> concentrations in ferromagnesian silicates and oxides from microprobe analyses, using stoichiometric criteria. *Mineralogical Magazine*, 51(361), 431–435.
- Dumond, G., Goncalves, P., Williams, M. L., & Jercinovic, M. J. (2015). Monazite as a monitor of melting, garnet growth and feldspar recrystallization in continental lower crust. *Journal of Metamorphic Geology*, 33(7), 735–762.
- Farquhar, J., Chacko, T., & Ellis, D. J. (1996). Preservation of oxygen isotope compositions in granulites from Northwestern Canada and Enderby Land, Antarctica: implications for high-temperature isotopic thermometry. In *Contributions to Mineralogy and Petrology* (Vol. 125, Issues 2-3, pp. 213–224).
- Forshaw, J. B., Waters, D. J., Pattison, D. R. M., Palin, R. M., & Gojon, P. (2019). A comparison of observed and thermodynamically predicted phase equilibria and mineral compositions in mafic granulites. *Journal of Metamorphic Geology*, 37(2), 153–179.

- Frisch, T. (1988). Reconnaissance geology of the Precambrian Shield of Ellesmere, Devon and Coburg islands, Canadian Arctic Archipelago. Geological Survey of Canada, Memoir, 409, 1–102.
- Frisch, T., & Hunt, P. A. (1988). U-Pb zircon and monazite ages from the Precambrian Shield of Ellesmere and Devon Islands, Arctic Archipelago. Geological Survey of Canada, Paper, 88-2, 117–125.
- Frisch, T., & Hunt, P. A. (1993). Reconnaissance U-Pb geochronology of the crystalline core of the Boothia Uplift, District of Franklin, Northwest Territories. Geological Survey of Canada, Paper, 93-2, 3–22.
- Garde, A. A., Glassley, W. E., & Nutman, A. P. (1984). Two-stage corona growth during Precambrian granulite facies metamorphism of Smitbson Bjerger, north-west Greenland. *Journal of Metamorphic Geology*, 2(3), 237–247.
- Gibb, R. A., & Thomas, M. D. (1977). The Thelon front: A cryptic suture in the Canadian shield? *Tectonophysics*, 38(3-4), 211–222.
- Gilotti, J. A., McClelland, W. C., Piepjohn, K., & von Gosen, W. (2018). U–Pb geochronology of Paleoproterozoic gneiss from southeastern Ellesmere Island: implications for displacement estimates on the Wegener fault. *Arktos*, 4(1), 12.
- Green, E. C. R., White, R. W., Diener, J. F. A., Powell, R., Holland, T. J. B., & Palin, R. M. (2016). Activity–composition relations for the calculation of partial melting equilibria in metabasic rocks. *Journal of Metamorphic Geology*, 34(9), 845–869.
- Grover, T. W., Pattison, D. R. M., McDonough, M. R., & McNicoll, V. J. (1997). Tectonometamorphic evolution of the southern Taltson magmatic zone and associated shear zones, northeastern Alberta. *Canadian Mineralogist*, 35(5), 1051–1067.
- Harrison, J. C. (1984). Eastern Ellesmere, Coburg and eastern Devon islands mineral inventory, NTS 29G, 38F and G, 39B, C, D, E, F, G and H, 48E and H, District of Franklin, N.W.T. Northwest Territories Mineral Assessment report no. 81743, 1-125.



- Hartlaub, R. P., Heaman, L. M., Chacko, T., & Ashton, K. E. (2007). Circa 2.3-Ga Magmatism of the Arrowsmith Orogeny, Uranium City Region, Western Churchill Craton, Canada. *The Journal of Geology*, 115(2), 181–195.
- Hegner, E., & Jackson, G. D. (1990). Nd isotopic constraints on Late Archean and Early Proterozoic crust formation in Baffin and Ellesmere islands, northern Labrador and Ungava Peninsula, eastern Canada. *Eos, Transactions, American Geophysical Union*, 71, 1689.
- Hoffman, P. F. (1988). United Plates of America, The Birth of a Craton: Early Proterozoic Assembly and Growth of Laurentia. *Annual Review of Earth and Planetary Sciences*, 16(1), 543–603.
- Powell, R., & Holland, T. J. B. (1988). An internally consistent dataset with uncertainties and correlations: 3. Applications to geobarometry, worked examples and a computer program. *Journal of metamorphic Geology*, 6(2), 173-204.
- Holland, T. J. B., & Powell, R. (2011). An improved and extended internally consistent thermodynamic dataset for phases of petrological interest, involving a new equation of state for solids. *Journal of Metamorphic Geology*, 29(3), 333–383.
- Kelsey, D. E., & Hand, M. (2015). On ultrahigh temperature crustal metamorphism: Phase equilibria, trace element thermometry, bulk composition, heat sources, timescales and tectonic settings. *Geoscience Frontiers*, 6(3), 311–356.
- Kitsul, V. I., Glebovitsky, V. A., Vapnik, Y. A., & Frisch, T. (2000). Gneisses from the granulite terrane of the central Boothia Uplift, Arctic Canada. *Canadian Mineralogist*, 38, 443–454.
- Krupička, J. (1973). Granulite facies rocks on northeastern Devon Island, Arctic Archipelago. *Geological Survey of Canada, Paper, 73-8*, 1–41.
- Lanari, P., Vidal, O., De Andrade, V., Dubacq, B., Lewin, E., Grosch, E. G., & Schwartz, S. (2014). XMapTools: A MATLAB©-based program for electron microprobe X-

- ray image processing and geothermobarometry. *Computers & Geosciences*, 62, 227–240.
- McDonough, W. F., & Sun, S.-S. (1995). The composition of the earth. *Chemical Geology*, 120(3-4), 223–253.
- Metzler, A., Ostertag, R., Redeker, H.-J., & Stöffler, D. (1988). Composition of the crystalline basement and shock metamorphism of crystalline and sedimentary target rocks at the Haughton impact crater, Devon Island, Canada. *Meteoritics*, 23(3), 197–207.
- Montel, J. M., Foret, S., Veschambre, M., Nicollet, C., & Provost, A. (1996). Electron microprobe dating of monazite. *Chemical Geology*, 131(1–4), 37–53.
- Morimoto, N. (1988). Nomenclature of Pyroxenes. *Mineralogy and Petrology*, 39(1), 55–76.
- Nutman, A. P., Dawes, P. R., Kalsbeek, F., & Hamilton, M. A. (2008). Palaeoproterozoic and Archaean gneiss complexes in northern Greenland: Palaeoproterozoic terrane assembly in the High Arctic. *Precambrian Research*, 161(3-4), 419–451.
- Oriolo, S., Wemmer, K., Oyhantçabal, P., Fossen, H., Schulz, B., Siegesmund, S. (2018). Geochronology of shear zones – A review. *Earth-Sci. Rev.* 185, 665–683.
- Paton, C., Hellstrom, J., Paul, B., Woodhead, J., & Hergt, J. (2011). Iolite: Freeware for the visualisation and processing of mass spectrometric data. *Journal of Analytical Atomic Spectrometry*, 26(12), 2508–2518.
- Peterson, T. D., Van Breemen, O., Sandeman, H., & Cousens, B. (2002). Proterozoic (1.85–1.75 Ga) igneous suites of the Western Churchill Province: granitoid and ultrapotassic magmatism in a reworked Archean hinterland. *Precambrian Research*, 119(1), 73–100.

- Powell, R., & Holland, T. J. B. (1988). An internally consistent dataset with uncertainties and correlations: 3. Applications to geobarometry, worked examples and a computer program. *Journal of Metamorphic Geology*, 6(2), 173–204.
- Regis, D., Sanborn-Barrie, M., & Moum, T. (2019). GEM-2 Boothia Peninsula-Somerset Island project, Nunavut: mineral assay results and potential carving stone localities from the 2017 and 2018 field seasons Geological Survey of Canada, Open File, 8592.
- Sanborn-Barrie, M., Davis, W. J., Berman, R. G., Rayner, N., Skulski, T., & Sandeman, H. (2014). Neoproterozoic continental crust formation and Paleoproterozoic deformation of the central Rae craton, Committee Bay belt, Nunavut. *Canadian Journal of Earth Sciences*, 51(6), 635–667.
- Sanborn-Barrie, M., Regis, D., & Ford, A. (2019). Integrated geoscience of the Northwest Passage, Nunavut; GEM-2 Boothia Peninsula-Somerset Island project, report of activities 2018. Geological Survey of Canada, Open File, 8557.
- Schärer, U., & Deutsch, A. (1990). Isotope systematics and shock-wave metamorphism: II. U–Pb and Rb–Sr in naturally shocked rocks: the Haughton Impact Structure, Canada. *Geochimica et Cosmochimica Acta*, 54, 3435–3447.
- Schultz, M. E. J., Chacko, T., Heaman, L. M., Sandeman, H. A., Simonetti, A., & Creaser, R. A. (2007). Queen Maud block: A newly recognized Paleoproterozoic (2.4–2.5 Ga) terrane in northwest Laurentia. *Geology*, 35(8), 707.
- Sláma, J., Košler, J., Condon, D. J., Crowley, J. L., Gerdes, A., Hanchar, J. M., Horstwood, M. S. A., Morris, G. A., Nasdala, L., Norberg, N., Schaltegger, U., Schoene, B., Tubrett, M. N., & Whitehouse, M. J. (2008). Plešovice zircon — A new natural reference material for U–Pb and Hf isotopic microanalysis. *Chemical Geology*, 249(1-2), 1–35.
- Thorsteinsson, R., & Mayr, U. (1987). The sedimentary rocks of Devon Island, Canadian Arctic Archipelago. Geological Survey of Canada, Memoir, 411, 1–182.

- Van Breemen, O., Thompson, P. H., Hunt, P. A., & Culshaw, N. (1987). U - Pb Zircon Monazite Geochronology From the northern Thelon Tectonic Zone, District of Mackenzie. Geological Survey of Canada, Paper, 87-2, 81–93.
- Vermeesch, P. (2018). IsoplotR: A free and open toolbox for geochronology. *Geoscience Frontiers*, 9(5), 1479–1493.
- Whitney, D. L., & Evans, B. W. (2010). Abbreviations for names of rock-forming minerals. *The American Mineralogist*, 95, 185–187.
- Wheller, C. J., & Powell, R. (2014). A new thermodynamic model for sapphirine: calculated phase equilibria in K<sub>2</sub>O-FeO-MgO-Al<sub>2</sub>O<sub>3</sub>-SiO<sub>2</sub>-H<sub>2</sub>O-TiO<sub>2</sub>-Fe<sub>2</sub>O<sub>3</sub>. *Journal of Metamorphic Geology*, 32(3), 287–299.
- White, R. W., Powell, R., Holland, T. J. B., Johnson, T. E., & Green, E. C. R. (2014a). New mineral activity-composition relations for thermodynamic calculations in metapelitic systems. *Journal of Metamorphic Geology*, 32(3), 261–286.
- White, R. W., Powell, R., & Johnson, T. E. (2014b). The effect of Mn on mineral stability in metapelites revisited: New a-x relations for manganese-bearing minerals. *Journal of Metamorphic Geology*, 32(8), 809–828.
- Whitehouse, M. J., Ravindra Kumar, G. R. and Rimša, A. (2014). Behaviour of radiogenic Pb in zircon during ultrahigh-temperature metamorphism: an ion imaging and ion tomography case study from the Kerala Khondalite Belt, southern India. *Contributions to Mineralogy and Petrology. Beitrage zur Mineralogie und Petrologie*, 168(2).
- Wiedenbeck, M., Allé, P., Corfu, F., Griffin, W. L., Meier, M., Oberli, F., Quadt, A. V. O. N., Roddick, J. C., & Spiegel, W. (1995). Three natural zircon standards for U-Th-Pb, Lu-hf, trace element and Ree analyses. *Geostandards and Geoanalytical Research*, 19(1), 1–23.

- Williams, M. L., Jercinovic, M. J., Goncalves, P., & Mahan, K. (2006). Format and philosophy for collecting, compiling, and reporting microprobe monazite ages. *Chemical Geology*, 225(1-2), 1–15. <https://doi.org/10.1016/j.chemgeo.2005.07.024>
- Williams, M.L., Jercinovic, M.J., Mahan, K.H., Dumond, G. (2017). Electron Microprobe Petrochronology. *Rev. Mineral. Geochem.* 83, 153–182.
- Yakymchuk, C., Rehm, A., Liao, Z., & Cottle, J. M. (2019). Petrochronology of oxidized granulites from southern Peru. *Journal of Metamorphic Geology*, 37(6), 839–862.

## Chapter 3

### 3 Late Neoproterozoic terrane and juvenile Paleoproterozoic rocks on northern Devon Island, Canadian Arctic

#### 3.1 Introduction

The Canadian Shield is made up of Archean cratons merged by Paleoproterozoic collision zones. The Archean Rae craton at the core of the Canadian Shield, is merged with the Slave craton by the Paleoproterozoic Thelon tectonic zone (Fig. 3.1a, e.g., Hoffman, 1988). The Rae craton is primarily composed of ca. 2.8–2.6 Ga plutonic crust with ca. 2.7 Ga supracrustal metavolcanic–metasedimentary belts, and ca. 2.6 Ga plutonism (e.g., Sanborn-Barrie et al., 2014), while the Thelon tectonic zone is composed of ca. 2.07–1.96 Ga plutonics (van Breemen et al., 1987; Berman et al., 2018) and a ca. 2.09–1.91 Ga supracrustal sequence (Davis et al., 2021).

The northernmost extreme of the Canadian Shield outcrops on Devon and Ellesmere islands in the Canadian Arctic Archipelago but the oldest rocks here are distinct from typical Rae cratonic crust. Previous work on Devon and Ellesmere islands has established the southern portion of Devon Island as a late Neoproterozoic terrane (ca. 2.55–2.47 Ga; Frisch 1988; Frisch and Hunt, 1988; Chapter 2), of which similar late Neoproterozoic rocks have been recently established along the western portion of the Rae craton (e.g., Regis and Sanborn-Barrie, 2022). On Ellesmere Island, juvenile middle Paleoproterozoic crust (ca. 2.0–1.9 Ga, Frisch, 1988; Frisch and Hunt, 1988; Gilotti et al., 2018), likely represents a northern extension of the Thelon tectonic zone (e.g., Gilotti et al., 2018). Little is known about northern Devon Island, which lies between the late Neoproterozoic terrane of southern Devon Island and the juvenile middle Paleoproterozoic crust of Ellesmere Island.

Defining the extent of late Neoproterozoic rocks and the Thelon tectonic zone in the Canadian Arctic is important to understanding the tectonic and metamorphic history of northern Laurentia throughout the late Neoproterozoic and Paleoproterozoic including their involvement in orogenic events like the Thelon and Arrowsmith orogenies, and the architecture pre- and syn-assembly of the Nuna supercontinent. For this study, we use LA-ICP-MS U–Pb zircon dating on a collection of metaigneous and metasedimentary samples

from the northern coast of Devon Island to document the presence of late Neoproterozoic crust and/or juvenile Paleoproterozoic crust. Additionally, we use EPMA Th–U–Pb monazite dating and phase equilibrium modelling to determine the timing and pressure–temperature (P–T) conditions of high–temperature metamorphism on northern Devon Island.

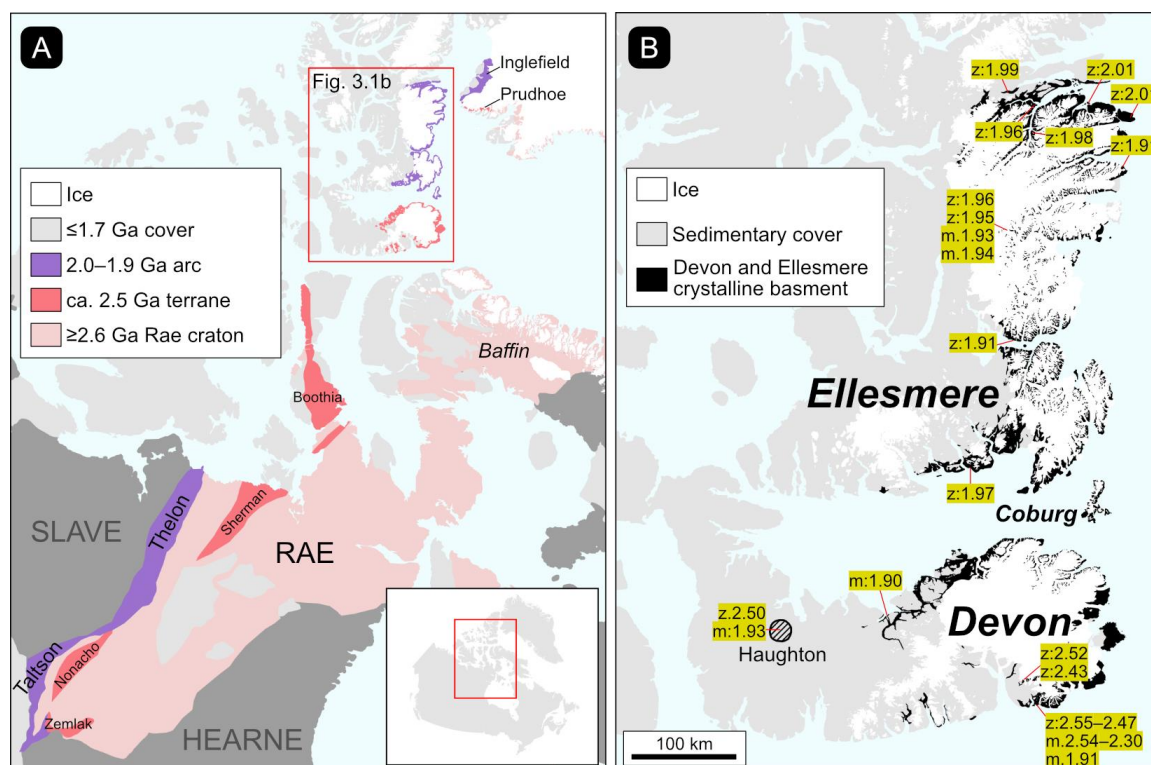


**Figure 3.1. (a) Map of northern Laurentia highlighting the Rae craton and other relevant Archean–Paleoproterozoic units. Modified after Chapter 2 and Regis and Sanborn-Barrie (2022). (b) Map of Devon and Ellesmere islands displaying all previously published (Th)–U–Pb zircon (z) and monazite (m) ages from the crystalline basement rocks. Modified after Chapter 2.**

### 3.2 Geological setting

The crystalline basement of eastern Devon and southeastern Ellesmere islands is exposed along the coasts or as nunataks within the Devon Ice Cap and Prince of Wales Icefields respectively (Fig. 3.1b). On Devon Island, the structural fabric of the crystalline basement trends east–west, with rock-types including pyroxene quartzofeldspathic gneisses, metasedimentary rocks, quartzite, metabasite, and rare marble (Frisch, 1988; Chapter 2).

On southern Devon Island, pyroxene quartzofeldspathic gneisses and metabasite have ca. 2.55–2.51 Ga crystallization ages, interleaved with rutile–garnet metasedimentary rocks deposited at ca.  $\geq 2.47$  Ga (Chapter 2). Monazite ages and younger zircon growth indicate these late polymetamorphic Neoproterozoic rocks were subject to granulite facies metamorphism during the Thelon–Inglefield orogeny (ca. 1.91 Ga) and potentially during the Arrowsmith orogeny (ca. 2.5–2.3 Ga, Chapter 2).

On northern Devon Island, hints of late Neoproterozoic crust have been suggested by dating of crystalline basement clasts within the impact melt rocks of the Haughton impact structure, which penetrated through ~1.9 km of the sedimentary cover rocks. Shocked zircon from these clasts have yielded dates as old as ca. 2.50 Ga, with most between ca. 2.3–1.8 Ga (Schärer and Deutsch, 1990; Erickson et al., 2021). However, the late Neoproterozoic and earliest Paleoproterozoic ages reported on northern Devon Island are from oscillatory zoned grains in metasedimentary gneiss clasts, hence they may represent detrital ages, not Archean protolith crystallization or deposition ages. The only in situ crystalline basement sample dated on northern Devon is a garnet–biotite metapelite from Sverdrup Inlet with a late Neoproterozoic whole-rock Nd model age (ca. 2.57 Ga, Schärer and Deutsch, 1990), suggesting a late Neoproterozoic to early Paleoproterozoic protolith deposition age or a late Neoproterozoic provenance for the metasedimentary protolith. Monazite from the crystalline impact melt clasts and the in-situ garnet–biotite metapelite yielded ca. 1.9 Ga ages, likely representing growth during Thelon–Inglefield metamorphism.

To the north, on Ellesmere Island, the crystalline basement is comprised of generally north–south trending orthopyroxene quartzofeldspathic gneisses, garnet–sillimanite–cordierite metasedimentary rocks, orthopyroxene granitoids, quartzite, marble, and metabasite (Frisch, 1988). The abundance of granitoids and marble in particular, marks a significant difference to the lithology of Devon Island. Zircon and monazite ages from Ellesmere Island are all middle Paleoproterozoic in age (ca. 2.0–1.9 Ga; Frisch, 1988; Frisch and Hunt, 1988; Gilotti et al., 2018). The oldest zircon ages between ca. 2.01–1.96 Ga are igneous protolith crystallization ages of granitoid gneisses comparable to the Thelon tectonic zone plutonics, while ca. 1.96–1.91 Ga ages from anatectic granite zircon and monazite are representative of Thelon–Inglefield anatexis and metamorphism (c.f. Gilotti



et al., 2018; Caswell et al., 2021). Whole-rock Nd model ages from Ellesmere Island are ca. 2.1–2.0 Ga (Hegner and Jackson, 1990), suggesting late Neoproterozoic crust does not outcrop on Ellesmere Island.

Peak P–T conditions of ca. 1.9 Ga Thelon–Inglefield metamorphism have been constrained by phase equilibrium modelling to ca. 9 kbar and >850 °C on southern Devon Island, locally obtaining ultrahigh temperature conditions as evidenced by a sapphirine–quartz assemblage in metapelite (Chapter 2). Elsewhere, on northern Devon and Ellesmere islands thermobarometry estimates yield P–T conditions of ca. 3–7 kbar and ca. 500–750 °C (Frisch, 1988); however, these have been suggested to be influenced by decompression and cooling, and thus are not representative of peak Thelon–Inglefield metamorphism in this region.

### 3.3 Sample descriptions and petrography

Eleven samples of the crystalline basement on northern Devon Island were collected between Sverdrup Inlet and Brae Bay (Fig. 3.2). South of Sverdrup Inlet, migmatitic orthogneisses and paragneisses are exposed along the valley. Sample HAU-16-1453A was collected from a dark grey migmatitic orthogneiss with hornblende–biotite tonalite melanosome and thin granodiorite leucosome (Fig. 3.3a). The melanosome has an assemblage of plagioclase, quartz, biotite, hornblende, apatite and magnetite (Fig. 3.4a), while the leucosome assemblage comprises quartz, plagioclase and K-feldspar. In thin section, zircon was primarily observed in the melanosome of the orthogneiss, and monazite was absent entirely.

Post-kinematic biotite granite dikes were observed intruding the migmatitic orthogneisses south of Sverdrup Inlet and appear to post-date anatexis of the orthogneiss (Fig. 3.3a). Two biotite granite dike samples were analyzed to constrain the minimum timing of deformation and anatexis of the host orthogneiss (HAU-16-1453C, HMP-00-200). Both samples contain an assemblage of K-feldspar, quartz, plagioclase, biotite, apatite, magnetite and ilmenite.

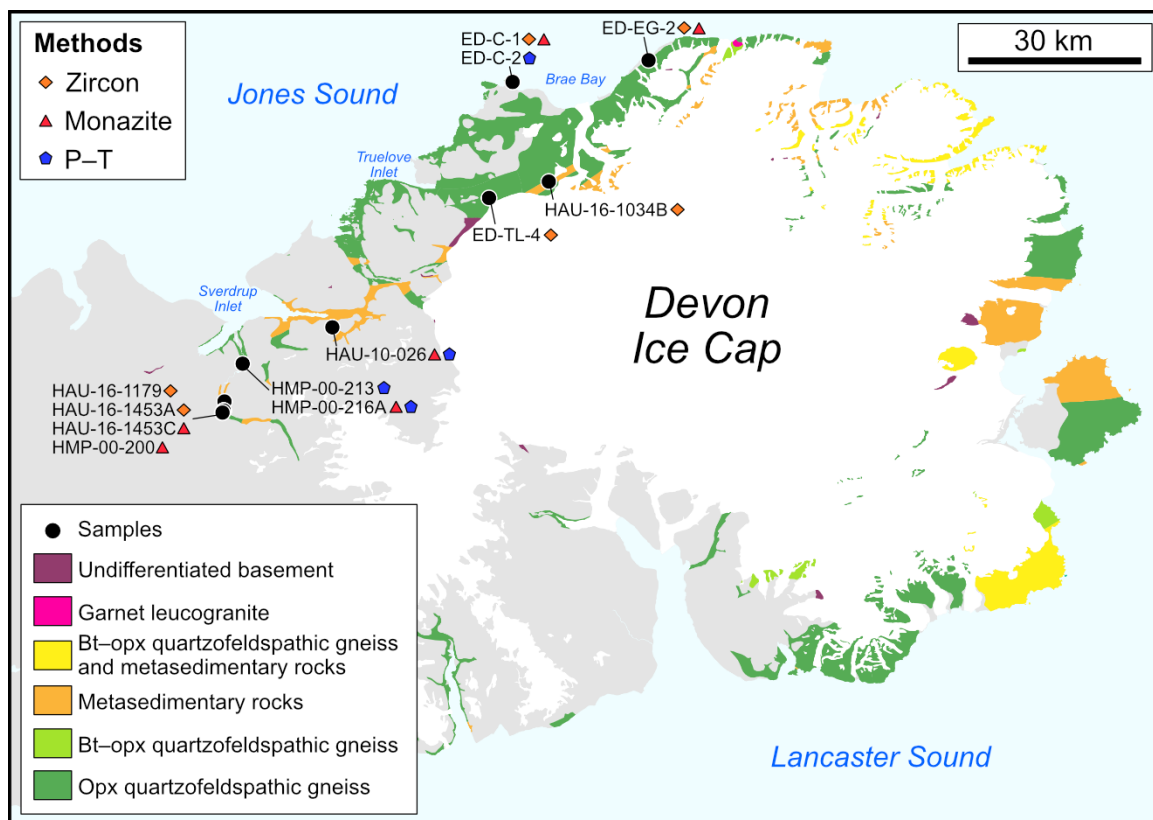


**Figure 3.2. Map of eastern Devon Island displaying the locations of samples used in this study. Geology of the crystalline basement is after Frisch (1984).**

Sample HAU-16-1179 was collected from the migmatitic paragneisses south of Sverdrup Inlet, consisting of a sillimanite–cordierite–biotite psammite melanosome with comparatively thick biotite granite leucosome (Fig. 3.3b). The full assemblage of the melanosome consists of quartz, plagioclase, biotite, K-feldspar, cordierite and sillimanite (Fig. 3.4b), while the leucosome consists of K-feldspar, quartz, plagioclase and biotite. In thin section, zircon was only observed in the melanosome, and monazite was present in both the melanosome and leucosome.

Sample HMP-00-216A was collected from an iron-stained outcrop of migmatitic paragneiss (Fig. 3.3c), comprising a garnet–biotite–cordierite metapelite melanosome (Fig. 3.4c). The peak assemblage includes quartz, plagioclase, K-feldspar, cordierite, biotite, garnet, rutile and ilmenite. Cordierite may represent a post-peak metamorphic retrograde phase as it is observed replacing garnet (Fig. 3.4d), which has been commonly noted for

metasedimentary rocks across Devon and Ellesmere islands (Frisch, 1988; Chapter 2). Spinel is also present but is mainly confined to inclusions in cordierite or feldspar, not in direct contact with quartz thus it is not included in the inferred peak assemblage. Monazite is mostly present in the matrix of the metapelite melanosome, but one monazite is included within cordierite. Sample HMP-00-213 was collected from a metabasite enclave within the migmatitic paragneiss where sample HMP-00-216A was collected. The metabasite has a granoblastic texture with a peak assemblage of plagioclase, orthopyroxene, clinopyroxene, hornblende, quartz, ilmenite and magnetite (Fig. 3.4e). Macroscopic evidence of partial melting could not be determined; however, thin quartz films along plagioclase and pyroxene grain boundaries are suggestive of partial melting (Fig. 3.4f).

Along the eastern valley of Sverdrup Inlet, HAU-10-026 was collected from an outcrop of biotite–sillimanite–garnet metapelite, comprising a peak assemblage of quartz, K-feldspar, garnet, sillimanite, biotite and rutile (Fig. 3.4g). Muscovite is observed replacing sillimanite and K-feldspar, which is interpreted as a retrograde reaction and is not included in the inferred peak assemblage. Monazite is present in both the matrix and as inclusions in garnet.

On the eastern side of the study area, two separate outcrops of granite–granodiorite gneisses were sampled. ED-TL-4 is from an orthopyroxene–biotite granodiorite gneiss southeast of Truelove Inlet (Fig. 3.3d), containing an assemblage of plagioclase, quartz, K-feldspar, biotite, orthopyroxene, magnetite, ilmenite and apatite. ED-C-1 is from a biotite granite gneiss on the western end of Brae Bay, containing an assemblage of K-feldspar, quartz, plagioclase, biotite, ilmenite and magnetite. A second metabasite enclave was sampled within this biotite granite gneiss, containing a peak assemblage of plagioclase, orthopyroxene, biotite, ilmenite and magnetite (Fig. 3.4h). Like the other metabasite sample, macroscopic evidence of partial melting could not be determined; however, thin quartz films along plagioclase and pyroxene grain boundaries are suggestive of partial melting (Fig. 3.4i).

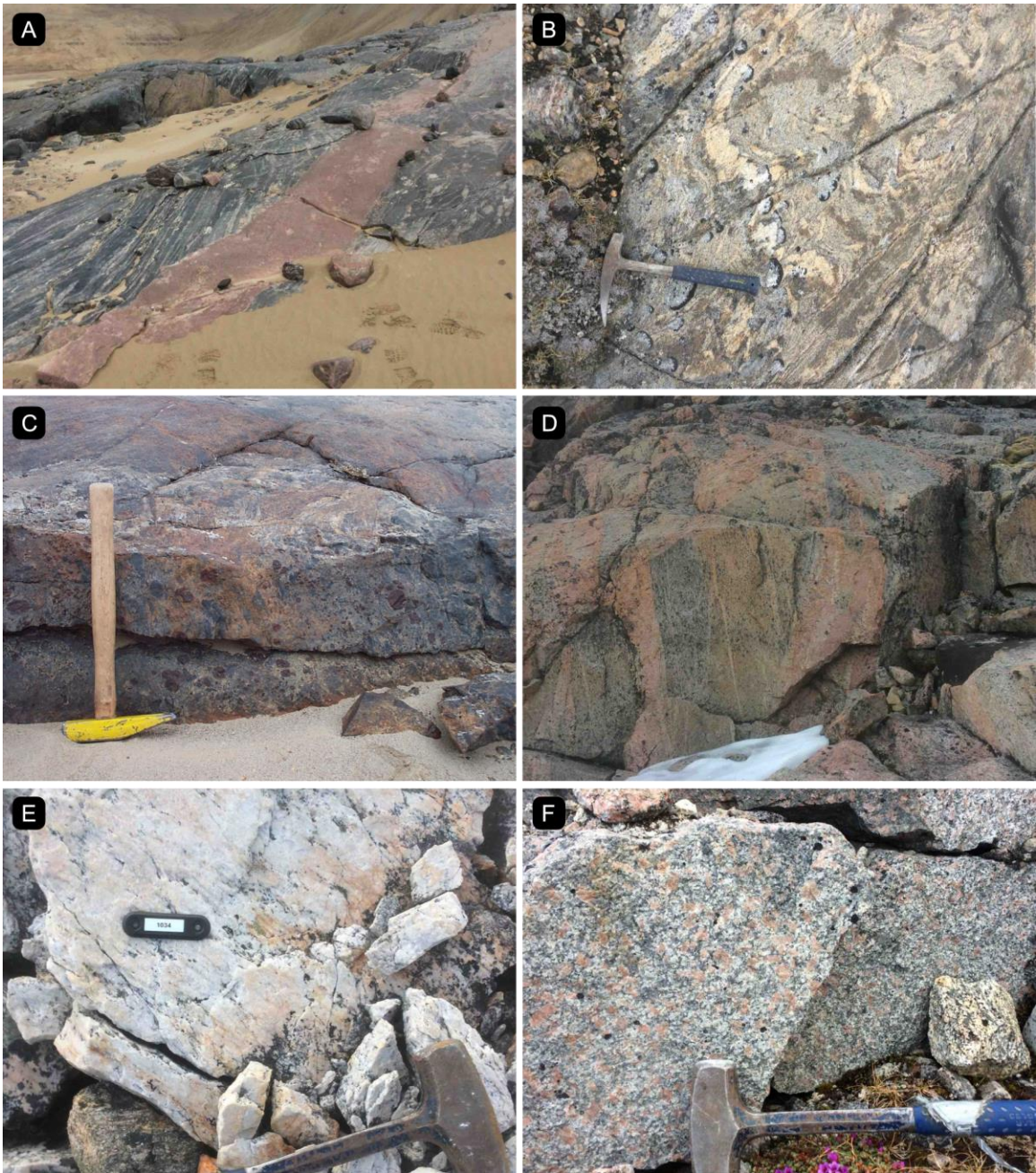


**Figure 3.3. Field photographs of the crystalline basement on northern Devon Island. (a) Migmatitic hornblende–biotite orthogneiss (HAU-16-1453A) intruded by a post-kinematic biotite granite dike (HAU-16-1453C) south of Sverdrup Inlet. Footprints are present in the bottom of the image for scale. (b) Migmatitic sillimanite–cordierite–biotite paragneiss (HAU-16-1179) south of Sverdrup Inlet. (c) Garnet–biotite–cordierite metapelite (HMP-00-216A) from an iron-stained outcrop of the migmatitic paragneiss south of Sverdrup Inlet. (d) Orthopyroxene–biotite granodiorite gneiss**

(ED-TL-4) with granite intrusions southeast of Truelove Inlet. The field of view for this image ~3 m. (e) Quartzite (HAU-16-1034B) with minor K-feldspar and sillimanite south of Brae Bay. (f) K-feldspar megacrystic granite (ED-EG-2) on the eastern end of Brae Bay.

To constrain the age of protolith sedimentary deposition on northern Devon Island, a relatively rare quartzite exposure was sampled south of Brae Bay (Fig. 3.3e). Quartzite sample HAU-16-1034B is composed of ~90% quartz, K-feldspar and sillimanite.

The most easterly collected sample, ED-EG-2, was sampled from an outcrop of massive, K-feldspar megacrystic granite on the eastern end of Brae Bay (Fig. 3.3f). The assemblage features 1–3 cm K-feldspar megacrysts, along with plagioclase, quartz, biotite, apatite, ilmenite and magnetite.

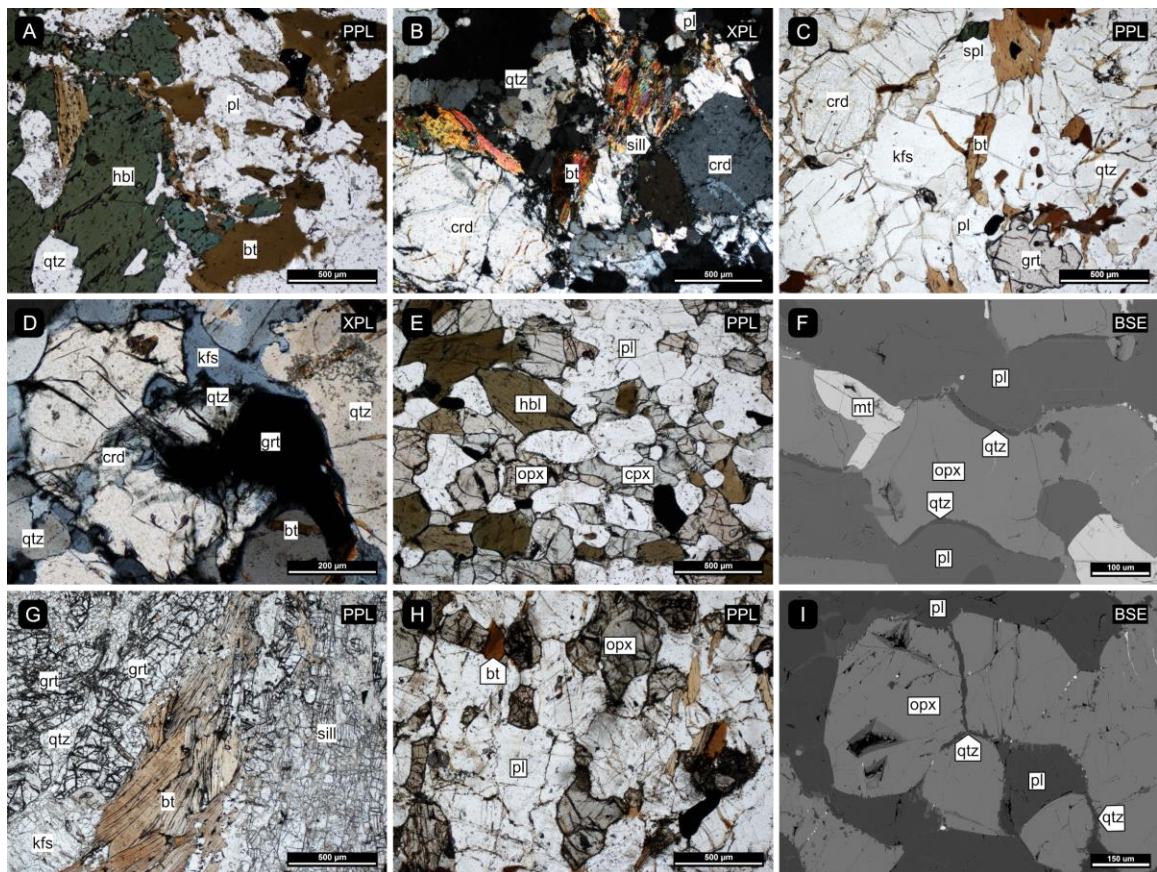


**Figure 3.4. Photomicrographs of the crystalline basement on northern Devon Island. (a) Migmatitic hornblende–biotite orthogneiss HAU-16-1453A. (b) Migmatitic**

**sillimanite–cordierite–biotite paragneiss HAU-16-1179. (c) Garnet–biotite–cordierite metapelite HMP-00-216A. (d) Cordierite replacing garnet in sample HMP-00-216. (e) Hornblende–clinopyroxene–orthopyroxene metabasite HMP-00-213. (f) Thin quartz films around feldspar and pyroxene in metabasite HMP-00-213 indicating possible partial melting. (g) Biotite–sillimanite–garnet metapelite HAU-10-026. (h) Biotite–orthopyroxene metabasite ED-C-2. (i) Thin quartz films around feldspar and pyroxene in metabasite ED-C-2 indicating possible partial melting. PPL: plane polarized light image. XPL: Crossed polarized light image. BSE: backscattered electron image. Mineral abbreviations from Whitney and Evans (2010).**

## 3.4 Methodology

### 3.4.1 LA-ICP-MS zircon dating

Standard crushing, magnetic separation, and heavy liquid techniques were used at the University of Western Ontario and University of Waterloo, Canada to separate zircon from six ~1 kg samples. Zircon was mounted and polished on 25 mm epoxy rounds and imaged under backscattered electron (BSE) and cathodoluminescence (CL) using a JEOL JXA-8530F field-emission electron microprobe at the University of Western Ontario.

U–Pb zircon isotopic analysis was performed using an Agilent 8800 QQQ-ICP-MS in sequence with an Analyte G2 193 nm Excimer laser ablation unit at the University of Waterloo. A 40 µm diameter spot size operating at 8 Hz and with an energy (measured at the sample surface) of 2 J/cm<sup>2</sup> was used for all analyses. Prior to analysis, two 50 µm pre-ablation shots were used to remove surface contamination. This was followed by a 30 s gas background measurement and then 30 s of ablation. Ablated aerosol was carried to the ICP-MS using 0.5 L/min He carrier gas in a Helex ablation cell and mixed with 0.75 L/min argon makeup gas added in a mixing bulb after the cell. The following masses were analyzed (integration times in ms): <sup>238</sup>U (20 ms), <sup>232</sup>Th (10 ms), <sup>207</sup>Pb (80 ms), <sup>206</sup>Pb (50 ms) and <sup>88</sup>Sr (10 ms) in single collector mode.

Several reference materials were analyzed to correct for instrumental and downhole fractionation every 10 analyses of unknowns; primary reference materials included 91500 (Wiedenbeck et al., 1995) for relatively low-U analyses and Plešovice (Slama et al., 2008)

for relatively high-U analyses. Data were processed in Iolite (v3.6) using the U–Pb geochronology 4 data reduction scheme (Paton et al., 2011). Secondary reference materials included Temora 2, which yielded a weighted mean  $^{206}\text{Pb}/^{238}\text{U}$  age of  $419 \pm 2$  (2s;  $n = 10$ ) that is slightly higher than the accepted age of 417 Ma (Black et al., 2004). An additional secondary zircon reference material (R33) yielded an age of  $^{206}\text{Pb}/^{238}\text{U}$  age  $415 \pm 2$  (2s;  $n = 10$ ), which is slightly lower than the accepted age of 419 Ma (Black et al., 2004). All calculated dates and ages are reported with a  $2\sigma$  error at the 95% confidence level. Zircon data analysis was performed with IsoplotR (Vermeesch, 2018).

### 3.4.2 EPMA monazite dating

Total Th–U–Pb chemical dating of monazite was conducted on six samples from northern Devon Island using a JEOL JXA-8530F field-emission electron microprobe at the University of Western Ontario, Canada. Full thin section element maps of Ce were produced to locate all monazite grains, followed by monazite element maps of Y, Th, Si, Nd and Ca to observe possible zoning patterns for informed spot analysis. Analytical conditions for monazite dating included a 15 kV accelerating voltage, 120 nA beam current and a 3  $\mu\text{m}$  spot size.  $\text{UM}\alpha$  and  $\text{PbM}\alpha$  were counted with a dwell time of 200 sec on peak and 100 sec on background (two-point), while  $\text{ThM}\beta$  and  $\text{YM}\alpha$  were counted with a dwell time of 100 sec on peak and 50 sec on background (two-point). Monazite dates were calculated using the age equation from Montel et al. (1996). Monazite consistency standards GSC-2908 ( $^{207}\text{Pb}/^{206}\text{Pb} = \text{ca. } 1795 \text{ Ma}$ ;  $\text{ThO}_2 = \text{ca. } 2.3 \text{ wt\%}$ ) and GSC-3345 ( $^{207}\text{Pb}/^{206}\text{Pb} = \text{ca. } 1821 \text{ Ma}$ ;  $\text{ThO}_2 = \text{ca. } 8.6 \text{ wt\%}$ ) were utilized throughout the analytical sessions (Stern and Berman, 2001), achieving EPMA weighted mean ages of  $1793 \pm 23 \text{ Ma}$  (MSWD = 0.1,  $n = 17$ ) and  $1823 \pm 11 \text{ Ma}$  (MSWD = 0.4,  $n = 17$ ) respectively.

### 3.4.3 Phase equilibrium modelling

Peak P–T conditions of metamorphism were estimated by phase equilibrium modelling of two suprasolidus metapelite samples (HMP-00-216A, HAU-10-026) and two suprasolidus metabasite samples (HMP-00-213, ED-C-2). The samples were modelled with the Theriak/Domino software package (de Capitani & Petrakakis, 2010) and the internally consistent thermodynamic database of Holland and Powell (2011). Metapelite assemblages

were modelled in the 11-component MnO-Na<sub>2</sub>O-CaO-K<sub>2</sub>O-FeO-MgO-Al<sub>2</sub>O<sub>3</sub>-SiO<sub>2</sub>-H<sub>2</sub>O-TiO<sub>2</sub>-Fe<sub>2</sub>O<sub>3</sub> (MnNCKFMASHTO) chemical system. The activity-composition (a-x) models used include plagioclase (pl) and K-feldspar (ksp) from Holland et al. (2021); granitic melt (liq), garnet (g), orthopyroxene (opx), biotite (bi) and cordierite (cd) from White et al. (2014a, b); sapphirine (sa) from Wheller and Powell (2014); magnetite (mt) and spinel (sp) from White et al. (2002); and ilmenite (ilm) from White et al. (2000). Pure phases considered include quartz (q), rutile (ru), sillimanite (sill) and kyanite (ky). Metabasite assemblages were modelled in the 10-component Na<sub>2</sub>O-CaO-K<sub>2</sub>O-FeO-MgO-Al<sub>2</sub>O<sub>3</sub>-SiO<sub>2</sub>-H<sub>2</sub>O-TiO<sub>2</sub>-Fe<sub>2</sub>O<sub>3</sub> (NCKFMASHTO) chemical system. The a-x models used include tonalitic melt (L), augite (aug) and hornblende (hb) from Green et al. (2016); garnet (g), orthopyroxene (opx), and biotite (bi) from White et al. (2014a); magnetite (mt) from White et al. (2002); ilmenite (ilm) from White et al. (2000); and plagioclase (pl, C1) and K-feldspar (ksp) from Holland and Powell (2003). Pure phases considered include quartz (q), rutile (ru) and titanite (sph).

Bulk-rock compositions for metapelite modelling were calculated from thin section element maps standardized to wt.% with XMapTools (Fig. 3.5, Lanari et al., 2014; Lanari et al., 2019). Element maps were collected with a JEOL JXA-8530F field-emission electron microprobe at the University of Western Ontario, Canada. Analytical conditions of mapping included a 15 kV accelerating voltage, 100 nA beam current, 20 µm step size, and 5 msec dwell time. Point analysis of all silicate phases was performed with a 15 kV accelerating voltage, 20 nA beam current, 1 µm spot size for garnet and 5 µm spot size for all other phases. Bulk-rock compositions for metabasite modelling were determined by whole-rock X-ray fluorescence at ALS Geochemistry, Sudbury, Canada. Maximum H<sub>2</sub>O content was estimated using loss on ignition values of whole-rock analysis. H<sub>2</sub>O-temperature (H<sub>2</sub>O-T) diagrams were constructed to further constrain H<sub>2</sub>O estimations, selecting the maximum amount of H<sub>2</sub>O required to preserve the inferred peak metamorphic assemblages at the solidus (Appendix A.6). Ferric iron ratios were estimated by whole-rock titration at ALS Geochemistry, Sudbury, Canada. Whole-rock data was also collected for metapelite HAU-10-026, but not for metapelite sample HMP-00-216A, therefore a H<sub>2</sub>O-T diagram with a relatively wide compositional range was used to constrain the H<sub>2</sub>O estimation. The ferric iron ratio for metabasite HMP-00-213 was also used for metapelite



HMP-00-216A since they are from the same locality. H<sub>2</sub>O–T models were constructed at 7 kbar for metapelite samples and at 6.5 kbar for metabasite samples. Metabasites were modelled at a lower pressure because P–T modelling suggested the preservation of lower pressure peak assemblages.

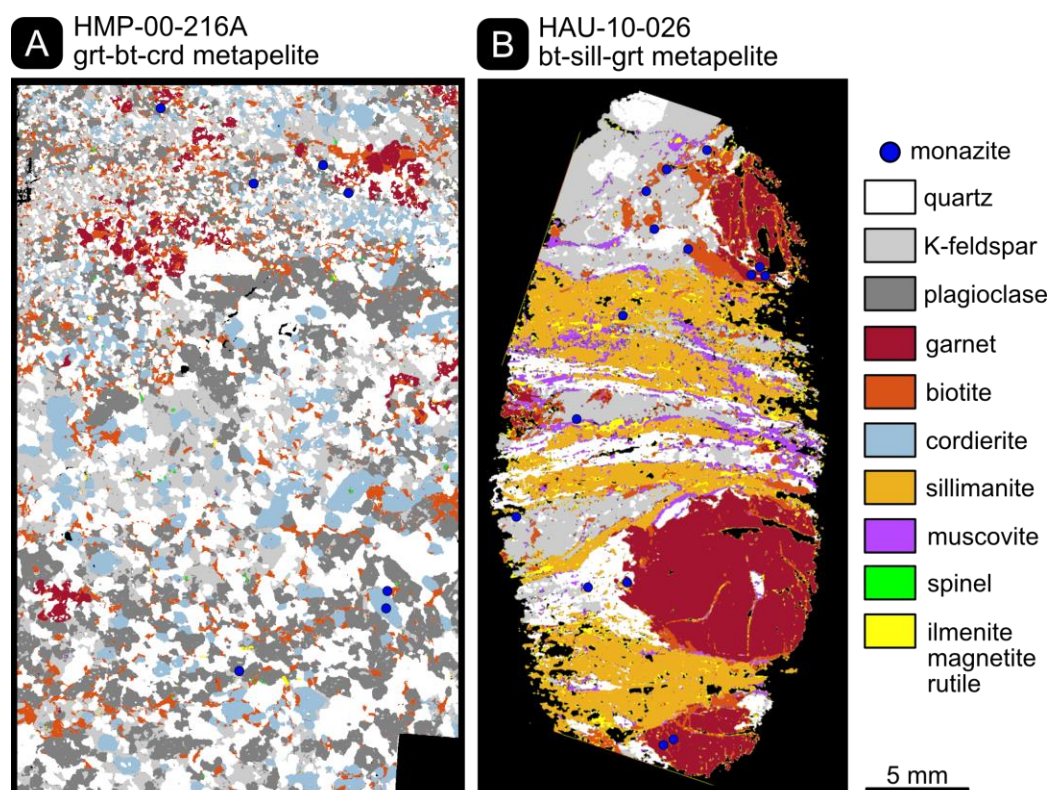


**Figure 3.5.** Thin section phase maps of metapelite samples used for phase equilibrium modelling and EPMA monazite dating.

### 3.5 LA-ICP-MS zircon dating

LA-ICP-MS zircon dating results are presented in Figure 3.6 for metaigneous samples and in Figure 3.7 for metasedimentary samples. A data table of all LA-ICP-MS zircon analyses is presented in Appendix A.4.

Zircon from migmatitic orthogneiss HAU-16-1453A are prismatic with bright-CL oscillatory zoned cores (Fig. 3.6a). These yield concordant to slightly discordant ( $\leq 5\%$ )  $^{207}\text{Pb}/^{206}\text{Pb}$  dates between ca. 2.56–2.30 Ga. The three oldest analyses yield a concordia

date of  $2.55 \pm 0.01$  Ga (MSWD = 1.1,  $n = 3/30$ ), which is interpreted as the minimum crystallization age.

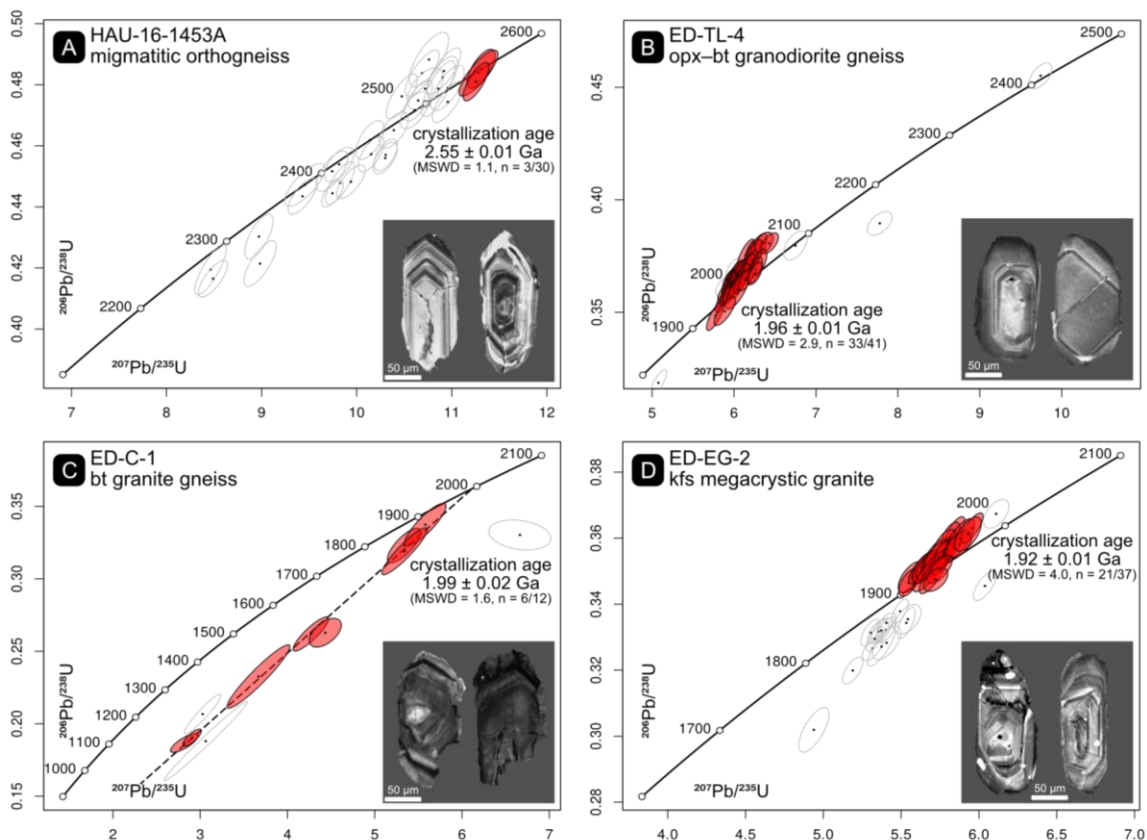


**Figure 3.6. Wetherill concordia diagrams and representative CL imagery of metaigneous LA-ICP-MS zircon dating results. Errors reported in  $2\sigma$ .**

Orthopyroxene–biotite granodiorite gneiss ED-TL-4 has prismatic oscillatory zoned zircon (Fig. 3.6b), yielding concordant to slightly discordant ( $\leq 6\%$ )  $^{207}\text{Pb}/^{206}\text{Pb}$  dates between ca. 2.01–1.94 Ga ( $n = 33/41$ ). These analyses yield a weighted mean age of  $1.96 \pm 0.01$  Ga (MSWD = 2.9,  $n = 33/41$ ), which is interpreted as the age of protolith crystallization. The three older (ca. 2.08–2.40 Ga) outlier zircon analyses are interpreted as inherited grains.

Biotite granite gneiss ED-C-1 has prismatic oscillatory zoned zircon (Fig. 3.6c), yielding a highly discordant array of analyses with  $^{207}\text{Pb}/^{206}\text{Pb}$  dates mostly between ca. 1.99–1.92 Ga ( $n = 6/12$ ). A discordia line yields an upper intercept date of  $1.99 \pm 0.02$  Ga (MSWD = 1.6,  $n = 8/12$ ) and a lower intercept date of  $359 \pm 65$  Ma. The upper intercept date is

interpreted as the age of protolith crystallization. The lower intercept date may be geologically meaningless but is notably like the lower intercept ages from metaplutonic rocks dated on Ellesmere Island (Gilotti et al., 2018), which was interpreted as disturbance during the late Paleozoic Ellesmerian orogeny.

K-feldspar megacrystic granite ED-EG-2 has prismatic oscillatory zoned zircon (Fig. 3.6d), yielding  $^{207}\text{Pb}/^{206}\text{Pb}$  dates primarily between ca. 1.96–1.90 Ga ( $n = 35/37$ ). These analyses yield a rough discordia upper intercept date of  $1.92 \pm 0.01$  Ga (MSWD = 4.2,  $n = 35/37$ ), and a geologically meaningless lower intercept date of  $64 \pm 137$  Ma. Analyses that have experienced little to no Pb-loss yield a weighted mean date of  $1.92 \pm 0.01$  Ga (MSWD = 4.0,  $n = 21/37$ ), which is interpreted as the age of crystallization.

Migmatitic paragneiss HAU-16-1179 has dark-CL oscillatory zoned detrital cores with thin bright-CL metamorphic rims (Fig. 3.7a). The oscillatory zoned detrital cores yield  $^{207}\text{Pb}/^{206}\text{Pb}$  dates between ca. 2.65–2.00 Ga. The dominant detrital mode is between ca. 2.5–2.4 Ga, with a subordinate mode around ca. 2.2 Ga. The youngest concordant to near concordant ( $\leq 2\%$ ) analyses yield a concordia date of ca.  $2.22 \pm 0.01$  Ga (MSWD = 1.4,  $n = 2/19$ ), which is interpreted as the maximum age of sedimentary protolith deposition.

Quartzite HAU-16-1034B has dominantly dark-CL oscillatory zoned detrital cores and lesser bright-CL oscillatory zoned detrital cores with dark-CL metamorphic rims (Fig. 3.7b). Analyses of oscillatory zoned detrital cores yield  $^{207}\text{Pb}/^{206}\text{Pb}$  dates between ca. 2.93–2.05 Ga. The youngest cluster of near concordant ( $\leq 3\%$ ) zircon with dates between ca. 2.08–2.05 Ga is interpreted to represent the maximum age of protolith sedimentary deposition. Two analyses from metamorphic rims on ca. 2.55 Ga cores yield the same date of ca. 1.96 Ga, which can be interpreted as the minimum age of sedimentary protolith deposition or the maximum of sedimentary protolith deposition if also detrital. The dominant detrital mode has dates around ca. 2.30–2.20 Ga, with subordinate modes around ca. 2.10, 2.45 and 2.55 Ga.

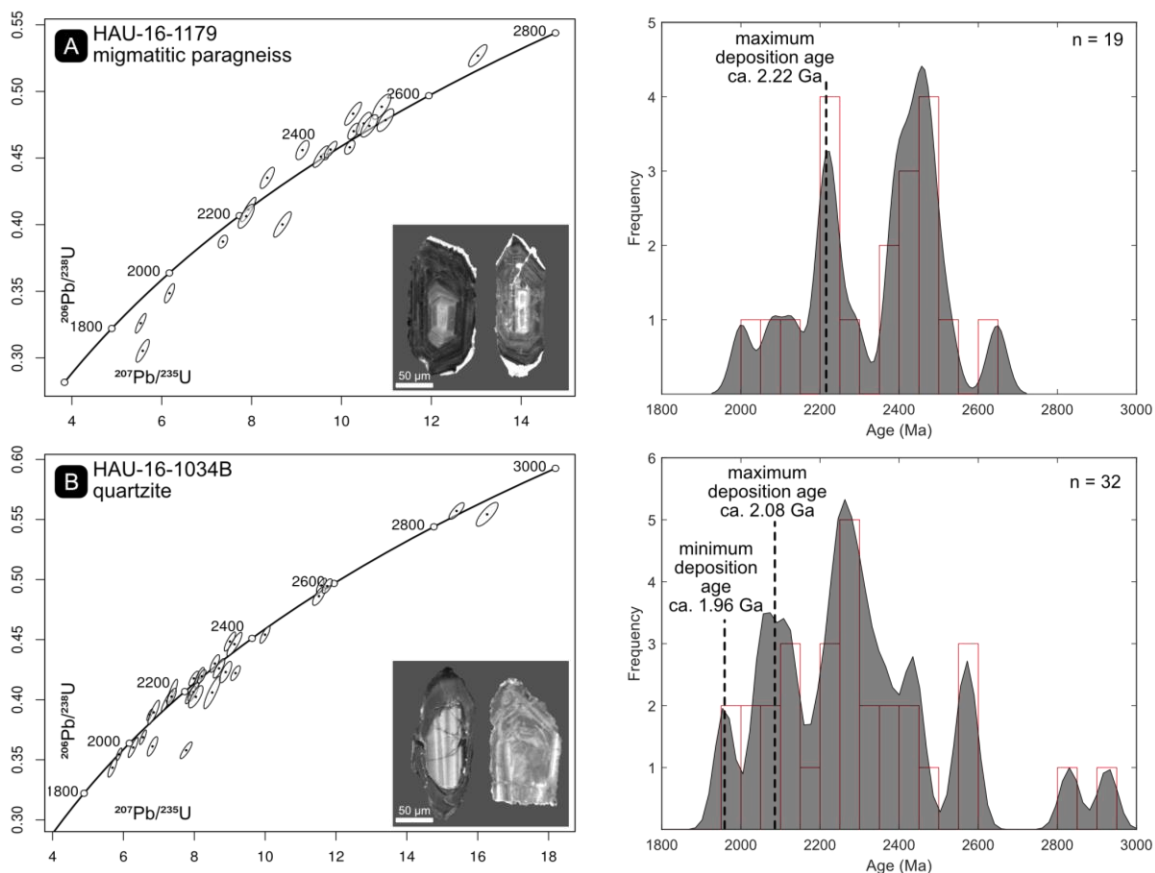


**Figure 3.7. Wetherill concordia diagrams, representative CL imagery, and histograms/probability density diagrams of metasedimentary LA-ICP-MS zircon dating results. Errors reported in  $2\sigma$ .**

### 3.6 EPMA monazite dating

EPMA monazite dating results are presented in Figure 3.8 for metaigneous samples and in Figure 3.9 for metasedimentary samples. A data table of all EPMA monazite analyses is presented in Appendix A.5.

Biotite granite gneiss ED-C-1 has monazite with high Th and Y content (ca. 7–20 wt%  $\text{ThO}_2$ , 2 wt%  $\text{Y}_2\text{O}_3$ ). Eighty-three analyses across thirteen monazite yield dates between ca. 1.94–1.87 Ga (Fig. 3.8a). Excluding four younger outliers, the remaining analyses yield a weighted mean date of  $1.91 \pm 0.01$  Ga (MSWD = 0.4,  $n = 79/83$ ), which is interpreted as the age of peak metamorphism.

K-feldspar megacrystic granite ED-EG-2 has large (~100–200  $\mu\text{m}$ ) amorphous monazite that have been partly replaced by allanite. Monazite is homogenous with low Th and Y content (ca. 2.0–4.2 wt%  $\text{ThO}_2$ , <0.3 wt%  $\text{Y}_2\text{O}_3$ ). The low Th content yields dates with large errors (ca.  $\pm 100$  Ma) between ca. 1.99–1.75 Ga (Fig. 3.8b). Combined, the monazite analyses yield a weighted mean date of  $1.87 \pm 0.02$  Ga (MSWD = 1.4;  $n = 23/23$ ), which is interpreted as a metamorphic age.

Post-kinematic biotite granite dike HAU-16-1453C has monazite with moderate Th and high Y content (ca. 5–12 wt%  $\text{ThO}_2$ , 0.6–2.5 wt%  $\text{Y}_2\text{O}_3$ ), which have been partly replaced by allanite. Excluding five young outliers, the remaining analyses yield dates between ca. 1.93–1.88 Ga ( $n = 12/17$ ; Fig. 3.8c). These analyses yield a weighted mean date of  $1.90 \pm 0.01$  Ga (MSWD = 0.4,  $n = 12/17$ ). The other post-kinematic biotite granite dike sample, HMP-00-200, has monazite with moderate to high Th and moderate Y content (ca. 5–18 wt%  $\text{ThO}_2$ , 0.1–1.0 wt%  $\text{Y}_2\text{O}_3$ ). Excluding five young outliers, the remaining analyses yield dates between ca. 1.93–1.86 Ga ( $n = 38/43$ ; Fig. 3.8d). These analyses yield an identical weighted mean date of  $1.90 \pm 0.01$  Ga (MSWD = 1.3,  $n = 38/43$ ). This date is interpreted as the age of crystallization or immediate metamorphism of the post-kinematic biotite granite dikes, therefore constraining the age of migmatitic host-rock deformation and anatexis to ca.  $\geq 1.90$  Ga.

Garnet–biotite–cordierite metapelite HMP-00-216A has monazite present in the matrix and one grain included in cordierite, which altogether yield dates between ca. 1.95–1.77 Ga ( $n = 28$ ; Fig. 3.9a). The monazite inclusion in cordierite has high Y and moderate Th content, yielding a weighted mean date of  $1.93 \text{ Ga} \pm 0.03 \text{ Ga}$  (MSWD = 0.3,  $n = 4/28$ ). This monazite is interpreted to have grown during prograde metamorphism before garnet and cordierite were part of the stable assemblage. The majority of the matrix monazite have low Y and moderate to high Th content, which yield a weighted mean date of  $1.91 \pm 0.01$  Ga (MSWD = 0.7,  $n = 14/28$ ), which is interpreted as the age of peak metamorphism during garnet stability. Two outlier matrix monazite, have significantly lower Th content and increased Y content compared to the other matrix monazite, yielding a weighted mean date of  $1.83 \pm 0.03$  Ga (MSWD = 0.2,  $n = 9/28$ ). This is interpreted as a later growth associated with garnet breakdown.

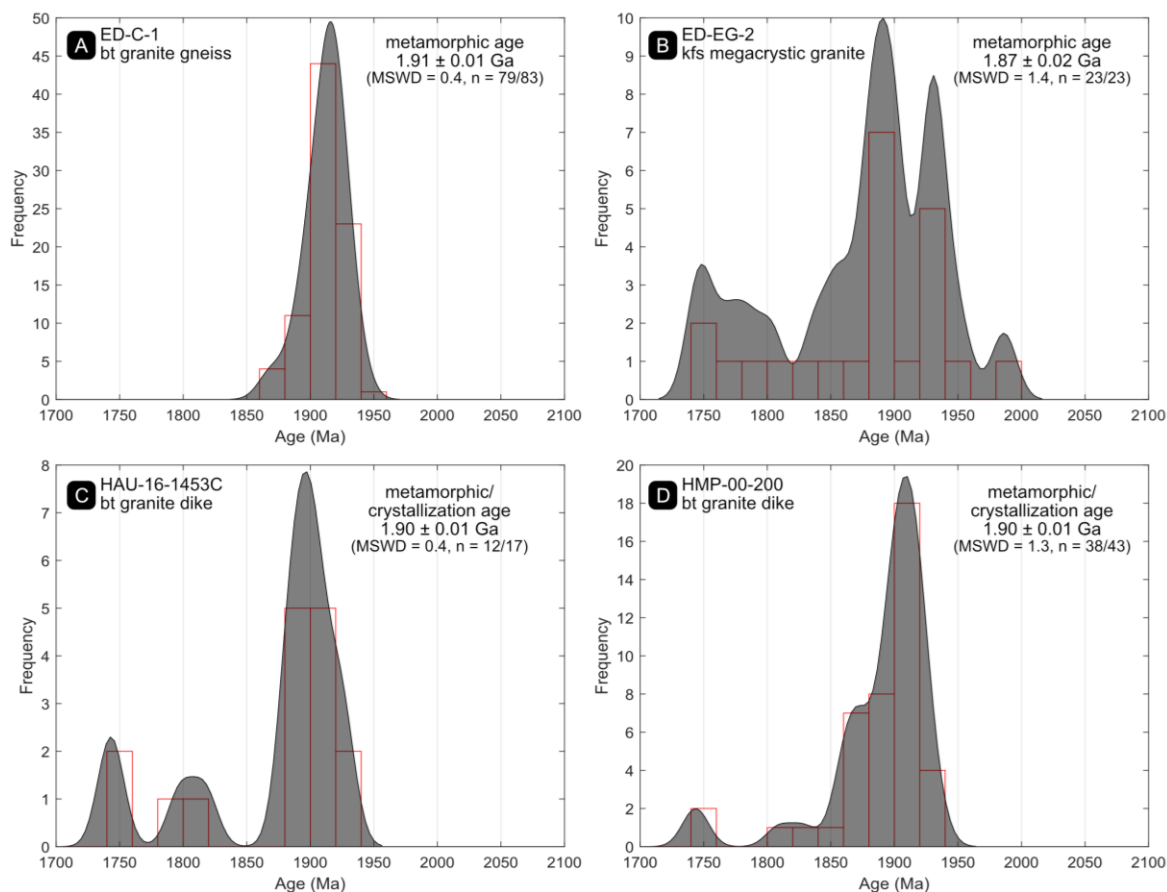


**Figure 3.8. Histograms/probability density diagrams of metaigneous EPMA monazite dating results. Errors reported in  $2\sigma$ .**

Biotite–sillimanite–garnet metapelite HAU-10-026 has monazite in the matrix and within fractured garnet rims, which altogether yield dates between ca. 1.94–1.79 Ga ( $n = 38$ ; Fig. 3.9b). Monazite in the matrix have low  $Y_2O_3$  and moderate to high  $ThO_2$ , which yield a weighted mean date of  $1.90 \text{ Ga} \pm 0.01 \text{ Ga}$  ( $MSWD = 1.1$ ,  $n = 21/38$ ). Monazite within the fractured garnet rims have higher  $Y_2O_3$  and low  $ThO_2$ , yielding a younger weight mean date of  $1.88 \pm 0.01 \text{ Ga}$  ( $MSWD = 1.7$ ,  $n = 17/38$ ). The ca. 1.90 Ga matrix monazite date is interpreted as the age of peak metamorphism during which garnet was stable resulting in the growth of low Y monazite, as yttrium was preferentially incorporated in the garnet (e.g., Gibson et al., 2004). This was followed by garnet breakdown at ca. 1.88 Ga resulting in the growth of high Y monazite within the fractured garnet rims.

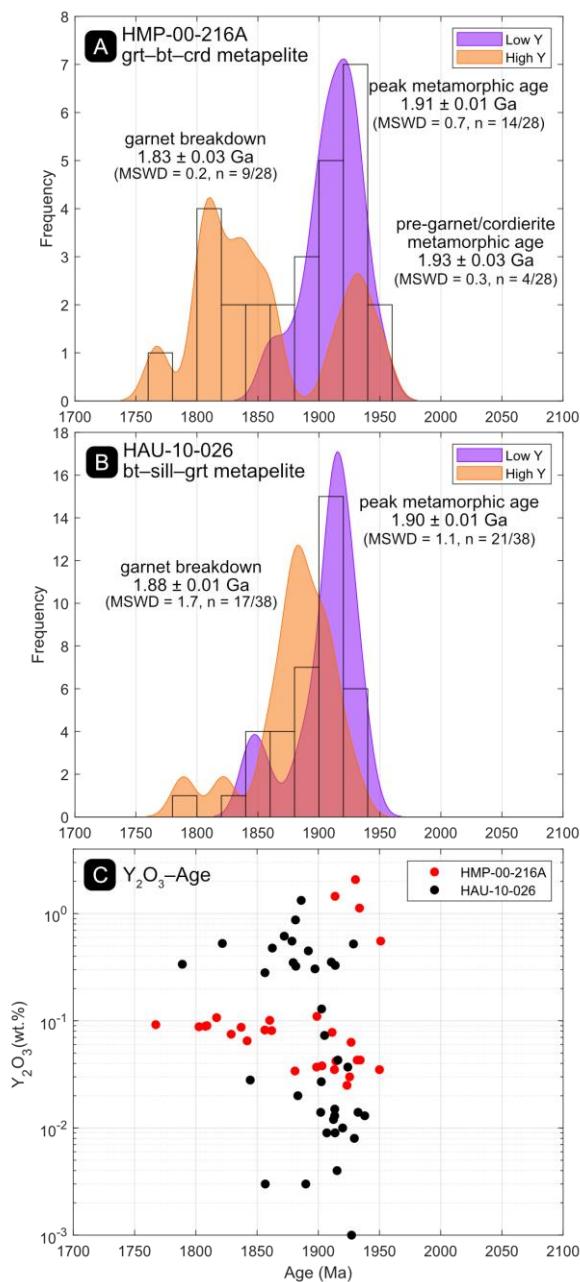


**Figure 3.9. (a–b) Histograms/probability density diagrams of metasedimentary EPMA monazite dating results. Probability density diagrams are separated by relative Y content in monazite. Errors reported in  $2\sigma$ . (c)  $Y_2O_3$  vs. monazite age (Ma) plot. The yttrium content has a general high–low–high trend, starting with high Y monazite growth before garnet stability, low Y monazite growth during garnet stability (peak metamorphism) and high Y monazite growth during garnet breakdown.**

### 3.7 Phase equilibrium modelling

The bulk-rock compositions used for phase equilibrium modelling are listed in Table 3.1. Suprasolidus P–T models for all four samples modelled are presented in Figure 3.10.

**Table 3.1. Bulk-rock compositions (mol.%) of metapelite and metabasite samples used for phase equilibrium modelling.  $X_{\text{Fe}^{3+}} = \text{O}(\text{Fe}_2\text{O}_3)/\text{FeO} \cdot 2$ .**

Sample	H <sub>2</sub> O	SiO <sub>2</sub>	Al <sub>2</sub> O <sub>3</sub>	CaO	MgO	FeO <sub>t</sub>	K <sub>2</sub> O	Na <sub>2</sub> O	TiO <sub>2</sub>	MnO	O	$X_{\text{Fe}^{3+}}$
HMP-00-216A	0.50	77.28	8.64	1.83	3.50	3.55	2.23	2.10	0.46	0.09	0.31	0.18
HAU-10-026	0.27	58.93	21.34	0.47	5.25	10.03	2.13	0.67	0.27	0.52	0.13	0.03
HMP-00-213	0.66	50.48	8.13	10.64	11.55	14.66	0.23	1.13	1.24	-	1.29	0.18
ED-C-2	1.28	57.84	10.99	6.04	7.37	9.69	0.75	4.48	0.91	-	0.65	0.13

Metapelite HMP-00-216A contains an interpreted peak assemblage of quartz, plagioclase, K-feldspar, cordierite, biotite, garnet, rutile, ilmenite and melt (Fig. 3.5a). The interpreted peak assemblage is predicted within a small stability field at ca. 7.2 kbar and 865 °C (Fig. 3.10a). If cordierite is considered a retrograde phase after garnet, it is possible peak metamorphism was in the garnet–biotite–rutile stability field (> 7.2 kbar and 850–870 °C) with minor sillimanite ( $\leq 2$  vol%). This would be followed by an isothermal decompression path during which garnet and sillimanite would be replaced. The absence of orthopyroxene limits the minimum pressure estimate to > 6.0 kbar. High–temperature spinel is only predicted above 990 °C within the orthopyroxene stability field (Fig. 3.5a), which further suggests the spinel in this metapelite is not part of this metamorphic assemblage but could represent an earlier(?) metamorphic assemblage.

Metapelite HAU-10-026 contains an interpreted peak assemblage of quartz, K-feldspar, garnet, sillimanite, biotite, garnet, rutile and melt (Fig. 3.5b). The interpreted peak assemblage is predicted between 7.3–9.9 kbar and 795–815 °C (Fig. 3.10b). Including ilmenite in the inferred peak assemblage limits P–T space to 6.8–7.4 kbar and 810–820 °C. The presence of rutile in this metapelite limits the minimum pressure estimate to 6.8 kbar. Since biotite is mostly present along broken-down garnet rims, it is possible biotite is a retrograde phase, therefore, peak temperatures may have surpassed 820 °C.



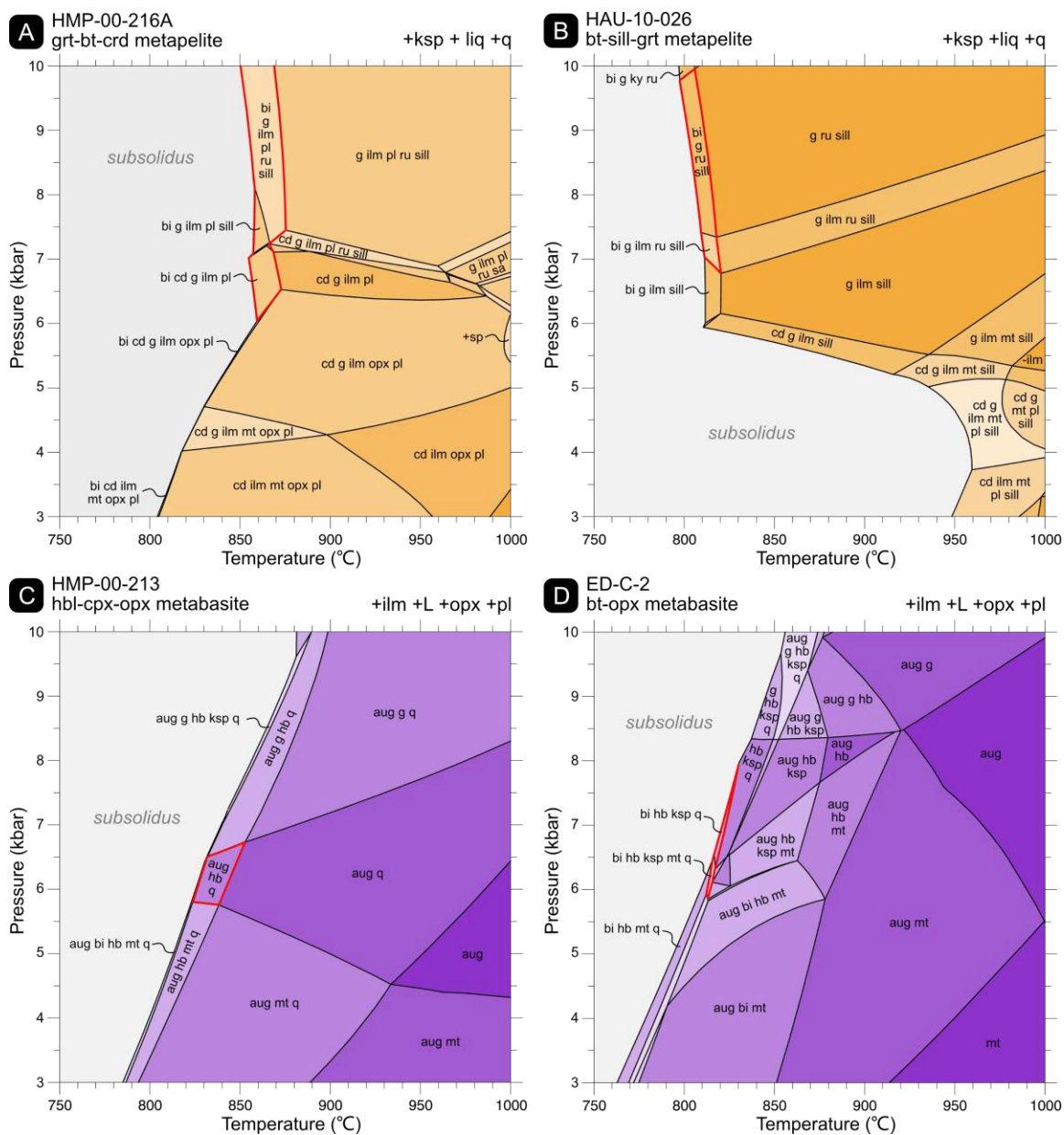


**Figure 3.10. Suprasolidus P–T models for two metapelite (a–b) and two metabasite (c–d) samples. The inferred peak stability fields are outlined in red. Mineral abbreviations follow the a–x models used and field shading corresponds to relative variance.**

Metabasite enclave HMP-00-213 contains an interpreted peak assemblage of plagioclase, orthopyroxene, clinopyroxene, amphibole, quartz, ilmenite and melt. The interpreted peak assemblage is predicted between 5.8–6.8 kbar and 825–855 °C (Fig. 3.10c). The absence

of garnet limits the maximum pressure estimate to < 6.8 kbar. Lower peak pressure and temperature estimates could be made if the minor amount of magnetite present is included in the peak assemblage.

Metabasite enclave ED-C-2 contains an interpreted peak assemblage of plagioclase, orthopyroxene, biotite, K-feldspar, ilmenite, magnetite and melt. The interpreted peak assemblage, along with hornblende, is predicted between 5.8–6.6 kbar and 810–820 °C (Fig. 3.10d). If magnetite is excluded, the peak stability field increases to 6.3–7.9 kbar and 815–830 °C. The absence of garnet and clinopyroxene from this metabasite limit peak P–T estimates to < 8.4 kbar and < 850 °C respectively.

## 3.8 Discussion

### 3.8.1 Late Neoproterozoic terrane with Paleoproterozoic metasedimentary rocks and plutonics on northern Devon Island

The ca. 2.55 Ga zircon crystallization age of migmatitic hornblende–biotite orthogneiss south of Sverdrup Inlet (Fig. 3.6a) confirms the presence of late Neoproterozoic crust on northern Devon Island, as has been alluded by previous work (Schärer and Deutsch, 1990; Hegner and Jackson, 1990; Erickson et al., 2021). However, this sample is the only definitive Archean outcrop from this study, which could suggest late Neoproterozoic crust is sparse on northern Devon Island, at least compared to southern Devon Island (Chapter 2). Ductile deformation and possibly anatexis of the migmatitic orthogneiss has been constrained to ca.  $\geq 1.90$  Ga based on the monazite ages of post-kinematic biotite granite dikes intruding the migmatitic orthogneiss (Figs. 3.3a, 3.8c–d).

Zircon from the other three metaigneous samples studied here yielded middle Paleoproterozoic crystallization ages (ca. 2.0–1.9 Ga; Figs. 3.6b–d). The granite–granodiorite gneisses (ED-TL-4, ED-C-1) are part of an older, ca. 2.01–1.95 Ga plutonic phase, similar to the majority of plutonic rocks from Ellesmere Island (Fig. 3.1b; Frisch, 1988; Frisch and Hunt 1988; Gilotti et al., 2018). The ca. 1.92 Ga zircon crystallization age from a massive K-feldspar megacrystic granite (ED-EG-2) represents a younger plutonic intrusion. Similarly, Frisch (1988) and Frisch and Hunt (1988) reported ca. 1.91 Ga zircon crystallization ages from anatectic granite and monzonite on Ellesmere Island (Fig. 3.1b),

suggestive of significant ca. 1.92–1.91 Ga plutonic/anatectic activity during widespread metamorphism on Devon and Ellesmere islands.

Detrital zircon from migmatitic paragneiss (HAU-16-1179) south of Sverdrup Inlet yielded a maximum deposition age of ca. 2.22 Ga (Fig. 3.7a), while a separate paragneiss sample (HMP-00-216A) yielded an earliest metamorphic monazite age of ca. 1.93 Ga (Fig. 3.9a). If both paragneiss samples belong to the same sedimentary sequence the timing of deposition could be constrained to ca. 2.2–1.9 Ga. Detrital zircon from quartzite (HAU-16-1034B) east of the paragneiss yielded a maximum deposition age of ca. 2.1 Ga with recrystallized metamorphic rims suggesting a minimum deposition age of ca. 1.9 Ga (Fig. 3.7b). The timing of deposition between the paragneiss and quartzite are generally within the same range and cannot be separated, however, they have different detrital zircon profiles. The dominant detrital mode of the paragneiss is ca. 2.5–2.4 Ga (Fig. 3.7a), which suggests sediment was at least partially derived from the late Neoproterozoic terrane in the area or reworked an older sedimentary package. In contrast, the quartzite has a younger dominant detrital mode at ca. 2.3–2.2 Ga and includes detritus as old as ca. 2.9 Ga (Fig. 3.7b). The older detritus ( $\geq 2.6$  Ga) from the quartzite could have been derived from Neoproterozoic Rae craton rocks to the south or east, while the dominant detrital mode (ca. 2.3–2.2 Ga) is not a widely recognized source in the region.

It is notable that the ca. 2.2–1.9 Ga metasedimentary rocks of northern Devon Island are younger than the ca.  $\geq 2.47$  Ga rutile–garnet metasedimentary rocks of southern Devon Island (Chapter 2), which demonstrates that the crystalline basement of Devon and Ellesmere islands comprises at least two distinct sedimentary sequences. Furthermore, since the metasedimentary rocks of Ellesmere Island contain significantly more marble than Devon Island (Frisch, 1988; Harrison, 1984), they may represent yet another distinct sedimentary sequence.

### 3.8.2 Paleoproterozoic metamorphism of northern Devon Island

Monazite ages from three of the four metagneiss samples (Figs. 3.8a, 3.8c–d) and low Y monazite ages from both metasedimentary samples (Figs. 3.9a–b) indicate the rocks experienced high-temperature peak metamorphism at ca. 1.91–1.90 Ga, which is

consistent with the majority of Devon and Ellesmere islands crystalline basement rocks (Chapter 2; Frisch and Hunt, 1988). This timeframe is widely attributed to granulite–amphibolite facies metamorphism associated with the Thelon orogeny in the Canadian Arctic (Davis et al., 2014; Berman et al., 2018), or its proposed extension in northwestern Greenland, the Inglefield orogeny (Nutman et al., 2008).

Phase equilibrium modelling results estimate that peak ca. 1.91 Ga Thelon–Inglefield metamorphism of northern Devon Island reached P–T conditions of ca. 6.5–7.5 kbar and 800–870 °C (Fig. 3.10). While peak temperatures are somewhat comparable, peak pressure estimates are lower compared to recent estimates of ca. 1.91 Ga metamorphism on southern Devon Island (ca. 9 kbar, > 850 °C; Chapter 2). Sapphirine–quartz assemblages on southern Devon Island provided diagnostic evidence of ultrahigh temperature conditions (Chapter 2); no such evidence was found on northern Devon Island, but spinel-bearing metapelite assemblages suggest these rocks may have also experienced ultrahigh temperature metamorphism. One interpretation for the pressure differences reported on Devon Island is that the higher-pressure southern Devon Island rocks represent a more deeply exhumed level of crustal rocks, while the lower-pressure northern Devon Island rocks represent a shallower exhumed level of crustal rocks. If the ca. 2.1–1.9 Ga sedimentary sequence(s) on northern Devon Island are interpreted as a cover sequence overlying the late Neoproterozoic Devon Island rocks (i.e., structurally above), this is also consistent with northern Devon representing a shallower level of crustal rocks, as little to no middle Paleoproterozoic rocks appear to be exposed on southern Devon Island (Chapter 2; Frisch, 1988; Frisch and Hunt, 1988).

Garnet growth associated with Thelon–Inglefield metamorphism is constrained to ca. 1.93–1.90 Ga. This is based on the ca. 1.93 Ga monazite age from high Y monazite inclusions in cordierite interpreted to have grown before garnet stability while the ca. 1.91–1.90 Ga low Y monazite likely formed during garnet stability with peak metamorphism (Fig. 3.9). Post-peak Thelon–Inglefield metamorphism there is evidence of high Y monazite growth likely associated with garnet breakdown between ca. 1.9–1.8 Ga, as was also reported on southern Devon Island (Chapter 2). This poorly constrained time interval has been associated with ductile shearing on Ellesmere Island (Caswell et al., 2021), and could

suggest monazite growth/alteration through deformation-induced dissolution-precipitation reactions (e.g., Williams et al., 2011).

Unlike the late Neoproterozoic rocks on southern Devon Island, this study has found no clear evidence of pre-Thelon–Inglefield metamorphism (e.g., Arrowsmith metamorphism). All monazite dates reported in this study are  $\leq 2.0$  Ga, which is consistent with previously published monazite ages from northern Devon Island and Ellesmere Island (Frisch and Hunt, 1988; Schärer and Deutsch, 1990; Erickson et al., 2021). However, this could be a result of all monazite-bearing samples dated on northern Devon Island and Ellesmere Island having middle Paleoproterozoic protolith ages (e.g., 2.0–1.9 Ga), post-dating earlier metamorphic events.

### 3.8.3 Regional Neoproterozoic–Paleoproterozoic correlations

The crystalline basement of Devon and Ellesmere islands comprises two major components, late Neoproterozoic to earliest Paleoproterozoic units (ca. 2.55–2.47 Ga) exposed on Devon Island (this study; Chapter 2; Frisch, 1988; Frisch and Hunt, 1988), and middle Paleoproterozoic juvenile crust largely of Thelon–Inglefield affinity (ca. 2.0–1.9 Ga) exposed on northern Devon Island and Ellesmere Island (this study; Gilotti et al., 2018; Frisch, 1988; Frisch and Hunt, 1988). Continuations of similar geological units are found to the southwest on Boothia Peninsula and Somerset Island, and the northeast in the Prudhoe and Inglefield lands area of northwestern Greenland (Fig. 3.1a).

On Boothia Peninsula, ca. 2.56–2.51 Ga orthogneiss is overlain by a ca. 2.5 Ga clastic sequence (Regis and Sanborn-Barrie, 2022), and on Somerset Island ca. 2.0–1.9 Ga sedimentary sequence(s) with quartzite, marble and calc-silicate are exposed (Regis et al., 2019). This suggests the likely continuation of a late Neoproterozoic terrane between Devon Island and Boothia Peninsula, and a continuation of middle Paleoproterozoic sedimentary sequence(s) between northern Devon and Ellesmere islands with Somerset Island.

On northwestern Greenland, a granulite facies orthogneiss from the Thule mixed-gneiss complex in Prudhoe Land yielded zircon dates between ca. 2.51–1.86 Ga suggesting a possible late Neoproterozoic protolith (Nutman et al., 2008). This is comparable to the late

Neoproterozoic Devon Island terrane; however, it appears this terrane thins out from Devon Island to northwestern Greenland as rocks dated ~50 km north and south of this orthogneiss yield significantly younger and older ages respectively (Nutman et al., 2008; Dawes et al., 1988). The Prudhoe Land supracrustal complex comprises a quartzite-bearing metasedimentary sequence which has a deposition age constrained to ca. 2.35–1.92 Ga, which is comparable to the ca. 2.2–1.9 Ga metasedimentary rocks on northern Devon Island. Additionally, the Prudhoe Land granulite complex comprises orthogneisses with ca. 1.99–1.98 Ga crystallization ages (Nutman et al., 2008). This crystallization age is in agreement with the granite–granodiorite gneisses from northern Devon Island (ca. 2.01–1.95 Ga) and granitoid gneisses on Ellesmere Island (ca. 2.01–1.96 Ga), all of which may represent a northern extension of the ca. 2.07–1.96 Ga Thelon tectonic zone arc rocks. In Inglefield Land, paragneiss of the Etah Group has a much younger detrital zircon profile (ca. 2.00–1.98 Ga) and a deposition age constrained to ca. 1.98–1.92 Ga, while orthogneiss and granitoids of the Etah meta-igneous complex have ca. 1.95–1.91 Ga crystallization ages (Nutman et al., 2008).

Inglefield Land also comprises the Sunrise Pynt Straight Belt (Dawes, 2004; Nutman et al., 2008), a late east-west trending ductile shear zone which has been proposed to represent a major tectonic juxtaposition separating the Etah group and meta-igneous complex from the Prudhoe Land supracrustal and granulite complexes. Widespread shearing noted throughout Devon Island (Christie, 1978; Harrison, 1984; Frisch, 1988; Chapter 2) and substantial east-west patterns in the low resolution regional aeromagnetic data (Miles and Oneschuk, 2016) suggest the possibility a similar large-scale east-west trending shear zone or a direct continuation of the Sunrise Pynt Straight Belt exists through the middle of Devon Island. This could further explain the possible tectonic juxtaposition previously discussed between higher pressure late Neoproterozoic rocks on southern Devon Island and the lower pressure mixed late Neoproterozoic and juvenile Paleoproterozoic rocks on northern Devon Island. An argument against the direct continuation of the Sunrise Pynt Straight Belt on Devon Island is the Sunrise Pynt Straight Belt comprises an abundance of marble (Nutman et al., 2008), of which is scarce on Devon Island (Harrison, 1984).

### 3.9 Conclusions

The crystalline basement on northeastern Devon Island comprises ca. 2.55 Ga late Neoproterozoic units interleaved with at least one middle Paleoproterozoic metasedimentary sequence consisting of ca. 2.2–1.9 Ga metapelite–metapsammites and ca. 2.1–1.9 Ga quartzite, distinct from the ca.  $\geq 2.47$  Ga metasedimentary rocks on southern Devon Island (Chapter 2). Before or after sedimentary deposition, northern Devon Island and Ellesmere Island were intruded by ca. 2.01–1.95 Ga plutonics which likely represent a northern extension of the Thelon tectonic zone. Devon and Ellesmere islands experienced widespread high-temperature metamorphism associated with the Thelon–Inglefield orogeny, peaking at ca. 1.91 Ga. On northern Devon Island peak P–T conditions of ca. 1.91 Ga metamorphism are estimated at ca. 6.5–7.5 kbar and 800–870 °C, which is lower than recent results from southern Devon Island (ca. 9 kbar, > 850 °C; Chapter 2), possibly representative of a shallower exhumed crustal level relative to southern Devon Island. Likely continuations of the late Neoproterozoic Devon Island terrane and younger metasedimentary sequences appear to the southwest on Boothia Peninsula (Regis and Sanborn-Barrie, 2022) and the northeast in the Prudhoe Land area of northwestern Greenland (Nutman et al., 2008).

### 3.10 References

- Berman, R. G., Davis, W. J., Whalen, J. B., Taylor, B. E., McMartin, I., Mccurdy, M. W., Mitchell, R. K., Ma, S., Coyle, M., Roberts, B., & Craven, J. A. (2018). Report of activities for the GEM-2 Chantrey-Thelon activity: Thelon tectonic zone project, Nunavut (pp. 1–22). Geological Survey of Canada.
- Berman, R. G., Pehrsson, S., Davis, W. J., Ryan, J. J., Qui, H., & Ashton, K. E. (2013). The Arrowsmith orogeny: Geochronological and thermobarometric constraints on its extent and tectonic setting in the Rae craton, with implications for pre-Nuna supercontinent reconstruction. *Precambrian Research*, 232, 44–69.
- Caswell, B., Gilotti, J. A., Webb, L. E., McClelland, W. C., Kościńska, K., Piepjohn, K., & von Gosen, W. (2021).  $^{40}\text{Ar}/^{39}\text{Ar}$  dating of Paleoproterozoic shear zones in the

- Ellesmere–Devon crystalline terrane, Nunavut, Canadian Arctic. *Canadian Journal of Earth Sciences*, 58, 1073–1084.
- Christie, R. L. (1978). A structural reconnaissance of Eastern Devon Island, Arctic Archipelago. Geological Survey of Canada, Open File 537, 1–63.
- Davis, W. J., Berman, R. G., Nadeau, L., & Percival, J. (2014). U-Pb zircon geochronology of a transect across the Thelon Tectonic Zone, Queen Maud region, and adjacent Rae Craton, Kitikmeot region, Nunavut, Canada (Geological Survey of Canada, Open File, Vol. 7652). Natural Resources Canada.
- Davis, W. J., Sanborn-Barrie, M., Berman, R. G., & Pehrsson, S. (2021). Timing and provenance of Paleoproterozoic supracrustal rocks in the central Thelon tectonic zone, Canada: implications for the tectonic evolution of western Laurentia from ca. 2.1 to 1.9 Ga. *Canadian Journal of Earth Sciences*, 58, 378–395.
- Dawes, P. R. (2004). Explanatory Notes to the Geological Map of Greenland, 1:500 000, Humboldt Gletscher, Sheet 6 (pp. 1–48). Geological Survey of Denmark and Greenland.
- Dawes, P. R., Larsen, O., & Kalsbeek, F. (1988). Archean and Proterozoic crust in North-West Greenland: evidence from Rb-Sr whole-rock age determinations. *Canadian Journal of Earth Sciences*, 25(9), 1365–1373.
- de Capitani, C., & Petrakakis, K. (2010). The computation of equilibrium assemblage diagrams with Theriak/Domino software. *The American Mineralogist*, 95(7), 1006–1016.
- Erickson, T. M., Kirkland, C. L., Jourdan, F., Schmieder, M., Hartnady, M. I. H., Cox, M. A., & Timms, N. E. (2021). Resolving the age of the Haughton impact structure using coupled  $^{40}\text{Ar}/^{39}\text{Ar}$  and U-Pb geochronology. *Geochimica et Cosmochimica Acta*, 304, 68–82.



- Frisch, T. (1988). Reconnaissance geology of the Precambrian shield of Ellesmere, Devon and Coburg Islands, Canadian Arctic Archipelago. *Bulletin Geological Survey of Canada, Memoir 409*, 102 p.
- Frisch, T., & Hunt, P. A. (1988). U-Pb zircon and monazite ages from the Precambrian Shield of Ellesmere and Devon islands, Arctic Archipelago. *Bulletin Geological Survey of Canada, Paper 88-2*, 117–125.
- Gibson, H. D., Carr, S. D., Brown, R. L., & Hamilton, M. A. (2004). Correlations between chemical and age domains in monazite, and metamorphic reactions involving major pelitic phases: an integration of ID-TIMS and SHRIMP geochronology with Y–Th–U X-ray mapping. *Chemical Geology*, 211(3-4), 237–260.
- Gilotti, J. A., McClelland, W. C., Piepjohn, K., & von Gosen, W. (2018). U–Pb geochronology of Paleoproterozoic gneiss from southeastern Ellesmere Island: implications for displacement estimates on the Wegener fault. *Arktos*, 4(1), 12.
- Green, E. C. R., White, R. W., Diener, J. F. A., Powell, R., Holland, T. J. B., & Palin, R. M. (2016). Activity–composition relations for the calculation of partial melting equilibria in metabasic rocks. *Journal of Metamorphic Geology*, 34(9), 845–869.
- Harrison, J. C. (1984). Eastern Ellesmere, Coburg and eastern Devon islands mineral inventory, NTS 29G, 38F and G, 39B, C, D, E, F, G and H, 48E and H, District of Franklin, N.W.T. Northwest Territories Mineral Assessment report no. 81743, 1-125.
- Hegner, E., & Jackson, G. D. (1990). Nd isotopic constraints on Late Archean and Early Proterozoic crust formation in Baffin and Ellesmere islands, northern Labrador and Ungava Peninsula, eastern Canada. *Eos, Transactions, American Geophysical Union*, 71, 1689.
- Hoffman, P. (1988). United plates of America, the birth of A craton: Early Proterozoic assembly and growth of Laurentia. *Annual Review of Earth and Planetary Sciences*, 16(1), 543–603.

- Holland, T. J. B., Green, E. C. R., & Powell, R. (2021). A thermodynamic model for feldspars in  $\text{KAlSi}_3\text{O}_8$ – $\text{NaAlSi}_3\text{O}_8$ – $\text{CaAl}_2\text{Si}_2\text{O}_8$  for mineral equilibrium calculations. *Journal of Metamorphic Geology*, 40(4), 587–600.
- Holland, T., & Powell, R. (2003). Activity–composition relations for phases in petrological calculations: an asymmetric multicomponent formulation. *Contributions to Mineralogy and Petrology*, 145(4), 492–501.
- Holland, T. J. B., & Powell, R. (2011). An improved and extended internally consistent thermodynamic dataset for phases of petrological interest, involving a new equation of state for solids. *Journal of Metamorphic Geology*, 29(3), 333–383.
- Miles, W., & Oneschuk, D. (2016). Magnetic anomaly map, Canada [Map]. Natural Resources Canada.
- Montel, J.-M., Foret, S., Veschambre, M., Nicollet, C., & Provost, A. (1996). Electron microprobe dating of monazite. *Chemical Geology*, 131(1), 37–53.
- Nutman, A. P., Dawes, P. R., Kalsbeek, F., & Hamilton, M. A. (2008). Palaeoproterozoic and Archaean gneiss complexes in northern Greenland: Palaeoproterozoic terrane assembly in the High Arctic. *Precambrian Research*, 161(3-4), 419–451.
- Regis, D., & Sanborn-Barrie, M. (2022). Delimiting the extent of “Boothia terrane” crust, Nunavut: new U-Pb geochronological results (No. 978-0-660-45346-0; Geological Survey of Canada, Open File, Vol. 8917). Natural Resources Canada.
- Regis, D., Sanborn-Barrie, M., & Moum, T. (2019). GEM-2 Boothia Peninsula-Somerset Island project, Nunavut: mineral assay results and potential carving stone localities from the 2017 and 2018 field seasons Geological Survey of Canada, Open File, 8592.
- Sanborn-Barrie, M., Davis, W. J., Berman, R. G., Rayner, N., Skulski, T., & Sandeman, H. (2014). Neoproterozoic continental crust formation and Paleoproterozoic deformation of the central Rae craton, Committee Bay belt, Nunavut. *Canadian Journal of Earth Sciences*, 51(6), 635–667.

- Schärer, U., & Deutsch, A. (1990). Isotope systematics and shock-wave metamorphism: II. U–Pb and Rb–Sr in naturally shocked rocks: the Haughton Impact Structure, Canada. *Geochimica et Cosmochimica Acta*, 54, 3435–3447.
- Schultz, M. E. J., Chacko, T., Heaman, L. M., Sandeman, H. A., Simonetti, A., & Creaser, R. A. (2007). Queen Maud block: A newly recognized Paleoproterozoic (2.4–2.5 Ga) terrane in northwest Laurentia. *Geology*, 35(8), 707.
- Stern, R. A., & Berman, R. G. (2001). Monazite U–Pb and Th–Pb geochronology by ion microprobe, with an application to in situ dating of an Archean metasedimentary rock. *Chemical Geology*, 172(1), 113–130.
- Van Breemen, O., Thompson, P. H., Hunt, P. A., & Culshaw, N. (1987). U-Pb zircon and monazite geochronology from the northern Thelon Tectonic Zone, District of Mackenzie. *Radiogenic Age and Isotopic Studies, Report*, 1, 87–82.
- Vermeesch, P. (2018). IsoplotR: A free and open toolbox for geochronology. *Geoscience Frontiers*, 9(5), 1479–1493.
- Wheller, C. J., & Powell, R. (2014). A new thermodynamic model for sapphirine: calculated phase equilibria in K<sub>2</sub>O–FeO–MgO–Al<sub>2</sub>O<sub>3</sub>–SiO<sub>2</sub>–H<sub>2</sub>O–TiO<sub>2</sub>–Fe<sub>2</sub>O<sub>3</sub>. *Journal of Metamorphic Geology*, 32(3), 287–299.
- White, R. W., Powell, R., & Clarke, G. L. (2002). The interpretation of reaction textures in Fe-rich metapelitic granulites of the Musgrave Block, central Australia: constraints from mineral equilibria calculations in the system K<sub>2</sub>O–FeO–MgO–Al<sub>2</sub>O<sub>3</sub>–SiO<sub>2</sub>–H<sub>2</sub>O–TiO<sub>2</sub>–Fe<sub>2</sub>O<sub>3</sub>. *Journal of Metamorphic Geology*, 20(1), 41–55.
- White, R. W., Powell, R., Holland, T. J. B., Johnson, T. E., & Green, E. C. R. (2014a). New mineral activity-composition relations for thermodynamic calculations in metapelitic systems. *Journal of Metamorphic Geology*, 32(3), 261–286.
- White, R. W., Powell, T., Holland, T. J. B., & Worley, B. A. (2000). The effect of TiO<sub>2</sub> and Fe<sub>2</sub>O<sub>3</sub> on metapelitic assemblages at greenschist and amphibolite facies

conditions: mineral equilibria calculations in the system  $K_2O-FeO-MgO-Al_2O_3-SiO_2-H_2O-TiO_2-Fe_2O_3$ . *Journal of Metamorphic Geology*, 18(5), 497–511.

White, R. W., Powell, R., & Johnson, T. E. (2014b). The effect of Mn on mineral stability in metapelites revisited: new  $a-x$  relations for manganese-bearing minerals. *Journal of Metamorphic Geology*, 32(8), 809–828.

Whitney, D. L., & Evans, B. W. (2010). Abbreviations for names of rock-forming minerals. *The American Mineralogist*, 95(1), 185–187.

Williams, M. L., Jercinovic, M. J., Harlov, D. E., Budzyń, B., & Hetherington, C. J. (2011). Resetting monazite ages during fluid-related alteration. *Chemical Geology*, 283(3-4), 218–225.

## Chapter 4

### 4 Paleoproterozoic metamorphism of the Ellesmere tectonic zone, Canadian Arctic

#### 4.1 Introduction

The Archean Rae and Slave cratons of northern Laurentia are merged by the Paleoproterozoic Thelon tectonic zone (Fig. 4.1, e.g., Gibb and Thomas, 1977; Hoffman, 1988). The Thelon tectonic zone is a northeast striking orogenic zone extending ~500 km on the Canadian mainland, from the McDonald Fault to the Queen Maud Gulf. It is generally accepted to represent a ca. 2.0 Ga continental magmatic arc formed along the western margin of the Rae craton and subsequently deformed at ca. < 1.97 Ga during the collision of the Rae and Slave cratons (e.g., Hoffman, 1988). The Thelon tectonic zone has a cogenetic southern extension termed the Taltson magmatic zone (e.g., Card et al., 2014), which formed during the collision of the Rae craton with the Buffalo Head terrane. The northern extension of the Thelon tectonic zone is not well established as it is covered by Paleozoic sedimentary rocks north of the Queen Maud Gulf and current geophysical data is of lesser quality in this region (Miles and Oneschuk, 2016). It is suggested to outcrop again on southeastern Ellesmere Island and northeastern Devon Island (e.g., Hoffman et al., 1989; Gilotti et al., 2018; Chapter 3). For ease of discussion, we will use the term “Ellesmere tectonic zone”, to refer to the juvenile ca. 2.0–1.9 Ga metaplutonic and metasedimentary rocks in the Ellesmere and Devon islands area.

Continued tectonic thickening between ca. 1.95–1.89 Ga caused widespread amphibolite–granulite facies metamorphism within the entire Taltson magmatic zone, Thelon tectonic zone and Ellesmere tectonic zone (e.g., Berman, 2010), along with varying grades of metamorphism within flanking domains (e.g., Kitsul et al., 2000; Tersmette, 2012; Chapter 2). Quantitative estimates of metamorphism are relatively well-documented within the Taltson magmatic zone, particularly highlighting the ultrahigh temperature conditions (e.g., >900 °C, Farquhar et al., 1996; Berman and Bostock, 1997; Grover et al., 1997). Conversely, quantitative metamorphic estimates are exceptionally limited for the Thelon tectonic zone and Ellesmere tectonic zone (e.g., Thompson, 1992; Henderson, 1999;

Frisch, 1988), largely limited to classical thermobarometry estimates, which are not ideal for granulite facies assemblages since continued diffusion during high temperature cooling has been shown to result in lower peak temperature estimates (e.g., Frost and Chacko, 1989). Using a legacy sample suite and whole-rock geochemical data from granulite facies paragneisses within the Ellesmere tectonic zone, we use phase equilibrium modelling techniques to constrain the metamorphic conditions associated with ca. 2.0–1.9 Ga orogenesis.

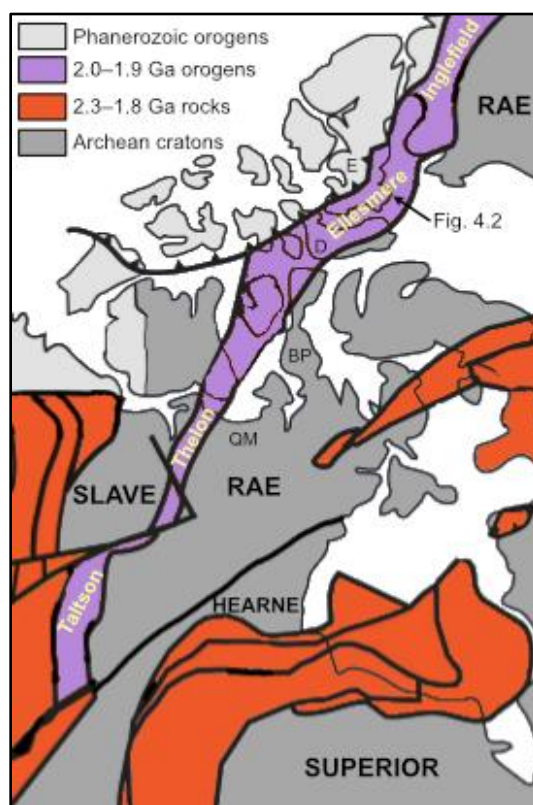


**Figure 4.1. Simplified map of north-central Laurentia highlighting the extent of the ca. 2.0–1.9 Ga Taltson, Thelon, Ellesmere, and Inglefield orogenic zones merging Archean cratons (modified after Caswell et al., 2021 and St-Onge et al., 2009). E, Ellesmere Island; D, Devon Island; BP, Boothia Peninsula; QM, Queen Maud.**

## 4.2 Geological setting

The Ellesmere tectonic zone of southeastern Ellesmere Island is exposed along the coast and within nunataks of the Prince of Wales icefield between Grise Fiord and the Bache

Peninsula (Fig. 4.2). The crystalline rocks comprise north trending and generally steeply dipping interleaved belts of granulite facies metasedimentary rocks and quartzofeldspathic gneisses, which are intruded by an extensive suite of granitoid rocks (Frisch 1984a; Frisch, 1984b; Frisch, 1988).

Zircon crystallization ages of granitoids within the Ellesmere tectonic zone are between ca. 2.01–1.95 Ga (Fig. 4.2, Frisch, 1988; Frisch and Hunt, 1988; Gilotti et al., 2018), which overlaps within error with the ca. 2.07–1.95 Ga granitoid ages of the Thelon tectonic zone (van Breemen et al., 1987; Davis et al., 2013; Davis et al., 2014; Berman et al., 2018). Zircon and monazite ages in anatectic granitoids and quartzofeldspathic gneisses are between ca. 1.96–1.91 Ga (Frisch, 1988; Frisch and Hunt, 1988), which potentially reflects the age of granulite facies metamorphism associated with the Ellesmere–Thelon orogeny. The metasedimentary rocks on Ellesmere Island have not been dated, but a possible extension of the Ellesmere Island metasedimentary rocks on northeastern Devon Island has been constrained to a depositional age of ca. 2.2–1.9 Ga (Chapter 3), roughly comparable to the ca. 2.1–1.9 Ga metasedimentary rocks within the Thelon tectonic zone (Davis et al., 2021).

The granulite facies metasedimentary rocks within the Ellesmere tectonic zone are predominantly composed of migmatitic garnet–sillimanite–cordierite paragneiss with granitic leucosomes, as well as lesser quartzite and marble (Frisch, 1988). Significant anatexis of the paragneiss is suggested as the source of widespread anatectic biotite granite bodies on Ellesmere Island (Fig. 4.2, Frisch, 1988). Mineral assemblages of the paragneiss comprise quartz, K-feldspar, plagioclase, biotite, garnet, sillimanite, cordierite, spinel, ilmenite, magnetite and/or rutile (Frisch, 1988). Cordierite is a major phase in paragneiss, commonly replacing garnet, likely during decompression reactions (Frisch, 1988). Hercynite spinel is also a significant constituent of the paragneiss, particularly common in the melanosome of most outcrops (Frisch, 1988). Notably, spinel is often present in quartz-rich paragneiss samples, sometimes in direct contact with quartz (Frisch, 1988), which is a potential indicator of ultrahigh temperature metamorphism (>900 °C, e.g., Kelsey, 2008). Previous estimates of ca. 1.9 Ga metamorphism of the paragneiss are based on garnet–cordierite and cordierite–spinel calibrations (Frisch, 1988), which yielded peak

temperatures between ca. 600–750 °C, while garnet–plagioclase–sillimanite–quartz barometry estimates yielded peak pressures between ca. 5–6 kbar.

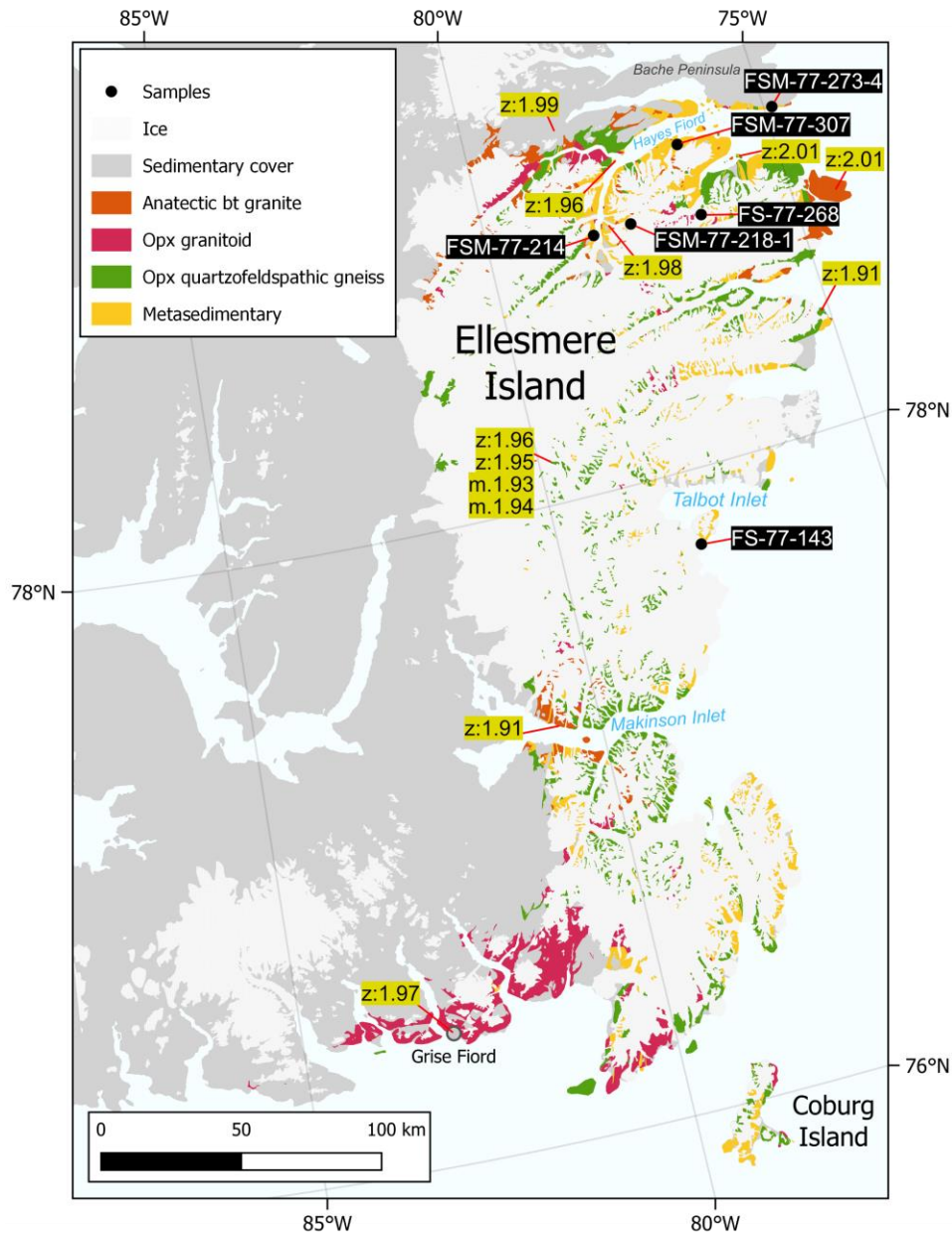


**Figure 4.2.** Simplified geological map of the southeastern Ellesmere Island crystalline basement showing the locations of paragneiss samples used in this study and zircon (z) and monazite (m) ages of metaigneous rocks from Frisch (1988), Frisch and Hunt (1988) and Gilotti et al. (2018). Geology is modified after Frisch (1984a) and Frisch (1984b).



### 4.3 Sample descriptions and petrography

A legacy collection of migmatitic paragneiss samples from the Ellesmere tectonic zone that were collected and reported on by Frisch (1988) were analyzed to study the metamorphic assemblages and reaction textures preserved. The locations of samples used in this study are shown in Figure 4.2. Samples were examined by optical microscopy (Fig. 4.3) and thin section element maps were produced for four samples with a Bruker M4 Tornado micro-XRF at the University of Western Ontario, Canada. Analytical conditions of micro-XRF analysis included a fixed 17  $\mu\text{m}$  spot size, a 34  $\mu\text{m}$  step size and a 5 ms dwell time, with the X-ray tube set at a 50 kV high voltage and 600  $\mu\text{A}$  anode current. Thin section phase maps were produced with XMapTools (Lanari et al., 2014) using the micro-XRF elemental map data (Fig. 4.4).

Sample FS-77-143 is from the central coast of southeastern Ellesmere Island, south of Talbot Inlet (Fig. 4.2). It is composed of quartz, K-feldspar, plagioclase, cordierite, garnet, biotite, sillimanite, spinel, ilmenite and magnetite. Spinel is mostly concentrated with layers of cordierite, prismatic sillimanite, and biotite near garnet rims, with at least one direct contact between spinel and quartz (Fig. 4.3a).

Sample FS-77-268 is from a paragneiss outcrop south of Hayes Fiord (Fig. 4.2). The sample is largely leucocratic, dominated by quartz, K-feldspar, plagioclase, and biotite, with thin melanocratic layers comprising lenticular garnets with abundant quartz inclusions and trails of sillimanite and spinel (Fig. 4.4a). Spinel is observed mantled by quartz and in contact with biotite (Fig. 4.3b).

Near the northern end of the Ellesmere Island crystalline exposure, paragneiss FSM-77-214 is from the end of Jokel Fiord (Fig. 4.2). It is composed of quartz, K-feldspar, plagioclase, cordierite, garnet, biotite, sillimanite, spinel and ilmenite. Spinel forms discrete grains, generally mantled by cordierite and sometimes near large quartz grains. (Fig. 4.3c).

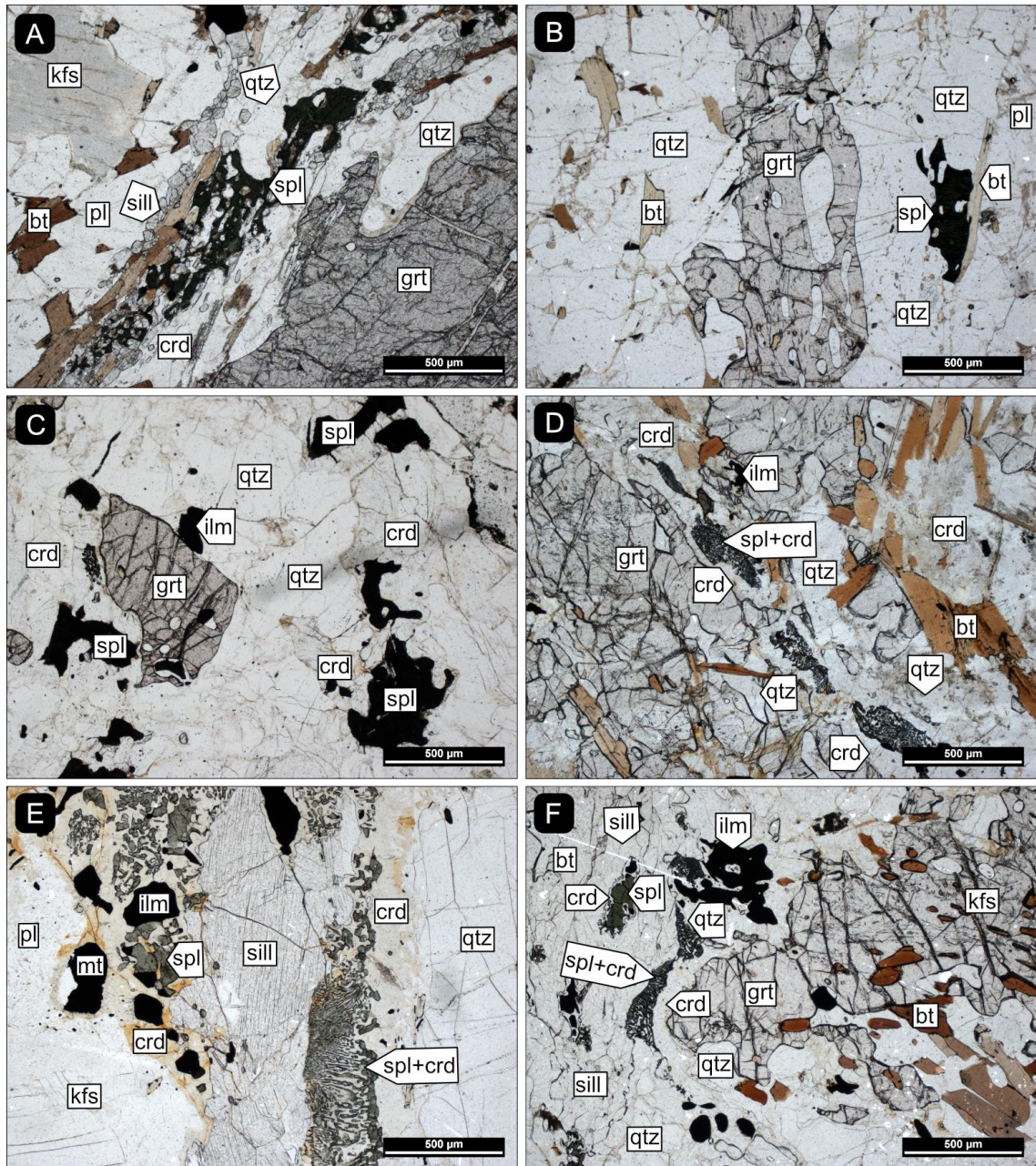


**Figure 4.3.** Plane polarized light photomicrographs of spinel-bearing migmatitic paragneiss from the Ellesmere tectonic zone. (a) Sample FS-77-143 showing a garnet rim surrounded by cordierite, spinel, biotite and sillimanite. Quartz is observed in direct contact with spinel. (b) Sample FS-77-268 showing a centred lenticular garnet with quartz inclusions. Spinel is in contact with biotite and is almost completely mantled by quartz. (c) Sample FSM-77-214 showing garnet nearby discrete spinel grains mantled by cordierite. A large quartz grain is centred between the spinel and

**garnet. (d) Sample FSM-77-218-1 showing spinel and cordierite symplectic intergrowths along garnet rims. Quartz is observed nearby spinel but not in direct contact. (e) Sample FSM-77-273-4 showing a melanocratic layer of sillimanite, cordierite, spinel and iron oxides between coarse quartz and feldspar grains. Spinel and cordierite symplectic intergrowths mantle sillimanite, and more discrete spinel is observed near iron oxides. (f) Sample FSM-77-307 showing a garnet with biotite inclusions. Spinel is present as symplectic intergrowths with cordierite, and as discrete grains within sillimanite and mantled by a cordierite film. Quartz is nearby but not observed in direct contact with spinel. Mineral abbreviations from Whitney and Evans (2010).**

Sample FSM-77-218-1 is from a paragneiss outcrop about fifteen kilometres east of Jokel Fiord (Fig. 4.2), and is composed of quartz, K-feldspar, plagioclase, cordierite, 1–2 cm broken-down garnet, biotite, sillimanite, spinel and ilmenite (Fig. 4.4b). Spinel is present along the broken-down garnet rims, mainly present as symplectic intergrowths with cordierite (Fig. 4.3d). Spinel is sometimes present near quartz but not observed in direct contact (Fig. 4.3d).

Sample FSM-77-273-4 is from the northernmost Ellesmere Island crystalline exposure, on the southern shore of Bache Peninsula (Fig. 4.2). This paragneiss sample is largely leucocratic, comprising coarse quartz, K-feldspar and plagioclase which likely represent crystallized pseudomorphs of anatectic melt (Fig. 4.4c). Between leucocratic layers is a melanocratic layer comprising garnet, cordierite, sillimanite, biotite, spinel, ilmenite and magnetite. Spinel is mostly present as symplectic intergrowths with cordierite on sillimanite but is also present as discrete grains near ilmenite and magnetite (Fig. 4.3e).

Sample FSM-77-307 is from the southern coast of Hayes Fiord (Fig. 4.2). Cordierite is abundant in the matrix of this sample along with quartz, K-feldspar and plagioclase (Fig. 4.4d). Garnet, biotite, sillimanite and spinel are also present, with spinel forming symplectic intergrowths with cordierite on sillimanite, or discrete grains mantle by cordierite near sillimanite (Fig. 4.3f). Spinel is not observed in direct contact with quartz; however, quartz is abundant in the sample.

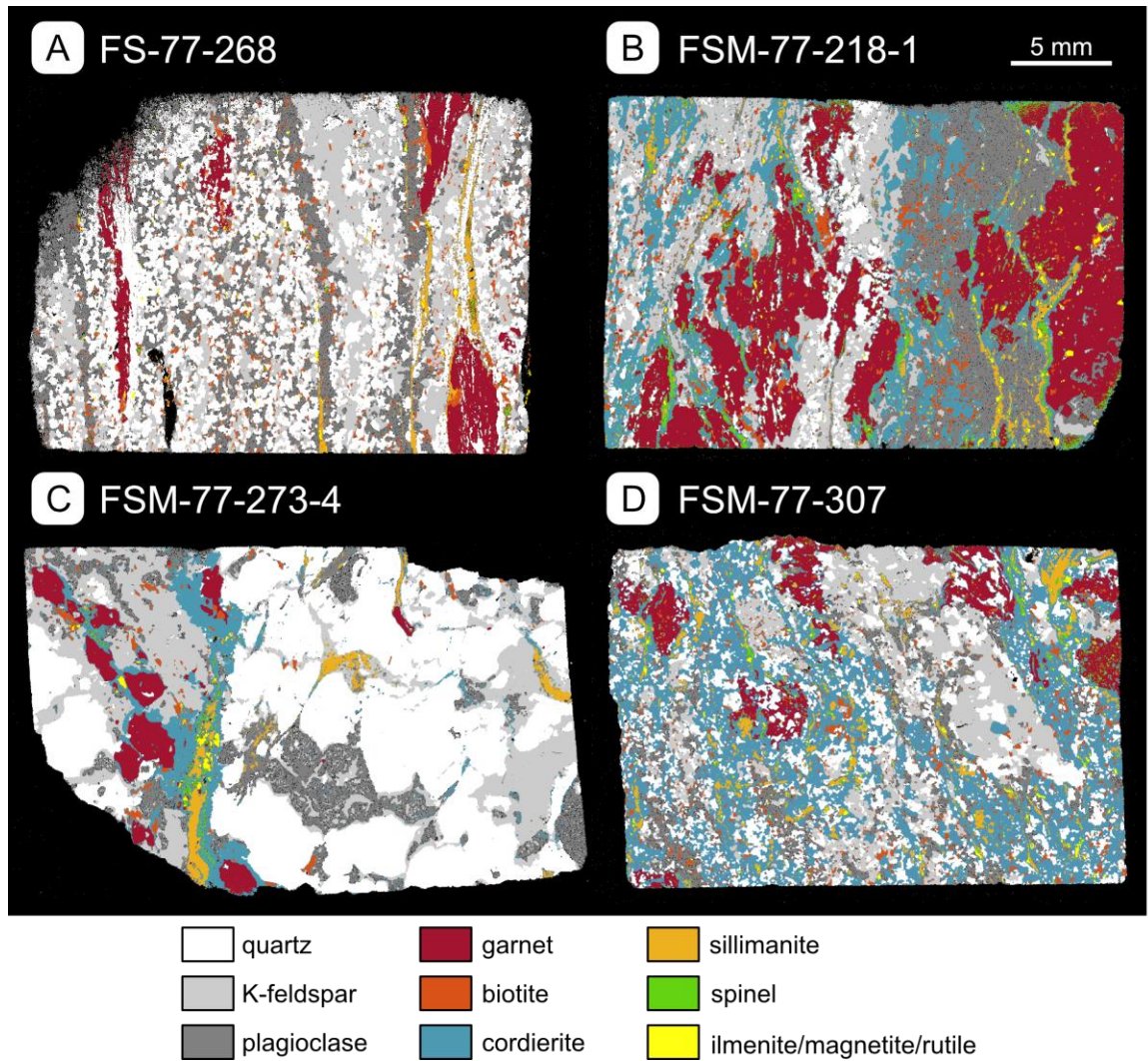


**Figure 4.4.** Phase maps of four migmatitic paragneiss thin sections from the Ellesmere tectonic zone. (a) FS-77-268 is mostly leucocratic and more strongly sheared compared to the other samples. Lenticular garnets contain quartz inclusions and have thin trails of sillimanite and spinel. (b) FSM-77-218-1 shows a leucocratic K-feldspar and quartz dominated layer on the left, and a melanocratic plagioclase dominated layer on the right. Large (1–2 cm) garnets with spinel and sillimanite mostly concentrated along garnet rims. Within the leucocratic portion of the sample, spinel is present near quartz but not in direct contact. Garnet contains numerous inclusions of biotite, sillimanite, and quartz. (c) Sample FSM-77-273-4 mostly comprises leucocratic layers of coarse quartz, K-feldspar and plagioclase, possibly representing melt pseudomorphs. Between the leucocratic layers is a melanocratic layer of garnet,

**cordierite, sillimanite, biotite, spinel, ilmenite and magnetite. (d) FSM-77-307 shows an abundance of cordierite in the matrix, along with quartz, K-feldspar and plagioclase. These garnets also contain many inclusions of biotite, sillimanite, and quartz. Spinel is mostly associated with sillimanite, cordierite and ilmenite.**

#### 4.4 Methodology

Phase equilibrium modelling was conducted on four representative migmatitic paragneiss samples (FS-77-143, FSM-77-214, FSM-77-218-1, FSM-77-273-4) from southeastern Ellesmere Island (Fig. 4.2) to investigate the metamorphic history of the Ellesmere tectonic zone. These samples were modelled with the internally consistent thermodynamic database of Holland and Powell (2011) in the 11-component MnO-Na<sub>2</sub>O-CaO-K<sub>2</sub>O-FeO-MgO-Al<sub>2</sub>O<sub>3</sub>-SiO<sub>2</sub>-H<sub>2</sub>O-TiO<sub>2</sub>-Fe<sub>2</sub>O<sub>3</sub> (MnNCKFMASHTO) chemical system. The activity-composition (a-x) models used include plagioclase (pl) and K-feldspar (ksp) from Holland et al. (2021); granitic melt (liq), garnet (g), orthopyroxene (opx), biotite (bi), cordierite (cd) and muscovite (mu) from White et al. (2014a) and White et al. (2014b); sapphirine (sa) from Wheller and Powell (2014); magnetite (mt) and spinel (sp) from White et al. (2002); and ilmenite (ilm) from White et al. (2000). Pure phases considered include quartz (q), rutile (ru), sillimanite (sill) and kyanite (ky).

The bulk-rock compositions used for this study are whole-rock compositions reported in the appendix of Frisch (1988). These compositions were determined by “everyday” whole-rock analysis methods at the Geological Survey of Canada, Ottawa, which are outlined in Abbey (1979). H<sub>2</sub>O content was estimated by constructing H<sub>2</sub>O–temperature (H<sub>2</sub>O–T) diagrams, using the loss on ignition values of whole-rock analysis as the H<sub>2</sub>O maximum estimate and selecting the maximum amount of H<sub>2</sub>O required to preserve the inferred peak metamorphic assemblages at the solidus (Appendix A.6). This method implies the peak metamorphic assemblage was in equilibrium with the last selvages of melt (e.g., White and Powell, 2002). The ferric iron ratios estimated by whole-rock analysis (Frisch, 1988) were also used for modelling. Two sets of peak P–T models were produced for each sample; one inferring that the peak assemblage includes biotite, cordierite, garnet and sillimanite without spinel (Fig. 4.5) and the other inferring the peak assemblage includes spinel and quartz (Fig. 4.6).

To investigate the suprasolidus prograde history, we estimated melt-reintegrated protolith compositions by constructing melt–temperature (melt–T) models and selecting the compositions which minimally saturated the solidus with H<sub>2</sub>O (Appendix A.6, e.g., Waters, 2019). The bulk-rock compositions used for the spinel-absent modelling and their corresponding melt compositions predicted at the solidus were used as the endmembers for melt–T modelling. These melt-reintegrated protolith compositions were then used to construct P–T models for each sample (Fig. 4.7). H<sub>2</sub>O–T and melt–T models were constructed at 6 kbar, corresponding to metamorphic pressures previously estimated for Ellesmere Island (Frisch, 1988). The Theriak/Domino software package (de Capitani & Petrakakis, 2010) was used to construct H<sub>2</sub>O–T and melt–T diagrams and the THERMOCALC software package (Powell and Holland, 1988) was used to construct P–T diagrams. The bulk-rock compositions used for modelling are listed in Table 4.1.

**Table 4.1. Bulk-rock compositions (mol.%) of migmatitic paragneiss samples from the Ellesmere tectonic zone used for phase equilibrium modelling.  $X_{\text{Fe}^{3+}} = \text{O}(\text{Fe}_2\text{O}_3)/\text{FeO} \cdot 2$ .  $X_{\text{Mg}} = \text{MgO}/(\text{MgO} + \text{FeO})$ .**

Sample	Figure	H <sub>2</sub> O	SiO <sub>2</sub>	Al <sub>2</sub> O <sub>3</sub>	CaO	MgO	FeO <sub>t</sub>	K <sub>2</sub> O	Na <sub>2</sub> O	TiO <sub>2</sub>	MnO	O	$X_{\text{Fe}^{3+}}$	$X_{\text{Mg}}$
FS-77-143	4.5	1.70	64.94	13.52	1.16	4.30	6.75	3.76	2.26	0.64	0.07	0.92	0.27	0.39
FS-77-143	4.6	0.53	65.71	13.68	1.18	4.35	6.83	3.81	2.28	0.65	0.07	0.93	0.27	0.39
FS-77-143	4.7	6.56	65.45	11.89	0.92	3.05	4.81	3.63	2.58	0.44	0.05	0.63	0.26	0.39
FSM-77-214	4.5	1.66	62.96	13.69	1.45	5.76	7.97	3.23	2.15	0.67	0.09	0.38	0.09	0.42
FSM-77-214	4.6	0.23	63.88	13.89	1.47	5.84	8.08	3.27	2.18	0.68	0.10	0.38	0.09	0.42
FSM-77-214	4.7	6.29	64.14	12.07	1.13	4.10	5.73	3.28	2.48	0.47	0.07	0.26	0.09	0.42
FSM-77-218-1	4.5	2.52	62.70	13.09	1.10	6.61	7.52	3.47	1.91	0.68	0.06	0.33	0.09	0.47
FSM-77-218-1	4.6	0.53	63.98	13.36	1.12	6.74	7.68	3.54	1.95	0.70	0.07	0.34	0.09	0.47
FSM-77-218-1	4.7	6.49	63.78	11.79	0.90	4.89	5.64	3.43	2.30	0.50	0.05	0.24	0.09	0.46
FSM-77-273-4	4.5	0.93	73.84	10.96	1.34	3.18	4.46	2.91	1.70	0.51	0.06	0.12	0.06	0.42
FSM-77-273-4	4.6	0.11	74.45	11.05	1.35	3.21	4.49	2.93	1.71	0.51	0.06	0.12	0.06	0.42
FSM-77-273-4	4.7	5.45	71.92	10.20	1.08	2.35	3.34	3.11	2.06	0.36	0.04	0.09	0.05	0.41

## 4.5 Results

Assuming a peak metamorphic assemblage comprising biotite, cordierite, garnet, and sillimanite, all four migmatitic paragneiss samples yield restricted P–T stability fields between ca. 5–7 kbar and 750–860 °C (Fig. 4.5), increasing in peak temperature with increasing pressure. Cordierite stability limits pressure estimates to ca.  $\leq 7$  kbar, while sillimanite stability limits pressure estimates to ca.  $\geq 5$  kbar. Sample FS-77-143 is the only one to include magnetite in addition to ilmenite (Fig. 4.5a), which correlates with the more oxidized ferric iron estimate ( $X_{\text{Fe}^{3+}} = 0.27$ ) compared to the other three samples with reduced ferric iron estimates ( $X_{\text{Fe}^{3+}} = 0.06\text{--}0.09$ ). The two rutile-bearing samples, FSM-77-214 and FSM-77-218-1, predict rutile stability above ca. 6.5 kbar and generally  $\geq 850$  °C (Figs. 4.5b, 4.5c). This suggests peak metamorphic estimates are closer to 6.5 kbar and 850 °C for the paragneiss, but these estimates could be altered with differing ferric iron estimates (e.g., White et al., 2014). If biotite is inferred as a retrograde mineral, thus not part of the peak assemblage, peak temperature estimates could increase to  $\sim 900$  °C (Fig. 4.5). Suprasolidus orthopyroxene stability is predicted at pressures  $< 4\text{--}5$  kbar, which likely restricts the retrograde path of metamorphism to  $> 4\text{--}5$  kbar to inhibit any orthopyroxene stability as it is extremely rare in Ellesmere Island paragneisses (Frisch, 1988). For these models, in the P–T space of 2–10 kbar and 700–900 °C, spinel is only predicted for samples FS-77-143 and FSM-77-273-4 at ca. 5 kbar and  $> 860$  °C.

Assuming an inferred peak metamorphic assemblage comprising spinel and quartz without orthopyroxene and/or sapphirine, the migmatitic paragneiss samples yield P–T stability fields primarily between ca. 5–6.5 kbar and  $\geq 940$  °C (Fig. 4.6). Spinel stability is generally predicted between 3–7 kbar, always with quartz except for low pressure, high temperature P–T space (ca. 3 kbar, 1000 °C). Garnet is predicted at pressures above ca. 4 kbar, within the higher-pressure spinel-bearing fields, and biotite is never predicted to be stable with spinel. Sillimanite and spinel stability is only predicted in a limited pressure range between 6–6.5 kbar, while cordierite is predicted in all spinel fields except for the higher pressure sapphirine or rutile plus spinel fields. Below 1000 °C, sapphirine is only predicted for samples FS-77-143 and FSM-77-218-1, at P–T conditions of ca. 6.5 kbar and  $\geq 950$  °C



(Figs. 4.6a, 4.6c). Orthopyroxene is predicted in all suprasolidus stability fields below ca. 5 kbar.

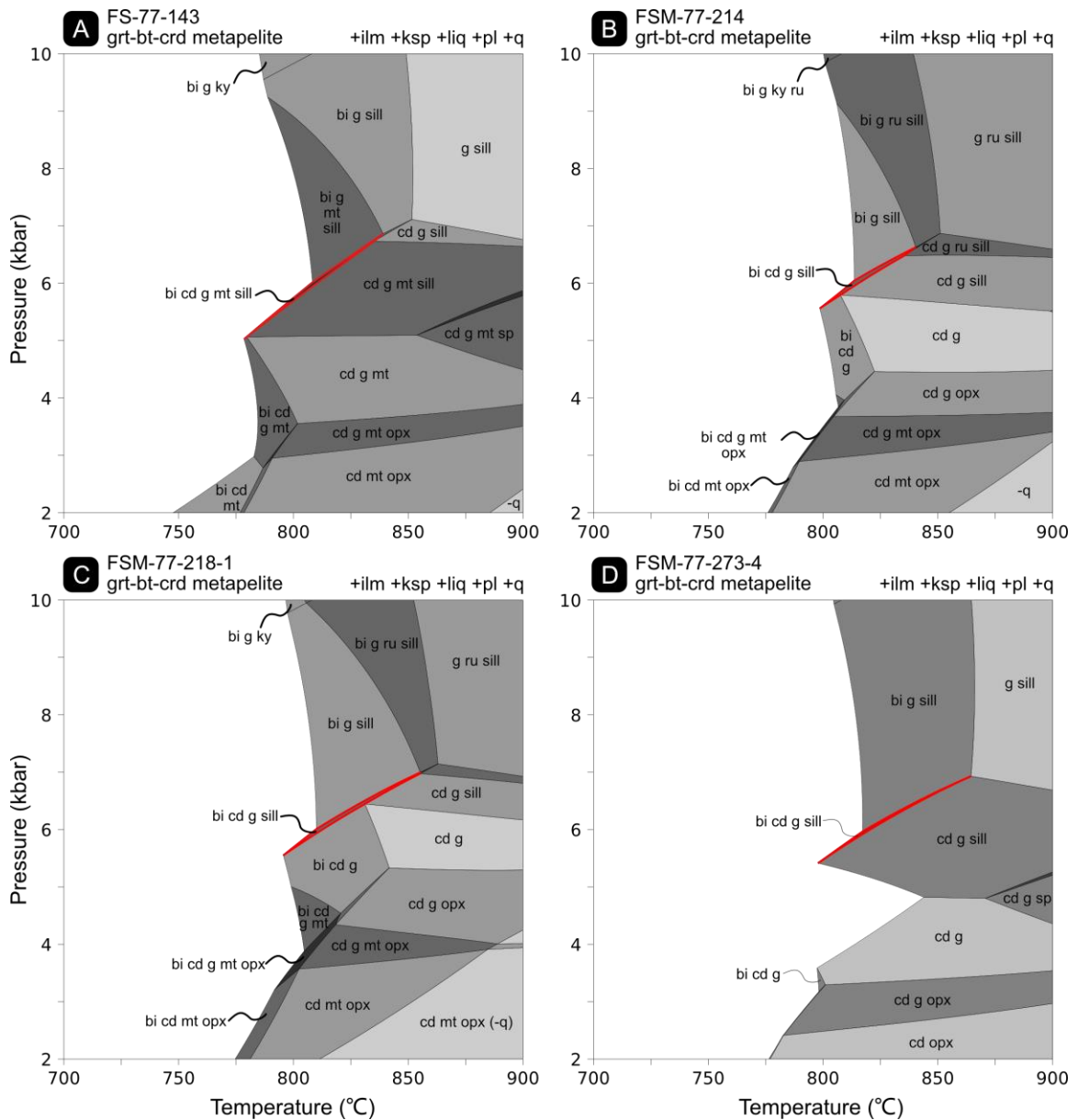


**Figure 4.5.** Suprasolidus P–T diagrams of peak metamorphic paragneiss compositions inferring spinel-absent peak metamorphic conditions. The inferred garnet–sillimanite–cordierite–biotite peak assemblages are outlined in red. H<sub>2</sub>O content was adjusted to intersect the inferred peak assemblages with the solidus at ca. 6 kbar. Stability field shading corresponds to variance with darker shading corresponding to lower variance.

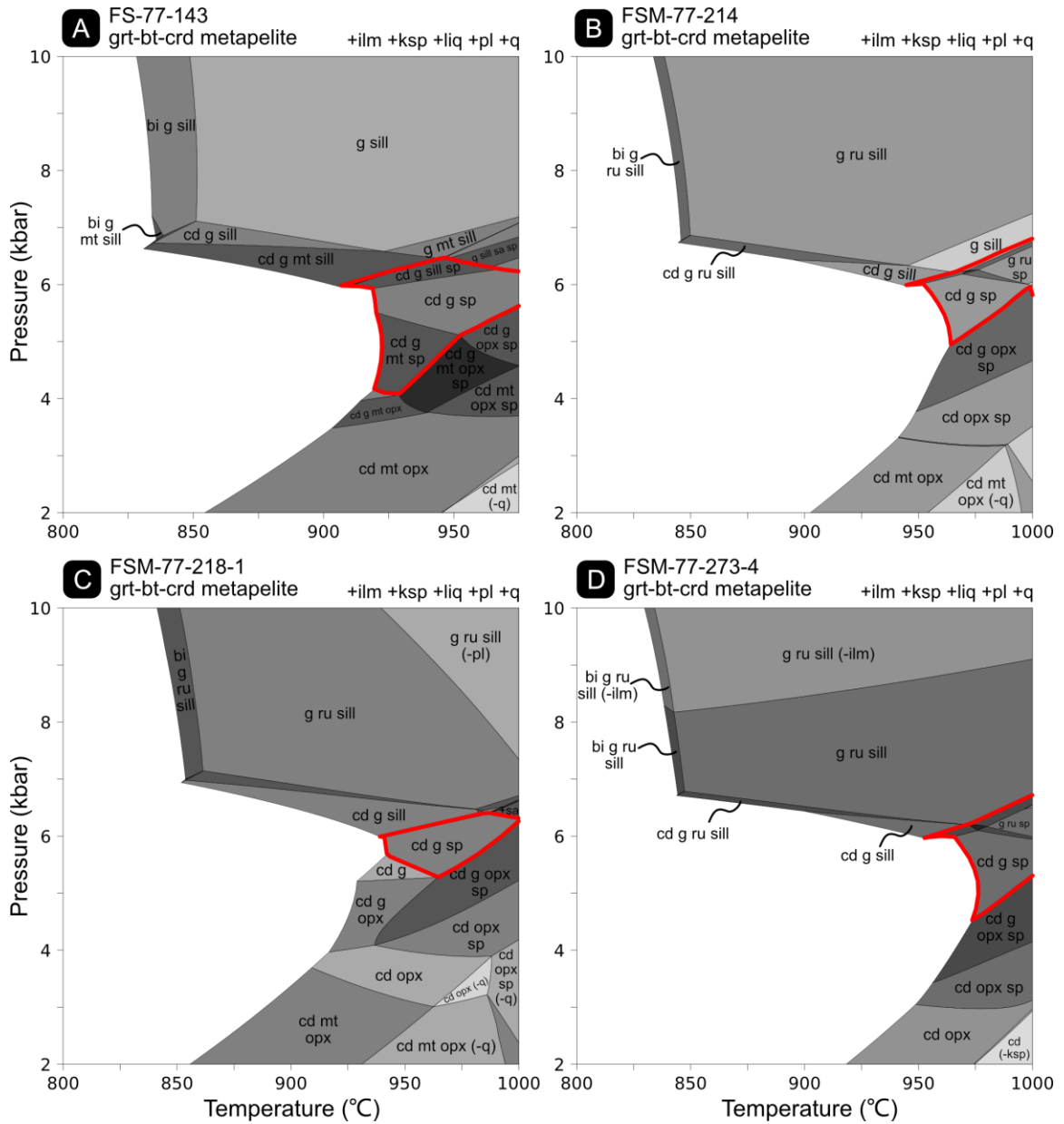


**Figure 4.6. Suprasolidus P–T diagrams of peak metamorphic paragneiss compositions inferring spinel-bearing peak metamorphic conditions. Spinel-bearing stability fields without orthopyroxene or sapphirine are outlined in red. H<sub>2</sub>O content was adjusted to intersect the spinel stability field with the solidus at ca. 6 kbar.**

Melt-reintegrated protolith compositions yield similar P–T topologies for the major phases (Figs. 4.7, 4.8a). At moderate to low pressures (ca. <7 kbar), garnet and cordierite are not stable at the solidus. At temperatures ca.  $\geq 750$  °C, garnet and cordierite both become stable,

with garnet stability limited to ca.  $\geq 3$  kbar and cordierite stability limited to ca.  $\leq 7$  kbar. Spinel stability is restricted to temperatures above ca. 875 °C and generally between 3–7 kbar. Unlike the spinel-bearing peak metamorphic models, the melt-reintegrated protolith models yield little to no P–T space where both spinel and quartz are stable. For all four samples, quartz is consumed around 900 °C at 6 kbar and becomes less stable with lower pressures. However, these melt-reintegrated protoliths assume a closed system where no melt is lost. At temperatures of ca. 900 °C where spinel is predicted the proportion of melt present is predicted at around 70–80 mol% (Appendix A.6) which is well above the suggested 7 mol% threshold before melt loss (Rosenberg and Handy, 2005). Thus, if spinel-bearing stability fields were reached during metamorphism, significant melt loss is likely to have occurred thus significantly altering the bulk composition (e.g., Yakymchuk and Brown, 2014).

A potential prograde metamorphic path for sample FSM-77-218-1 is presented with a modebox in Figure 4.8b. At 6 kbar, the prograde path would cross the solidus around 675 °C, during which muscovite dehydration reactions would be the primary melt-producing reaction until muscovite depletion around 700 °C with the appearance of K-feldspar. Following muscovite depletion, biotite dehydration reactions would then be the primary melt-producing reaction until biotite depletion is reached. Garnet would first appear around 750 °C in equilibrium with biotite and sillimanite, followed by the appearance of cordierite and depletion of biotite around 820 °C. After biotite, quartz is consumed to produce melt until ca. 875 °C and finally, spinel would be stable around 920 °C.

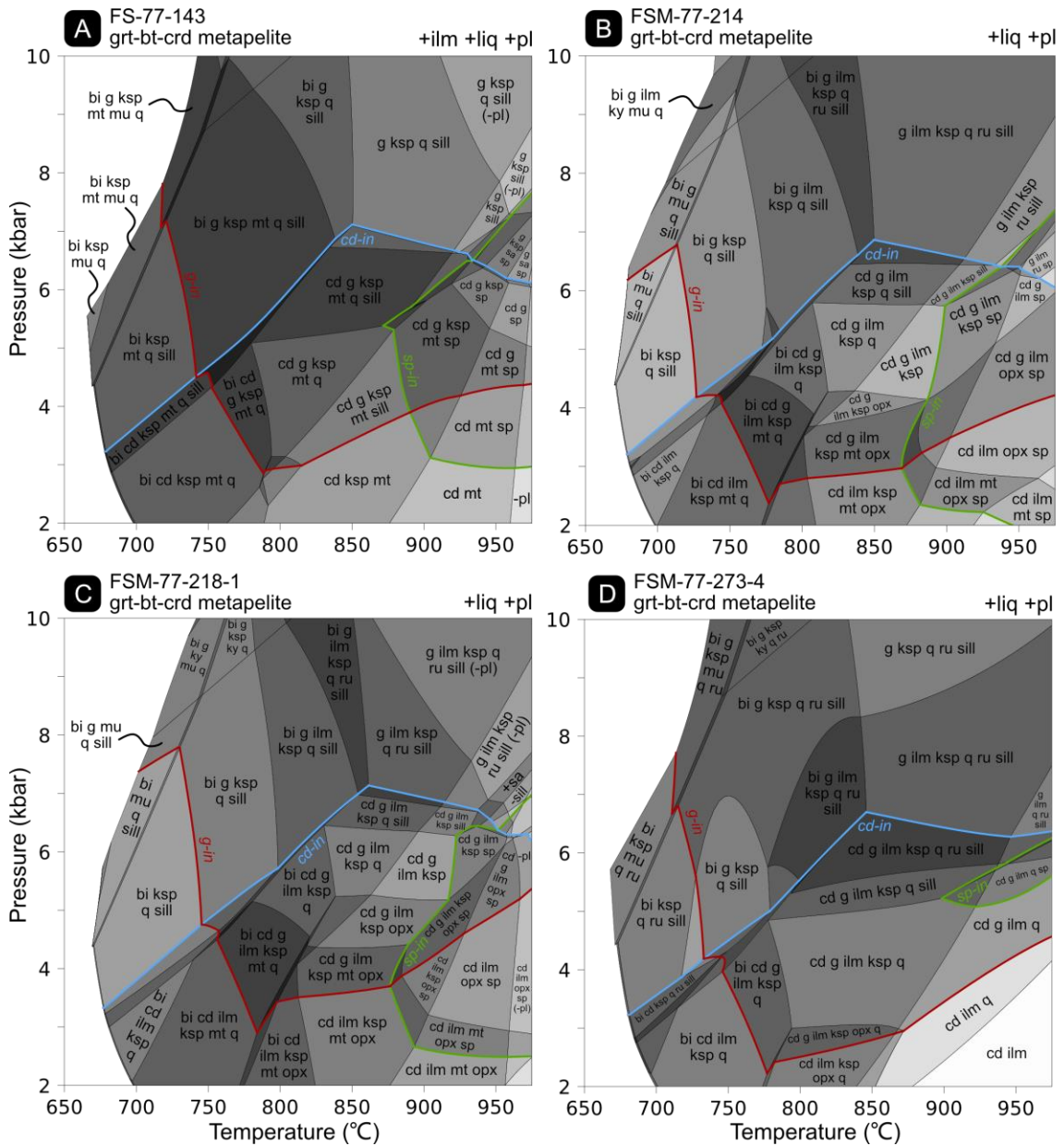


**Figure 4.7.** Suprasolidus P–T diagrams of melt reintegrated paragneiss compositions which are roughly representative of protolith (pre-anatexis) compositions. The stability limits of garnet, cordierite and spinel are outlined in red, blue and green respectively. The solidus for each model is minimally saturated with H<sub>2</sub>O at ca. 6 kbar.

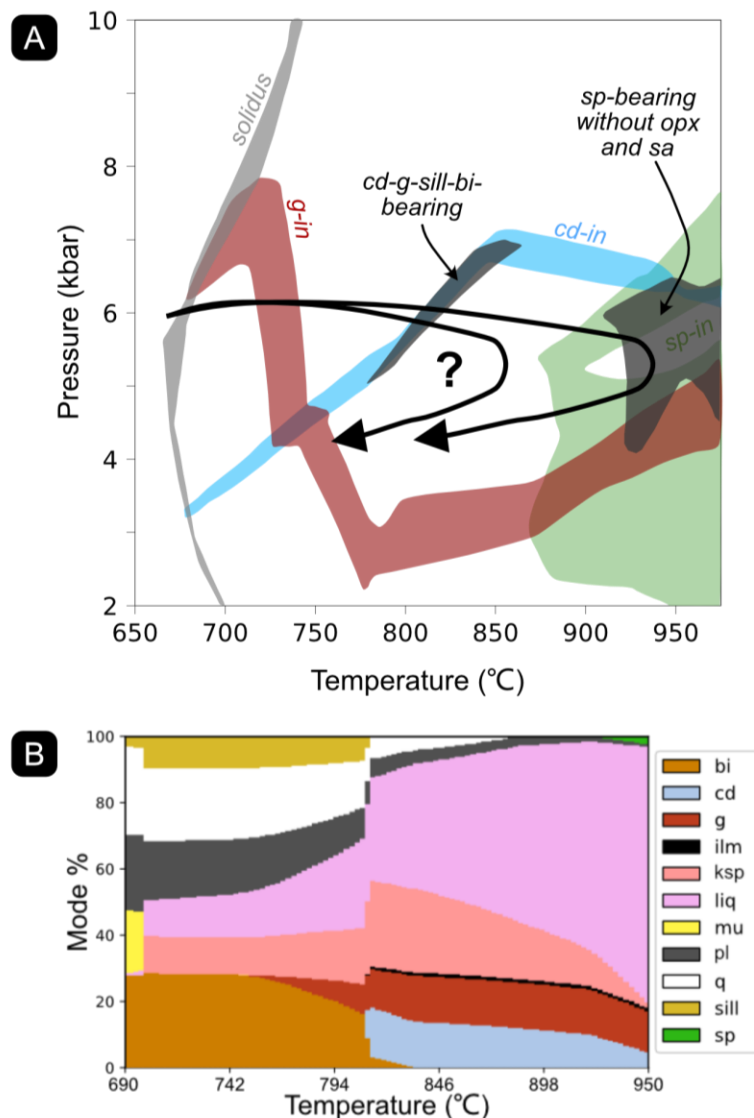


**Figure 4.8.** (a) P–T diagram summarizing the phase equilibrium modelling results and possible P–T paths of metamorphism. The extents of cordierite–garnet–sillimanite–biotite stability fields from Figure 4.5 and spinel-bearing stability fields without orthopyroxene or sapphirine from Figure 4.6 are shaded in dark grey. The boundaries of the solidus, garnet, cordierite, and spinel stability using the melt-reintegrated compositions from Figure 4.7 are shaded in light grey, red, blue, and green respectively. (b) Modebox showing the change in phase proportions during an isobaric closed system (no melt loss) prograde path of metamorphism at 6 kbar. Modal proportions are based on the melt-reintegrated protolith composition of sample FSM-77-218-1.

## 4.6 Discussion

### 4.6.1 Metamorphism within the Ellesmere tectonic zone

The migmatitic paragneisses of the Ellesmere tectonic zone on southeastern Ellesmere Island underwent high temperature to ultrahigh temperature metamorphism with anatexis during ca. 1.9 Ga orogenesis. Granulite facies assemblages comprising garnet, sillimanite, cordierite and biotite indicate minimum peak metamorphic conditions of ca. ca. 5–7 kbar and 750–860 °C (Figs. 4.5, 4.8a). Peak pressures may have been slightly higher (~7.5 kbar), especially for rutile-bearing samples (e.g., Fig. 4.5b), but pressure conditions during peak temperatures were likely around 6 kbar which is in agreement with previous barometry estimates for Ellesmere Island (Frisch, 1988). Previous thermometry based peak temperature estimates from the paragneiss maxed out around 750 °C but were suggested to likely be higher (ca. >750–800 °C, Frisch, 1988). Our results confirm this suggestion.

Nevertheless, these peak temperature estimates (ca. 750–860 °C) are considered a minimum because the abundance of spinel present in these quartz-rich paragneisses (Figs. 4.3, 4.4) which suggests ultrahigh temperature conditions (>900 °C) may have been reached. If spinel + quartz assemblages were in thermal equilibrium, our modelling results suggest peak metamorphic conditions of ca. 5–6.5 kbar and  $\geq 940$  °C (Figs. 4.6, 4.8a), ~100 °C higher than estimates using garnet–sillimanite–cordierite–biotite stability. With that said, there are many complexities in determining if spinel + quartz assemblages are an indication of ultrahigh temperature conditions (e.g., Harley, 2008; Kelsey and Hand, 2015).

It has been shown that the incorporation of minor elements in spinel such as  $\text{Fe}^{3+}$ , Zn, Cr and Ti can increase spinel stability (e.g., Dasgupta et al., 1995). Previous mineral analysis of the paragneiss mostly precludes this as estimated  $\text{Fe}^{3+}$  ( $\text{Fe}^{3+}/\text{Fe}^{2+}+\text{Fe}^{3+} = \sim 5\text{--}9\%$ ), Zn ( $\leq 0.050$  cpfu per 4 oxygen), Cr ( $\sim 0.012$  cpfu) and Ti ( $\sim 0.002$  cpfu) contents are low (Frisch, 1988). It has also been suggested that spinel + quartz assemblages in migmatitic gneisses may reflect the stability of spinel + melt, with quartz representing crystallized melt, thus not spinel + suprasolidus quartz stability (Harley, 2008). This is more difficult to confirm, however, crystallized granitic melt generally involves both quartz and feldspar (e.g., Sawyer, 1999), and at least one spinel + quartz occurrence in these samples is absent of

feldspar contact with quartz (Fig. 4.3a). It is possible some of the spinel growth occurred in micro-domains, generally melanocratic with silica-undersaturated effective bulk compositions, thus not diagnostic of ultrahigh temperature conditions. Nevertheless, the occurrence of spinel and quartz in direct contact (e.g., Figs. 4.3a, 4.3b) and the general abundance of quartz (e.g., ~10–40 vol%) implies spinel + quartz suprasolidus stability, thus a likely indication of high temperature conditions (850–900 °C), if not ultrahigh temperature conditions (>900 °C).

Suggesting ultrahigh temperature metamorphism is not unfounded in this region, as the occurrence of a sapphirine + quartz assemblage on Devon Island has already confirmed ultrahigh temperature conditions associated with ca. 1.9 Ga metamorphism in the area (Chapter 2). These new temperature estimates provide additional evidence that near to ultrahigh temperature conditions were potentially widespread in the Ellesmere and Devon islands region during ca. 1.9 Ga orogenesis. The lack of diagnostic ultrahigh temperature assemblages on Ellesmere Island such as sapphirine + quartz may be due to a lack of bulk-rock compositions suitable to forming diagnostic ultrahigh temperature assemblages (e.g., high MgO + Al<sub>2</sub>O<sub>3</sub>, Kelsey and Hand, 2015). P–T modelling of the paragneiss shows that below 1000 °C sapphirine is only predicted for two of the samples (Figs. 4.6a, 4.6c), at ca. 6.5 kbar and >950 °C. This demonstrates that if metamorphic conditions reached 900–1000 °C, sapphirine would still not appear in most paragneiss assemblages on Ellesmere Island. Furthermore, ultrahigh temperature conditions on Devon Island were confirmed based on a single sapphirine + quartz bearing sample, collected directly adjacent to outcrops which only preserve assemblages diagnostic up to high temperature conditions (ca. 850 °C), which demonstrates that sampling bias can have an effect or that ultrahigh temperature conditions are extremely localized. Lastly, the polymetamorphic history of Devon and/or Ellesmere islands is likely to have overprinted previously stable ultrahigh temperature assemblages unless they were developed during the most recent thermal event with minimal retrograde effects.

#### 4.6.2 Metamorphism across the Taltson–Thelon–Ellesmere–Inglefield orogenic zone

The results from this study and the previous two chapters have significantly constrained the metamorphic history associated with ca. 2.0–1.9 Ga Ellesmere–Thelon orogenesis in the Ellesmere and Devon islands region, demonstrating that high temperature to ultrahigh temperature ( $\geq 850$ – $950$  °C) granulite facies conditions were widespread with pressures mostly ranging between 6–9 kbar. Elsewhere along the ca. 2.0–1.9 Ga orogenic zones, along the western and northern margins of the Rae craton, quantitative P–T results are quite limited but give indications of similar metamorphic P–T conditions. On Boothia Peninsula (Fig. 4.1), east of the Thelon tectonic zone, a sample of garnet–orthopyroxene tonalite gneiss yielded peak estimates of 8.7 kbar and 960 °C, while the remainder of samples yielded estimates mainly between 6–8 kbar and 740–850 °C or lower (Kitsul et al., 2000). More recent, preliminary results from Boothia Peninsula, suggest ultrahigh temperature metamorphism occurred at 1.95 Ga, reaching temperatures of  $\sim 1020$  °C, followed by high temperature metamorphism ( $\sim 850$  °C) at 1.94–1.91 Ga (Sanborn-Barrie and Regis, 2020). Further southwest, in the Queen Maud area west of the Thelon tectonic zone (Fig. 4.1), one sample of a mafic dike with a 1.93 Ga age of metamorphism, yielded minimum P–T estimates of 7.5 kbar and 720 °C (Tersmette, 2012). Within the Thelon tectonic zone, similar spinel-bearing, garnet–cordierite–sillimanite–biotite assemblages have yielded P–T conditions up to 8.9 kbar and 880 °C (Thompson, 1992).

Across the ca. 2.0–1.9 Ga orogenic zones, the P–T conditions within the Taltson magmatic zone have been the most well-constrained (e.g., Berman and Bostock, 1997), with many similarities to the Ellesmere tectonic zone (Kitsul et al., 2000). Here, spinel + quartz paragneisses and associated granites have yielded thermometry estimates of 5–7 kbar and ca. 850–940 °C (Chacko et al., 1994; Grover et al., 1997; Berman and Bostock, 1997), with suggestions of temperatures up to  $\sim 1050$  °C based on isotopic thermometry (Farquhar et al., 1996) and  $\text{Al}_2\text{O}_3$  in orthopyroxene thermometry (Berman and Bostock, 1997). Previously it has been suggested that temperatures recorded in the Taltson magmatic zone were higher than those associated with the Thelon orogeny (e.g., Berman and Bostock, 1997), however, recent results from Ellesmere and Devon islands (this study; Chapter 2),



and Boothia Peninsula (Sanborn-Barrie and Regis, 2020) suggest they reached similar P–T conditions, at least locally.

Northeast of Ellesmere Island, on northwestern Greenland, migmatitic granulite facies rocks are widespread in the 2.0–1.9 Ga Inglefield mobile belt and flanking domains, but quantitative P–T estimates are exceptionally limited. South of the Inglefield mobile belt, granulite facies Archean rocks yielded P–T estimates of ca. 7.5 kbar and 700 °C (Garde et al., 1984), but are likely to be higher.

## 4.7 Conclusions

Granulite facies paragneiss assemblages from the Ellesmere tectonic zone comprise assemblages of garnet, sillimanite, cordierite, and/or biotite which indicates minimum peak metamorphic conditions between ca. 5–7 kbar and 750–860 °C associated with ca. 2.0–1.9 Ga Ellesmere–Thelon orogenesis. The consistent presence of spinel in these quartz-rich assemblages suggests higher peak temperature conditions of  $\geq 940$  °C, providing further evidence of ultrahigh temperature metamorphism for the Laurentian shield rocks in the Ellesmere and Devon islands region. Furthermore, quantitative metamorphic estimates throughout the ~3000 km long Taltson–Thelon–Ellesmere–Inglefield orogenic zones suggest that moderate pressure, ultrahigh temperature metamorphism was ubiquitous during ca. 1.9 Ga tectonic activity along the western Rae craton margin.

## 4.8 References

- Abbey, S. (1979). “Rock analysis” methods at the Geological Survey of Canada. *Geostandards Newsletter*, 3(1), 97-101.
- Berman, R. G. (2010). Metamorphic map of the western Churchill Province, Canada [Map]. Natural Resources Canada.
- Berman, R. G., & Bostock, H. H. (1997). Metamorphism in the northern Taltson magmatic zone, Northwest Territories. *Canadian Mineralogist*, 35(5), 1069–1091.
- Berman, R. G., Davis, W. J., Whalen, J. B., Taylor, B. E., McMartin, I., Mccurdy, M. W., Mitchell, R. K., Ma, S., Coyle, M., Roberts, B., & Craven, J. A. (2018). Report of

activities for the GEM-2 Chantrey-Thelon activity: Thelon tectonic zone project, Nunavut (pp. 1–22). Geological Survey of Canada.

Card, C. D., Bethune, K. M., Davis, W. J., Rayner, N., & Ashton, K. E. (2014). The case for a distinct Taltson orogeny: Evidence from northwest Saskatchewan, Canada. *Precambrian Research*, 255, 245–265.

Caswell, B., Gilotti, J. A., Webb, L. E., McClelland, W. C., Kościńska, K., Piepjohn, K., & von Gosen, W. (2021).  $^{40}\text{Ar}/^{39}\text{Ar}$  dating of Paleoproterozoic shear zones in the Ellesmere–Devon crystalline terrane, Nunavut, Canadian Arctic. *Canadian Journal of Earth Sciences*, 58, 1073–1084.

Chacko, T., Creaser, R. A., & Poon, D. (1994). Spinel+ quartz granites and associated metasedimentary enclaves from the Taltson magmatic zone, Alberta, Canada: a view into a root zone of a high temperature S-type granite batholith. *Mineralogical Magazine A*, 58, 161-162.

Dasgupta, S., Sengupta, P., Ehl, J., Raith, M., & Bardhan, S. (1995). Reaction textures in a suite of spinel granulites from the Eastern Ghats Belt, India: evidence for polymetamorphism, a partial petrogenetic grid in the system KFMASH and the roles of ZnO and Fe<sub>2</sub>O<sub>3</sub>. *Journal of Petrology*, 36(2), 435-461.

Davis, W. J., Berman, R. G., & MacKinnon, A. (2013). U-Pb geochronology of archival rock samples from the Queen Maud Block, Thelon Tectonic Zone and Rae Craton, Kitikmeot region, Nunavut, Canada (Geological Survey of Canada, Open File, Vol. 7409). Natural Resources Canada.

Davis, W. J., Berman, R. G., Nadeau, L., & Percival, J. (2014). U-Pb zircon geochronology of a transect across the Thelon Tectonic Zone, Queen Maud region, and adjacent Rae Craton, Kitikmeot region, Nunavut, Canada (Geological Survey of Canada, Open File, Vol. 7652). Natural Resources Canada.

Davis, W. J., Sanborn-Barrie, M., Berman, R. G., & Pehrsson, S. (2021). Timing and provenance of Paleoproterozoic supracrustal rocks in the central Thelon tectonic

- zone, Canada: implications for the tectonic evolution of western Laurentia from ca. 2.1 to 1.9 Ga. *Canadian Journal of Earth Sciences*, 58, 378–395.
- de Capitani, C., & Petrakakis, K. (2010). The computation of equilibrium assemblage diagrams with Theriak/Domino software. *The American Mineralogist*, 95(7), 1006–1016.
- Farquhar, J., Chacko, T., & Ellis, D. J. (1996). Preservation of oxygen isotope compositions in granulites from Northwestern Canada and Enderby Land, Antarctica: implications for high-temperature isotopic thermometry. *Contributions to Mineralogy and Petrology*, 125(2), 213-224.
- Frisch, T. (1984a). Geology, Prince of Wales Mountains, District of Franklin, Northwest Territories. Geological Survey of Canada, Map, 1572.
- Frisch, T. (1984b). Geology, Makinson Inlet, District of Franklin, Northwest Territories. Geological Survey of Canada, Map, 1573.
- Frisch, T. (1988). Reconnaissance geology of the Precambrian shield of Ellesmere, Devon and Coburg Islands, Canadian Arctic Archipelago. *Bulletin Geological Survey of Canada*, Memoir 409, 102 p.
- Frisch, T., & Hunt, P. A. (1988). U-Pb zircon and monazite ages from the Precambrian Shield of Ellesmere and Devon islands, Arctic Archipelago. *Bulletin Geological Survey of Canada*, Paper 88-2, 117–125.
- Frost, B. R., & Chacko, T. (1989). The Granulite Uncertainty Principle: Limitations on Thermobarometry in Granulites. *The Journal of Geology*, 97(4), 435–450.
- Gibb, R. A., & Thomas, M. D. (1977). The Thelon Front: a cryptic suture in the Canadian Shield?. *Tectonophysics*, 38(3-4), 211-222.
- Gilotti, J. A., McClelland, W. C., Piepjohn, K., & von Gosen, W. (2018). U–Pb geochronology of Paleoproterozoic gneiss from southeastern Ellesmere Island: implications for displacement estimates on the Wegener fault. *Arktos*, 4(1), 12.

- Grover, T. W., Pattison, D. R. M., McDonough, M. R., & McNicoll, V. J. (1997). Tectonometamorphic evolution of the southern Taltson magmatic zone and associated shear zones, northeastern Alberta. *Canadian Mineralogist*, 35(5), 1051–1067.
- Harley, S. L. (2008). Refining the P–T records of UHT crustal metamorphism. *Journal of Metamorphic Geology*, 26(2), 125–154.
- Henderson, J.B., James, D.T., and Thompson, P.H. (1999). Geology, Healey Lake–Artillery Lake, Northwest Territories–Nunavut; Geological Survey of Canada, Open File 3819, scale 1:250 000.
- Hoffman, P. (1988). United plates of America, the birth of a craton: Early Proterozoic assembly and growth of Laurentia. *Annual Review of Earth and Planetary Sciences*, 16(1), 543–603.
- Hoffman, P. F., Bally, A. W., & Palmer, A. R. (1989). Precambrian geology and tectonic history of North America. *The geology of North America—an overview*, 447–512.
- Holland, T. J. B., Green, E. C. R., & Powell, R. (2021). A thermodynamic model for feldspars in  $\text{KAlSi}_3\text{O}_8$ – $\text{NaAlSi}_3\text{O}_8$ – $\text{CaAl}_2\text{Si}_2\text{O}_8$  for mineral equilibrium calculations. *Journal of Metamorphic Geology*, 40(4), 587–600.
- Holland, T. J. B., & Powell, R. (2011). An improved and extended internally consistent thermodynamic dataset for phases of petrological interest, involving a new equation of state for solids. *Journal of Metamorphic Geology*, 29(3), 333–383.
- Kelsey, D. E. (2008). On ultrahigh-temperature crustal metamorphism. *Gondwana Research*, 13(1), 1–29.
- Kelsey, D. E., & Hand, M. (2015). On ultrahigh temperature crustal metamorphism: Phase equilibria, trace element thermometry, bulk composition, heat sources, timescales and tectonic settings. *Geoscience Frontiers*, 6(3), 311–356.

- Kitsul, V. I., Glebovitsky, V. A., Vapnik, Y. A., & Frisch, T. (2000). Gneisses from the granulite terrane of the central Boothia Uplift, Arctic Canada. *Canadian Mineralogist*, 38, 443–454.
- Lanari, P., Vidal, O., De Andrade, V., Dubacq, B., Lewin, E., Grosch, E. G., & Schwartz, S. (2014). XMapTools: A MATLAB©-based program for electron microprobe X-ray image processing and geothermobarometry. *Computers & Geosciences*, 62, 227–240.
- Miles, W., & Oneschuk, D. (2016). Magnetic anomaly map, Canada [Map]. Natural Resources Canada.
- Nutman, A. P., Dawes, P. R., Kalsbeek, F., & Hamilton, M. A. (2008). Palaeoproterozoic and Archaean gneiss complexes in northern Greenland: Palaeoproterozoic terrane assembly in the High Arctic. *Precambrian Research*, 161(3-4), 419–451.
- Powell, R., & Holland, T. J. B. (1988). An internally consistent dataset with uncertainties and correlations: 3. Applications to geobarometry, worked examples and a computer program. *Journal of Metamorphic Geology*, 6(2), 173-204.
- Rosenberg, C. L., & Handy, M. R. (2005). Experimental deformation of partially melted granite revisited: implications for the continental crust. *Journal of Metamorphic Geology*, 23(1), 19-28.
- Sanborn-Barrie, M., and Regis, R. (2020). 2.56–1.87 Ga evolution of the Rae cratonic margin: micro- to macro-scale constraints from Boothia Peninsula-Somerset Island, Nunavut, Geoconvention Abstracts.
- Sawyer, E. W. (1999). Criteria for the recognition of partial melting. *Physics and Chemistry of the Earth, Part A: Solid Earth and Geodesy*, 24(3), 269–279.
- St-Onge, M. R., Van Gool, J. M., Garde, A., & Scott, D. J. (2009). Correlation of Archaean and Palaeoproterozoic units between northeastern Canada and western Greenland: constraining the pre-collisional upper plate accretionary history of the Trans-Hudson orogen. *Geological Society, London, Special Publications*, 318(1), 193–235.

- Tersmette, D.B., (2012). Geology, geochronology, thermobarometry, and tectonic evolution of the Queen Maud block, Churchill craton, Nunavut, Canada. University of Alberta, Master of Science, 170 pp.
- Thompson, D.L. (1992): Proterozoic Evolution of the Northern Thelon Tectonic Zone. Ph.D. diss., Princeton Univ., Princeton, New Jersey.
- Van Breemen, O., Thompson, P. H., Hunt, P. A., & Culshaw, N. (1987). U-Pb zircon and monazite geochronology from the northern Thelon Tectonic Zone, District of Mackenzie. Radiogenic Age and Isotopic Studies, Report, 1, 87–82.
- Waters, D. J. (2019). Metamorphic constraints on the tectonic evolution of the High Himalaya in Nepal: the art of the possible. Geological Society, London, Special Publications, 483(1), 325-375.
- Wheller, C. J., & Powell, R. (2014). A new thermodynamic model for sapphirine: calculated phase equilibria in  $K_2O-FeO-MgO-Al_2O_3-SiO_2-H_2O-TiO_2-Fe_2O_3$ . *Journal of Metamorphic Geology*, 32(3), 287-299.
- White, R. W., & Powell, R. (2002). Melt loss and the preservation of granulite facies mineral assemblages. *Journal of Metamorphic Geology*, 20(7), 621–632.
- White, R. W., Powell, R., & Clarke, G. L. (2002). The interpretation of reaction textures in Fe-rich metapelitic granulites of the Musgrave Block, central Australia: constraints from mineral equilibria calculations in the system  $K_2O-FeO-MgO-Al_2O_3-SiO_2-H_2O-TiO_2-Fe_2O_3$ . *Journal of Metamorphic Geology*, 20(1), 41–55.
- White, R. W., Powell, R., Holland, T. J. B., Johnson, T. E., & Green, E. C. R. (2014a). New mineral activity-composition relations for thermodynamic calculations in metapelitic systems. *Journal of Metamorphic Geology*, 32(3), 261–286.
- White, R. W., Powell, T., Holland, T. J. B., & Worley B. A. (2000). The effect of  $TiO_2$  and  $Fe_2O_3$  on metapelitic assemblages at greenschist and amphibolite facies conditions: mineral equilibria calculations in the system  $K_2O-FeO-MgO-Al_2O_3-SiO_2-H_2O-TiO_2-Fe_2O_3$ . *Journal of Metamorphic Geology*, 18(5), 497–511.

- White, R. W., Powell, R., & Johnson, T. E. (2014b). The effect of Mn on mineral stability in metapelites revisited: new  $a-x$  relations for manganese-bearing minerals. *Journal of Metamorphic Geology*, 32(8), 809–828.
- Whitney, D. L., & Evans, B. W. (2010). Abbreviations for names of rock-forming minerals. *The American Mineralogist*, 95(1), 185–187.
- Yakymchuk, C., & Brown, M. (2014). Consequences of open-system melting in tectonics. *Journal of the Geological Society*, 171(1), 21-40.

## Chapter 5

### 5 Tectonic summary and conclusions

#### 5.1 Late Neoproterozoic and middle Paleoproterozoic geology of Devon and Ellesmere islands

The northernmost Laurentian shield rocks in Canada are exposed on Devon and Ellesmere islands, encompassing rocks formed during at least two distinct tectonic events. The older rocks are late Neoproterozoic (ca. 2.55–2.47 Ga), comprising interleaved orthogneisses and paragneisses (Chapter 2–3; Frisch, 1988). These late Neoproterozoic units are exposed on southeastern Devon Island (Chapter 2; Frisch, 1988) and to a lesser extent on northeastern Devon Island (Chapter 3). The younger rocks, ca. 2.2–1.9 Ga metasedimentary rocks intruded by ca. 2.01–1.95 Ga granitoids, could represent a northern extension of the ca. 2.0–1.9 Ga Thelon tectonic zone (Chapter 3; Frisch, 1988; Gilotti et al., 2018). These juvenile middle Paleoproterozoic rocks are exposed on southern Ellesmere and Coburg islands (Frisch, 1988; Gilotti et al., 2018), as well as northeastern Devon Island (Chapter 3).

The entire crystalline basement of Devon and Ellesmere islands appears to have been thermally active between ca. 1.95–1.87 Ga, peaking at ca. 1.91 Ga (Chapters 2–3). Peak temperature conditions are estimated at  $>800$  °C throughout Devon and Ellesmere islands, however, near to ultrahigh temperatures around or above 850–900 °C were likely reached (Chapters 2–4). A sapphirine + quartz assemblage on southern Devon Island provides diagnostic evidence of ultrahigh temperature metamorphism, while the abundance of spinel + quartz assemblages on Ellesmere Islands further supports widespread ultrahigh temperature metamorphism with estimates up to ca.  $\geq 940$  °C (Chapter 4). The possible lack of ultrahigh temperature assemblages preserved in the area could be due to a lack of bulk-rock compositions suitable to the formation of diagnostic ultrahigh temperature assemblages (e.g., sapphirine + quartz), overprinting of ultrahigh temperature assemblages by later high temperature metamorphism, or only localized ultrahigh temperature conditions. Metamorphic pressure estimates vary across Devon and Ellesmere islands (Frisch, 1988; Chapters 2–4), with southern Devon Island recording pressure of ca. 9 kbar



(Chapter 2), compared to estimates of ca. 6–7 kbar for northern Devon and Ellesmere islands (Chapters 3–4). A possible interpretation for the varying pressures in the area is that the rocks of southern Devon Island represent a deeper level of exhumed crust compared to northern Devon and Ellesmere which represent a shallower level of exhumed crust (Chapter 3).

Earlier metamorphism of the late Neoproterozoic rocks on Devon Island is poorly constrained (Chapter 2). Possible metamorphic events are recorded at ca. 2.54, 2.47 and 2.30 Ga (Chapter 2); one or more of which could be associated with metamorphism during the Arrowsmith orogeny (Berman et al., 2013).

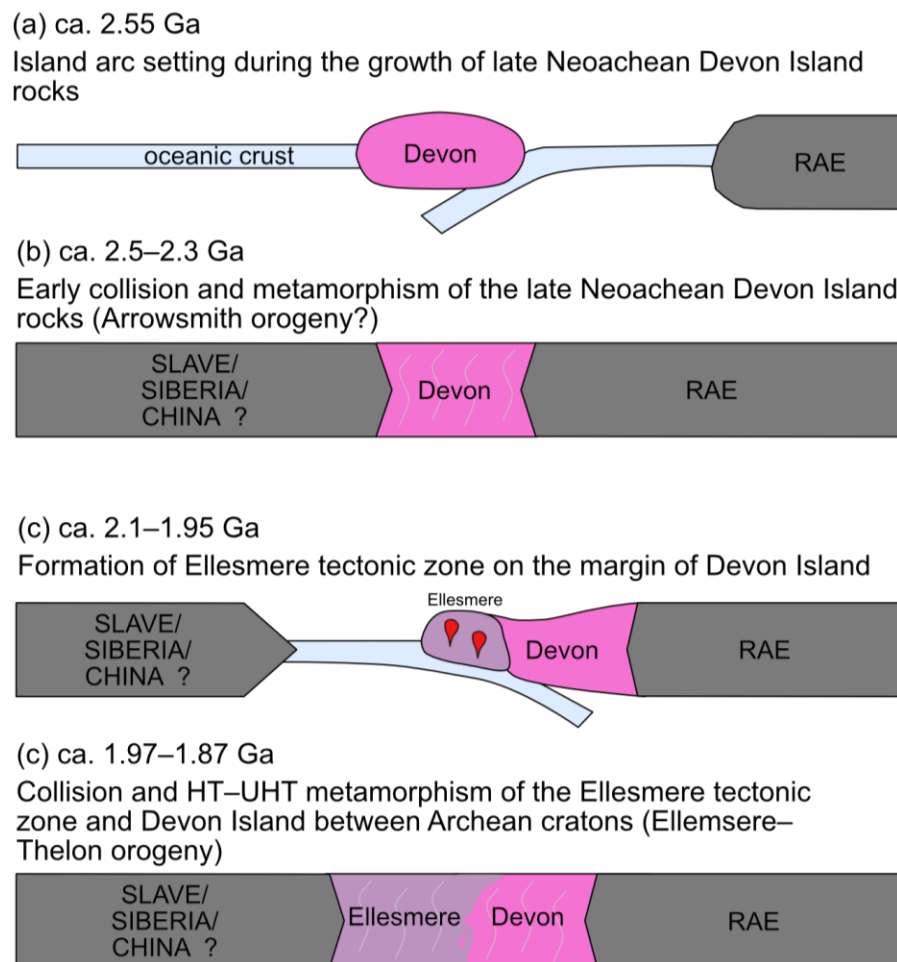


**Figure 5.1. Simplified summary of possible ca. 2.5–1.9 Ga tectonic events involving the formation and metamorphism of the crystalline basement on Devon and Ellesmere islands.**

A simplified interpretation of tectonic events related to the crystalline basement rocks of Devon and Ellesmere islands is provided in Figure 5.1. Following the ca. 2.8–2.6 Ga growth of typical Rae cratonic rocks, at ca. 2.55 Ga the Devon Island terrane may have formed as a island arc that was subsequently accreted to the Rae craton (Fig. 5.1a). Shortly after protolith formation (ca. 2.5 Ga) to ca. 2.3 Ga, one or more metamorphic events are likely to have occurred in association with the Arrowsmith orogeny (Fig. 5.1b). Around 2.1 Ga, deposition of the metasedimentary rocks on northern Devon and Ellesmere islands may have occurred on the margin of the late Neoproterozoic Devon terrane during rifting (e.g., Davis et al., 2021). This was likely followed by the formation of a magmatic arc during subduction, forming the ca. 2.01–1.95 Ga granitoids exposed on Ellesmere and northern Devon islands (Fig. 5.1c). Continued convergence and thickening associated with the collision of another tectonic block caused high temperature to ultrahigh temperature metamorphism between ca. 1.95–1.87 Ga (Fig. 5.1d). At this time is also possible another sedimentary sequence was deposited and subsequently deformed on Ellesmere or northern Devon islands, receiving detritus material from the exhumed magmatic arc (e.g., Davis et al., 2021; Sanborn-Barrie and Regis, 2020).

Previously, the term “Ellesmere-Devon crystalline terrane” has been used when referring to the basement rocks of Ellesmere and Devon islands (Frisch, 1988; St-Onge et al., 2009; Gilotti et al., 2018; Caswell et al., 2021). Given the newfound results from this study and the known differences in geologic history between the late Neoproterozoic rocks of Devon Island and the juvenile middle Paleoproterozoic rocks of Ellesmere Island with continuations on northern Devon Island, we do not recommend the use of this term in a geologic sense. Instead, we propose the terms “late Neoproterozoic Devon terrane”, a northern extension of the late Neoproterozoic Boothia terrane (Regis and Sanborn-Barrie, 2022) and “Ellesmere tectonic zone”, a northern extension of the Thelon tectonic zone.

## 5.2 Neoproterozoic–Paleoproterozoic tectonics in the Canadian Arctic and northwestern Greenland

The northernmost Laurentian shield rocks in Canada are distinct from the typical Rae cratonic crust to the south. The Rae craton comprises rocks  $\geq 2.6$  Ga in age (e.g., Sanborn-Barrie et al., 2014), whereas the oldest rocks identified on Devon or Ellesmere islands are

ca. 2.55 Ga (Chapters 2–3). The most likely continuation of the late Neoproterozoic Devon rocks is the crystalline basement of Boothia Peninsula (e.g., Regis and Sanborn-Barrie, 2022). Here, ca. 2.56–2.51 Ga plutonic rocks are overlain by a ca. 2.5 Ga metasedimentary sequence (Regis and Sanborn-Barrie, 2022), which is similar to the ca. 2.55–2.47 Ga orthogneisses and metasedimentary rocks of Devon Island (Chapter 2–3). Regis and Sanborn-Barrie (2022) suggest that late Neoproterozoic rocks extend further southwest in the Sherman domain in the Queen Maud area (Schultz et al., 2007), as well as the Nonacho basement complex (Regis et al., 2022) and Zemlak domain (Cloutier et al., 2021), which flank the Taltson magmatic zone. Continuations of the late Neoproterozoic Devon terrane to the northeast would most likely be exposed in the Prudhoe Land area of northwestern Greenland (Nutman et al., 2008). However, this is largely based on a single orthogneiss sample with a possible ca. 2.5 Ga age (Nutman et al., 2008), and the assumption that late Neoproterozoic rocks are likely to occur between Rae cratonic crust and juvenile middle Paleoproterozoic crust as shown for Devon and Ellesmere islands.

The ca. 2.01–1.95 Ga age of granitoids on Ellesmere and north Devon islands (Frisch, 1988; Frisch and Hunt, 1988; Gilotti et al., 2018; Chapter 3), in addition to correlations of regional geophysical data (Miles and Oneschuk, 2016) suggests Ellesmere and northern Devon islands are a northern extension of the Thelon tectonic zone on the Canadian mainland. Additionally, middle Paleoproterozoic metasedimentary sequences in the Thelon tectonic zone (Davis et al., 2021) appear to have cogenetic extensions on northern Devon and/or Ellesmere islands (Chapter 3). Thelon affinity plutonic rocks do not outcrop in the Boothia–Somerset corridor (Sanborn-Barrie and Regis, 2020), however, middle Paleoproterozoic metasedimentary sequence(s) on Somerset Island could be correlated with middle Paleoproterozoic metasedimentary sequence(s) on Ellesmere and northern Devon islands (Chapter 3). In northwestern Greenland, the ca. 1.99–1.98 Ga plutonic rocks of the Prudhoe Land granulite complex and ca. 2.3–1.9 Ga metasedimentary rocks of the Prudhoe Lane supracrustal complex (Nutman et al., 2008) seemingly correlate with the plutonic and metasedimentary rocks of Ellesmere and northern Devon islands (Chapter 3). Younger metasedimentary rocks of the Etah group (ca. 1.98–1.92 Ga, Nutman et al., 2008) could make up a younger metasedimentary succession on Ellesmere Island and correlate with the metasedimentary rocks of Somerset Island (Sanborn-Barrie and Regis, 2020).

Lastly, orthogneiss and granitoids of the Etah meta-igneous complex (ca. 1.95–1.91 Ga, Nutman et al., 2008) have similar ages to the anatectic granitoids of Ellesmere Island (Frisch, 1988).

### 5.3 Future work

Even with this updated framework of the Neoproterozoic–Paleoproterozoic geology on Devon and Ellesmere islands, there is considerable work left to further constrain the Precambrian history of this remote area. Below we provide suggestions for future projects focused on the Neoproterozoic–Paleoproterozoic geology of Devon and Ellesmere islands.

Large-scale remapping projects, especially on Devon Island, would assist in constraining the boundaries of late Neoproterozoic and middle Paleoproterozoic domains in the area. More specifically, a north-south traverse along the eastern coast of Devon Island would be ideal for identifying possible domain transitions. Expanded zircon dating of orthogneiss units on Ellesmere Island, especially in the southernmost area near Grise Fiord, is needed to confirm if late Neoproterozoic rocks extend to Ellesmere Island. Additionally, detrital zircon dating of metasedimentary rocks on Ellesmere Island is needed to determine the distributions of middle Paleoproterozoic sedimentary succession(s); in particular to distinguish between pre-Thelon plutonism and post-Thelon plutonism deposition (e.g., Davis et al., 2021).

With the confirmation of widespread high temperature to ultrahigh temperature conditions recorded on Devon and Ellesmere islands (Chapters 2–4), a more in-depth study utilizing phase equilibrium modelling of sapphirine + quartz assemblages or Zr-in-rutile thermometry (e.g., Kohn, 2020) of rutile-bearing metasedimentary rocks could further constrain the maximum P–T conditions of metamorphism in the area.

This thesis provides evidence of earlier ca. 2.5–2.3 Ga metamorphism on Devon Island (Chapter 2), but more detailed structural analysis and isotopic monazite dating would further constrain the timing and P–T conditions associated with these earlier metamorphic events.

Directly south of Devon Island, future geochronology studies on Bylot Island are needed to constrain the extent of late Neoproterozoic rocks southward. Currently, there is only one

unpublished zircon date for the crystalline basement on Bylot Island, yielding a date of ca. 2.54 Ga (Jackson and Berman, 2000), which may indicate an extension of late Neoproterozoic rocks on Bylot or northern Baffin islands. Northeast of Devon Island, expanded geochronology studies in the Prudhoe Land area of northwestern Greenland are needed to accurately delineate the distribution of Rae cratonic crust, late Neoproterozoic terrane, and middle Paleoproterozoic rocks.

Since the crystalline basement of Devon and Ellesmere islands is presently bounded to the northwest by a younger Paleozoic orogeny (e.g., Piepjohn et al., 2018), it is more difficult to determine the other tectonic blocks involved in the tectonic history of Devon and Ellesmere islands (Fig. 5.1), as is relatively well-established on the Laurentian mainland (e.g., Rae–Slave cratons). Further investigations into the potential connections between the Siberian and China cratons and their Paleoproterozoic orogens with northern Laurentia are needed (e.g., Condie and Rosen, 1994; Wang et al., 2016; Donskaya, 2020).

## 5.4 References

- Berman, R. G., Pehrsson, S., Davis, W. J., Ryan, J. J., Qui, H., & Ashton, K. E. (2013). The Arrowsmith orogeny: Geochronological and thermobarometric constraints on its extent and tectonic setting in the Rae craton, with implications for pre-Nuna supercontinent reconstruction. *Precambrian Research*, 232, 44–69.
- Caswell, B., Gilotti, J. A., Webb, L. E., McClelland, W. C., Kościńska, K., Piepjohn, K., & von Gosen, W. (2021).  $^{40}\text{Ar}/^{39}\text{Ar}$  dating of Paleoproterozoic shear zones in the Ellesmere–Devon crystalline terrane, Nunavut, Canadian Arctic. *Canadian Journal of Earth Sciences*, 58, 1073–1084.
- Cloutier, M. A., Bethune, K. M., Ashton, K. E., & Deane, J. M. K. (2021). U–Pb geochronology, geochemistry, and isotopic composition of granitoids across the Nolan–Zemlak domain boundary in the SW Rae craton, Laurentia: Evidence for a late Neoproterozoic suture reworked during Arrowsmith orogen. *Precambrian Research*, 362, 106303.

- Condie, K. C., & Rosen, O. M. (1994). Laurentia-Siberia connection revisited. *Geology*, 22(2), 168–170.
- Davis, W. J., Sanborn-Barrie, M., Berman, R. G., & Pehrsson, S. (2021). Timing and provenance of Paleoproterozoic supracrustal rocks in the central Thelon tectonic zone, Canada: implications for the tectonic evolution of western Laurentia from ca. 2.1 to 1.9 Ga. In *Canadian Journal of Earth Sciences* (pp. 1–18).
- Donskaya, T. V. (2020). Assembly of the Siberian Craton: Constraints from Paleoproterozoic granitoids. *Precambrian Research*, 348(July), 105869.
- Frisch, T. (1988). Reconnaissance geology of the Precambrian shield of Ellesmere, Devon and Coburg Islands, Canadian Arctic Archipelago. *Bulletin Geological Survey of Canada, Memoir 409*, 102 p.
- Frisch, T., & Hunt, P. A. (1988). U-Pb zircon and monazite ages from the Precambrian Shield of Ellesmere and Devon islands, Arctic Archipelago. *Bulletin Geological Survey of Canada, Paper 88-2*, 117–125.
- Gilotti, J. A., McClelland, W. C., Piepjohn, K., & von Gosen, W. (2018). U-Pb geochronology of Paleoproterozoic gneiss from southeastern Ellesmere Island: implications for displacement estimates on the Wegener fault. *Arktos*, 4(1), 12.
- Jackson, G. D., & Berman, R. G. (2000). Precambrian metamorphic and tectonic evolution of northern Baffin Island, Nunavut, Canada. *Canadian Mineralogist*, 38(2), 399–421.
- Kohn, M. J. (2020). A refined zirconium-in-rutile thermometer. *The American Mineralogist*, 105(6), 963–971.
- Miles, W., & Oneschuk, D. (2016). Magnetic anomaly map, Canada [Map]. Natural Resources Canada.
- Piepjohn, K., & von Gosen, W. (2018). Structural transect through Ellesmere Island (Canadian Arctic): superimposed Palaeozoic Ellesmerian and Cenozoic Eurekan deformation. *Geological Society, London, Special Publications*, 460(1), 33–56.

- Regis, D., Canam, R., & Martel, E. (2022). U-Pb geochronological results from the Nonacho Lake area (NTS 75-F), Northwest Territories (Geological Survey of Canada, Open File, Vol. 8880). Natural Resources Canada.
- Regis, D., & Sanborn-Barrie, M. (2022). Delimiting the extent of “Boothia terrane” crust, Nunavut: new U-Pb geochronological results (No. 978-0-660-45346-0; Geological Survey of Canada, Open File, Vol. 8917). Natural Resources Canada.
- Sanborn-Barrie, M., and Regis, R. (2020). 2.56–1.87 Ga evolution of the Rae cratonic margin: micro- to macro-scale constraints from Boothia Peninsula-Somerset Island, Nunavut, Geoconvention Abstracts.
- Schultz, M. E. J., Chacko, T., Heaman, L. M., Sandeman, H. A., Simonetti, A., & Creaser, R. A. (2007). Queen Maud block: A newly recognized Paleoproterozoic (2.4–2.5 Ga) terrane in northwest Laurentia. *Geology*, 35(8), 707.
- St-Onge, M. R., Van Gool, J. M., Garde, A., & Scott, D. J. (2009). Correlation of Archaean and Palaeoproterozoic units between northeastern Canada and western Greenland: constraining the pre-collisional upper plate accretionary history of the Trans-Hudson orogen. Geological Society, London, Special Publications, 318(1), 193–235.
- Wang, W., Cawood, P. A., Zhou, M.-F., & Zhao, J.-H. (2016). Paleoproterozoic magmatic and metamorphic events link Yangtze to northwest Laurentia in the Nuna supercontinent. *Earth and Planetary Science Letters*, 433, 269–279.

## Appendices

### A.1 Sample locations

#### Appendix 1. List of Devon and Ellesmere islands samples used in this thesis.

Sample	Rock Type	Latitude	Longitude	Island/Chapter
DI-18-3152	opx quartzofeldspathic gneiss	74.572462	-82.234340	Southern Devon Island
DI-18-3237	cpx–grt quartzofeldspathic gneiss	74.529591	-82.325165	Southern Devon Island
DI-18-3238	cpx–opx metabasite	74.501371	-82.125420	Southern Devon Island
DI-18-3239	cpx–opx metabasite	74.542447	-82.341255	Southern Devon Island
DI-18-3240	cpx–grt quartzofeldspathic gneiss	74.532572	-82.361993	Southern Devon Island
DI-18-3244	cpx–opx metabasite	74.474220	-81.835972	Southern Devon Island
DI-18-3245	bt diorite	74.487006	-81.692003	Southern Devon Island
DI-18-3248	bt granite gneiss	74.488452	-82.027463	Southern Devon Island
DI-18-3257	opx–cpx–grt quartzofeldspathic gneiss	74.523614	-82.550523	Southern Devon Island
DI-18-3294	spr–qtz metapelite	74.532594	-82.385924	Southern Devon Island
DI-18-3301	rt–grt metapelite	74.542507	-82.341875	Southern Devon Island
DI-18-3351	bt granite gneiss	74.581921	-82.394733	Southern Devon Island
DI-18-3448	cpx amphibolite	74.488452	-82.027463	Southern Devon Island
ED-C-1	bt granite gneiss	75.812743	-83.745194	Northern Devon Island
ED-C-2	bt–opx metabasite	75.812849	-83.744073	Northern Devon Island
ED-EG-2	kfs megacrystic granite	75.805026	-82.604696	Northern Devon Island
ED-TL-4	opx–bt granodiorite gneiss	75.589347	-84.101406	Northern Devon Island
HAU-10-026	bt–sill–grt metapelite	75.380898	-85.524314	Northern Devon Island
HAU-16-1034B	quartzite	75.600921	-83.596922	Northern Devon Island
HAU-16-1179	sill–crd–bt migmatitic paragneiss	75.262546	-86.466529	Northern Devon Island
HAU-16-1453A	hbl–bt migmatitic orthogneiss	75.244479	-86.482144	Northern Devon Island
HAU-16-1453C	post-kinematic bt granite dike	75.244479	-86.482144	Northern Devon Island
HMP-00-200	post-kinematic bt granite dike	75.240804	-86.493968	Northern Devon Island
HMP-00-213	hbl–cpx–opx metabasite	75.333674	-86.281005	Northern Devon Island
HMP-00-216A	grt–bt–crd metapelite	75.333674	-86.281005	Northern Devon Island
FS-77-143	grt–sill–crd paragneiss	77.763868	-77.914140	Ellesmere Island
FS-77-268	grt–sill–crd paragneiss	78.766961	-76.500658	Ellesmere Island
FSM-77-214	grt–sill–crd paragneiss	78.796391	-78.270992	Ellesmere Island
FSM-77-218-1	grt–sill–crd paragneiss	78.800355	-77.641307	Ellesmere Island
FSM-77-273-4	grt–sill–crd paragneiss	79.025087	-74.869591	Ellesmere Island
FSM-77-307	grt–sill–crd paragneiss	79.000302	-76.547865	Ellesmere Island

### A.2 Southern Devon Island mineral chemistry methodology

Nineteen southern Devon Island thin sections with a 20 nm thick layer of carbon coating were analyzed. Phases investigated include garnet, clinopyroxene, orthopyroxene, amphibole, biotite, sapphirine, plagioclase, and K-feldspar. Both synthetic and natural



mineral standards were utilized for element calibration. Wavelength dispersive spectroscopy (WDS) spot measurements were carried out with a 15 kV acceleration voltage, 20 nA probe current, 1  $\mu\text{m}$  spot size for garnet, pyroxene, and sapphirine, and a defocused 10  $\mu\text{m}$  spot size for plagioclase, K-feldspar, biotite, and amphibole. Ferric iron proportions of sapphirine were calculated using the methods of Droop (1987). Garnet major element mapping was carried out to check for element zoning. Analytical conditions for garnet mapping included a 100 nA probe current, defocused 1  $\mu\text{m}$  spot size, 0.5–35  $\mu\text{m}$  step size depending on the size of the garnet and 10 msec dwell time. Full thin section WDS element maps were produced for Al, Ca, and Mg for phase identification and modal abundances, along with maps of Ce and Zr for monazite and zircon identification respectively. Other elements of interest were analyzed by energy dispersive spectroscopy (EDS). Analytical conditions for full thin sections maps included a 350 nA beam current, 35  $\mu\text{m}$  beam diameter, 35  $\mu\text{m}$  step size and 10 msec dwell time. Element maps were analyzed with the XMapTools 3.4.1 software program (Lanari et al., 2014).

### A.3 Southern Devon Island whole-rock chemistry

#### Appendix 2. Whole-rock major chemistry (wt.%) of southern Devon Island samples. b.d., below detection.

Lithology	cpx-grt gneiss 3237	cpx-grt gneiss 3240	cpx-grt gneiss 3306	opx gneiss 3152	opx gneiss 3257	opx gneiss 3389	rt-grt metasediment/ leucogranite 3301	rt-grt metasediment/ leucogranite 3433	biotite granite gneiss 3235	biotite granite gneiss 3351
SiO <sub>2</sub>	62.5	62.1	57.8	56.0	62.2	61.0	58.3	75.2	74.1	74.9
TiO <sub>2</sub>	0.97	1.13	1.01	1.22	1.19	0.77	0.35	0.05	0.23	0.22
Al <sub>2</sub> O <sub>3</sub>	16.1	15.4	18.6	18.5	14.8	15.2	21.4	14.5	13.1	13.6
Fe <sub>2</sub> O <sub>3</sub>	6.82	7.07	6.49	7.82	8.20	6.75	7.01	1.87	2.06	1.24
MnO	0.11	0.11	0.09	0.09	0.10	0.07	0.11	0.06	0.01	b.d.
MgO	1.08	1.05	1.05	2.56	1.87	3.31	2.07	0.55	0.49	0.14
CaO	4.04	4.11	6.66	5.89	4.28	5.17	3.41	1.34	0.90	1.22
Na <sub>2</sub> O	3.44	3.31	3.81	3.68	2.96	2.73	5.04	4.04	2.06	2.64
K <sub>2</sub> O	3.09	3.25	1.89	1.86	2.96	3.90	1.67	3.00	6.32	5.72
P <sub>2</sub> O <sub>5</sub>	0.53	0.57	0.53	0.39	0.40	0.21	0.06	0.05	0.06	0.07
BaO	0.28	0.23	0.24	0.09	0.14	0.19	0.03	0.14	0.39	0.11
SrO	0.06	0.06	0.08	0.05	0.04	0.05	0.03	0.03	0.05	0.02
Cr <sub>2</sub> O <sub>3</sub>	b.d.	b.d.	b.d.	0.00	0.00	0.02	0.01	b.d.	b.d.	b.d.
LOI	0.69	0.55	0.84	0.38	0.19	1.30	0.26	0.36	0.91	0.53
Total	99.71	98.94	99.04	98.53	99.33	100.62	99.75	101.19	100.63	100.41

**Appendix 3: Whole-rock trace chemistry (ppm) of southern Devon Island samples.**

Lithology	cpx-grt gneiss 3237	cpx-grt gneiss 3240	cpx-grt gneiss 3306	opx gneiss 3152	opx gneiss 3257	opx gneiss 3389	rt-grt metasediment/ leucogranite 3301	rt-grt metasediment/ leucogranite 3433	biotite granite gneiss 3235	biotite granite gneiss 3351
Li	10	10	20	30	10	20	20	10	10	10
C	0.01	0.01	0.18	0.01	0.05	0.06	0.05	0.01	0.04	0.04
S	0.04	0.03	0.07	0.03	0.06	0.11	0.03	0.01	0.04	0.01
Sc	16	18	13	18	19	18	52	11	2	2
V	47	66	74	134	133	110	75	6	41	14
Cr	10	10	10	30	20	150	70	20	10	10
Co	8	10	11	21	17	22	15	3	3	2
Ni	3	3	4	20	11	39	11	1	5	3
Cu	4	4	6	16	14	18	12	2	20	7
Zn	122	111	134	112	117	79	42	12	21	7
Ga	28.7	24.3	26.4	29.4	24.4	19.7	26.8	14.2	14.9	18.3
As	0.2	0.2	0.3	0.3	0.3	0.2	0.2	0.2	4.5	0.2
Rb	45.5	51	17.4	36	53.3	76.4	27.2	28.6	111	111
Sr	577	544	706	451	340	460	275	318	498	177.5
Y	41.3	39.5	25.9	23.5	29.7	20.5	82.1	58.2	3.1	4.8
Zr	567	537	78	401	550	342	218	54	405	189
Nb	15.8	15.5	9.5	13.2	18	9.1	7.6	1.4	1.1	2.7
Cs	0.13	0.11	0.09	0.12	0.07	0.13	0.11	0.09	0.17	0.07
Ba	2600	2210	2260	865	1350	1725	318	1300	3630	1085

Lithology	cpx-grt gneiss 3237	cpx-grt gneiss 3240	cpx-grt gneiss 3306	opx gneiss 3152	opx gneiss 3257	opx gneiss 3389	rt-grt metasediment/ leucogranite 3301	rt-grt metasediment/ leucogranite 3433	biotite granite gneiss 3235	biotite granite gneiss 3351
La	67.2	63.7	47.6	52	55.7	35	78.2	30	21.9	62.5
Ce	150	141	99.8	108	127	75.6	172.5	61.2	34.1	116.5
Pr	19.7	18.65	12.7	14.35	16.45	10.05	20.9	6.82	3.49	12.4
Nd	79.3	75.6	50.6	60.9	66.8	40.6	74.7	22.2	11.7	40.4
Sm	14.6	13.95	9.93	10.85	12.5	7.91	13.85	2.82	1.64	5.21
Eu	5.92	4.12	4.76	2.13	2.17	2.06	1.26	0.98	1.3	1.17
Gd	11.7	11.1	7.52	7.93	9.01	6.01	11.05	2.65	1.16	2.47
Tb	1.56	1.51	0.94	0.92	1.17	0.75	1.92	0.67	0.12	0.26
Dy	8.46	8.02	5.27	4.97	5.84	4.37	13.4	6.89	0.55	1.13
Ho	1.5	1.45	0.96	0.92	1.07	0.74	2.8	1.9	0.1	0.17
Er	4.29	3.98	2.53	2.29	2.97	2.12	9.17	6.92	0.33	0.49
Tm	0.55	0.57	0.33	0.26	0.43	0.29	1.44	1.19	0.06	0.07
Yb	3.58	3.29	2.02	1.78	2.34	1.8	8.87	7.93	0.28	0.3
Lu	0.57	0.48	0.33	0.26	0.36	0.25	1.43	1.29	0.09	0.06
Hf	13.1	12.5	2	9.7	13.1	8.2	6.4	1.5	10.5	5.3
Ta	0.7	0.7	0.4	0.7	0.9	0.5	0.3	b.d.	0.1	0.1
Pb	15	17	12	12	17	15	24	33	21	33
Th	1.02	1.24	0.98	0.17	0.95	0.69	17.5	0.24	1.15	20.3
U	0.24	0.29	0.15	0.25	0.55	0.29	1.28	0.06	0.4	0.62
∑REE	370	349	246	268	305	189	430	154	78	264
Gd <sub>N</sub> /Yb <sub>N</sub>	2.6	2.7	3.0	3.6	3.1	2.7	1.0	0.3	3.4	6.7

## A.4 LA-ICP-MS zircon data

**Appendix 4. LA-ICP-MS zircon dating results of southern Devon Island samples. c: core; r: rim; h: homogenous. Discordancy =  $(^{206}\text{Pb}/^{238}\text{U} \text{ Age} / ^{207}\text{Pb}/^{206}\text{Pb} \text{ Age} - 1) * 100$ .**

Spot	Note	Th	U	Th/U	$^{207}\text{Pb}/^{235}\text{U}$		$^{206}\text{Pb}/^{238}\text{U}$		$^{238}\text{U}/^{206}\text{Pb}$		$^{207}\text{Pb}/^{206}\text{Pb}$		$^{207}\text{Pb}/^{235}\text{U}$		$^{206}\text{Pb}/^{238}\text{U}$		$^{207}\text{Pb}/^{206}\text{Pb}$		Disc.
		ppm	ppm	Ratio	Ratio	2 $\sigma$	Ratio	2 $\sigma$	Ratio	2 $\sigma$	Ratio	2 $\sigma$	Date	2 $\sigma$	Date	2 $\sigma$	Date	2 $\sigma$	
<b>3152 - orthopyroxene quartzofeldspathic gneiss (coordinates: 74.572462, -82.23434)</b>																			
14.3	r	38	157	0.24	5.70	0.14	0.3591	0.0084	2.7847	0.0651	0.1149	0.0026	1922	20	1972	38	1872	30	5
14.2	r	48	200	0.24	5.53	0.16	0.3436	0.0061	2.9104	0.0517	0.1161	0.0024	1899	19	1901	29	1883	31	1
4.2	r	22	122	0.18	6.30	0.15	0.3736	0.0089	2.6767	0.0638	0.1232	0.0025	2016	21	2050	40	1986	37	3
15.1	c	98	313	0.31	6.21	0.11	0.3508	0.0052	2.8506	0.0423	0.1279	0.0021	2001	15	1936	25	2061	30	-6
19.3	r	16	72	0.22	7.91	0.47	0.4090	0.0160	2.4450	0.0956	0.1364	0.0042	2166	51	2201	72	2138	52	3
5.2	r	13	50	0.26	8.20	0.27	0.4280	0.0110	2.3364	0.0600	0.1392	0.0038	2239	29	2292	52	2191	47	5
11.2	r	15	32	0.47	8.54	0.27	0.4200	0.0110	2.3810	0.0624	0.1470	0.0036	2271	29	2251	50	2302	41	-2
17.2	c	111	438	0.25	8.99	0.18	0.4347	0.0071	2.3004	0.0376	0.1502	0.0016	2329	18	2323	32	2346	19	-1
6.1	c	122	296	0.41	9.25	0.20	0.4352	0.0094	2.2978	0.0496	0.1539	0.0029	2358	20	2323	42	2376	32	-2
18.1	c	233	401	0.58	9.03	0.16	0.4254	0.0079	2.3507	0.0437	0.1540	0.0021	2336	16	2285	35	2387	23	-4
14.1	c	215	496	0.43	9.77	0.50	0.4640	0.0270	2.1552	0.1254	0.1557	0.0032	2385	27	2380	80	2403	27	-1
9.1	c	107	317	0.34	9.69	0.21	0.4440	0.0110	2.2523	0.0558	0.1573	0.0027	2399	20	2367	46	2411	30	-2
1.1	c	357	884	0.40	9.53	0.22	0.4392	0.0098	2.2769	0.0508	0.1575	0.0023	2382	21	2345	44	2421	25	-3
17.1	c	105	697	0.15	9.83	0.14	0.4508	0.0071	2.2183	0.0349	0.1594	0.0017	2419	13	2399	31	2445	18	-2
20.2	c	81	282	0.29	9.51	0.16	0.4331	0.0081	2.3089	0.0432	0.1603	0.0027	2383	16	2319	36	2448	29	-5
21.1	c	275	601	0.46	9.24	0.16	0.4165	0.0070	2.4010	0.0404	0.1610	0.0024	2360	16	2241	32	2458	26	-9
5.1	c	174	405	0.43	10.32	0.25	0.4610	0.0110	2.1692	0.0518	0.1620	0.0024	2452	23	2435	51	2474	25	-2
12.1	r	93	330	0.28	10.83	0.21	0.4774	0.0096	2.0947	0.0421	0.1627	0.0022	2503	18	2509	43	2476	22	1
8.1	c	219	516	0.42	9.97	0.21	0.4378	0.0094	2.2841	0.0490	0.1634	0.0029	2428	21	2335	42	2477	29	-6
11.1	c	165	466	0.35	10.79	0.19	0.4725	0.0090	2.1164	0.0403	0.1632	0.0022	2499	16	2489	40	2480	23	0
19.2	c	46	105	0.43	10.83	0.23	0.4765	0.0094	2.0986	0.0414	0.1640	0.0028	2499	21	2506	42	2486	28	1
13.1	c	106	346	0.31	10.92	0.24	0.4800	0.0100	2.0833	0.0434	0.1637	0.0023	2509	21	2534	43	2487	24	2

Spot	Note	Th	U	Th/U	<sup>207</sup> Pb/ <sup>235</sup> U		<sup>206</sup> Pb/ <sup>238</sup> U		<sup>238</sup> U/ <sup>206</sup> Pb		<sup>207</sup> Pb/ <sup>206</sup> Pb		<sup>207</sup> Pb/ <sup>235</sup> U		<sup>206</sup> Pb/ <sup>238</sup> U		<sup>207</sup> Pb/ <sup>206</sup> Pb		Disc.	
		ppm	ppm	Ratio	Ratio	2σ	Ratio	2σ	Ratio	2σ	Ratio	2σ	Date	2σ	Date	2σ	Date	2σ		%
19.1	c	32	67	0.48	11.13	0.26	0.4880	0.0110	2.0492	0.0462	0.1649	0.0032	2523	23	2553	48	2489	33	3	
16.1	c	126	461	0.27	10.84	0.15	0.4776	0.0068	2.0938	0.0298	0.1643	0.0019	2508	13	2517	29	2494	19	1	
20.1	c	148	398	0.37	11.25	0.24	0.4960	0.0110	2.0161	0.0447	0.1651	0.0022	2540	19	2590	47	2500	23	4	
7.1	c	123	490	0.25	11.41	0.27	0.4940	0.0120	2.0243	0.0492	0.1666	0.0029	2552	22	2580	51	2517	30	3	
2.1	c	34	83	0.41	11.39	0.28	0.4910	0.0110	2.0367	0.0456	0.1674	0.0032	2544	23	2579	45	2518	34	2	
12.2	c	48	130	0.37	12.21	0.24	0.5224	0.0097	1.9142	0.0355	0.1693	0.0028	2613	19	2703	41	2540	28	6	
4.1	c	132	213	0.62	10.85	0.23	0.4670	0.0110	2.1413	0.0504	0.1691	0.0027	2503	21	2473	46	2545	27	-3	
<b>3240 - clinopyroxene-garnet quartzofeldspathic gneiss (coordinates: 74.532572, -82.361993)</b>																				
20.2	c	16	176	0.09	5.43	0.09	0.3384	0.0042	2.9551	0.0367	0.1160	0.0016	1887	13	1880	20	1893	23	-1	
9.2	r	86	135	0.64	5.58	0.10	0.3457	0.0044	2.8927	0.0368	0.1167	0.0018	1909	15	1913	21	1895	27	1	
20.1	c	219	258	0.85	5.50	0.09	0.3420	0.0047	2.9240	0.0402	0.1166	0.0015	1896	14	1895	23	1896	23	0	
3.1	c	25	29	0.88	5.78	0.19	0.3508	0.0088	2.8506	0.0715	0.1190	0.0034	1925	29	1932	42	1919	54	1	
4.1	c	30	41	0.74	5.84	0.17	0.3558	0.0076	2.8106	0.0600	0.1195	0.0029	1939	25	1958	36	1919	44	2	
4.2	c	44	46	0.96	6.14	0.16	0.3729	0.0073	2.6817	0.0525	0.1202	0.0030	1985	23	2043	34	1929	45	6	
14.1	c	96	155	0.62	5.92	0.18	0.3454	0.0068	2.8952	0.0570	0.1219	0.0021	1948	21	1909	32	1969	31	-3	
3.2	r	34	62	0.54	6.51	0.17	0.3752	0.0073	2.6652	0.0519	0.1256	0.0028	2038	24	2054	35	2022	41	2	
5.1	c	128	104	1.23	6.84	0.12	0.3893	0.0056	2.5687	0.0370	0.1282	0.0019	2085	15	2117	26	2062	26	3	
10.2	r	64	90	0.71	6.99	0.19	0.3890	0.0083	2.5707	0.0549	0.1291	0.0022	2104	24	2113	38	2076	28	2	
3.3	c	42	69	0.61	6.77	0.15	0.3653	0.0062	2.7375	0.0465	0.1340	0.0024	2077	19	2004	29	2142	32	-6	
7.1	c	50	58	0.87	7.27	0.17	0.3917	0.0055	2.5530	0.0358	0.1349	0.0032	2137	22	2132	26	2146	41	-1	
11.1	c	51	62	0.83	7.74	0.23	0.4058	0.0084	2.4643	0.0510	0.1360	0.0025	2190	27	2191	39	2168	33	1	
17.1	c	67	100	0.67	7.93	0.18	0.4085	0.0079	2.4480	0.0473	0.1409	0.0020	2219	20	2204	36	2232	25	-1	
1.2	c	28	31	0.90	8.43	0.20	0.4147	0.0070	2.4114	0.0407	0.1485	0.0038	2269	22	2237	32	2303	46	-3	
9.1	c	42	49	0.85	8.83	0.23	0.4334	0.0082	2.3073	0.0437	0.1479	0.0031	2309	23	2316	37	2309	36	0	
7.2	c	34	43	0.80	9.04	0.27	0.4385	0.0096	2.2805	0.0499	0.1493	0.0029	2329	27	2343	43	2323	35	1	
10.1	c	42	56	0.76	8.99	0.16	0.4332	0.0062	2.3084	0.0330	0.1494	0.0027	2331	16	2317	28	2325	31	0	
19.1	c	56	58	0.95	9.02	0.19	0.4290	0.0070	2.3310	0.0380	0.1523	0.0031	2334	20	2298	32	2366	34	-3	
13.1	c	36	56	0.65	9.25	0.22	0.4310	0.0088	2.3202	0.0474	0.1540	0.0032	2353	22	2310	39	2376	35	-3	
2.1	c	27	37	0.74	10.07	0.46	0.4560	0.0130	2.1930	0.0625	0.1548	0.0046	2405	41	2411	56	2407	57	0	

Spot	Note	Th	U	Th/U	<sup>207</sup> Pb/ <sup>235</sup> U		<sup>206</sup> Pb/ <sup>238</sup> U		<sup>238</sup> U/ <sup>206</sup> Pb		<sup>207</sup> Pb/ <sup>206</sup> Pb		<sup>207</sup> Pb/ <sup>235</sup> U		<sup>206</sup> Pb/ <sup>238</sup> U		<sup>207</sup> Pb/ <sup>206</sup> Pb		Disc.	
		ppm	ppm	Ratio	Ratio	2σ	Ratio	2σ	Ratio	2σ	Ratio	2σ	Date	2σ	Date	2σ	Date	2σ		%
8.1	c	63	69	0.92	10.14	0.16	0.4659	0.0062	2.1464	0.0286	0.1570	0.0024	2445	15	2463	28	2412	27	2	
15.1	c	32	44	0.73	10.24	0.23	0.4617	0.0077	2.1659	0.0361	0.1588	0.0033	2447	21	2447	35	2425	34	1	
12.1	c	59	73	0.82	10.12	0.19	0.4543	0.0080	2.2012	0.0388	0.1605	0.0027	2444	18	2410	36	2455	30	-2	
9.3	c	38	55	0.69	10.22	0.20	0.4578	0.0068	2.1844	0.0324	0.1617	0.0028	2448	18	2427	30	2459	30	-1	
12.2	c	30	40	0.76	10.27	0.23	0.4565	0.0087	2.1906	0.0417	0.1622	0.0034	2453	21	2419	39	2459	36	-2	
18.2	c	37	49	0.75	11.07	0.30	0.4860	0.0100	2.0576	0.0423	0.1643	0.0028	2518	25	2546	43	2488	29	2	
18.1	c	40	62	0.64	10.75	0.19	0.4724	0.0070	2.1169	0.0314	0.1643	0.0028	2498	17	2491	31	2491	28	0	
16.1	c	317	434	0.73	10.05	0.19	0.4362	0.0080	2.2925	0.0420	0.1659	0.0015	2435	17	2329	36	2515	15	-7	
<b>3244 - two-pyroxene metabasite (coordinates: 74.47422, -81.835972)</b>																				
11.1	c	205	151	1.36	5.63	0.14	0.3572	0.0073	2.7996	0.0572	0.1140	0.0021	1913	21	1965	35	1846	33	6	
12.1	c	195	148	1.31	5.61	0.15	0.3540	0.0095	2.8249	0.0758	0.1143	0.0024	1905	24	1951	45	1846	38	6	
7.1	c	97	57	1.71	6.01	0.18	0.3707	0.0081	2.6976	0.0589	0.1168	0.0029	1962	26	2027	38	1876	45	8	
14.1	c	379	267	1.42	5.37	0.10	0.3293	0.0072	3.0367	0.0664	0.1177	0.0021	1877	16	1835	35	1907	33	-4	
10.1	c	117	116	1.01	5.73	0.16	0.3334	0.0066	2.9994	0.0594	0.1234	0.0032	1921	25	1858	31	1977	47	-6	
5.3	r	132	98	1.34	6.19	0.16	0.3571	0.0077	2.8003	0.0604	0.1247	0.0022	1996	23	1963	37	2007	32	-2	
14.2	c	231	189	1.22	6.50	0.13	0.3709	0.0077	2.6961	0.0560	0.1265	0.0023	2041	17	2037	35	2036	33	0	
5.2	r	56	928	0.06	7.96	0.16	0.4000	0.0076	2.5000	0.0475	0.1414	0.0016	2224	17	2164	35	2240	19	-3	
6.2	c	428	281	1.52	8.08	0.12	0.4023	0.0064	2.4857	0.0395	0.1440	0.0019	2237	14	2176	30	2267	23	-4	
15.3	c	100	75	1.34	8.95	0.20	0.4321	0.0089	2.3143	0.0477	0.1500	0.0030	2323	20	2310	40	2326	35	-1	
2.1	c	252	171	1.47	9.46	0.25	0.4370	0.0100	2.2883	0.0524	0.1555	0.0025	2369	25	2327	46	2398	28	-3	
4.2	c	216	163	1.33	10.07	0.23	0.4602	0.0098	2.1730	0.0463	0.1578	0.0023	2431	22	2434	43	2421	25	1	
5.1	c	255	183	1.40	9.75	0.20	0.4423	0.0086	2.2609	0.0440	0.1585	0.0025	2405	19	2360	38	2428	26	-3	
15.2	c	129	109	1.18	10.50	0.22	0.4720	0.0110	2.1186	0.0494	0.1591	0.0028	2473	20	2490	46	2431	30	2	
15.1	c	105	78	1.33	10.39	0.23	0.4568	0.0093	2.1891	0.0446	0.1628	0.0032	2460	21	2419	41	2483	34	-3	
6.1	c	648	306	2.12	10.62	0.23	0.4616	0.0093	2.1664	0.0436	0.1639	0.0023	2481	20	2440	41	2486	24	-2	

Spot	Note	Th	U	Th/U	<sup>207</sup> Pb/ <sup>235</sup> U		<sup>206</sup> Pb/ <sup>238</sup> U		<sup>238</sup> U/ <sup>206</sup> Pb		<sup>207</sup> Pb/ <sup>206</sup> Pb		<sup>207</sup> Pb/ <sup>235</sup> U		<sup>206</sup> Pb/ <sup>238</sup> U		<sup>207</sup> Pb/ <sup>206</sup> Pb		Disc.	
		ppm	ppm	Ratio	Ratio	2σ	Ratio	2σ	Ratio	2σ	Ratio	2σ	Date	2σ	Date	2σ	Date	2σ		%
16.1	c	341	230	1.48	10.28	0.25	0.4520	0.0110	2.2124	0.0538	0.1645	0.0030	2457	22	2402	49	2490	31	-4	
8.1	c	211	169	1.25	10.62	0.20	0.4629	0.0093	2.1603	0.0434	0.1647	0.0024	2486	17	2446	41	2494	25	-2	
3.1	c	59	79	0.75	10.99	0.26	0.4800	0.0100	2.0833	0.0434	0.1653	0.0033	2514	22	2521	46	2495	34	1	
13.2	c	239	166	1.44	11.34	0.21	0.4890	0.0091	2.0450	0.0381	0.1668	0.0029	2545	18	2560	40	2513	30	2	
16.2	c	254	622	0.41	10.77	0.29	0.4670	0.0130	2.1413	0.0596	0.1664	0.0024	2504	27	2474	60	2514	24	-2	
3.2	c	66	62	1.06	11.89	0.29	0.5090	0.0110	1.9646	0.0425	0.1680	0.0036	2586	23	2645	47	2519	37	5	
1.1	r	106	56	1.89	11.68	0.34	0.5000	0.0130	2.0000	0.0520	0.1690	0.0032	2565	28	2603	58	2531	32	3	
4.1	c	106	198	0.54	10.46	0.23	0.4471	0.0089	2.2366	0.0445	0.1691	0.0032	2471	21	2377	39	2536	31	-6	
13.1	c	222	172	1.29	11.29	0.21	0.4801	0.0090	2.0829	0.0390	0.1688	0.0026	2542	18	2522	40	2541	25	-1	
9.1	c	474	293	1.62	11.56	0.21	0.4835	0.0088	2.0683	0.0376	0.1706	0.0025	2565	17	2542	38	2557	24	-1	
<b>3301 - rutile-garnet metapelite (coordinates: 74.542507, -82.341875)</b>																				
1.2	c	80	380	0.21	8.30	1.30	0.3890	0.0440	2.5707	0.2908	0.1386	0.0056	2057	86	2020	170	2158	59	-6	
12.1	c	168	876	0.19	9.37	0.54	0.4330	0.0190	2.3095	0.1013	0.1526	0.0015	2327	27	2301	72	2375	17	-3	
9.1	c	147	1092	0.13	9.53	0.24	0.4391	0.0086	2.2774	0.0446	0.1568	0.0022	2378	23	2346	38	2415	23	-3	
2.2	c	280	1052	0.27	9.32	0.16	0.4242	0.0075	2.3574	0.0417	0.1592	0.0017	2364	16	2275	34	2443	18	-7	
3.2	c	219	710	0.31	10.54	0.15	0.4735	0.0078	2.1119	0.0348	0.1604	0.0017	2479	13	2495	35	2457	18	2	
3.1	c	225	761	0.30	10.61	0.18	0.4777	0.0081	2.0934	0.0355	0.1607	0.0015	2488	15	2517	35	2458	16	2	
14.1	c	661	904	0.73	10.46	0.17	0.4638	0.0087	2.1561	0.0404	0.1633	0.0019	2473	16	2455	38	2483	20	-1	
2.1	c	201	753	0.27	10.83	0.34	0.4470	0.0120	2.2371	0.0601	0.1752	0.0025	2489	29	2373	55	2598	24	-9	
<b>3351 - biotite monzogranite gneiss (coordinates: 74.581921, -82.394733)</b>																				
9.1	c	124	226	0.55	10.24	0.13	0.4589	0.0062	2.1791	0.0294	0.1620	0.0018	2455	12	2432	28	2475	19	-2	
8.1	c	654	1073	0.61	11.04	0.12	0.4895	0.0065	2.0429	0.0271	0.1626	0.0012	2524	10	2566	28	2480	12	3	
7.1	c	359	422	0.85	11.16	0.13	0.4798	0.0059	2.0842	0.0256	0.1680	0.0015	2534	11	2524	26	2535	15	0	
1.1	c	54	818	0.07	10.78	0.10	0.4645	0.0046	2.1529	0.0213	0.1682	0.0016	2503	8.9	2461	20	2537	16	-3	
1.2	c	106	154	0.69	10.95	0.15	0.4728	0.0063	2.1151	0.0282	0.1686	0.0020	2517	13	2493	28	2540	20	-2	
1.3	c	68	169	0.40	11.56	0.21	0.4943	0.0084	2.0231	0.0344	0.1699	0.0019	2564	17	2585	36	2550	19	1	
6.1	c	126	309	0.41	11.53	0.15	0.4900	0.0068	2.0408	0.0283	0.1696	0.0015	2563	13	2568	30	2550	15	1	



Spot	Note	Th	U	Th/U	<sup>207</sup> Pb/ <sup>235</sup> U		<sup>206</sup> Pb/ <sup>238</sup> U		<sup>238</sup> U/ <sup>206</sup> Pb		<sup>207</sup> Pb/ <sup>206</sup> Pb		<sup>207</sup> Pb/ <sup>235</sup> U		<sup>206</sup> Pb/ <sup>238</sup> U		<sup>207</sup> Pb/ <sup>206</sup> Pb		Disc.	
		ppm	ppm	Ratio	Ratio	2σ	Ratio	2σ	Ratio	2σ	Ratio	2σ	Date	2σ	Date	2σ	Date	2σ		%
<b>3448 - clinopyroxene amphibolite (coordinates: 74.533905, -82.378566)</b>																				
9.1	c	22	22	0.99	5.37	0.21	0.3456	0.0085	2.8935	0.0712	0.1123	0.0042	1855	34	1908	41	1768	70	8	
8.1	h	36	16	2.31	5.42	0.21	0.3501	0.0089	2.8563	0.0726	0.1123	0.0047	1871	34	1929	42	1785	76	8	
15.5	h	20	30	0.65	5.18	0.15	0.3345	0.0067	2.9895	0.0599	0.1131	0.0036	1842	26	1857	32	1800	59	3	
8.2	h	19	23	0.82	5.42	0.19	0.3475	0.0077	2.8777	0.0638	0.1128	0.0041	1874	32	1918	37	1812	66	6	
14.2	h	59	61	0.97	5.07	0.11	0.3237	0.0049	3.0893	0.0468	0.1131	0.0023	1824	18	1806	24	1833	38	-1	
11.1	h	26	21	1.22	5.30	0.16	0.3392	0.0077	2.9481	0.0669	0.1152	0.0038	1857	26	1878	37	1836	60	2	
14.4	h	59	57	1.04	5.04	0.12	0.3204	0.0051	3.1211	0.0497	0.1142	0.0028	1820	21	1790	25	1844	44	-3	
14.1	h	34	48	0.72	5.16	0.12	0.3250	0.0062	3.0769	0.0587	0.1145	0.0028	1837	20	1811	30	1854	43	-2	
5.1	h	79	90	0.87	5.20	0.12	0.3312	0.0055	3.0193	0.0501	0.1144	0.0024	1845	19	1842	27	1855	37	-1	
11.4	h	37	42	0.87	5.18	0.13	0.3264	0.0051	3.0637	0.0479	0.1156	0.0030	1845	22	1819	25	1855	48	-2	
13.2	h	50	47	1.05	5.44	0.13	0.3462	0.0061	2.8885	0.0509	0.1146	0.0028	1887	21	1914	29	1856	44	3	
3.1	h	120	141	0.86	4.94	0.09	0.3166	0.0042	3.1586	0.0419	0.1142	0.0019	1806	15	1772	21	1857	29	-5	
4.1	h	57	67	0.84	5.13	0.11	0.3260	0.0056	3.0675	0.0527	0.1154	0.0025	1836	18	1817	27	1863	39	-2	
8.4	h	20	29	0.68	5.37	0.18	0.3330	0.0074	3.0030	0.0667	0.1173	0.0039	1863	28	1853	36	1866	64	-1	
6.1	h	46	39	1.19	5.14	0.13	0.3269	0.0067	3.0590	0.0627	0.1158	0.0031	1835	23	1820	33	1867	50	-3	
11.3	h	31	31	1.02	5.41	0.16	0.3406	0.0078	2.9360	0.0672	0.1160	0.0034	1876	26	1889	38	1868	52	1	
15.1	h	26	30	0.86	5.37	0.16	0.3337	0.0073	2.9967	0.0656	0.1157	0.0034	1867	26	1852	35	1875	53	-1	
3.2	h	74	77	0.96	5.24	0.10	0.3289	0.0051	3.0404	0.0471	0.1161	0.0021	1856	16	1834	24	1885	31	-3	
14.3	h	42	47	0.90	5.08	0.12	0.3165	0.0050	3.1596	0.0499	0.1167	0.0028	1830	20	1771	24	1887	44	-6	

Spot	Note	Th	U	Th/U	$^{207}\text{Pb}/^{235}\text{U}$		$^{206}\text{Pb}/^{238}\text{U}$		$^{238}\text{U}/^{206}\text{Pb}$		$^{207}\text{Pb}/^{206}\text{Pb}$		$^{207}\text{Pb}/^{235}\text{U}$		$^{206}\text{Pb}/^{238}\text{U}$		$^{207}\text{Pb}/^{206}\text{Pb}$		Disc.
		ppm	ppm	Ratio	Ratio	2 $\sigma$	Ratio	2 $\sigma$	Ratio	2 $\sigma$	Ratio	2 $\sigma$	Date	2 $\sigma$	Date	2 $\sigma$	Date	2 $\sigma$	
8.5	h	19	21	0.91	5.49	0.19	0.3393	0.0076	2.9472	0.0660	0.1174	0.0038	1888	31	1883	36	1897	59	-1
8.3	h	35	42	0.84	5.72	0.14	0.3505	0.0064	2.8531	0.0521	0.1180	0.0030	1925	22	1937	31	1901	46	2
7.1	h	28	69	0.40	5.41	0.12	0.3306	0.0054	3.0248	0.0494	0.1186	0.0024	1878	20	1839	26	1920	37	-4
1.1	h	63	65	0.97	5.53	0.12	0.3392	0.0056	2.9481	0.0487	0.1191	0.0023	1901	19	1883	26	1928	35	-2
2.3	r	124	96	1.30	5.42	0.12	0.3296	0.0045	3.0340	0.0414	0.1201	0.0024	1883	20	1835	22	1946	36	-6
5.2	h	55	70	0.78	5.26	0.11	0.3190	0.0053	3.1348	0.0521	0.1206	0.0023	1855	19	1783	26	1952	34	-9
15.3	h	23	36	0.63	6.24	0.16	0.3537	0.0065	2.8273	0.0520	0.1275	0.0036	1999	23	1949	31	2028	49	-4
12.3	c	44	47	0.93	6.34	0.27	0.3569	0.0082	2.8019	0.0644	0.1281	0.0041	2004	37	1962	39	2033	55	-3
15.2	h	32	40	0.81	6.57	0.15	0.3682	0.0063	2.7159	0.0465	0.1286	0.0030	2049	19	2018	30	2055	40	-2
15.4	h	60	68	0.89	7.22	0.13	0.3826	0.0060	2.6137	0.0410	0.1356	0.0025	2138	17	2089	27	2163	32	-3
2.2	c	247	203	1.22	7.91	0.12	0.4054	0.0047	2.4667	0.0286	0.1423	0.0019	2217	14	2192	22	2247	23	-2
2.1	c	120	127	0.95	8.07	0.13	0.4111	0.0059	2.4325	0.0349	0.1444	0.0021	2237	15	2218	27	2270	25	-2

**Appendix 5. LA-ICP-MS zircon dating results of northern Devon Island samples.**

**Discordancy = (<sup>206</sup>Pb/<sup>238</sup>U Age / <sup>207</sup>Pb/<sup>206</sup>Pb Age - 1) \* 100.**

Sample	Spot	<sup>238</sup> U/ <sup>206</sup> Pb	σ	<sup>207</sup> Pb/ <sup>206</sup> Pb	σ	rho	<sup>207</sup> Pb/ <sup>235</sup> U Date	σ	<sup>206</sup> Pb/ <sup>238</sup> U Date	σ	<sup>207</sup> Pb/ <sup>206</sup> Pb Date	σ	Disc. %
ED-EG-2	43	2.872	0.016	0.1160	0.0006	0.343	1911	5	1926	9	1895	9	2
ED-EG-2	40	3.018	0.015	0.1162	0.0005	0.452	1870	4	1845	8	1898	8	-3
ED-EG-2	54	2.886	0.014	0.1162	0.0005	0.493	1908	4	1918	8	1898	7	1
ED-EG-2	42	2.851	0.015	0.1166	0.0005	0.504	1922	4	1938	9	1904	8	2
ED-EG-2	46	2.847	0.017	0.1166	0.0005	0.132	1923	6	1941	10	1904	7	2
ED-EG-2	44	2.847	0.016	0.1169	0.0006	0.396	1925	5	1941	9	1909	9	2
ED-EG-2	52	2.841	0.015	0.1170	0.0005	0.293	1928	5	1944	9	1910	8	2
ED-EG-2	12	2.760	0.013	0.1171	0.0004	0.477	1953	4	1993	8	1912	6	4
ED-EG-2	14	2.775	0.014	0.1171	0.0005	0.573	1949	4	1984	9	1912	7	4
ED-EG-2	37	3.015	0.013	0.1171	0.0005	0.292	1877	4	1846	7	1912	8	-3
ED-EG-2	6	2.823	0.019	0.1172	0.0006	0.412	1935	6	1955	11	1913	9	2
ED-EG-2	35	2.991	0.011	0.1173	0.0004	0.280	1886	4	1859	6	1915	6	-3
ED-EG-2	28	3.012	0.014	0.1174	0.0005	0.417	1880	4	1848	7	1916	8	-4
ED-EG-2	31	3.035	0.014	0.1174	0.0004	0.483	1874	4	1836	7	1916	7	-4
ED-EG-2	17	2.806	0.020	0.1175	0.0007	0.613	1942	5	1965	12	1918	10	2
ED-EG-2	33	3.126	0.016	0.1177	0.0005	0.433	1851	4	1789	8	1921	8	-7
ED-EG-2	56	2.826	0.018	0.1177	0.0007	0.394	1937	6	1953	10	1921	10	2
ED-EG-2	5	2.812	0.013	0.1179	0.0005	0.387	1943	4	1961	8	1924	7	2
ED-EG-2	7	2.856	0.021	0.1180	0.0005	0.071	1930	7	1935	12	1925	7	1
ED-EG-2	25	2.960	0.013	0.1180	0.0004	0.544	1900	3	1876	7	1925	6	-3
ED-EG-2	29	3.010	0.014	0.1180	0.0005	0.406	1885	4	1849	7	1925	8	-4
ED-EG-2	36	3.062	0.014	0.1181	0.0005	0.377	1871	4	1822	7	1927	8	-5
ED-EG-2	11	2.796	0.013	0.1184	0.0004	0.421	1952	4	1971	8	1931	7	2
ED-EG-2	21	2.779	0.019	0.1185	0.0006	0.409	1958	6	1981	11	1933	8	3
ED-EG-2	22	2.866	0.019	0.1186	0.0005	0.439	1932	5	1929	11	1934	7	0
ED-EG-2	1	3.312	0.030	0.1187	0.0008	0.524	1809	7	1701	14	1936	12	-12
ED-EG-2	4	2.792	0.013	0.1190	0.0006	0.357	1957	5	1973	8	1940	8	2
ED-EG-2	9	2.754	0.014	0.1190	0.0004	0.402	1969	4	1997	9	1940	7	3
ED-EG-2	55	2.853	0.014	0.1190	0.0005	0.230	1939	5	1937	8	1940	8	0
ED-EG-2	2	2.768	0.016	0.1191	0.0006	0.423	1966	5	1988	10	1942	8	2
ED-EG-2	23	3.057	0.022	0.1192	0.0005	0.424	1881	6	1824	12	1943	8	-6
ED-EG-2	34	3.046	0.019	0.1195	0.0007	0.374	1886	6	1830	10	1948	10	-6
ED-EG-2	48	2.878	0.012	0.1195	0.0006	0.284	1935	5	1922	7	1948	9	-1
ED-EG-2	41	2.981	0.016	0.1199	0.0007	0.390	1907	5	1865	9	1954	10	-5
ED-EG-2	24	2.991	0.017	0.1201	0.0005	0.673	1906	4	1859	9	1957	7	-5
ED-EG-2	10	2.722	0.013	0.1207	0.0006	0.386	1992	5	2017	8	1966	9	3
ED-EG-2	3	2.894	0.015	0.1268	0.0005	0.453	1981	4	1913	8	2053	6	-7
ED-TL-4	14	3.138	0.023	0.1156	0.0006	0.227	1832	7	1783	11	1888	9	-6
ED-TL-4	6	2.768	0.013	0.1178	0.0006	0.258	1956	5	1988	8	1922	8	3
ED-TL-4	33	2.708	0.014	0.1178	0.0006	0.209	1975	6	2026	9	1922	8	5
ED-TL-4	18	2.663	0.020	0.1187	0.0006	0.420	1996	6	2055	13	1936	9	6
ED-TL-4	8	2.743	0.016	0.1188	0.0007	0.270	1971	6	2004	10	1937	10	3
ED-TL-4	10	2.720	0.014	0.1190	0.0006	0.324	1980	5	2018	9	1940	9	4
ED-TL-4	11	2.737	0.014	0.1191	0.0007	0.178	1975	6	2008	9	1942	10	3
ED-TL-4	35	2.790	0.014	0.1192	0.0006	0.305	1959	5	1975	8	1943	8	2
ED-TL-4	5	2.707	0.011	0.1193	0.0007	0.323	1986	5	2027	7	1945	10	4
ED-TL-4	36	2.755	0.017	0.1193	0.0006	0.584	1971	4	1996	11	1945	8	3
ED-TL-4	16	2.763	0.019	0.1194	0.0007	0.352	1969	6	1991	12	1946	10	2
ED-TL-4	42	2.738	0.018	0.1194	0.0006	0.425	1977	6	2007	12	1946	9	3

Sample	Spot	$^{238}\text{U}/^{206}\text{Pb}$	$\sigma$	$^{207}\text{Pb}/^{206}\text{Pb}$	$\sigma$	rho	$^{207}\text{Pb}/^{235}\text{U}$ Date	$\sigma$	$^{206}\text{Pb}/^{238}\text{U}$ Date	$\sigma$	$^{207}\text{Pb}/^{206}\text{Pb}$ Date	$\sigma$	Disc. %
ED-TL-4	29	2.826	0.013	0.1198	0.0005	0.407	1953	4	1953	8	1952	7	0
ED-TL-4	9	2.744	0.020	0.1199	0.0006	0.104	1979	7	2003	13	1954	8	3
ED-TL-4	37	2.789	0.018	0.1199	0.0006	0.349	1965	6	1975	11	1954	8	1
ED-TL-4	38	2.732	0.017	0.1199	0.0006	0.356	1983	5	2011	11	1954	8	3
ED-TL-4	32	2.652	0.016	0.1200	0.0007	0.417	2010	5	2063	11	1955	10	5
ED-TL-4	17	2.706	0.012	0.1201	0.0007	0.252	1993	5	2027	8	1957	10	4
ED-TL-4	19	2.869	0.022	0.1202	0.0006	0.332	1943	7	1928	13	1958	8	-2
ED-TL-4	40	2.789	0.014	0.1202	0.0006	0.406	1967	5	1975	9	1958	8	1
ED-TL-4	43	2.737	0.014	0.1204	0.0005	0.353	1985	5	2008	9	1961	7	2
ED-TL-4	46	2.793	0.015	0.1204	0.0005	0.356	1967	5	1973	9	1961	7	1
ED-TL-4	24	2.755	0.017	0.1205	0.0005	0.497	1980	5	1996	10	1963	7	2
ED-TL-4	15	2.662	0.027	0.1206	0.0008	0.315	2011	9	2056	18	1964	11	5
ED-TL-4	39	2.674	0.024	0.1208	0.0007	0.524	2008	7	2048	16	1967	10	4
ED-TL-4	30	2.680	0.013	0.1209	0.0005	0.514	2007	4	2044	9	1969	7	4
ED-TL-4	27	2.695	0.015	0.1210	0.0005	0.586	2003	4	2034	9	1970	7	3
ED-TL-4	25	2.769	0.016	0.1211	0.0006	0.494	1980	5	1988	10	1972	9	1
ED-TL-4	45	2.740	0.021	0.1211	0.0006	0.524	1989	6	2006	13	1972	9	2
ED-TL-4	1	2.625	0.013	0.1213	0.0008	0.290	2028	6	2081	9	1975	12	5
ED-TL-4	31	2.751	0.016	0.1214	0.0005	0.530	1988	5	1999	10	1976	7	1
ED-TL-4	20	2.780	0.026	0.1219	0.0008	0.289	1982	8	1981	16	1983	11	0
ED-TL-4	44	2.853	0.021	0.1219	0.0007	0.075	1960	8	1937	12	1983	9	-2
ED-TL-4	34	2.743	0.015	0.1222	0.0006	0.411	1996	5	2004	9	1988	9	1
ED-TL-4	3	2.627	0.013	0.1226	0.0007	0.147	2037	6	2079	9	1994	10	4
ED-TL-4	13	2.687	0.017	0.1229	0.0007	0.456	2019	6	2040	11	1998	10	2
ED-TL-4	26	2.711	0.017	0.1232	0.0006	0.553	2013	5	2024	11	2002	9	1
ED-TL-4	28	2.723	0.015	0.1236	0.0006	0.372	2012	5	2016	10	2008	8	0
ED-TL-4	7	2.634	0.018	0.1290	0.0010	0.324	2079	8	2075	13	2084	14	0
ED-TL-4	47	2.567	0.014	0.1449	0.0010	0.207	2206	7	2121	10	2286	12	-7
ED-TL-4	41	2.197	0.011	0.1553	0.0008	0.363	2411	5	2418	11	2404	9	1
HAU-16-1034B	14	4.136	0.022	0.0877	0.0006	0.424	1388	5	1396	7	1375	12	2
HAU-16-1034B	26	3.851	0.022	0.0904	0.0004	0.542	1466	4	1488	8	1433	8	4
HAU-16-1034B	41	2.821	0.017	0.1202	0.0005	0.413	1957	5	1956	10	1958	7	0
HAU-16-1034B	44	2.912	0.027	0.1202	0.0007	0.364	1930	8	1903	15	1958	10	-3
HAU-16-1034B	16	2.581	0.013	0.1263	0.0004	0.313	2078	5	2111	9	2046	6	3
HAU-16-1034B	19	2.776	0.026	0.1264	0.0006	0.310	2015	8	1983	16	2048	8	-3
HAU-16-1034B	38	2.568	0.027	0.1277	0.0007	0.425	2093	8	2120	19	2066	10	3
HAU-16-1034B	4	2.712	0.018	0.1289	0.0005	0.467	2053	5	2023	11	2082	6	-3
HAU-16-1034B	9	2.507	0.022	0.1315	0.0005	0.183	2140	8	2164	16	2117	7	2
HAU-16-1034B	27	2.456	0.024	0.1316	0.0007	0.614	2159	7	2202	18	2119	9	4
HAU-16-1034B	35	2.484	0.017	0.1326	0.0007	0.304	2156	6	2181	13	2132	9	2
HAU-16-1034B	3	2.769	0.025	0.1370	0.0008	0.377	2088	8	1988	15	2189	10	-9
HAU-16-1034B	13	2.394	0.014	0.1387	0.0006	0.117	2229	6	2250	11	2210	8	2
HAU-16-1034B	32	2.391	0.020	0.1411	0.0007	0.512	2246	6	2253	16	2240	9	1
HAU-16-1034B	20	2.476	0.018	0.1418	0.0006	0.262	2219	7	2187	14	2249	7	-3
HAU-16-1034B	2	2.384	0.013	0.1420	0.0006	0.337	2254	5	2258	10	2251	7	0
HAU-16-1034B	6	2.461	0.019	0.1424	0.0007	0.320	2228	7	2198	14	2256	8	-3
HAU-16-1034B	17	2.325	0.016	0.1447	0.0007	0.451	2294	6	2306	13	2283	8	1
HAU-16-1034B	33	2.485	0.023	0.1450	0.0010	0.229	2236	9	2180	17	2287	12	-5

Sample	Spot	$^{238}\text{U}/^{206}\text{Pb}$	$\sigma$	$^{207}\text{Pb}/^{206}\text{Pb}$	$\sigma$	rho	$^{207}\text{Pb}/^{235}\text{U}$ Date	$\sigma$	$^{206}\text{Pb}/^{238}\text{U}$ Date	$\sigma$	$^{207}\text{Pb}/^{206}\text{Pb}$ Date	$\sigma$	Disc. %
HAU-16-1034B	18	2.230	0.016	0.1457	0.0006	0.296	2338	6	2388	14	2295	6	4
HAU-16-1034B	7	2.347	0.018	0.1481	0.0007	0.328	2307	7	2288	15	2323	8	-2
HAU-16-1034B	34	2.241	0.020	0.1485	0.0007	0.157	2351	8	2379	17	2328	8	2
HAU-16-1034B	28	2.463	0.033	0.1520	0.0010	0.548	2287	10	2197	25	2368	11	-7
HAU-16-1034B	8	2.364	0.020	0.1524	0.0009	0.466	2326	7	2274	16	2372	10	-4
HAU-16-1034B	1	2.369	0.014	0.1575	0.0007	0.367	2354	6	2270	12	2428	8	-7
HAU-16-1034B	23	2.794	0.022	0.1575	0.0007	0.082	2205	8	1972	13	2428	7	-19
HAU-16-1034B	49	2.202	0.014	0.1597	0.0006	0.455	2434	5	2414	13	2452	6	-2
HAU-16-1034B	10	2.020	0.010	0.1698	0.0006	0.400	2571	4	2593	11	2555	6	1
HAU-16-1034B	51	2.057	0.013	0.1719	0.0008	0.380	2566	6	2554	13	2575	7	-1
HAU-16-1034B	40	2.022	0.010	0.1724	0.0007	0.461	2585	4	2590	10	2580	6	0
HAU-16-1034B	15	1.795	0.009	0.2006	0.0007	0.168	2840	5	2855	12	2830	6	1
HAU-16-1034B	42	1.804	0.013	0.2129	0.0010	0.238	2892	7	2843	17	2927	7	-3
HAU-16-1179	9	3.067	0.028	0.1231	0.0006	0.353	1906	7	1819	15	2001	8	-9
HAU-16-1179	26	2.869	0.024	0.1285	0.0007	0.507	2001	6	1928	14	2077	10	-7
HAU-16-1179	38	3.275	0.037	0.1325	0.0009	0.397	1912	9	1718	17	2131	12	-19
HAU-16-1179	4	2.582	0.013	0.1379	0.0008	0.448	2156	5	2110	9	2200	9	-4
HAU-16-1179	21	2.298	0.017	0.1392	0.0007	0.309	2270	7	2329	15	2217	9	5
HAU-16-1179	13	2.431	0.022	0.1398	0.0006	0.344	2223	8	2221	17	2224	7	0
HAU-16-1179	14	2.461	0.022	0.1407	0.0009	0.324	2217	8	2198	16	2235	11	-2
HAU-16-1179	12	2.193	0.014	0.1453	0.0008	0.423	2351	6	2422	13	2291	9	6
HAU-16-1179	17	2.217	0.016	0.1535	0.0007	0.311	2392	7	2400	15	2385	8	1
HAU-16-1179	41	2.069	0.015	0.1540	0.0006	0.246	2458	7	2542	15	2390	6	6
HAU-16-1179	1	2.191	0.012	0.1551	0.0006	0.244	2412	5	2424	11	2402	7	1
HAU-16-1179	34	2.499	0.024	0.1575	0.0008	0.356	2306	8	2170	18	2428	9	-11
HAU-16-1179	39	2.127	0.011	0.1585	0.0007	0.444	2459	5	2484	11	2439	7	2
HAU-16-1179	36	2.101	0.015	0.1600	0.0008	0.491	2480	6	2510	15	2455	8	2
HAU-16-1179	3	2.183	0.010	0.1613	0.0007	0.485	2452	4	2431	9	2469	7	-2
HAU-16-1179	5	2.047	0.016	0.1618	0.0009	0.391	2514	7	2564	16	2474	9	4
HAU-16-1179	16	2.109	0.015	0.1625	0.0009	0.368	2490	7	2502	14	2481	9	1
HAU-16-1179	8	2.090	0.015	0.1665	0.0009	0.442	2521	6	2521	15	2522	9	0
HAU-16-1179	18	1.898	0.012	0.1795	0.0007	0.305	2682	6	2728	14	2648	6	3
HAU-16-1453A	47	2.384	0.019	0.1464	0.0007	0.305	2282	7	2258	16	2304	8	-2
HAU-16-1453A	8	2.401	0.014	0.1479	0.0007	0.062	2285	6	2245	11	2321	8	-3
HAU-16-1453A	45	2.324	0.016	0.1513	0.0008	0.429	2335	6	2307	13	2360	8	-2
HAU-16-1453A	9	2.236	0.014	0.1534	0.0009	-0.091	2383	8	2383	13	2383	9	0
HAU-16-1453A	1	2.255	0.012	0.1543	0.0007	0.149	2381	6	2366	11	2393	8	-1
HAU-16-1453A	34	2.373	0.017	0.1547	0.0008	0.267	2336	7	2267	13	2398	8	-5
HAU-16-1453A	16	2.214	0.013	0.1565	0.0008	0.228	2411	6	2403	11	2417	8	-1
HAU-16-1453A	33	2.203	0.011	0.1569	0.0008	0.218	2418	6	2413	10	2422	8	0
HAU-16-1453A	24	2.250	0.009	0.1591	0.0006	0.265	2411	4	2371	8	2445	6	-3
HAU-16-1453A	49	2.233	0.014	0.1592	0.0007	0.360	2419	6	2386	13	2446	7	-2
HAU-16-1453A	39	2.165	0.012	0.1593	0.0008	0.387	2448	5	2448	11	2447	8	0
HAU-16-1453A	48	2.100	0.013	0.1596	0.0007	0.338	2478	6	2511	13	2451	7	2
HAU-16-1453A	42	2.048	0.015	0.1599	0.0009	0.300	2503	7	2563	16	2454	10	4
HAU-16-1453A	35	2.067	0.013	0.1603	0.0007	0.236	2496	6	2544	13	2458	7	3
HAU-16-1453A	25	2.231	0.011	0.1609	0.0007	0.146	2429	6	2387	10	2464	7	-3
HAU-16-1453A	38	2.187	0.011	0.1611	0.0007	0.339	2449	5	2427	11	2466	7	-2
HAU-16-1453A	36	2.150	0.011	0.1621	0.0008	0.292	2470	6	2462	11	2477	8	-1
HAU-16-1453A	10	2.089	0.012	0.1625	0.0010	0.291	2499	6	2522	12	2481	10	2

Sample	Spot	$^{238}\text{U}/^{206}\text{Pb}$	$\sigma$	$^{207}\text{Pb}/^{206}\text{Pb}$	$\sigma$	rho	$^{207}\text{Pb}/^{235}\text{U}$ Date	$\sigma$	$^{206}\text{Pb}/^{238}\text{U}$ Date	$\sigma$	$^{207}\text{Pb}/^{206}\text{Pb}$ Date	$\sigma$	Disc. %
HAU-16-1453A	4	2.106	0.012	0.1627	0.0007	0.407	2493	5	2505	11	2483	7	1
HAU-16-1453A	40	2.120	0.011	0.1632	0.0008	0.356	2490	5	2491	11	2488	8	0
HAU-16-1453A	30	2.064	0.013	0.1635	0.0007	0.268	2516	6	2547	14	2491	7	2
HAU-16-1453A	31	2.188	0.010	0.1636	0.0007	0.429	2463	4	2426	10	2492	7	-3
HAU-16-1453A	37	2.193	0.010	0.1639	0.0007	0.373	2462	5	2422	9	2496	7	-3
HAU-16-1453A	28	2.073	0.012	0.1640	0.0008	0.387	2515	5	2538	12	2497	8	2
HAU-16-1453A	41	2.089	0.016	0.1646	0.0008	0.536	2511	6	2522	16	2503	8	1
HAU-16-1453A	29	2.088	0.013	0.1660	0.0008	0.350	2519	6	2523	13	2517	8	0
HAU-16-1453A	46	2.108	0.012	0.1676	0.0007	0.302	2520	6	2503	12	2533	7	-1
HAU-16-1453A	20	2.061	0.011	0.1691	0.0007	0.404	2549	5	2550	12	2548	6	0
HAU-16-1453A	11	2.067	0.013	0.1692	0.0007	0.062	2547	7	2544	13	2549	7	0
HAU-16-1453A	26	2.079	0.011	0.1698	0.0006	0.452	2545	5	2532	11	2555	6	-1
ED-C-1	23	4.838	0.129	0.1063	0.0010	0.033	1415	21	1211	29	1736	17	-30
ED-C-1	14	5.356	0.075	0.1095	0.0016	-0.252	1360	17	1103	14	1790	27	-38
ED-C-1	21	5.252	0.066	0.1108	0.0010	0.101	1384	11	1124	13	1812	16	-38
ED-C-1	16	4.299	0.163	0.1144	0.0015	0.040	1564	32	1348	46	1870	24	-28
ED-C-1	18	5.319	0.311	0.1182	0.0012	-0.356	1423	48	1111	60	1928	18	-42
ED-C-1	20	3.818	0.069	0.1182	0.0011	0.142	1687	16	1500	24	1928	17	-22
ED-C-1	22	3.096	0.046	0.1199	0.0012	0.375	1875	12	1804	23	1954	18	-8
ED-C-1	12	2.964	0.052	0.1200	0.0011	0.301	1913	15	1874	28	1955	16	-4
ED-C-1	13	3.135	0.064	0.1215	0.0010	0.296	1876	17	1785	32	1978	15	-10
ED-C-1	19	3.805	0.058	0.1224	0.0019	0.409	1719	14	1504	20	1991	28	-24
ED-C-1	17	3.028	0.038	0.1464	0.0040	0.642	2068	19	1840	20	2304	47	-20
ED-C-1	15	7.570	0.120	0.2561	0.0018	0.383	1761	12	800	12	3222	11	-75

## A.5 EPMA monazite data

**Appendix 6. EPMA monazite dating results of southern Devon Island samples. c: core; r: rim; ir: inner rim; or: outer rim; n: no obvious domain morphology. b.d., below detection.**

Spot	Note	Date	2σ	ThO <sub>2</sub>	UO <sub>2</sub>	PbO	Y <sub>2</sub> O <sub>3</sub>	SiO <sub>2</sub>	P <sub>2</sub> O <sub>5</sub>	SO <sub>3</sub>	CaO	La <sub>2</sub> O <sub>3</sub>	Ce <sub>2</sub> O <sub>3</sub>	Pr <sub>2</sub> O <sub>3</sub>	Nd <sub>2</sub> O <sub>3</sub>	Sm <sub>2</sub> O <sub>3</sub>	Gd <sub>2</sub> O <sub>3</sub>	Tb <sub>2</sub> O <sub>3</sub>	Dy <sub>2</sub> O <sub>3</sub>	Ho <sub>2</sub> O <sub>3</sub>	Er <sub>2</sub> O <sub>3</sub>	Tm <sub>2</sub> O <sub>3</sub>	Yb <sub>2</sub> O <sub>3</sub>	Lu <sub>2</sub> O <sub>3</sub>	F		
<b>3245 - biotite diorite (coordinates: 74.487006, -81.692003)</b>																											
9.6	n	1253	22	9.06	0.09	0.51	0.10	1.69	26.17	1.05	1.97	11.36	28.79	3.39	13.33	1.65	0.63	0.02	b.d.	b.d.	b.d.	0.03	0.05	0.01	0.80		
10.2	n	1296	23	8.77	0.06	0.50	0.02	1.48	26.46	1.06	1.52	12.88	30.32	3.32	12.31	1.11	0.39	b.d.	b.d.	b.d.	0.03	b.d.	0.01	b.d.	0.82		
9.2	r	1585	28	6.10	0.33	0.51	0.22	0.55	28.00	0.85	1.58	12.21	30.35	3.53	13.81	1.99	0.71	0.04	0.02	b.d.	b.d.	b.d.	0.05	0.02	0.77		
10.5	n	1686	34	5.09	0.20	0.43	0.34	0.31	28.41	1.07	1.54	12.33	30.36	3.50	13.72	1.95	0.87	0.06	0.05	0.02	0.01	0.00	0.07	0.04	0.81		
10.4	n	1708	38	4.58	0.16	0.39	0.36	0.37	28.41	1.15	1.43	13.80	30.28	3.41	13.68	1.90	0.96	0.04	0.06	b.d.	b.d.	0.03	0.07	b.d.	0.78		
10.6	n	1728	47	3.40	0.16	0.30	0.10	0.07	28.59	0.41	0.87	13.90	32.40	3.60	14.47	2.08	0.76	0.01	b.d.	0.05	b.d.	0.03	b.d.	0.03	0.76		
10.7	n	1738	49	3.29	0.15	0.29	0.04	0.07	28.91	0.37	0.82	13.55	32.17	3.66	14.74	2.12	0.69	0.00	b.d.	b.d.	b.d.	0.00	0.06	b.d.	0.77		
8.8	or	1741	42	3.89	0.19	0.35	0.33	0.27	28.18	1.14	1.46	13.71	30.36	3.49	13.54	1.88	0.81	0.04	0.07	b.d.	0.03	0.02	0.09	b.d.	0.78		
9.8	r	1751	34	5.32	0.19	0.46	0.29	0.32	29.20	0.83	1.54	12.52	30.66	3.48	14.07	2.13	0.87	0.04	0.03	0.05	b.d.	b.d.	0.00	b.d.	0.85		
9.7	n	1764	24	8.95	0.10	0.72	0.11	1.33	26.56	1.43	1.86	11.68	28.41	3.43	13.43	1.75	0.59	0.03	b.d.	b.d.	b.d.	b.d.	0.06	0.01	0.78		
1.13	or	1767	24	8.44	0.21	0.72	0.36	0.95	27.68	1.00	1.88	12.32	27.85	3.32	12.74	1.94	0.94	0.03	0.06	0.05	0.01	0.01	0.01	0.02	0.74		
5.9	or	1772	30	6.10	0.18	0.53	0.22	0.43	27.85	0.72	1.44	12.15	29.51	3.42	13.84	1.84	0.96	0.03	0.01	0.00	0.01	0.02	0.01	0.04	0.72		
10.1	n	1773	32	5.78	0.20	0.51	0.32	0.31	28.37	0.80	1.51	12.55	29.82	3.38	13.73	1.82	0.95	0.05	0.04	0.04	b.d.	0.05	0.04	0.04	0.76		
3.2	or	1789	31	5.94	0.21	0.53	0.36	0.37	28.11	0.98	1.63	12.43	28.52	3.43	13.53	1.95	1.10	0.05	0.03	0.06	b.d.	0.04	0.08	0.01	0.80		
2.7	r	1796	32	5.80	0.18	0.51	0.33	0.40	28.43	0.95	1.55	12.02	30.28	3.47	13.64	1.99	0.78	0.02	0.01	0.01	0.01	0.04	b.d.	0.01	0.76		
8.3	or	1797	34	5.16	0.18	0.46	0.34	0.31	28.83	0.92	1.52	12.67	30.83	3.58	13.88	1.95	0.70	0.05	0.06	0.07	b.d.	0.01	0.06	0.01	0.75		
4.4	or	1799	29	6.36	0.18	0.56	0.34	0.40	28.05	0.79	1.56	11.99	29.14	3.44	13.74	2.03	1.02	0.04	0.08	0.01	0.01	b.d.	0.05	0.00	0.77		
5.5	or	1802	29	6.47	0.18	0.56	0.36	0.36	27.85	0.84	1.65	12.14	29.15	3.40	13.71	1.89	1.17	0.01	0.06	b.d.	b.d.	0.04	0.05	b.d.	0.73		
5.2	or	1807	27	7.34	0.16	0.63	0.31	0.62	27.84	0.97	1.73	11.77	29.16	3.46	13.39	1.84	0.94	0.02	0.02	0.00	0.01	b.d.	0.03	0.00	0.81		
12.4	c	1812	43	3.80	0.20	0.36	0.35	0.17	28.86	0.99	1.46	13.25	31.06	3.56	13.90	2.04	0.95	0.04	0.09	0.04	b.d.	b.d.	0.04	0.03	0.79		
4.2	or	1812	30	6.14	0.21	0.55	0.34	0.43	28.01	1.13	1.75	12.58	29.01	3.38	13.61	1.84	0.95	0.06	0.03	b.d.	b.d.	0.03	0.04	0.03	0.75		
5.1	or	1815	30	6.11	0.19	0.54	0.24	0.43	27.54	0.64	1.41	12.51	29.36	3.43	13.83	2.00	0.92	0.05	0.04	b.d.	b.d.	b.d.	0.04	0.02	0.77		
3.1	or	1819	31	5.85	0.20	0.53	0.37	0.33	28.65	0.99	1.71	11.84	29.90	3.45	13.74	1.89	0.69	0.03	0.05	0.03	0.01	0.03	0.08	b.d.	0.75		
8.7	ir	1820	28	7.11	0.08	0.59	0.03	1.12	27.46	0.31	0.73	12.60	30.80	3.66	14.55	1.76	0.47	0.00	b.d.	b.d.	b.d.	b.d.	b.d.	b.d.	0.74		
2.1	r	1821	30	6.31	0.19	0.56	0.30	0.50	28.11	0.94	1.63	12.34	29.73	3.43	13.90	1.99	0.77	0.04	0.04	b.d.	b.d.	b.d.	0.01	0.00	0.74		
8.1	or	1823	35	5.23	0.17	0.47	0.29	0.33	28.23	0.96	1.50	12.82	29.84	3.49	13.85	1.85	0.78	0.02	0.00	b.d.	0.00	0.02	0.05	0.02	0.73		
8.2	or	1823	46	3.50	0.18	0.33	0.35	0.18	28.12	1.18	1.45	14.02	30.76	3.44	13.79	1.91	1.04	0.05	0.07	0.05	b.d.	0.02	0.04	b.d.	0.72		

Spot	Note	Date	2 $\sigma$	ThO <sub>2</sub>	UO <sub>2</sub>	PbO	Y <sub>2</sub> O <sub>3</sub>	SiO <sub>2</sub>	P <sub>2</sub> O <sub>5</sub>	SO <sub>3</sub>	CaO	La <sub>2</sub> O <sub>3</sub>	Ce <sub>2</sub> O <sub>3</sub>	Pr <sub>2</sub> O <sub>3</sub>	Nd <sub>2</sub> O <sub>3</sub>	Sm <sub>2</sub> O <sub>3</sub>	Gd <sub>2</sub> O <sub>3</sub>	Tb <sub>2</sub> O <sub>3</sub>	Dy <sub>2</sub> O <sub>3</sub>	Ho <sub>2</sub> O <sub>3</sub>	Er <sub>2</sub> O <sub>3</sub>	Tm <sub>2</sub> O <sub>3</sub>	Yb <sub>2</sub> O <sub>3</sub>	Lu <sub>2</sub> O <sub>3</sub>	F
15.2	r	1826	32	5.63	0.21	0.51	0.34	0.45	28.16	1.13	1.72	12.98	29.32	3.38	13.31	2.02	1.02	0.01	0.05	0.06	b.d.	b.d.	0.03	0.04	0.76
13.1	r	1830	30	6.27	0.19	0.56	0.31	0.50	28.49	0.90	1.67	12.20	28.84	3.46	13.65	1.86	0.82	b.d.	0.03	b.d.	b.d.	b.d.	0.05	0.03	0.75
3.5	or	1831	31	5.95	0.19	0.54	0.36	0.33	27.67	0.79	1.55	13.04	28.71	3.40	13.93	2.02	1.07	0.04	0.06	0.02	0.00	0.01	0.05	0.00	0.70
14.9	r	1833	32	5.83	0.20	0.53	0.38	0.32	28.37	0.75	1.54	12.32	29.89	3.49	13.68	1.92	0.85	0.00	0.06	b.d.	b.d.	0.02	0.02	b.d.	0.70
4.7	or	1833	30	6.15	0.19	0.55	0.35	0.33	27.30	0.84	1.62	11.92	29.18	3.46	13.76	1.94	0.92	0.03	0.05	0.05	0.00	0.04	0.07	0.03	0.77
14.3	r	1834	30	6.22	0.19	0.56	0.26	0.46	28.47	0.83	1.57	12.74	29.81	3.50	13.99	1.95	0.71	0.05	0.03	0.00	b.d.	b.d.	0.06	0.00	0.75
15.3	r	1836	31	6.00	0.20	0.54	0.25	0.44	28.19	0.80	1.49	12.01	29.44	3.52	13.78	2.05	0.93	0.02	0.03	b.d.	0.01	b.d.	0.02	b.d.	0.77
11.4	ir	1838	25	8.52	0.07	0.71	0.04	1.18	26.56	1.20	1.66	12.16	29.63	3.37	12.86	1.19	0.42	0.00	b.d.	b.d.	0.00	b.d.	0.04	b.d.	0.74
15.1	r	1838	32	5.74	0.22	0.53	0.33	0.37	28.54	1.09	1.77	13.04	28.93	3.41	13.56	1.85	0.92	0.02	0.03	0.00	b.d.	b.d.	0.01	0.02	0.80
9.1	r	1839	32	5.87	0.17	0.53	0.21	0.48	28.29	0.90	1.55	12.79	30.45	3.44	13.81	1.86	0.77	0.00	b.d.	0.08	b.d.	b.d.	0.06	0.00	0.75
14.5	r	1842	31	5.99	0.18	0.54	0.33	0.40	28.07	0.98	1.64	12.14	29.63	3.42	13.54	1.89	0.80	0.06	0.06	0.00	b.d.	b.d.	0.07	0.05	0.75
5.3	ir	1843	23	9.26	0.07	0.77	0.02	1.35	25.99	0.77	1.51	12.63	29.91	3.33	11.89	1.00	0.28	b.d.	b.d.	b.d.	b.d.	b.d.	0.05	b.d.	0.80
7.5	r	1843	35	4.93	0.19	0.46	0.33	0.42	28.03	1.21	1.65	12.14	29.85	3.38	13.56	1.97	0.86	0.04	0.04	0.04	b.d.	b.d.	0.04	0.01	0.73
9.9	r	1846	31	6.05	0.18	0.54	0.34	0.49	28.06	0.97	1.74	12.38	29.14	3.52	13.72	1.86	0.82	0.05	0.06	b.d.	0.02	0.02	0.08	0.04	0.77
3.10	or	1849	32	5.73	0.19	0.52	0.35	0.42	28.32	1.20	1.72	12.14	29.62	3.48	13.61	1.94	0.98	0.03	0.08	0.01	b.d.	b.d.	0.02	b.d.	0.76
8.4	ir	1853	34	5.68	0.06	0.48	0.02	0.87	27.54	0.38	0.71	12.85	30.85	3.63	14.76	1.57	0.54	0.02	b.d.	0.01	b.d.	0.01	0.02	b.d.	0.79
13.2	r	1856	31	5.91	0.21	0.55	0.35	0.27	28.85	0.97	1.76	12.44	29.05	3.42	13.75	1.91	0.81	0.05	0.07	b.d.	b.d.	0.02	0.04	0.01	0.71
6.2	ir	1857	43	4.27	0.06	0.37	0.06	0.54	27.63	0.34	0.59	11.52	31.44	3.87	15.78	2.30	0.82	b.d.	b.d.	0.04	b.d.	0.02	0.01	b.d.	0.70
13.3	r	1860	32	5.75	0.21	0.53	0.34	0.44	28.33	1.16	1.71	12.87	28.77	3.48	13.55	1.90	0.85	0.03	0.04	0.07	b.d.	0.00	0.03	0.00	0.70
15.6	c	1862	27	7.64	0.08	0.65	0.12	1.03	26.75	0.10	0.79	12.03	29.20	3.49	14.29	1.89	0.83	0.01	b.d.	0.06	b.d.	b.d.	0.08	0.04	0.81
15.5	c	1862	28	7.45	0.10	0.64	0.11	1.07	27.23	0.14	0.74	11.83	29.78	3.60	14.26	1.82	0.70	0.03	b.d.	b.d.	0.00	0.00	0.02	0.03	0.76
6.7	or	1863	34	5.24	0.20	0.49	0.35	0.38	27.91	1.15	1.62	12.83	29.57	3.55	13.46	1.87	1.05	0.04	0.07	0.06	b.d.	0.01	0.04	b.d.	0.69
2.4	c	1864	20	11.53	0.12	0.98	0.06	2.19	25.60	0.33	0.85	11.42	27.39	3.25	13.07	1.58	0.61	0.00	b.d.	b.d.	b.d.	0.03	0.05	0.00	0.71
11.11	or	1864	29	6.77	0.20	0.62	0.34	0.65	28.00	1.08	1.70	12.50	29.24	3.33	13.19	1.83	0.86	0.01	0.01	0.02	0.02	b.d.	0.06	b.d.	0.74
6.4	ir	1867	40	4.61	0.07	0.40	0.08	0.60	27.89	0.34	0.60	12.23	31.16	3.77	15.72	2.12	0.93	0.01	b.d.	0.03	b.d.	b.d.	0.01	b.d.	0.75
14.1	r	1870	32	5.70	0.20	0.53	0.34	0.43	28.50	1.12	1.70	12.52	30.00	3.50	13.43	2.06	0.75	0.07	0.05	b.d.	0.02	0.01	0.01	b.d.	0.73
2.8	r	1871	33	5.53	0.20	0.52	0.33	0.44	28.42	1.19	1.67	12.63	29.38	3.33	13.41	1.79	1.15	0.02	0.08	0.03	b.d.	0.01	0.02	b.d.	0.74
11.1	ir	1874	23	9.75	0.08	0.83	0.02	1.82	25.72	1.72	1.48	11.74	28.06	3.37	13.52	1.54	0.34	0.03	b.d.	0.05	b.d.	b.d.	0.05	0.02	0.73
4.5	ir	1876	21	10.54	0.09	0.90	0.01	1.84	25.82	0.79	1.23	12.22	29.13	3.27	12.24	1.15	0.37	0.02	b.d.	b.d.	b.d.	0.02	0.05	0.01	0.73
1.12	c	1878	29	6.98	0.06	0.60	0.05	1.01	27.98	0.23	0.74	11.92	30.33	3.57	14.91	1.78	0.72	0.02	b.d.	0.05	b.d.	b.d.	0.03	0.02	0.78
1.3	or	1879	24	8.10	0.26	0.75	0.32	0.90	28.25	0.51	1.79	11.31	28.44	3.27	13.64	1.83	0.72	0.09	0.06	0.02	b.d.	0.01	0.05	0.03	0.81
10.3	n	1882	20	11.21	0.09	0.96	0.05	2.37	25.06	0.74	0.95	12.13	27.58	3.26	12.73	1.39	0.37	0.02	b.d.	b.d.	b.d.	b.d.	0.05	b.d.	0.78



Spot	Note	Date	2 $\sigma$	ThO <sub>2</sub>	UO <sub>2</sub>	PbO	Y <sub>2</sub> O <sub>3</sub>	SiO <sub>2</sub>	P <sub>2</sub> O <sub>5</sub>	SO <sub>3</sub>	CaO	La <sub>2</sub> O <sub>3</sub>	Ce <sub>2</sub> O <sub>3</sub>	Pr <sub>2</sub> O <sub>3</sub>	Nd <sub>2</sub> O <sub>3</sub>	Sm <sub>2</sub> O <sub>3</sub>	Gd <sub>2</sub> O <sub>3</sub>	Tb <sub>2</sub> O <sub>3</sub>	Dy <sub>2</sub> O <sub>3</sub>	Ho <sub>2</sub> O <sub>3</sub>	Er <sub>2</sub> O <sub>3</sub>	Tm <sub>2</sub> O <sub>3</sub>	Yb <sub>2</sub> O <sub>3</sub>	Lu <sub>2</sub> O <sub>3</sub>	F
3.4	ir	1884	16	15.80	0.14	1.35	0.02	3.40	23.50	0.59	0.97	11.53	25.38	2.92	11.66	1.39	0.70	0.01	b.d.	b.d.	b.d.	0.02	0.03	b.d.	0.69
5.4	ir	1886	24	8.89	0.08	0.76	0.02	1.29	26.40	0.87	1.41	12.61	29.87	3.34	12.12	0.93	0.34	b.d.	b.d.	b.d.	b.d.	0.02	0.12	b.d.	0.77
6.9	ir	1887	31	6.33	0.07	0.55	0.07	1.02	27.95	0.44	0.71	12.20	31.11	3.64	15.13	1.97	0.65	b.d.	b.d.	0.01	b.d.	b.d.	0.06	0.01	0.70
7.4	r	1888	38	4.16	0.28	0.43	0.40	0.36	28.41	1.23	1.49	13.81	30.05	3.37	13.26	1.98	1.28	0.05	0.10	b.d.	0.01	0.01	0.04	b.d.	0.67
6.1	ir	1889	33	5.91	0.07	0.51	0.08	0.95	26.81	0.46	0.66	12.14	29.68	3.68	15.06	2.01	0.91	0.01	b.d.	0.02	b.d.	0.01	0.03	0.01	0.72
3.9	ir	1890	14	18.50	0.16	1.59	0.02	4.04	22.43	0.51	0.91	11.12	25.57	2.71	10.93	1.25	0.62	b.d.	b.d.	b.d.	b.d.	0.02	0.03	0.03	0.63
15.4	c	1892	30	6.56	0.07	0.57	0.09	1.04	27.34	0.46	0.73	12.43	30.30	3.41	14.06	1.84	0.76	0.00	b.d.	0.01	b.d.	0.02	0.02	b.d.	0.72
7.2	r	1892	35	5.03	0.19	0.48	0.34	0.40	28.28	1.24	1.61	12.52	30.36	3.43	13.60	1.97	0.97	0.07	0.06	0.06	0.02	b.d.	0.06	b.d.	0.75
6.8	ir	1892	37	5.09	0.07	0.45	0.09	0.70	27.88	0.33	0.62	11.61	31.02	3.78	15.87	2.24	0.93	0.00	b.d.	0.02	b.d.	0.02	0.01	b.d.	0.69
3.3	ir	1894	19	12.33	0.12	1.07	0.07	2.23	25.38	0.31	0.84	12.07	26.54	3.13	13.10	1.74	0.64	0.02	b.d.	b.d.	0.00	b.d.	0.04	0.02	0.72
1.9	ir	1896	23	9.47	0.09	0.82	0.01	1.63	26.17	1.56	1.90	12.57	28.70	3.28	12.66	1.29	0.45	0.02	b.d.	b.d.	0.01	b.d.	0.04	b.d.	0.80
2.5	c	1896	31	6.27	0.08	0.55	0.08	0.86	27.60	0.25	0.69	11.88	30.12	3.76	14.89	2.06	0.76	0.04	b.d.	0.02	b.d.	0.04	0.04	0.00	0.71
7.6	c	1898	36	5.31	0.07	0.47	0.05	0.82	27.38	0.45	0.66	12.04	31.20	3.68	15.17	2.01	0.63	b.d.	b.d.	b.d.	b.d.	b.d.	0.03	b.d.	0.71
2.6	c	1898	34	5.60	0.06	0.49	0.08	0.76	28.09	0.29	0.67	12.05	31.33	3.84	15.21	2.11	0.47	0.02	b.d.	0.01	b.d.	b.d.	0.04	0.04	0.73
5.7	ir	1901	32	6.13	0.07	0.53	0.07	0.94	26.50	0.37	0.70	12.73	29.66	3.70	15.04	1.95	0.88	0.00	b.d.	b.d.	b.d.	0.05	0.05	0.00	0.75
1.1	c	1904	48	3.54	0.10	0.33	0.53	0.38	28.01	1.46	1.46	11.71	29.79	3.56	14.70	2.04	1.09	0.04	0.13	0.03	b.d.	b.d.	0.02	0.05	0.69
7.3	c	1904	37	5.05	0.07	0.45	0.07	0.74	28.06	0.31	0.58	11.79	32.45	3.71	14.85	1.79	0.85	b.d.	b.d.	b.d.	b.d.	b.d.	0.02	0.04	0.76
12.1	c	1906	59	2.60	0.15	0.27	0.39	0.02	29.23	1.54	1.65	14.01	31.31	3.49	13.33	2.03	0.89	0.05	0.08	0.02	b.d.	0.02	0.01	0.02	0.74
14.6	c	1907	29	6.97	0.08	0.61	0.06	1.21	26.86	0.37	0.80	11.38	30.14	3.62	14.29	1.90	0.69	0.00	b.d.	0.03	b.d.	0.01	0.03	b.d.	0.74
13.5	c	1908	36	5.31	0.07	0.47	0.08	0.80	27.91	0.33	0.67	12.75	31.24	3.75	14.55	1.91	0.76	0.02	b.d.	b.d.	b.d.	b.d.	0.03	0.02	0.76
2.2	c	1909	24	8.82	0.10	0.77	0.06	1.52	26.76	0.33	0.78	12.02	28.96	3.39	14.04	1.76	0.61	0.04	b.d.	b.d.	b.d.	0.02	b.d.	b.d.	0.74
1.2	c	1910	46	3.90	0.05	0.34	0.08	0.31	29.02	0.16	0.60	11.74	31.63	3.82	15.75	2.17	0.79	0.03	b.d.	b.d.	b.d.	0.04	0.08	0.03	0.75
7.1	c	1912	35	5.45	0.07	0.48	0.07	0.80	27.60	0.41	0.72	11.37	31.54	3.60	15.24	1.96	0.59	0.03	b.d.	b.d.	b.d.	0.03	0.03	0.01	0.77
14.7	c	1913	27	7.72	0.10	0.68	0.06	1.39	26.89	0.45	0.76	12.17	30.24	3.51	14.28	1.77	0.41	0.02	b.d.	b.d.	b.d.	b.d.	0.03	0.04	0.75
2.3	c	1915	17	13.93	0.13	1.22	0.05	2.81	24.68	0.35	0.84	11.67	26.74	3.07	12.29	1.55	0.57	b.d.	b.d.	b.d.	b.d.	b.d.	0.04	0.02	0.69
14.4	r	1915	34	5.33	0.20	0.51	0.37	0.42	28.21	1.20	1.67	12.98	29.64	3.38	13.25	2.06	0.88	0.06	0.05	b.d.	0.00	b.d.	0.06	b.d.	0.79
1.5	ir	1917	20	11.93	0.10	1.04	0.14	2.46	25.55	0.38	0.75	11.48	27.72	3.28	13.27	1.71	0.62	0.02	b.d.	0.03	b.d.	b.d.	0.01	0.01	0.75
11.10	ir	1918	25	8.50	0.08	0.74	0.02	1.56	25.92	2.14	2.24	11.87	29.16	3.35	12.65	1.16	0.47	0.00	b.d.	0.01	b.d.	0.02	0.07	b.d.	0.70
14.2	c	1925	31	6.50	0.08	0.58	0.07	1.08	27.53	0.40	0.78	11.83	31.45	3.69	14.58	1.77	0.58	0.03	b.d.	b.d.	b.d.	0.01	0.01	b.d.	0.77
1.11	ir	1927	16	15.82	0.11	1.38	0.13	3.38	23.94	0.32	0.72	10.71	25.51	2.97	12.06	1.53	0.69	0.02	b.d.	0.03	b.d.	b.d.	0.04	b.d.	0.69
12.3	c	1927	46	3.50	0.19	0.36	0.35	0.15	29.20	1.18	1.46	13.19	31.06	3.54	13.75	1.93	0.95	0.02	0.05	0.04	b.d.	0.02	0.04	0.05	0.78
13.6	c	1928	31	6.37	0.08	0.57	0.08	1.06	27.40	0.38	0.69	12.19	30.52	3.65	14.63	1.79	0.62	b.d.	b.d.	0.06	b.d.	0.03	0.05	0.02	0.77
11.9	ir	1930	24	9.13	0.09	0.80	0.03	1.74	25.84	1.66	1.74	11.51	28.66	3.39	13.77	1.75	0.60	b.d.	b.d.	0.01	b.d.	b.d.	0.02	b.d.	0.71

Spot	Note	Date	2 $\sigma$	ThO <sub>2</sub>	UO <sub>2</sub>	PbO	Y <sub>2</sub> O <sub>3</sub>	SiO <sub>2</sub>	P <sub>2</sub> O <sub>5</sub>	SO <sub>3</sub>	CaO	La <sub>2</sub> O <sub>3</sub>	Ce <sub>2</sub> O <sub>3</sub>	Pr <sub>2</sub> O <sub>3</sub>	Nd <sub>2</sub> O <sub>3</sub>	Sm <sub>2</sub> O <sub>3</sub>	Gd <sub>2</sub> O <sub>3</sub>	Tb <sub>2</sub> O <sub>3</sub>	Dy <sub>2</sub> O <sub>3</sub>	Ho <sub>2</sub> O <sub>3</sub>	Er <sub>2</sub> O <sub>3</sub>	Tm <sub>2</sub> O <sub>3</sub>	Yb <sub>2</sub> O <sub>3</sub>	Lu <sub>2</sub> O <sub>3</sub>	F
14.8	c	1933	30	6.86	0.07	0.61	0.07	1.13	27.06	0.37	0.68	11.79	30.16	3.57	14.60	1.86	0.78	0.02	b.d.	b.d.	b.d.	b.d.	0.03	0.04	0.74
4.9	ir	1936	23	9.23	0.08	0.81	0.05	1.57	26.10	0.41	0.94	12.26	29.79	3.37	13.31	1.41	0.52	0.02	b.d.	0.03	b.d.	b.d.	b.d.	b.d.	0.77
12.2	c	1944	68	2.30	0.11	0.23	0.37	0.11	29.36	1.45	1.44	13.60	32.50	3.63	13.59	2.07	1.07	0.04	0.06	b.d.	b.d.	0.02	0.02	0.01	0.74
1.4	ir	1946	23	9.79	0.08	0.87	0.12	1.86	26.15	1.22	1.45	11.37	27.97	3.47	13.61	1.79	0.60	0.03	b.d.	b.d.	b.d.	0.00	b.d.	0.02	0.74
13.4	c	1960	32	6.20	0.06	0.56	0.08	1.01	27.19	0.36	0.68	12.13	31.00	3.67	14.74	1.83	0.69	0.02	b.d.	b.d.	b.d.	0.02	0.04	0.01	0.75
5.6	c	2041	29	6.93	0.09	0.66	0.22	0.85	26.60	0.77	1.21	11.78	29.47	3.44	13.87	2.07	0.93	0.07	0.02	b.d.	0.01	b.d.	0.01	b.d.	0.76
5.8	c	2045	31	6.60	0.09	0.63	0.21	0.75	27.63	0.70	1.18	12.80	29.46	3.43	13.91	1.80	1.05	0.05	0.02	b.d.	0.00	0.02	b.d.	0.01	0.79
11.5	c	2050	30	6.96	0.08	0.66	0.20	0.66	28.07	0.65	1.36	12.59	29.19	3.39	13.63	1.62	0.80	0.06	0.03	0.03	b.d.	b.d.	0.01	0.01	0.70
4.3	c	2088	28	7.44	0.10	0.72	0.20	0.96	26.92	0.66	1.18	12.32	29.46	3.51	13.89	1.90	0.90	0.06	0.03	b.d.	b.d.	0.01	0.03	0.04	0.75
8.5	c	2126	28	7.70	0.07	0.75	0.20	1.09	27.56	0.57	1.11	13.21	30.08	3.42	13.19	1.57	0.64	0.01	0.01	b.d.	b.d.	0.03	0.07	0.03	0.73
3.7	c	2128	28	7.59	0.10	0.75	0.22	1.06	27.32	0.89	1.37	12.17	29.11	3.37	13.56	1.92	1.03	0.04	0.03	0.06	b.d.	0.00	0.05	b.d.	0.76
6.3	c	2129	25	8.75	0.11	0.86	0.22	1.39	26.35	0.79	1.24	11.82	28.80	3.40	13.51	1.98	0.77	0.03	0.04	0.04	b.d.	b.d.	0.07	b.d.	0.70
4.8	c	2148	28	7.42	0.10	0.74	0.23	0.90	26.88	0.68	1.27	11.81	29.91	3.42	13.83	2.09	0.84	0.00	0.05	b.d.	b.d.	b.d.	0.01	0.02	0.78
8.6	c	2151	29	7.40	0.10	0.74	0.18	1.06	26.95	0.73	1.17	12.36	29.24	3.48	13.56	1.91	0.88	0.04	b.d.	0.03	b.d.	b.d.	0.06	b.d.	0.69
3.8	c	2153	29	7.35	0.10	0.74	0.18	1.05	27.16	0.89	1.27	12.01	29.17	3.34	13.94	2.06	0.86	0.05	0.04	b.d.	0.03	b.d.	0.02	b.d.	0.74
11.8	ir	2159	19	12.86	0.10	1.27	0.18	2.05	25.74	0.99	1.80	10.19	25.69	3.19	13.02	1.71	0.90	b.d.	b.d.	0.00	b.d.	0.00	0.05	0.01	0.75
3.6	c	2159	29	7.11	0.10	0.72	0.21	1.02	27.22	0.91	1.27	12.53	29.53	3.59	13.70	1.95	1.01	0.01	0.06	b.d.	b.d.	0.01	0.04	b.d.	0.79
11.7	c	2164	30	7.14	0.10	0.72	0.19	0.86	27.85	0.94	1.48	11.93	29.38	3.43	13.79	1.81	0.74	0.06	0.03	b.d.	b.d.	0.01	0.05	b.d.	0.76
6.6	c	2175	26	8.54	0.10	0.86	0.21	1.30	26.56	0.78	1.28	12.06	29.02	3.41	13.29	2.07	0.84	0.04	0.02	0.02	b.d.	b.d.	0.01	0.00	0.66
6.10	ir	2182	22	10.90	0.07	1.08	0.11	1.92	25.85	0.67	1.16	11.69	28.35	3.28	13.51	1.79	0.82	0.03	b.d.	b.d.	b.d.	b.d.	0.04	b.d.	0.67
11.2	ir	2192	20	12.79	0.11	1.29	0.15	1.85	26.18	0.66	1.68	9.78	26.07	3.25	13.35	1.64	0.68	0.02	b.d.	b.d.	b.d.	b.d.	0.06	b.d.	0.68
4.1	ir	2200	22	10.69	0.09	1.08	0.18	1.54	26.50	0.65	1.52	10.54	27.30	3.37	13.64	1.89	0.86	0.01	0.00	b.d.	b.d.	b.d.	0.05	b.d.	0.71
11.6	c	2205	31	6.63	0.09	0.68	0.23	0.81	27.84	0.84	1.38	11.70	29.10	3.50	14.29	1.99	0.82	0.02	0.05	b.d.	0.03	b.d.	0.05	0.01	0.76
11.3	c	2206	31	6.67	0.09	0.69	0.21	0.73	27.99	0.85	1.39	12.20	29.82	3.45	13.68	1.92	0.81	0.01	0.01	0.03	b.d.	0.04	0.06	0.04	0.71
6.5	c	2213	27	8.20	0.11	0.85	0.23	1.19	26.46	0.75	1.27	11.55	28.46	3.44	13.86	2.14	1.00	0.04	0.02	b.d.	b.d.	0.01	0.03	0.02	0.69
4.6	c	2265	29	7.25	0.10	0.77	0.25	0.97	26.59	0.81	1.31	11.62	29.38	3.41	13.99	2.10	1.04	0.05	0.05	b.d.	b.d.	b.d.	b.d.	0.01	0.73
9.4	c	2294	32	6.70	0.09	0.72	0.24	0.75	27.73	0.76	1.32	11.39	29.55	3.59	14.22	2.01	0.72	0.08	0.02	0.00	b.d.	0.07	0.02	0.04	0.75
1.6	c	2294	29	7.31	0.11	0.79	0.23	0.70	28.32	0.62	1.37	11.96	28.88	3.49	13.90	2.07	0.84	0.04	0.07	0.02	b.d.	b.d.	0.04	b.d.	0.75
9.5	c	2299	31	6.88	0.08	0.74	0.23	0.82	27.75	0.86	1.32	11.70	30.02	3.48	13.99	2.00	1.04	0.02	0.05	0.07	0.00	b.d.	0.06	0.01	0.77
1.8	c	2314	29	7.54	0.10	0.82	0.25	0.70	28.14	0.64	1.43	11.98	29.31	3.44	13.90	2.03	0.99	0.04	0.03	0.01	b.d.	0.03	b.d.	0.01	0.78
1.10	c	2329	30	7.09	0.09	0.77	0.24	0.90	27.66	0.75	1.28	12.16	29.58	3.44	14.02	1.96	0.92	b.d.	0.02	b.d.	0.01	0.02	0.03	b.d.	0.78
9.3	c	2424	31	6.87	0.10	0.79	0.26	0.53	28.21	0.58	1.36	11.41	28.63	3.37	14.07	2.18	1.15	0.05	0.05	0.02	b.d.	b.d.	0.03	0.00	0.71

Spot	Note	Date	2σ	ThO <sub>2</sub>	UO <sub>2</sub>	PbO	Y <sub>2</sub> O <sub>3</sub>	SiO <sub>2</sub>	P <sub>2</sub> O <sub>5</sub>	SO <sub>3</sub>	CaO	La <sub>2</sub> O <sub>3</sub>	Ce <sub>2</sub> O <sub>3</sub>	Pr <sub>2</sub> O <sub>3</sub>	Nd <sub>2</sub> O <sub>3</sub>	Sm <sub>2</sub> O <sub>3</sub>	Gd <sub>2</sub> O <sub>3</sub>	Tb <sub>2</sub> O <sub>3</sub>	Dy <sub>2</sub> O <sub>3</sub>	Ho <sub>2</sub> O <sub>3</sub>	Er <sub>2</sub> O <sub>3</sub>	Tm <sub>2</sub> O <sub>3</sub>	Yb <sub>2</sub> O <sub>3</sub>	Lu <sub>2</sub> O <sub>3</sub>	F		
<b>3248 - biotite syenogranite gneiss (coordinates: 74.488452, -82.027463)</b>																											
6.6	r	1493	18	11.97	0.13	0.81	0.27	2.83	25.31	0.80	1.28	12.34	27.66	3.03	11.67	1.69	0.84	0.00	0.08	0.05	b.d.	b.d.	0.09	b.d.	0.73		
2.1	c	1739	32	5.85	0.08	0.47	0.73	1.19	26.78	0.96	1.00	13.42	29.95	3.36	12.67	1.74	1.12	0.10	0.17	b.d.	0.03	0.04	0.06	0.03	0.80		
1.10	r	1803	28	7.07	0.08	0.58	0.06	1.45	26.55	1.06	1.08	13.79	31.12	3.38	12.36	1.39	0.77	b.d.	b.d.	0.01	b.d.	0.00	0.01	b.d.	0.78		
6.12	r	1847	30	6.72	0.08	0.57	0.69	0.99	28.30	0.26	0.71	12.68	30.20	3.50	13.47	2.18	1.15	0.10	0.17	b.d.	0.00	b.d.	0.03	0.02	0.76		
6.7	r	1852	18	13.10	0.14	1.11	0.28	2.98	24.51	1.18	1.21	12.14	26.89	2.95	11.52	1.52	0.88	0.01	0.06	b.d.	b.d.	0.04	0.09	0.02	0.63		
2.7	r	1868	26	7.98	0.11	0.69	0.27	1.52	26.73	1.07	1.14	12.59	29.41	3.34	12.80	1.67	1.01	0.07	0.06	b.d.	0.00	b.d.	0.02	b.d.	0.79		
7.7	r	1873	23	9.43	0.12	0.81	0.14	2.14	25.27	1.34	1.24	12.26	28.83	3.28	12.27	1.60	0.76	0.02	0.00	b.d.	b.d.	b.d.	0.01	b.d.	0.81		
2.6	r	1873	25	8.19	0.10	0.71	0.17	1.42	26.94	0.88	1.21	12.94	30.09	3.25	12.34	1.45	0.78	0.02	0.01	b.d.	b.d.	0.04	0.03	0.01	0.77		
2.9	r	1876	27	7.88	0.10	0.68	0.22	1.78	26.00	1.54	1.29	12.75	30.37	3.31	12.73	1.76	1.00	0.04	0.03	b.d.	b.d.	b.d.	0.05	b.d.	0.77		
6.4	r	1879	18	13.86	0.14	1.19	0.26	2.91	24.32	0.86	1.17	11.65	26.33	3.00	11.13	1.45	0.78	0.01	0.05	0.04	b.d.	0.02	0.02	b.d.	0.69		
2.10	r	1883	25	8.49	0.12	0.74	0.26	1.80	26.12	1.28	1.24	12.79	29.14	3.36	12.68	1.76	1.08	0.03	0.04	b.d.	b.d.	0.02	0.06	b.d.	0.79		
1.6	r	1883	30	6.56	0.10	0.57	0.42	1.32	27.01	0.78	0.80	13.67	30.41	3.41	12.68	1.75	1.08	0.03	0.13	0.06	b.d.	0.03	b.d.	0.00	0.76		
6.2	r	1883	43	4.32	0.06	0.38	0.52	0.95	27.60	1.31	1.01	12.39	30.74	3.66	14.20	2.18	1.25	0.08	0.14	0.01	0.00	b.d.	0.01	0.02	0.72		
4.8	r	1889	27	7.83	0.09	0.68	0.36	1.75	26.29	1.23	1.19	12.38	29.58	3.31	12.86	1.79	0.86	0.05	0.12	b.d.	b.d.	0.01	0.05	0.01	0.75		
4.7	r	1892	27	7.55	0.09	0.66	0.38	1.75	25.99	1.64	1.36	11.69	29.43	3.27	12.86	1.65	1.11	0.08	0.11	b.d.	b.d.	b.d.	0.07	0.01	0.77		
1.8	r	1893	29	6.97	0.09	0.61	0.69	1.46	26.77	0.73	0.69	14.17	30.50	3.28	11.83	1.61	0.99	0.03	0.15	0.04	b.d.	0.05	0.07	b.d.	0.72		
6.3	r	1896	32	6.11	0.10	0.54	0.52	1.37	26.63	1.37	1.13	12.12	29.90	3.44	13.50	2.06	1.12	0.05	0.12	0.05	0.00	b.d.	0.06	0.04	0.72		
5.4	r	1897	27	7.85	0.11	0.69	0.20	1.31	27.05	0.84	1.11	13.06	30.01	3.36	12.79	1.75	0.73	0.03	0.05	b.d.	0.00	b.d.	0.01	0.04	0.75		
3.5	r	1897	38	4.94	0.08	0.44	0.10	0.92	27.68	0.69	0.74	14.32	32.08	3.39	12.75	1.57	0.67	0.00	b.d.	0.07	0.00	0.01	0.00	0.02	0.78		
6.1	r	1898	30	6.77	0.11	0.60	0.55	1.44	26.70	0.97	0.83	12.16	29.22	3.52	13.62	1.89	1.02	0.08	0.15	0.03	0.01	0.05	b.d.	0.02	0.71		
2.8	r	1900	26	8.09	0.11	0.71	0.26	1.45	26.02	0.81	1.10	12.43	29.41	3.35	12.80	1.89	1.02	0.07	0.07	0.09	b.d.	b.d.	0.02	b.d.	0.77		
1.9	r	1900	29	6.94	0.08	0.60	0.06	1.56	25.96	1.39	1.14	13.51	30.72	3.39	12.41	1.66	0.62	0.04	b.d.	0.04	b.d.	b.d.	0.02	0.04	0.75		
5.7	r	1900	27	7.74	0.08	0.67	0.34	1.60	25.74	1.61	1.54	11.78	29.79	3.34	12.86	1.77	0.90	0.05	0.06	b.d.	0.00	b.d.	0.03	0.00	0.79		
4.6	r	1909	27	7.89	0.09	0.69	0.22	1.69	26.16	1.79	1.57	12.30	29.71	3.26	12.58	1.62	0.84	0.01	0.03	0.01	b.d.	0.03	0.03	b.d.	0.72		
6.13	r	1909	30	6.74	0.09	0.59	0.58	1.12	28.24	0.30	0.59	12.55	30.03	3.44	13.19	1.97	0.95	0.08	0.19	0.05	b.d.	0.02	0.09	0.02	0.72		
8.9	r	1912	32	6.21	0.10	0.56	0.30	1.35	27.02	1.18	1.10	12.91	30.37	3.58	13.34	1.93	0.94	0.07	0.09	b.d.	b.d.	b.d.	0.00	0.02	0.78		
1.7	r	1917	29	6.99	0.10	0.62	0.12	1.48	26.29	1.29	1.13	13.02	30.16	3.36	12.77	1.87	0.83	0.04	b.d.	0.03	b.d.	b.d.	0.10	0.00	0.78		
5.6	r	1920	25	8.68	0.09	0.76	0.14	2.01	25.33	2.08	1.74	12.64	29.51	3.27	12.10	1.61	0.79	0.03	0.01	b.d.	b.d.	b.d.	b.d.	0.01	0.68		
8.7	r	1921	27	7.82	0.07	0.68	0.23	1.55	26.31	1.50	1.50	13.06	30.18	3.29	12.37	1.67	0.69	0.01	0.04	0.00	b.d.	b.d.	0.03	0.03	0.74		
4.9	r	1923	27	7.64	0.11	0.68	0.51	1.48	25.99	1.33	1.36	12.02	29.32	3.44	12.96	1.93	0.95	0.03	0.14	0.01	b.d.	b.d.	0.07	0.03	0.72		
6.8	r	1923	42	4.34	0.08	0.39	0.57	1.03	27.56	1.40	1.05	12.25	30.39	3.63	14.06	2.28	1.19	0.07	0.18	0.02	0.01	0.06	0.03	b.d.	0.74		
8.2	r	1926	41	4.65	0.08	0.42	0.37	0.72	27.94	1.02	1.13	11.96	30.84	3.56	14.25	2.05	1.04	0.04	0.11	b.d.	0.04	0.03	0.08	0.02	0.77		

Spot	Note	Date	2 $\sigma$	ThO <sub>2</sub>	UO <sub>2</sub>	PbO	Y <sub>2</sub> O <sub>3</sub>	SiO <sub>2</sub>	P <sub>2</sub> O <sub>5</sub>	SO <sub>3</sub>	CaO	La <sub>2</sub> O <sub>3</sub>	Ce <sub>2</sub> O <sub>3</sub>	Pr <sub>2</sub> O <sub>3</sub>	Nd <sub>2</sub> O <sub>3</sub>	Sm <sub>2</sub> O <sub>3</sub>	Gd <sub>2</sub> O <sub>3</sub>	Tb <sub>2</sub> O <sub>3</sub>	Dy <sub>2</sub> O <sub>3</sub>	Ho <sub>2</sub> O <sub>3</sub>	Er <sub>2</sub> O <sub>3</sub>	Tm <sub>2</sub> O <sub>3</sub>	Yb <sub>2</sub> O <sub>3</sub>	Lu <sub>2</sub> O <sub>3</sub>	F
5.5	r	1926	30	6.72	0.09	0.60	0.48	1.31	27.05	1.06	1.11	11.73	28.78	3.54	14.13	2.39	1.21	0.06	0.19	0.01	b.d.	0.02	0.05	0.00	0.78
6.5	r	1928	23	9.91	0.09	0.87	0.17	2.16	25.42	1.46	1.43	13.08	28.61	3.23	11.78	1.45	0.54	0.07	0.04	0.03	b.d.	b.d.	0.06	b.d.	0.72
9.3	r	1934	28	7.63	0.10	0.68	0.24	1.52	26.60	1.14	1.18	12.57	29.81	3.51	12.75	1.82	0.81	0.04	0.05	b.d.	b.d.	b.d.	0.03	0.01	0.72
8.8	r	1936	26	8.33	0.08	0.74	0.20	2.11	25.12	2.16	1.67	12.73	29.49	3.30	12.28	1.58	0.79	0.04	0.04	b.d.	b.d.	0.03	b.d.	0.04	0.72
9.1	r	1939	25	8.58	0.10	0.77	0.14	1.80	25.63	1.56	1.62	12.79	29.37	3.15	11.94	1.48	0.59	0.01	0.01	b.d.	b.d.	b.d.	0.06	b.d.	0.77
3.7	r	1952	38	4.95	0.06	0.45	0.58	0.58	28.75	0.57	0.95	15.57	31.85	3.41	12.26	1.61	0.93	0.06	0.14	0.02	0.04	0.04	0.08	0.07	0.81
8.4	r	1956	31	6.72	0.08	0.61	0.26	1.20	27.32	0.60	0.80	12.52	30.20	3.43	13.42	1.91	0.89	0.04	0.05	0.03	0.00	0.03	0.02	b.d.	0.74
5.3	c	1965	27	7.62	0.09	0.69	0.37	1.52	26.01	1.53	1.48	12.40	30.07	3.33	12.85	1.73	0.98	0.02	0.10	0.01	0.01	0.01	0.03	b.d.	0.74
8.5	r	1965	28	7.65	0.09	0.69	0.44	1.60	26.20	1.62	1.55	11.67	28.92	3.30	12.91	2.01	0.98	0.03	0.11	b.d.	0.00	0.01	0.03	0.01	0.72
9.2	r	1975	22	10.49	0.12	0.95	0.42	2.21	25.66	0.51	0.67	10.97	28.35	3.50	13.31	1.89	0.89	0.05	0.11	0.05	b.d.	b.d.	0.05	0.00	0.74
9.5	c	1987	33	6.10	0.05	0.55	0.50	1.13	27.41	0.79	0.88	13.18	30.09	3.44	12.94	1.86	0.92	0.03	0.15	0.03	0.00	0.03	0.06	0.03	0.78
5.2	c	1995	32	6.24	0.08	0.58	0.63	1.00	27.44	0.80	1.01	13.24	29.75	3.43	12.76	1.98	1.00	0.09	0.19	0.00	0.01	0.03	b.d.	b.d.	0.76
2.3	c	2005	42	4.50	0.05	0.42	0.49	0.72	28.21	0.75	0.80	14.64	32.03	3.24	12.35	1.65	0.90	0.04	0.12	0.04	0.01	b.d.	0.02	b.d.	0.78
7.1	r	2015	29	7.27	0.09	0.68	0.56	1.54	26.45	0.87	0.83	11.61	29.62	3.43	13.68	1.96	0.97	0.09	0.16	0.00	b.d.	0.02	0.04	0.02	0.70
2.4	c	2016	44	4.20	0.05	0.39	0.45	0.90	27.52	1.01	0.79	15.14	31.49	3.33	12.40	1.65	0.91	0.02	0.12	0.01	b.d.	0.02	0.04	0.02	0.74
3.4	c	2019	44	4.21	0.05	0.39	0.41	0.47	28.57	0.72	0.93	15.45	32.18	3.22	11.72	1.31	0.72	0.03	0.06	0.00	0.02	0.02	0.10	0.03	0.79
8.6	c	2029	28	7.60	0.08	0.71	0.33	1.37	27.01	1.24	1.33	12.32	29.73	3.29	12.54	1.73	0.89	0.03	0.08	0.05	b.d.	b.d.	0.02	0.02	0.79
2.5	c	2035	33	5.95	0.06	0.55	0.68	1.07	27.41	0.81	0.84	13.12	30.61	3.25	12.79	1.91	1.12	0.05	0.16	0.04	0.04	b.d.	0.05	0.01	0.80
7.2	r	2048	22	10.85	0.12	1.02	0.43	2.58	24.36	0.87	0.83	10.73	27.71	3.39	13.55	1.91	0.92	0.03	0.11	b.d.	0.03	0.03	0.04	b.d.	0.74
7.3	c	2051	34	5.86	0.09	0.56	1.08	1.29	26.67	1.15	0.87	12.91	29.74	3.41	12.63	1.79	1.11	0.07	0.26	0.03	0.05	0.03	0.07	0.05	0.76
4.5	c	2067	34	5.81	0.06	0.55	0.68	1.00	27.42	1.06	1.08	12.76	31.05	3.33	12.61	1.75	0.94	0.06	0.17	0.03	0.00	0.02	0.00	0.01	0.75
9.6	c	2070	23	10.27	0.14	0.99	0.51	2.18	25.70	0.74	0.81	10.31	28.14	3.45	13.67	2.00	1.05	0.06	0.16	b.d.	b.d.	b.d.	0.03	0.02	0.74
5.1	c	2101	36	5.54	0.05	0.53	0.76	1.14	26.68	1.15	0.98	13.56	30.09	3.31	12.56	1.84	1.12	0.04	0.20	b.d.	0.02	0.03	0.06	b.d.	0.72
2.2	c	2108	38	5.03	0.06	0.49	0.75	0.93	27.39	1.06	0.97	14.18	30.75	3.27	12.36	1.72	1.01	0.09	0.22	0.02	b.d.	0.04	0.06	b.d.	0.78
9.4	c	2120	35	5.77	0.05	0.56	0.62	1.23	27.00	1.02	0.84	13.08	30.53	3.43	12.93	1.85	0.98	0.04	0.18	0.04	b.d.	0.00	0.05	0.01	0.81
7.6	c	2126	37	5.28	0.09	0.53	1.05	1.28	26.87	1.13	0.79	13.35	30.30	3.38	12.49	1.83	1.11	0.10	0.23	b.d.	0.03	b.d.	0.06	0.00	0.71
4.2	c	2127	33	6.07	0.05	0.59	0.73	1.23	26.76	1.11	1.03	13.00	29.50	3.39	12.72	1.87	1.14	0.06	0.17	0.04	b.d.	0.01	b.d.	0.03	0.75
4.3	c	2135	35	5.65	0.05	0.55	0.70	1.09	27.42	1.16	1.06	13.93	30.37	3.35	12.59	1.75	1.13	0.11	0.19	0.02	0.01	0.02	0.03	0.01	0.75
4.1	c	2140	35	5.71	0.07	0.57	0.69	1.01	27.51	1.06	1.05	13.39	29.77	3.35	12.64	1.83	1.08	0.08	0.18	0.02	0.00	0.01	0.00	0.01	0.78
7.4	c	2141	36	5.44	0.12	0.56	1.05	1.24	26.98	1.04	0.82	13.76	30.34	3.26	12.10	1.82	1.04	0.06	0.32	0.02	0.05	0.01	0.03	0.03	0.76
3.2	c	2170	42	4.64	0.04	0.46	0.43	1.00	27.45	0.96	0.77	15.51	31.20	3.25	11.85	1.52	0.77	0.05	0.06	b.d.	b.d.	0.01	0.01	0.01	0.80
3.6	c	2174	47	4.04	0.04	0.40	0.42	0.84	27.64	1.09	0.84	15.53	31.45	3.22	12.25	1.57	0.77	0.05	0.08	0.01	b.d.	b.d.	0.05	0.03	0.76

Spot	Note	Date	2σ	ThO <sub>2</sub>	UO <sub>2</sub>	PbO	Y <sub>2</sub> O <sub>3</sub>	SiO <sub>2</sub>	P <sub>2</sub> O <sub>5</sub>	SO <sub>3</sub>	CaO	La <sub>2</sub> O <sub>3</sub>	Ce <sub>2</sub> O <sub>3</sub>	Pr <sub>2</sub> O <sub>3</sub>	Nd <sub>2</sub> O <sub>3</sub>	Sm <sub>2</sub> O <sub>3</sub>	Gd <sub>2</sub> O <sub>3</sub>	Tb <sub>2</sub> O <sub>3</sub>	Dy <sub>2</sub> O <sub>3</sub>	Ho <sub>2</sub> O <sub>3</sub>	Er <sub>2</sub> O <sub>3</sub>	Tm <sub>2</sub> O <sub>3</sub>	Yb <sub>2</sub> O <sub>3</sub>	Lu <sub>2</sub> O <sub>3</sub>	F	
1.5	c	2192	47	3.97	0.05	0.41	0.47	0.87	27.58	1.17	0.86	15.48	32.73	3.35	11.94	1.47	0.88	0.05	0.08	b.d.	b.d.	b.d.	0.02	0.02	0.77	
8.3	c	2203	26	8.69	0.11	0.89	0.47	1.80	26.28	0.70	0.84	10.97	29.12	3.55	13.79	1.92	0.92	0.05	0.13	0.07	0.01	0.03	0.05	b.d.	0.75	
1.4	c	2209	38	5.11	0.07	0.53	0.70	0.94	27.47	0.91	0.82	14.80	30.94	3.22	12.06	1.76	1.08	0.07	0.17	0.03	0.02	0.01	0.06	0.03	0.79	
7.5	c	2214	38	5.25	0.06	0.54	1.11	1.31	26.78	1.23	0.85	13.43	30.32	3.31	12.30	1.91	1.03	0.12	0.26	0.05	0.03	b.d.	0.02	0.02	0.74	
6.10	c	2225	37	5.53	0.05	0.57	0.84	0.96	27.87	1.09	1.08	13.74	30.26	3.34	12.47	1.79	1.08	0.07	0.21	b.d.	0.03	0.03	0.07	0.01	0.73	
1.2	c	2247	38	5.07	0.09	0.54	0.77	0.83	27.77	1.07	1.15	15.08	30.62	3.24	12.02	1.71	1.09	0.08	0.23	0.00	0.03	0.01	0.06	0.04	0.76	
4.4	c	2250	38	5.27	0.05	0.55	0.69	0.86	27.77	1.13	1.16	13.11	31.15	3.40	12.57	1.76	1.01	0.07	0.17	0.01	0.03	0.03	0.06	b.d.	0.77	
1.3	c	2258	38	5.21	0.06	0.55	0.78	0.95	27.76	0.86	0.87	14.65	31.13	3.16	12.00	1.72	1.03	0.05	0.22	0.08	0.06	0.00	0.03	b.d.	0.79	
1.1	c	2271	38	5.17	0.08	0.55	0.66	0.88	27.44	1.12	1.14	14.19	31.28	3.35	12.06	1.72	1.10	0.09	0.17	b.d.	0.01	b.d.	b.d.	b.d.	0.76	
6.9	c	2272	38	5.29	0.06	0.56	0.81	0.96	27.90	1.07	1.09	13.24	30.87	3.26	12.46	1.71	1.02	0.07	0.21	0.02	0.01	0.01	0.07	0.01	0.74	
3.1	c	2287	42	4.62	0.05	0.49	0.55	0.86	27.56	0.88	0.77	15.95	31.90	3.22	12.09	1.63	0.77	0.04	0.12	0.03	0.02	b.d.	0.03	b.d.	0.78	
3.3	c	2350	45	4.32	0.03	0.46	0.47	0.97	27.29	1.17	0.86	15.88	32.12	3.33	12.00	1.32	0.81	b.d.	0.11	0.03	0.01	b.d.	0.04	b.d.	0.79	
6.11	c	2364	36	5.85	0.06	0.64	0.75	0.93	27.83	1.02	1.14	12.24	29.67	3.46	12.73	2.00	1.04	0.06	0.19	0.12	0.04	b.d.	0.02	b.d.	0.75	
<b>3301 - rutile-garnet metapelite (coordinates: 74.542507, -82.341875)</b>																										
6.2	c	1879	60	2.60	0.12	0.25	0.16	b.d.	25.62	0.00	0.57	12.65	30.69	3.82	15.58	2.54	1.03	0.04	0.00	0.03	b.d.	b.d.	0.04	0.02	0.80	
2.1	r	1886	28	7.10	0.15	0.64	0.34	0.41	28.07	0.02	1.22	11.08	27.41	3.33	14.06	3.63	1.39	0.05	0.09	b.d.	b.d.	b.d.	b.d.	b.d.	0.83	
2.5	r	1894	27	7.40	0.17	0.67	0.22	0.49	28.48	0.01	1.19	11.20	28.89	3.57	14.44	2.51	0.90	0.04	0.01	0.05	b.d.	b.d.	0.04	0.00	0.83	
8.4	c	1902	91	1.62	0.08	0.16	0.12	b.d.	25.12	b.d.	0.38	12.64	31.02	3.78	15.84	2.60	1.14	0.03	b.d.	b.d.	b.d.	0.01	0.06	b.d.	0.88	
2.6	r	1921	22	9.95	0.22	0.91	0.20	0.99	27.32	0.01	1.35	11.08	27.41	3.29	12.63	2.26	0.98	0.03	0.00	b.d.	b.d.	0.03	0.03	0.00	0.83	
4.5	r	1929	23	8.94	0.24	0.84	0.21	0.94	25.25	0.00	1.19	11.40	28.61	3.20	12.54	1.90	1.11	0.03	0.05	0.05	b.d.	b.d.	0.05	0.01	0.73	
6.1	c	1930	51	3.27	0.12	0.32	0.20	0.00	25.74	0.01	0.66	11.32	30.59	3.63	15.56	2.69	1.33	0.06	0.02	0.01	b.d.	b.d.	0.06	0.01	0.85	
2.2	r	1942	31	6.17	0.14	0.57	0.22	0.35	28.32	0.02	1.03	11.08	29.35	3.48	15.24	2.74	0.96	0.01	b.d.	b.d.	b.d.	b.d.	0.04	0.02	0.85	
1.5	r	1956	23	9.43	0.18	0.87	0.21	1.26	26.55	0.01	1.03	11.13	28.08	3.30	12.88	2.44	0.95	0.06	0.07	0.03	b.d.	b.d.	0.02	0.02	0.81	
8.3	c	1958	94	1.53	0.09	0.16	0.13	b.d.	24.30	0.02	0.37	12.60	32.26	3.85	15.75	2.51	1.00	0.02	b.d.	0.01	b.d.	b.d.	0.03	0.04	0.79	
3.3	r	2273	21	10.58	0.39	1.22	0.19	1.40	26.10	0.02	1.25	10.26	26.78	3.28	13.40	2.51	1.07	0.06	0.05	0.02	b.d.	b.d.	0.05	0.02	0.76	
1.1	r	2279	23	8.61	0.56	1.09	1.16	0.55	29.22	0.02	1.51	11.30	27.63	3.10	11.72	2.13	1.32	0.12	0.32	0.02	0.04	0.03	0.05	b.d.	0.65	
2.3	c	2283	15	18.28	0.28	1.97	0.17	2.73	24.51	0.03	1.69	7.84	22.12	2.98	13.27	2.10	0.72	0.03	b.d.	b.d.	b.d.	0.01	0.04	0.00	0.71	
2.4	c	2293	21	11.08	0.31	1.25	0.63	0.78	27.89	0.02	1.82	10.69	26.24	2.96	12.09	2.70	1.62	0.11	0.25	0.02	b.d.	b.d.	0.02	b.d.	0.73	
5.2	c	2338	23	9.35	0.44	1.15	1.31	0.71	25.11	0.04	1.53	11.16	25.53	2.89	11.38	2.06	1.09	0.08	0.31	0.06	0.10	b.d.	0.11	0.06	0.71	
10.4	c	2355	22	10.65	0.28	1.23	0.25	1.31	22.80	0.03	1.36	8.47	25.42	3.47	14.81	2.71	1.16	0.02	0.05	0.06	b.d.	0.03	0.00	0.04	0.81	
5.4	r	2359	43	4.31	0.13	0.51	0.74	0.08	26.15	0.02	0.85	10.93	26.65	3.30	15.25	4.92	3.09	0.16	0.29	0.03	b.d.	0.03	0.03	b.d.	0.70	
10.5	c	2404	28	7.69	0.12	0.88	0.49	0.42	23.96	0.05	1.35	12.61	28.61	3.18	12.12	1.76	1.07	0.07	0.13	0.04	0.00	0.01	0.07	0.02	0.84	
4.1	c	2425	25	8.38	0.40	1.08	1.24	0.40	26.82	0.04	1.59	11.96	27.06	2.99	11.53	1.98	1.71	0.10	0.42	b.d.	0.03	b.d.	0.07	0.01	0.66	
1.2	c	2430	22	8.36	0.71	1.22	2.01	0.35	29.72	0.06	1.75	11.91	27.32	3.05	11.46	1.79	1.04	0.09	0.45	0.09	0.12	0.01	0.08	b.d.	0.68	

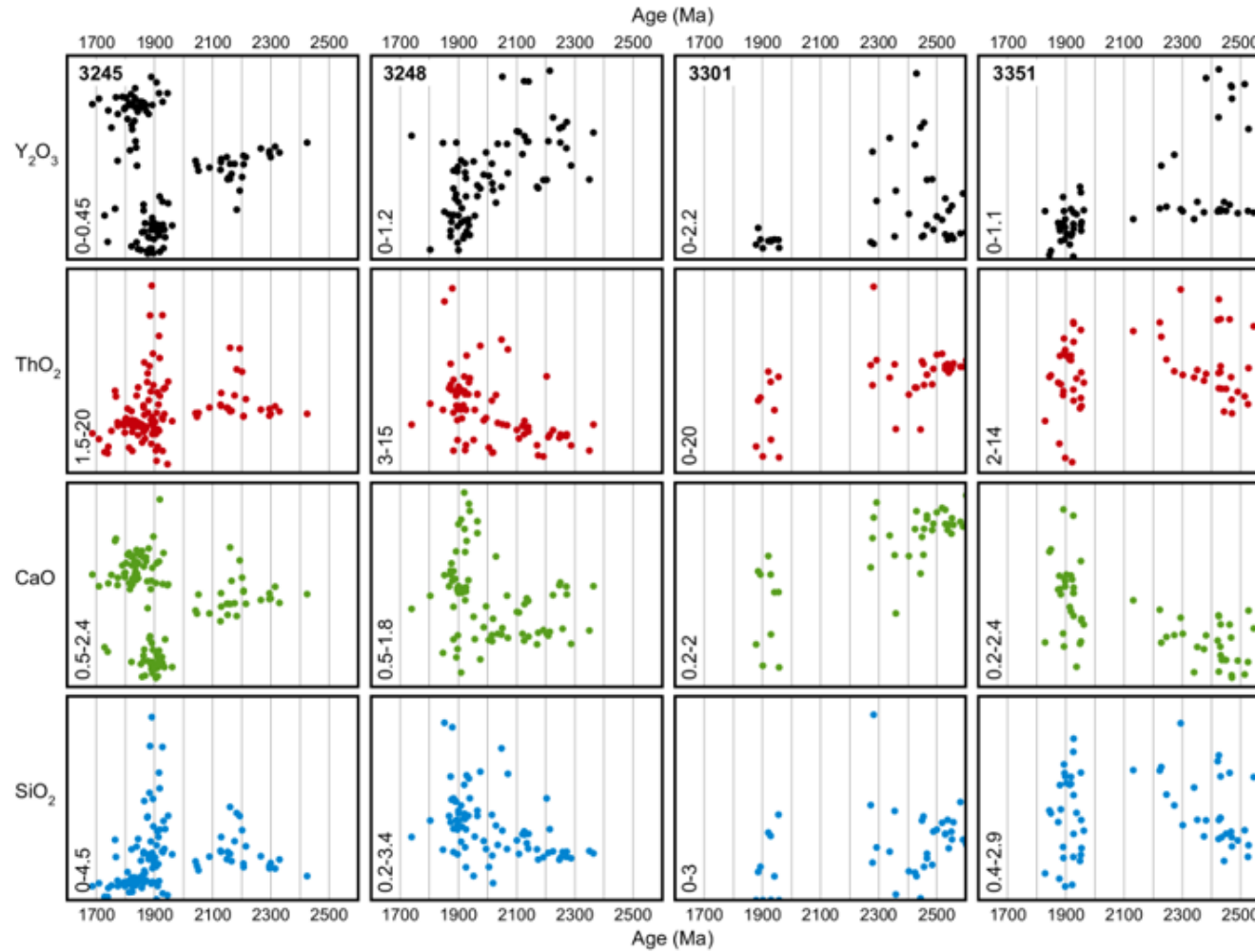
Spot	Note	Date	2σ	ThO <sub>2</sub>	UO <sub>2</sub>	PbO	Y <sub>2</sub> O <sub>3</sub>	SiO <sub>2</sub>	P <sub>2</sub> O <sub>5</sub>	SO <sub>3</sub>	CaO	La <sub>2</sub> O <sub>3</sub>	Ce <sub>2</sub> O <sub>3</sub>	Pr <sub>2</sub> O <sub>3</sub>	Nd <sub>2</sub> O <sub>3</sub>	Sm <sub>2</sub> O <sub>3</sub>	Gd <sub>2</sub> O <sub>3</sub>	Tb <sub>2</sub> O <sub>3</sub>	Dy <sub>2</sub> O <sub>3</sub>	Ho <sub>2</sub> O <sub>3</sub>	Er <sub>2</sub> O <sub>3</sub>	Tm <sub>2</sub> O <sub>3</sub>	Yb <sub>2</sub> O <sub>3</sub>	Lu <sub>2</sub> O <sub>3</sub>	F		
1.10	c	2444	24	4.26	1.28	1.02	1.43	0.03	28.82	0.07	1.20	13.89	29.74	3.05	11.18	1.98	1.04	0.14	0.39	0.05	0.05	0.02	0.04	b.d.	0.70		
1.7	c	2449	20	10.97	0.58	1.45	0.25	1.17	27.92	0.04	1.52	10.55	26.59	3.31	12.87	2.13	0.84	0.07	0.06	b.d.	b.d.	b.d.	0.02	0.02	0.79		
10.8	c	2454	22	10.69	0.30	1.30	0.26	1.23	23.49	0.04	1.36	8.34	25.05	3.48	14.85	2.67	1.24	0.05	0.06	0.10	0.01	b.d.	0.03	b.d.	0.74		
1.6	c	2456	23	8.63	0.59	1.21	1.48	0.49	29.20	0.03	1.59	11.47	27.32	3.02	11.78	2.16	1.37	0.11	0.39	b.d.	0.06	b.d.	0.06	0.02	0.76		
7.7	r	2466	23	9.64	0.34	1.21	0.37	0.68	23.97	0.07	1.71	10.73	26.27	3.02	11.80	2.13	1.53	0.05	0.12	0.07	0.00	b.d.	b.d.	b.d.	0.70		
1.3	c	2466	23	9.65	0.41	1.24	0.86	0.62	29.01	0.04	1.68	11.47	26.91	3.01	11.53	2.28	1.35	0.17	0.29	0.06	0.00	b.d.	0.05	b.d.	0.69		
4.2	c	2484	24	8.69	0.44	1.16	0.87	0.52	26.51	0.06	1.58	11.05	27.10	3.06	11.82	2.26	1.53	0.12	0.32	0.00	0.03	0.01	0.04	b.d.	0.73		
3.4	c	2488	22	10.21	0.46	1.34	0.32	1.01	27.07	0.02	1.64	11.03	26.62	3.11	12.32	2.39	1.36	0.07	0.08	0.02	b.d.	0.02	0.03	0.04	0.74		
5.1	c	2500	21	11.60	0.26	1.41	0.47	1.04	24.59	0.02	1.74	10.62	25.44	2.93	11.74	2.38	1.66	0.05	0.21	0.02	0.01	b.d.	0.04	0.01	0.70		
4.6	c	2518	21	11.69	0.27	1.44	0.43	1.14	24.47	0.01	1.78	9.87	24.53	3.02	11.79	2.54	1.75	0.11	0.15	0.04	0.03	b.d.	0.06	0.00	0.65		
3.6	c	2529	22	10.19	0.46	1.36	0.27	0.97	25.87	0.03	1.64	10.95	26.37	3.10	12.32	2.12	1.31	0.06	0.05	b.d.	b.d.	0.02	0.05	b.d.	0.77		
3.7	c	2529	22	10.54	0.35	1.35	0.66	0.98	26.00	0.08	1.76	10.24	25.35	3.07	11.95	2.53	1.59	0.14	0.24	0.02	b.d.	b.d.	0.06	0.00	0.63		
4.3	c	2537	22	10.69	0.42	1.41	0.21	1.18	25.50	0.03	1.58	10.00	25.73	3.12	12.26	2.27	1.16	0.08	0.04	0.06	0.00	b.d.	0.04	b.d.	0.69		
1.4	c	2541	24	9.84	0.29	1.25	0.53	0.76	28.00	0.04	1.63	10.82	26.17	3.05	11.95	2.42	1.48	0.16	0.21	0.04	b.d.	b.d.	0.06	0.01	0.69		
3.5	c	2550	22	10.18	0.45	1.37	0.26	1.01	25.65	0.02	1.55	10.97	27.04	3.17	12.06	2.11	1.28	0.04	0.09	b.d.	b.d.	0.01	0.05	0.01	0.77		
3.1	c	2552	23	10.48	0.32	1.35	0.58	0.89	28.93	0.03	1.69	10.67	26.59	2.94	11.93	2.30	1.61	0.08	0.23	b.d.	b.d.	b.d.	0.01	b.d.	0.75		
4.4	c	2557	22	10.75	0.41	1.42	0.22	1.15	25.55	0.01	1.63	10.64	26.29	3.16	12.29	2.17	1.25	0.07	0.07	0.01	b.d.	0.03	0.06	0.05	0.67		
1.9	c	2581	21	10.43	0.62	1.50	0.28	1.44	28.01	0.05	1.65	10.35	26.15	3.16	12.22	2.12	0.90	0.02	0.08	0.07	0.03	0.01	0.02	b.d.	0.78		
3.2	c	2590	23	10.43	0.32	1.36	0.71	0.89	28.24	0.01	1.61	10.89	26.89	2.89	12.04	2.42	1.68	0.13	0.23	b.d.	0.00	b.d.	b.d.	0.02	0.76		
1.8	c	2601	22	11.04	0.34	1.45	0.30	0.82	29.22	0.02	1.89	10.90	27.42	3.14	12.15	2.08	1.18	0.08	0.06	0.01	0.00	0.01	0.03	b.d.	0.71		
<b>3351 - biotite monzogranite gneiss (coordinates: 74.581921, -82.394733)</b>																											
4.2	c	1828	36	5.06	0.12	0.44	0.26	0.73	24.78	0.36	0.68	16.29	31.63	3.09	10.61	1.08	0.76	0.06	0.06	b.d.	b.d.	b.d.	0.05	0.03	0.74		
1.7	r	1843	26	7.65	0.09	0.65	0.02	1.50	24.63	1.61	1.65	15.09	29.66	2.93	10.47	0.97	0.55	b.d.	b.d.	b.d.	b.d.	b.d.	0.03	0.06	0.79		
1.6	r	1848	26	7.75	0.08	0.65	0.05	1.46	24.71	1.58	1.68	14.75	30.99	3.04	10.28	1.08	0.50	b.d.	b.d.	b.d.	b.d.	b.d.	0.01	0.01	0.77		
8.1	r	1873	27	7.32	0.11	0.64	0.20	1.36	25.80	1.15	1.25	15.80	30.55	3.08	10.51	0.85	0.67	b.d.	0.02	b.d.	0.03	0.00	0.02	b.d.	0.76		
4.8	c	1877	47	3.73	0.07	0.33	0.17	0.66	24.77	1.70	1.39	17.70	32.30	2.95	9.32	0.90	0.43	0.00	b.d.	0.03	b.d.	b.d.	0.03	b.d.	0.80		
6.7	r	1879	24	8.90	0.16	0.79	0.16	1.81	24.74	1.02	1.25	14.07	30.14	3.15	10.51	1.08	0.48	0.02	0.00	0.04	b.d.	b.d.	0.05	0.02	0.69		
8.2	r	1882	28	7.23	0.13	0.64	0.10	1.51	26.62	1.27	1.19	14.43	31.61	3.33	11.24	1.15	0.59	0.02	b.d.	b.d.	b.d.	b.d.	0.06	0.01	0.77		
8.12	r	1890	30	6.58	0.13	0.59	0.34	1.05	28.13	0.44	0.77	15.05	31.07	3.22	11.67	1.45	0.80	0.06	0.04	0.01	b.d.	b.d.	0.03	0.01	0.77		
8.10	r	1891	29	6.82	0.11	0.60	0.20	0.92	27.38	1.66	2.11	15.72	30.26	3.07	10.48	1.15	0.55	b.d.	0.01	b.d.	0.00	b.d.	0.08	0.01	0.73		
3.8	r	1893	22	9.91	0.14	0.87	0.26	2.06	22.88	0.37	0.63	14.21	29.78	2.94	10.52	1.08	0.61	0.03	0.05	0.02	0.01	0.03	0.03	0.00	0.73		
2.6	r	1895	23	9.12	0.15	0.81	0.11	1.96	21.79	1.43	1.36	13.18	29.88	2.91	10.08	0.93	0.71	0.01	b.d.	b.d.	b.d.	0.00	0.05	b.d.	0.76		
6.10	r	1897	23	9.24	0.15	0.82	0.22	1.92	25.69	1.14	1.28	13.84	30.10	3.03	10.31	1.21	0.59	0.01	b.d.	0.03	0.00	0.01	0.07	0.00	0.72		
4.3	c	1897	59	2.89	0.06	0.26	0.17	0.57	24.33	1.67	1.34	19.01	32.13	2.83	9.16	0.92	0.64	0.05	0.01	0.04	b.d.	b.d.	0.03	0.03	0.73		
2.8	r	1901	24	8.90	0.14	0.79	0.14	1.83	22.00	1.43	1.41	13.46	29.27	3.01	10.42	1.28	0.73	0.03	0.02	b.d.	b.d.	b.d.	0.05	0.03	0.73		

Spot	Note	Date	2 $\sigma$	ThO <sub>2</sub>	UO <sub>2</sub>	PbO	Y <sub>2</sub> O <sub>3</sub>	SiO <sub>2</sub>	P <sub>2</sub> O <sub>5</sub>	SO <sub>3</sub>	CaO	La <sub>2</sub> O <sub>3</sub>	Ce <sub>2</sub> O <sub>3</sub>	Pr <sub>2</sub> O <sub>3</sub>	Nd <sub>2</sub> O <sub>3</sub>	Sm <sub>2</sub> O <sub>3</sub>	Gd <sub>2</sub> O <sub>3</sub>	Tb <sub>2</sub> O <sub>3</sub>	Dy <sub>2</sub> O <sub>3</sub>	Ho <sub>2</sub> O <sub>3</sub>	Er <sub>2</sub> O <sub>3</sub>	Tm <sub>2</sub> O <sub>3</sub>	Yb <sub>2</sub> O <sub>3</sub>	Lu <sub>2</sub> O <sub>3</sub>	F
1.1	r	1913	24	8.67	0.17	0.78	0.08	1.81	25.04	0.98	1.06	14.51	30.85	2.99	10.43	0.96	0.43	b.d.	b.d.	0.02	b.d.	0.01	0.07	b.d.	0.79
2.7	r	1917	24	8.92	0.15	0.80	0.13	1.91	22.88	1.47	1.40	13.28	29.44	3.10	10.48	1.04	0.69	0.04	b.d.	0.01	b.d.	b.d.	0.02	0.01	0.67
6.8	r	1917	24	8.64	0.16	0.78	0.27	1.82	24.97	0.84	1.01	13.76	30.49	3.09	10.88	1.22	0.60	0.03	0.03	0.02	0.01	0.02	0.06	b.d.	0.66
4.4	c	1921	63	2.64	0.06	0.24	0.14	0.59	24.05	1.84	1.36	19.23	32.94	2.81	8.81	0.93	0.67	0.05	0.03	b.d.	b.d.	b.d.	0.02	0.02	0.77
8.9	r	1925	29	6.91	0.11	0.62	0.19	0.93	27.43	1.61	2.04	14.72	30.73	2.95	10.22	1.15	0.46	0.02	0.01	b.d.	b.d.	b.d.	0.01	b.d.	0.73
7.3	r	1925	21	10.88	0.18	0.98	0.02	2.22	24.96	0.94	1.21	13.55	29.04	2.96	10.93	1.39	0.38	0.01	b.d.	0.02	b.d.	b.d.	0.02	b.d.	0.68
7.2	r	1926	21	10.79	0.15	0.96	0.01	2.38	24.60	1.03	1.27	14.01	29.46	3.06	10.73	1.21	0.41	0.02	b.d.	0.00	b.d.	b.d.	0.04	0.01	0.77
7.10	r	1926	23	9.72	0.10	0.86	0.25	1.69	27.55	0.55	1.21	13.69	29.14	3.10	11.02	1.21	0.70	0.03	0.00	b.d.	b.d.	0.03	0.02	b.d.	0.83
4.7	c	1926	31	6.26	0.13	0.57	0.17	1.21	24.36	0.86	0.96	16.08	31.38	2.91	10.36	1.16	0.77	0.02	0.01	b.d.	b.d.	0.04	0.03	b.d.	0.76
8.6	r	1936	27	7.56	0.09	0.68	0.24	1.47	27.06	0.31	0.41	15.25	31.33	3.05	10.98	1.23	0.62	0.03	0.03	b.d.	0.01	0.01	0.07	0.00	0.71
7.11	r	1948	33	5.81	0.13	0.54	0.39	0.88	28.60	0.27	0.66	15.45	32.58	3.16	11.14	1.43	0.65	0.05	0.07	b.d.	0.00	0.02	0.02	b.d.	0.77
6.9	r	1951	21	10.42	0.17	0.95	0.19	1.96	25.11	1.18	1.55	14.12	28.55	2.87	10.17	1.14	0.69	0.03	0.01	0.00	b.d.	b.d.	0.04	b.d.	0.64
8.11	r	1951	31	6.41	0.14	0.60	0.36	0.95	27.18	0.31	0.69	14.78	31.66	3.25	11.33	1.27	0.63	b.d.	0.07	b.d.	b.d.	b.d.	0.03	0.03	0.64
1.2	r	1952	26	7.92	0.16	0.73	0.16	1.38	25.17	0.72	0.91	14.45	30.49	3.02	10.63	1.07	0.58	0.01	0.00	0.03	b.d.	0.03	0.05	0.03	0.74
4.6	c	1953	32	5.94	0.13	0.55	0.20	1.04	24.43	0.74	0.93	15.55	31.33	3.03	10.53	1.17	0.63	0.01	b.d.	0.01	b.d.	0.05	0.03	b.d.	0.78
8.7	r	1961	28	7.32	0.11	0.67	0.27	1.25	27.10	0.61	0.87	15.34	31.25	2.96	10.84	1.23	0.52	0.01	0.04	0.04	b.d.	b.d.	0.01	b.d.	0.72
7.1	r	2131	22	10.35	0.13	1.02	0.22	1.99	25.74	0.82	1.13	13.66	29.95	2.98	10.76	1.01	0.34	0.03	0.00	0.06	b.d.	0.02	0.02	b.d.	0.71
6.5	c	2222	22	10.86	0.12	1.12	0.28	1.99	24.49	0.42	1.03	12.70	28.14	2.94	11.00	1.28	0.79	0.03	0.05	0.05	b.d.	b.d.	0.04	b.d.	0.73
3.1	c	2227	22	10.02	0.32	1.11	0.51	2.03	23.39	0.37	0.67	15.08	28.87	2.95	9.84	1.23	0.73	0.03	0.10	0.03	0.03	0.03	0.07	0.02	0.72
3.7	c	2245	26	8.68	0.07	0.89	0.29	1.69	22.82	0.55	0.74	13.10	30.34	3.16	11.49	1.44	0.71	0.01	0.07	0.05	b.d.	b.d.	0.04	0.01	0.72
3.2	c	2272	26	7.99	0.27	0.91	0.57	1.56	23.52	0.50	0.75	15.13	29.77	2.82	9.80	1.24	0.76	0.04	0.11	0.06	0.01	0.03	0.02	b.d.	0.79
3.5	c	2294	20	12.80	0.11	1.35	0.27	2.57	21.31	0.52	0.94	12.52	27.15	2.87	10.72	1.26	0.81	0.04	0.03	b.d.	0.00	0.01	0.09	0.00	0.67
2.3	c	2301	28	7.78	0.08	0.83	0.26	1.32	23.50	0.42	0.77	15.04	29.82	2.97	10.31	1.20	0.77	0.06	0.05	b.d.	b.d.	0.00	0.10	b.d.	0.71
8.4	c	2340	29	7.63	0.12	0.84	0.22	1.78	26.30	0.47	0.35	14.87	32.43	3.16	11.18	1.14	0.42	0.04	0.01	b.d.	b.d.	b.d.	0.03	0.03	0.73
6.2	c	2351	28	8.06	0.10	0.88	0.31	1.38	25.85	0.26	0.63	14.56	30.84	3.17	11.04	1.29	0.91	0.04	0.06	0.00	0.00	0.01	0.08	0.02	0.74
6.1	c	2374	29	7.43	0.05	0.81	0.26	1.18	26.61	0.18	0.60	15.32	31.38	3.04	10.92	1.11	0.70	0.06	0.02	b.d.	b.d.	b.d.	0.11	0.07	0.73
6.3	c	2381	27	7.83	0.32	0.97	0.98	1.38	26.13	0.34	0.75	14.46	29.46	3.01	10.54	1.32	0.82	0.05	0.19	0.09	0.06	0.06	0.00	0.01	0.70
2.5	c	2421	22	11.01	0.15	1.25	0.26	2.10	23.06	0.32	0.70	12.65	28.25	3.09	10.93	1.17	0.82	0.01	b.d.	0.02	b.d.	0.01	0.03	0.05	0.71
7.4	c	2424	27	7.88	0.22	0.95	0.77	1.15	27.28	0.26	0.97	13.94	30.17	3.06	10.99	1.53	0.82	0.07	0.15	0.03	0.02	0.01	0.06	0.02	0.73
1.4	c	2425	21	12.22	0.11	1.37	0.27	2.17	23.87	0.24	0.96	12.99	28.09	2.95	10.64	1.22	0.77	0.02	0.02	b.d.	b.d.	b.d.	0.03	b.d.	0.70
7.7	c	2425	30	6.99	0.23	0.86	1.03	1.38	27.13	0.17	0.36	14.60	30.74	3.08	11.19	1.61	1.13	0.06	0.17	0.04	0.04	0.04	0.07	0.03	0.77

Spot	Note	Date	2σ	ThO <sub>2</sub>	UO <sub>2</sub>	PbO	Y <sub>2</sub> O <sub>3</sub>	SiO <sub>2</sub>	P <sub>2</sub> O <sub>5</sub>	SO <sub>3</sub>	CaO	La <sub>2</sub> O <sub>3</sub>	Ce <sub>2</sub> O <sub>3</sub>	Pr <sub>2</sub> O <sub>3</sub>	Nd <sub>2</sub> O <sub>3</sub>	Sm <sub>2</sub> O <sub>3</sub>	Gd <sub>2</sub> O <sub>3</sub>	Tb <sub>2</sub> O <sub>3</sub>	Dy <sub>2</sub> O <sub>3</sub>	Ho <sub>2</sub> O <sub>3</sub>	Er <sub>2</sub> O <sub>3</sub>	Tm <sub>2</sub> O <sub>3</sub>	Yb <sub>2</sub> O <sub>3</sub>	Lu <sub>2</sub> O <sub>3</sub>	F
8.3	c	2430	28	7.94	0.11	0.91	0.27	1.41	27.33	0.25	0.63	14.64	31.54	3.23	11.53	1.27	0.57	0.04	b.d.	b.d.	b.d.	b.d.	0.08	0.03	0.72
1.5	c	2431	22	11.06	0.10	1.25	0.26	1.92	24.90	0.12	0.87	13.52	28.89	3.03	10.64	1.21	0.62	0.01	0.05	b.d.	0.01	b.d.	0.04	0.00	0.81
8.5	c	2431	27	8.29	0.08	0.94	0.27	1.41	27.06	0.16	0.54	14.93	31.13	3.16	11.20	1.16	0.43	0.03	0.02	0.06	b.d.	b.d.	0.05	0.02	0.71
1.9	c	2435	31	6.96	0.07	0.79	0.27	1.17	25.28	0.12	0.49	15.03	31.11	3.11	10.93	1.13	0.76	0.01	0.03	b.d.	0.01	0.01	0.03	b.d.	0.78
1.11	c	2443	36	5.61	0.10	0.65	0.31	0.88	25.33	0.20	0.49	15.14	32.86	3.06	10.89	1.17	0.67	0.07	0.06	0.01	b.d.	b.d.	0.06	b.d.	0.84
1.10	c	2450	31	6.95	0.08	0.79	0.26	1.21	24.92	0.16	0.49	14.59	31.09	3.13	11.15	1.23	0.79	0.04	0.04	0.02	b.d.	b.d.	0.06	b.d.	0.75
6.6	c	2462	22	11.05	0.12	1.27	0.30	1.96	24.99	0.21	0.87	13.50	28.83	2.91	11.27	1.21	0.68	0.03	0.04	b.d.	b.d.	0.03	0.01	0.03	0.74
6.4	c	2467	27	7.64	0.29	0.97	0.94	1.24	25.77	0.19	0.73	13.80	30.03	2.99	10.51	1.52	1.07	0.09	0.21	0.01	0.07	b.d.	0.03	b.d.	0.75
7.6	c	2469	32	6.31	0.21	0.79	0.93	1.17	27.59	0.07	0.32	15.14	30.91	3.25	11.08	1.54	0.68	0.09	0.22	b.d.	0.04	b.d.	0.02	0.01	0.79
7.9	c	2470	35	5.51	0.20	0.70	0.87	1.06	27.96	0.06	0.30	15.89	31.52	3.09	10.71	1.45	0.82	0.05	0.18	0.06	0.05	b.d.	0.08	0.03	0.86
1.8	c	2490	32	6.78	0.08	0.79	0.25	1.13	25.14	0.10	0.48	14.92	31.14	3.12	10.94	1.17	0.82	0.02	0.00	b.d.	b.d.	b.d.	0.05	0.00	0.72
7.8	c	2514	31	6.51	0.21	0.83	0.95	1.26	26.33	0.12	0.33	14.89	30.92	3.13	11.07	1.52	0.92	0.07	0.21	0.06	0.06	0.00	0.03	0.03	0.78
8.8	c	2525	35	6.05	0.06	0.71	0.26	0.93	28.21	0.18	0.46	15.09	32.49	3.23	11.36	1.19	0.39	0.04	0.01	0.05	b.d.	0.00	0.03	b.d.	0.77
7.5	c	2527	27	8.17	0.27	1.05	0.70	1.07	27.68	0.14	1.02	14.46	29.73	2.95	10.41	1.41	0.80	0.05	0.14	0.04	b.d.	0.01	0.03	0.00	0.80
2.4	c	2545	23	10.63	0.12	1.26	0.25	1.91	22.25	0.23	0.83	13.20	27.93	3.01	10.74	1.25	0.72	0.03	0.01	0.03	0.01	b.d.	0.05	0.01	0.74



Appendix 7. Monazite age vs.  $Y_2O_3$ ,  $ThO_2$ ,  $CaO$ , and  $SiO_2$  for southern Devon Island samples. Oxide abundances are in wt.%.  
 3245: biotite diorite, 3248: biotite granite gneiss, 3301: rutile-garnet metapelite, 3351: biotite granite gneiss.



**Appendix 8. EPMA monazite dating results of northern Devon Island samples.**

Sample	Grain	Spot	Date (Ma)	2 $\sigma$	ThO <sub>2</sub>	UO <sub>2</sub>	PbO	Y <sub>2</sub> O <sub>3</sub>	SiO <sub>2</sub>	P <sub>2</sub> O <sub>5</sub>
ED-C-1	16	85	1867	34	12.098	0.699	1.207	1.825	1.609	23.940
ED-C-1	14	65	1868	51	6.718	0.510	0.708	1.040	4.142	22.792
ED-C-1	15	70	1872	50	7.056	0.551	0.750	1.378	0.618	25.407
ED-C-1	5	30	1872	35	12.253	0.628	1.202	1.691	1.578	23.814
ED-C-1	1	6	1886	39	10.383	0.508	1.019	1.545	1.208	24.410
ED-C-1	16	81	1891	42	8.302	0.825	0.947	2.425	0.468	25.700
ED-C-1	1	2	1892	36	10.240	0.896	1.131	2.042	0.697	25.634
ED-C-1	15	75	1892	41	9.903	0.506	0.982	1.809	1.060	24.508
ED-C-1	15	69	1893	41	8.479	0.866	0.976	2.535	0.485	25.828
ED-C-1	10	60	1894	38	10.042	0.781	1.080	2.257	0.894	25.462
ED-C-1	15	66	1895	41	9.549	0.605	0.985	1.948	0.822	25.013
ED-C-1	6	33	1895	45	7.760	0.670	0.856	1.829	0.477	25.450
ED-C-1	1	5	1895	38	9.648	0.880	1.079	1.794	0.631	25.628
ED-C-1	15	76	1896	40	9.230	0.750	1.004	1.993	0.756	24.997
ED-C-1	9	50	1899	41	9.181	0.648	0.970	1.639	0.808	24.968
ED-C-1	9	52	1900	39	9.228	0.855	1.039	1.294	0.605	25.528
ED-C-1	8	48	1901	38	11.304	0.441	1.084	1.670	1.167	24.474
ED-C-1	6	35	1901	38	9.720	0.791	1.061	1.847	0.721	25.085
ED-C-1	6	36	1902	38	9.922	0.803	1.082	1.856	0.740	25.111
ED-C-1	5	25	1902	42	8.372	0.779	0.945	2.392	0.478	25.556
ED-C-1	16	83	1904	41	8.386	0.856	0.971	2.418	0.495	25.774
ED-C-1	15	74	1906	41	9.725	0.563	0.993	2.036	0.870	24.834
ED-C-1	6	32	1908	41	9.404	0.652	0.995	1.580	0.841	24.783
ED-C-1	1	10	1909	38	10.650	0.581	1.078	1.843	0.975	25.010
ED-C-1	10	59	1909	39	9.070	0.889	1.042	2.757	0.580	25.376
ED-C-1	3	19	1909	42	8.309	0.768	0.940	2.219	0.479	25.990
ED-C-1	10	57	1909	37	8.871	1.222	1.130	1.471	0.275	25.779
ED-C-1	4	24	1910	43	7.918	0.815	0.922	2.288	0.455	25.680
ED-C-1	2	13	1910	38	9.801	0.785	1.071	1.713	0.808	25.579
ED-C-1	8	46	1910	38	9.925	0.783	1.081	1.908	0.706	25.234
ED-C-1	7	41	1910	37	10.165	0.817	1.112	1.931	0.736	25.366
ED-C-1	4	20	1910	43	8.095	0.776	0.925	2.311	0.484	25.251
ED-C-1	15	67	1911	40	9.807	0.600	1.014	1.927	0.879	25.168
ED-C-1	14	63	1911	39	9.589	0.820	1.065	1.305	0.605	25.277
ED-C-1	5	29	1911	35	12.823	0.526	1.245	1.778	1.624	23.783
ED-C-1	5	28	1912	34	12.566	0.648	1.262	1.803	1.670	23.817
ED-C-1	9	51	1913	38	10.349	0.740	1.105	1.930	0.886	25.244
ED-C-1	7	40	1913	43	8.344	0.654	0.909	1.858	0.632	25.300
ED-C-1	15	73	1913	41	9.640	0.615	1.006	1.947	0.870	24.959
ED-C-1	14	62	1914	38	9.929	0.778	1.082	1.761	0.761	25.307
ED-C-1	1	3	1914	37	10.112	0.862	1.124	2.001	0.686	25.635
ED-C-1	7	39	1914	44	8.052	0.670	0.890	2.151	0.540	25.494
ED-C-1	1	9	1914	37	9.871	0.856	1.102	1.969	0.684	25.551

Sample	Grain	Spot	Date (Ma)	2 $\sigma$	ThO <sub>2</sub>	UO <sub>2</sub>	PbO	Y <sub>2</sub> O <sub>3</sub>	SiO <sub>2</sub>	P <sub>2</sub> O <sub>5</sub>
ED-C-1	9	54	1914	35	13.267	0.328	1.222	1.527	1.613	24.384
ED-C-1	4	23	1914	42	8.142	0.826	0.947	2.338	0.466	25.853
ED-C-1	14	61	1916	43	8.307	0.745	0.936	1.526	0.379	25.517
ED-C-1	16	80	1916	40	9.500	0.726	1.031	1.939	0.825	25.259
ED-C-1	7	38	1916	45	8.395	0.527	0.875	1.638	0.854	24.905
ED-C-1	16	79	1916	32	16.040	0.285	1.444	1.423	2.227	23.105
ED-C-1	9	55	1917	36	13.119	0.323	1.210	1.538	1.534	24.467
ED-C-1	4	21	1918	50	7.064	0.510	0.758	1.472	0.669	24.907
ED-C-1	7	42	1918	41	8.828	0.740	0.980	2.071	0.634	25.373
ED-C-1	16	77	1919	36	12.191	0.546	1.203	1.971	1.508	24.105
ED-C-1	15	72	1919	42	9.377	0.542	0.964	1.707	0.899	24.904
ED-C-1	8	47	1919	39	11.363	0.365	1.076	1.511	1.205	24.481
ED-C-1	3	18	1919	44	8.962	0.478	0.909	1.450	0.871	25.200
ED-C-1	7	37	1920	45	7.953	0.621	0.869	1.934	0.618	25.195
ED-C-1	2	16	1920	36	13.492	0.218	1.210	1.135	1.938	23.701
ED-C-1	6	34	1920	44	8.162	0.672	0.903	1.918	0.566	25.300
ED-C-1	1	4	1921	38	10.076	0.769	1.096	1.871	0.736	25.455
ED-C-1	15	68	1921	41	8.496	0.850	0.988	2.589	0.475	25.835
ED-C-1	6	31	1921	48	7.730	0.514	0.817	1.555	0.758	24.963
ED-C-1	1	8	1922	37	9.412	0.995	1.112	1.964	0.579	25.479
ED-C-1	15	71	1922	43	8.271	0.738	0.934	2.248	0.499	25.597
ED-C-1	8	45	1922	43	8.050	0.759	0.922	2.359	0.490	25.613
ED-C-1	10	58	1922	30	17.341	0.305	1.565	1.608	2.707	22.360
ED-C-1	16	78	1923	36	12.669	0.374	1.192	1.707	1.523	24.095
ED-C-1	16	82	1924	40	10.186	0.535	1.033	1.912	0.913	24.941
ED-C-1	16	84	1924	39	10.232	0.620	1.064	2.068	0.857	25.042
ED-C-1	4	22	1926	44	7.781	0.745	0.897	2.144	0.416	25.636
ED-C-1	1	1	1927	43	8.104	0.752	0.927	2.304	0.459	25.992
ED-C-1	16	86	1927	29	18.254	0.284	1.640	1.539	2.969	22.110
ED-C-1	2	17	1927	34	13.876	0.355	1.291	1.443	1.871	23.664
ED-C-1	2	12	1928	39	9.774	0.751	1.069	1.690	0.863	25.420
ED-C-1	8	43	1928	46	8.004	0.566	0.860	1.811	0.638	25.340
ED-C-1	1	7	1929	38	9.893	0.836	1.107	1.913	0.713	25.340
ED-C-1	5	27	1929	33	14.591	0.319	1.342	1.700	2.011	23.141
ED-C-1	8	49	1930	37	12.740	0.310	1.182	1.597	1.512	24.042
ED-C-1	2	15	1930	39	9.550	0.828	1.076	1.986	0.667	25.419
ED-C-1	8	44	1930	40	8.616	0.901	1.020	2.620	0.553	25.209
ED-C-1	14	64	1938	27	20.702	0.360	1.883	1.419	3.433	21.497
ED-C-1	2	14	1939	39	9.589	0.770	1.066	1.762	0.723	24.664
ED-C-1	5	26	1940	36	12.107	0.563	1.216	1.791	1.131	24.697
ED-EG-2	3	18	1745	108	3.320	0.089	0.279	0.265	0.700	25.054
ED-EG-2	1	1	1750	99	3.696	0.097	0.311	0.204	0.808	25.025
ED-EG-2	2	7	1769	108	3.346	0.078	0.282	0.150	0.715	24.939
ED-EG-2	2	15	1785	104	3.394	0.111	0.298	0.201	0.741	25.005

Sample	Grain	Spot	Date (Ma)	2 $\sigma$	ThO <sub>2</sub>	UO <sub>2</sub>	PbO	Y <sub>2</sub> O <sub>3</sub>	SiO <sub>2</sub>	P <sub>2</sub> O <sub>5</sub>
ED-EG-2	2	5	1804	92	4.075	0.086	0.348	0.131	0.871	24.709
ED-EG-2	2	13	1836	112	3.223	0.083	0.285	0.132	0.676	25.094
ED-EG-2	1	3	1852	107	3.440	0.082	0.305	0.197	0.669	25.209
ED-EG-2	1	4	1861	104	3.474	0.107	0.317	0.210	0.713	25.323
ED-EG-2	3	19	1880	123	2.940	0.064	0.263	0.258	0.574	25.178
ED-EG-2	2	10	1881	157	2.112	0.088	0.202	0.180	0.462	25.383
ED-EG-2	3	30	1884	95	3.942	0.104	0.359	0.233	0.808	25.002
ED-EG-2	2	8	1886	128	2.619	0.112	0.252	0.204	0.592	25.203
ED-EG-2	2	11	1897	113	3.177	0.089	0.293	0.177	0.786	24.901
ED-EG-2	3	20	1898	123	2.859	0.090	0.267	0.128	0.610	25.327
ED-EG-2	3	29	1899	108	3.285	0.110	0.309	0.198	0.795	24.734
ED-EG-2	1	2	1902	102	3.539	0.114	0.332	0.234	0.742	25.287
ED-EG-2	2	14	1926	133	2.492	0.115	0.248	0.199	0.598	25.210
ED-EG-2	2	9	1928	152	2.160	0.096	0.214	0.168	0.581	25.157
ED-EG-2	3	28	1931	111	3.254	0.088	0.305	0.209	0.701	25.024
ED-EG-2	3	17	1932	136	2.548	0.088	0.245	0.135	0.526	25.153
ED-EG-2	2	12	1935	136	2.572	0.071	0.242	0.171	0.531	25.188
ED-EG-2	2	16	1952	125	2.829	0.073	0.267	0.200	0.572	25.167
ED-EG-2	3	21	1986	113	3.198	0.096	0.312	0.148	0.675	24.930
HAU-10-026	5	14	1789	50	6.307	0.634	0.679	0.337	0.621	24.854
HAU-10-026	1	2	1822	57	6.045	0.392	0.600	0.527	2.584	24.269
HAU-10-026	4	13	1844	46	9.461	0.233	0.837	0.000	1.942	23.844
HAU-10-026	7	23	1844	54	7.227	0.279	0.670	0.028	3.945	23.078
HAU-10-026	15	41	1856	49	6.752	0.698	0.763	0.281	0.411	25.880
HAU-10-026	4	11	1857	47	9.518	0.141	0.820	0.003	1.950	23.737
HAU-10-026	1	4	1862	48	6.633	0.767	0.777	0.477	0.375	25.833
HAU-10-026	1	3	1872	49	6.494	0.757	0.767	0.616	0.473	25.744
HAU-10-026	2	7	1878	49	6.546	0.724	0.764	0.554	0.561	26.088
HAU-10-026	2	6	1880	49	6.558	0.755	0.775	0.349	0.428	26.171
HAU-10-026	15	42	1881	48	6.752	0.752	0.791	0.873	0.594	25.626
HAU-10-026	1	1	1882	49	7.146	0.594	0.775	0.323	0.487	25.464
HAU-10-026	5	17	1883	50	7.921	0.335	0.760	0.020	1.564	23.534
HAU-10-026	12	35	1886	51	5.995	0.738	0.726	1.329	0.579	25.819
HAU-10-026	7	20	1890	37	11.302	0.654	1.143	0.003	2.293	23.117
HAU-10-026	13	38	1892	48	6.488	0.836	0.800	0.449	0.415	25.875
HAU-10-026	2	5	1897	49	6.404	0.738	0.765	0.305	0.486	26.017
HAU-10-026	8	26	1902	51	8.155	0.240	0.758	0.014	1.615	23.819
HAU-10-026	12	37	1902	48	8.399	0.385	0.824	0.027	1.617	24.016
HAU-10-026	12	34	1903	55	6.760	0.408	0.694	0.129	0.919	25.074
HAU-10-026	14	40	1905	56	6.954	0.286	0.673	0.073	0.615	25.788
HAU-10-026	12	36	1907	53	7.886	0.216	0.730	0.009	1.532	24.138
HAU-10-026	5	15	1911	47	7.146	0.708	0.824	0.353	0.454	25.711
HAU-10-026	4	12	1912	47	9.140	0.226	0.841	0.012	1.805	23.909
HAU-10-026	9	28	1913	58	7.365	0.128	0.661	0.013	1.368	24.267
HAU-10-026	7	22	1913	44	9.446	0.387	0.918	0.015	1.860	23.859
HAU-10-026	10	31	1914	55	7.498	0.200	0.695	0.009	1.408	23.992
HAU-10-026	2	8	1914	49	7.272	0.587	0.798	0.329	0.500	25.920

Sample	Grain	Spot	Date (Ma)	2 $\sigma$	ThO <sub>2</sub>	UO <sub>2</sub>	PbO	Y <sub>2</sub> O <sub>3</sub>	SiO <sub>2</sub>	P <sub>2</sub> O <sub>5</sub>
HAU-10-026	8	25	1914	53	8.089	0.152	0.730	0.000	1.562	24.071
HAU-10-026	3	10	1915	45	9.858	0.166	0.884	0.004	1.965	23.770
HAU-10-026	8	27	1916	59	6.393	0.312	0.638	0.043	1.053	24.946
HAU-10-026	9	29	1920	59	6.960	0.175	0.644	0.010	1.261	24.192
HAU-10-026	5	16	1924	61	6.469	0.210	0.615	0.037	0.639	25.105
HAU-10-026	3	9	1927	52	8.244	0.129	0.741	0.001	1.714	24.030
HAU-10-026	13	39	1929	60	6.217	0.288	0.620	0.521	1.611	24.717
HAU-10-026	11	33	1929	57	7.187	0.201	0.675	0.008	1.374	24.452
HAU-10-026	10	30	1932	54	7.635	0.244	0.728	0.014	1.437	24.036
HAU-10-026	11	32	1938	57	7.177	0.200	0.677	0.013	1.348	24.325
HAU-16-1453C	6	15	1661	59	6.432	0.070	0.486	0.606	1.126	25.336
HAU-16-1453C	6	16	1741	45	9.131	0.210	0.756	0.561	3.629	22.829
HAU-16-1453C	7	19	1745	46	8.305	0.393	0.746	1.688	0.882	25.553
HAU-16-1453C	5	12	1798	66	6.098	0.026	0.489	0.704	0.597	25.361
HAU-16-1453C	9	24	1817	37	10.432	0.715	1.044	1.986	0.890	25.227
HAU-16-1453C	5	11	1882	50	7.636	0.326	0.733	1.823	1.388	22.935
HAU-16-1453C	2	7	1885	36	9.695	1.125	1.152	2.247	0.407	26.353
HAU-16-1453C	7	18	1886	36	10.242	0.915	1.133	2.037	0.570	25.860
HAU-16-1453C	2	4	1891	34	10.389	1.154	1.223	2.479	0.513	26.115
HAU-16-1453C	2	5	1896	35	9.625	1.212	1.181	2.349	0.377	26.564
HAU-16-1453C	9	20	1900	39	10.024	0.664	1.046	1.815	0.711	24.896
HAU-16-1453C	9	22	1900	38	9.769	0.879	1.092	1.902	0.478	26.134
HAU-16-1453C	2	6	1902	32	11.994	1.118	1.354	2.373	0.763	25.660
HAU-16-1453C	9	23	1907	36	10.135	0.977	1.158	2.121	0.471	26.213
HAU-16-1453C	9	21	1916	38	10.235	0.676	1.077	1.921	0.835	24.979
HAU-16-1453C	9	26	1925	74	4.518	0.264	0.467	1.706	2.900	24.697
HAU-16-1453C	9	25	1927	50	7.288	0.470	0.768	1.818	0.950	24.941
HMP-00-200	5	17	1659	31	14.577	0.374	1.157	0.424	2.299	22.808
HMP-00-200	4	25	1742	31	14.730	0.553	1.280	0.709	3.043	21.956
HMP-00-200	4	29	1746	79	4.924	0.025	0.384	0.726	0.856	24.642
HMP-00-200	2	10	1809	57	7.115	0.118	0.600	0.686	1.234	23.024
HMP-00-200	1	3	1829	30	16.220	0.465	1.442	0.620	2.565	22.695
HMP-00-200	8	34	1856	41	10.679	0.239	0.944	0.630	1.984	23.759
HMP-00-200	1	7	1861	31	15.902	0.391	1.421	0.695	3.208	23.110
HMP-00-200	4	30	1864	81	4.858	0.025	0.406	0.741	0.859	24.585
HMP-00-200	2	11	1865	77	5.054	0.037	0.426	0.896	0.754	25.038
HMP-00-200	2	12	1868	28	16.995	0.689	1.607	0.742	3.649	20.792
HMP-00-200	3	23	1872	33	14.515	0.374	1.310	0.659	2.980	23.171
HMP-00-200	6	49	1874	29	18.049	0.240	1.562	0.997	3.800	21.164
HMP-00-200	6	47	1879	31	15.723	0.374	1.415	0.650	3.067	22.187
HMP-00-200	5	13	1883	37	13.167	0.110	1.125	0.156	1.832	24.066
HMP-00-200	4	28	1888	30	15.544	0.643	1.491	0.746	3.314	21.850
HMP-00-200	5	19	1893	28	17.200	0.662	1.639	0.720	3.664	21.042
HMP-00-200	7	38	1896	34	13.546	0.448	1.270	0.868	1.456	23.743
HMP-00-200	3	24	1897	31	15.339	0.504	1.438	0.661	3.526	21.159

Sample	Grain	Spot	Date (Ma)	2 $\sigma$	ThO <sub>2</sub>	UO <sub>2</sub>	PbO	Y <sub>2</sub> O <sub>3</sub>	SiO <sub>2</sub>	P <sub>2</sub> O <sub>5</sub>
HMP-00-200	6	48	1899	31	15.348	0.460	1.427	0.585	2.706	22.905
HMP-00-200	1	1	1899	31	15.958	0.437	1.471	0.560	2.471	23.189
HMP-00-200	3	21	1900	33	14.013	0.486	1.324	0.647	2.897	23.362
HMP-00-200	8	35	1900	42	10.752	0.197	0.961	0.680	2.025	23.580
HMP-00-200	1	4	1902	31	15.134	0.457	1.410	0.594	1.708	24.196
HMP-00-200	8	32	1902	47	9.442	0.151	0.838	0.712	1.721	23.960
HMP-00-200	4	27	1903	30	15.790	0.640	1.523	0.740	3.373	21.575
HMP-00-200	6	43	1906	39	11.861	0.126	1.035	0.189	1.561	24.297
HMP-00-200	5	15	1909	32	16.146	0.087	1.385	0.082	2.670	23.254
HMP-00-200	5	18	1909	30	16.364	0.512	1.537	0.699	3.583	21.595
HMP-00-200	5	16	1910	35	14.075	0.093	1.213	0.116	2.076	23.825
HMP-00-200	7	41	1910	30	16.284	0.475	1.519	0.596	2.914	22.681
HMP-00-200	5	14	1910	32	15.941	0.101	1.373	0.115	2.634	23.277
HMP-00-200	1	5	1913	30	16.439	0.476	1.535	0.589	2.456	23.244
HMP-00-200	7	39	1914	30	16.923	0.455	1.570	0.632	3.437	21.735
HMP-00-200	6	46	1915	31	15.065	0.484	1.423	0.550	2.169	23.256
HMP-00-200	3	22	1917	30	16.609	0.448	1.544	0.612	3.315	22.986
HMP-00-200	1	2	1918	30	16.778	0.452	1.560	0.603	3.296	21.714
HMP-00-200	6	44	1919	36	13.280	0.263	1.206	0.428	1.548	24.393
HMP-00-200	7	40	1920	29	16.824	0.488	1.577	0.605	3.444	21.378
HMP-00-200	6	45	1920	36	12.250	0.439	1.175	0.695	1.088	25.152
HMP-00-200	8	33	1920	37	12.873	0.184	1.147	0.304	1.657	24.485
HMP-00-200	8	37	1924	30	16.247	0.519	1.542	0.617	3.005	22.601
HMP-00-200	8	36	1927	29	16.310	0.616	1.581	0.668	3.390	21.877
HMP-00-200	6	42	1934	37	12.541	0.222	1.140	0.336	1.663	24.160
HMP-00-216A	6	19	1767	80	0.489	1.108	0.354	0.092	0.070	25.415
HMP-00-216A	6	24	1803	94	0.520	0.899	0.304	0.088	0.077	25.276
HMP-00-216A	6	23	1808	95	0.693	0.852	0.305	0.089	0.075	25.262
HMP-00-216A	4	14	1809	81	0.959	0.997	0.369	0.090	0.061	25.155
HMP-00-216A	4	13	1817	80	0.879	1.029	0.374	0.107	0.068	25.159
HMP-00-216A	4	12	1829	78	2.179	0.752	0.399	0.075	0.140	25.260
HMP-00-216A	6	21	1837	101	0.743	0.765	0.289	0.087	0.083	25.353
HMP-00-216A	6	20	1842	102	2.137	0.436	0.304	0.065	0.150	25.383
HMP-00-216A	6	22	1856	102	1.908	0.492	0.305	0.082	0.137	25.428
HMP-00-216A	2	8	1860	64	6.018	0.186	0.549	0.101	3.505	24.149
HMP-00-216A	7	31	1862	90	3.564	0.250	0.368	0.081	0.766	25.134
HMP-00-216A	3	10	1881	51	8.600	0.062	0.731	0.034	1.126	24.774
HMP-00-216A	7	29	1899	54	8.024	0.065	0.691	0.037	0.983	23.926
HMP-00-216A	2	7	1899	64	6.064	0.202	0.570	0.110	0.592	25.374

Sample	Grain	Spot	Date (Ma)	2 $\sigma$	ThO <sub>2</sub>	UO <sub>2</sub>	PbO	Y <sub>2</sub> O <sub>3</sub>	SiO <sub>2</sub>	P <sub>2</sub> O <sub>5</sub>
HMP-00-216A	3	11	1903	45	10.343	0.049	0.882	0.038	1.466	24.150
HMP-00-216A	2	5	1911	28	19.462	0.028	1.647	0.078	3.855	21.084
HMP-00-216A	7	25	1913	41	11.560	0.041	0.987	0.035	1.739	23.593
HMP-00-216A	5	16	1914	55	6.772	0.337	0.677	1.451	0.389	25.466
HMP-00-216A	2	6	1914	36	14.123	0.026	1.199	0.042	2.425	22.906
HMP-00-216A	7	26	1923	40	12.200	0.048	1.049	0.025	1.856	23.359
HMP-00-216A	7	27	1926	43	10.871	0.037	0.934	0.030	1.551	23.679
HMP-00-216A	2	4	1927	32	16.291	0.019	1.389	0.063	2.991	22.199
HMP-00-216A	5	15	1930	53	6.663	0.481	0.720	2.077	0.297	25.689
HMP-00-216A	3	9	1932	51	8.855	0.051	0.770	0.043	1.148	24.414
HMP-00-216A	5	17	1934	60	6.427	0.236	0.623	1.126	0.379	25.443
HMP-00-216A	7	30	1934	77	4.608	0.223	0.464	0.043	0.523	24.793
HMP-00-216A	7	28	1950	49	9.320	0.046	0.816	0.035	1.188	24.004
HMP-00-216A	5	18	1951	60	6.593	0.198	0.631	0.555	0.432	25.267

## A.6 Composition–temperature modelling

### Appendix 9. Bulk-rock compositions (mol.%) for H<sub>2</sub>O–T modelling of metapelite and metabasite samples from northern Devon

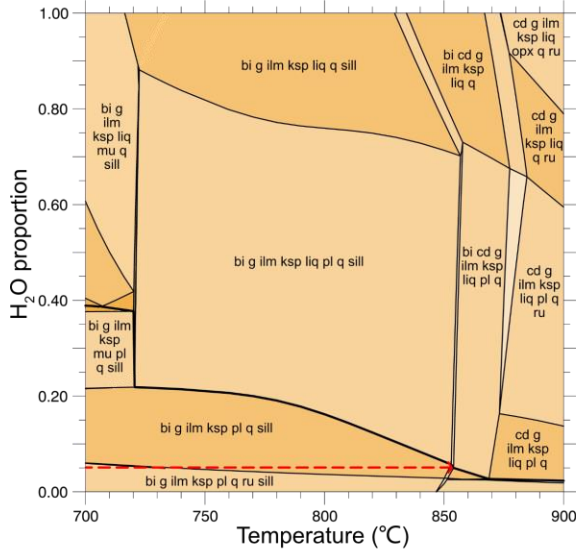
Island.  $X_{\text{Fe}^{3+}} = \text{O}(\text{Fe}_2\text{O}_3)/\text{FeO} \cdot 2$ .

Sample	H <sub>2</sub> O	SiO <sub>2</sub>	Al <sub>2</sub> O <sub>3</sub>	CaO	MgO	FeO <sub>t</sub>	K <sub>2</sub> O	Na <sub>2</sub> O	TiO <sub>2</sub>	MnO	O	$X_{\text{Fe}^{3+}}$
HMP-00-216A	0.01	77.28	8.64	1.83	3.50	3.55	2.23	2.10	0.46	0.09	0.31	0.18
HMP-00-216A	10.00	69.56	7.78	1.64	3.15	3.20	2.01	1.89	0.42	0.08	0.28	0.18
HAU-10-026	0.01	59.08	21.39	0.47	5.26	10.05	2.14	0.67	0.27	0.52	0.13	0.03
HAU-10-026	6.68	55.14	19.97	0.44	4.91	9.38	1.99	0.63	0.25	0.49	0.12	0.03
HMP-00-213	0.01	50.81	8.18	10.71	11.62	14.75	0.23	1.13	1.24	-	1.30	0.18
HMP-00-213	2.40	49.60	7.99	10.46	11.34	14.40	0.22	1.11	1.21	-	1.27	0.18
ED-C-2	0.01	58.59	11.14	6.12	7.46	9.81	0.76	4.54	0.92	-	0.66	0.13
ED-C-2	2.00	57.42	10.91	6.00	7.31	9.61	0.75	4.44	0.90	-	0.65	0.13

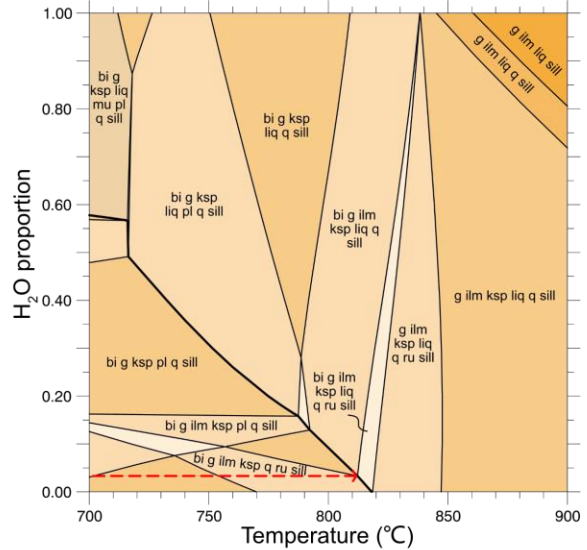


**Appendix 10. H<sub>2</sub>O–T models for two metapelite (a–b) and two metabasite (c–d) northern Devon Island samples. The proportion of H<sub>2</sub>O selected for P–T modelling is shown as a dashed red line. Mineral abbreviations follow the a–x models used, and field shading corresponds to relative variance.**

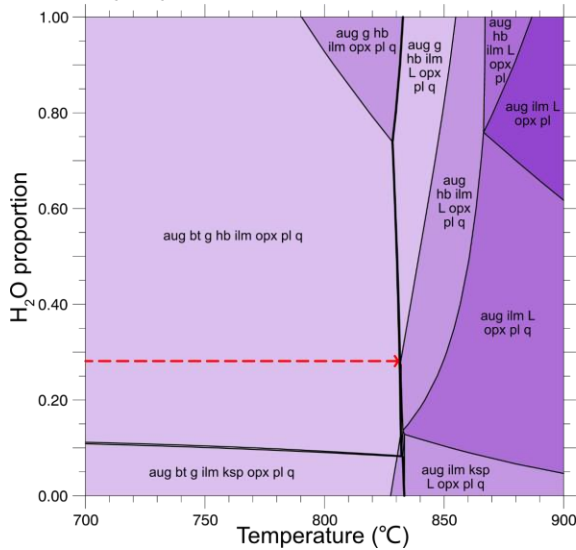
**A** HMP-00-216A  
grt-bt-crd metapelite



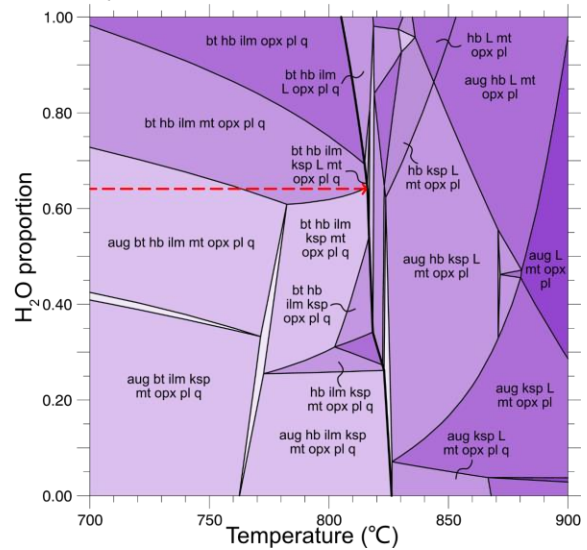
**B** HAU-10-026  
bt-sill-grt metapelite



**C** HMP-00-213  
hbl-cpx-opx metabasite



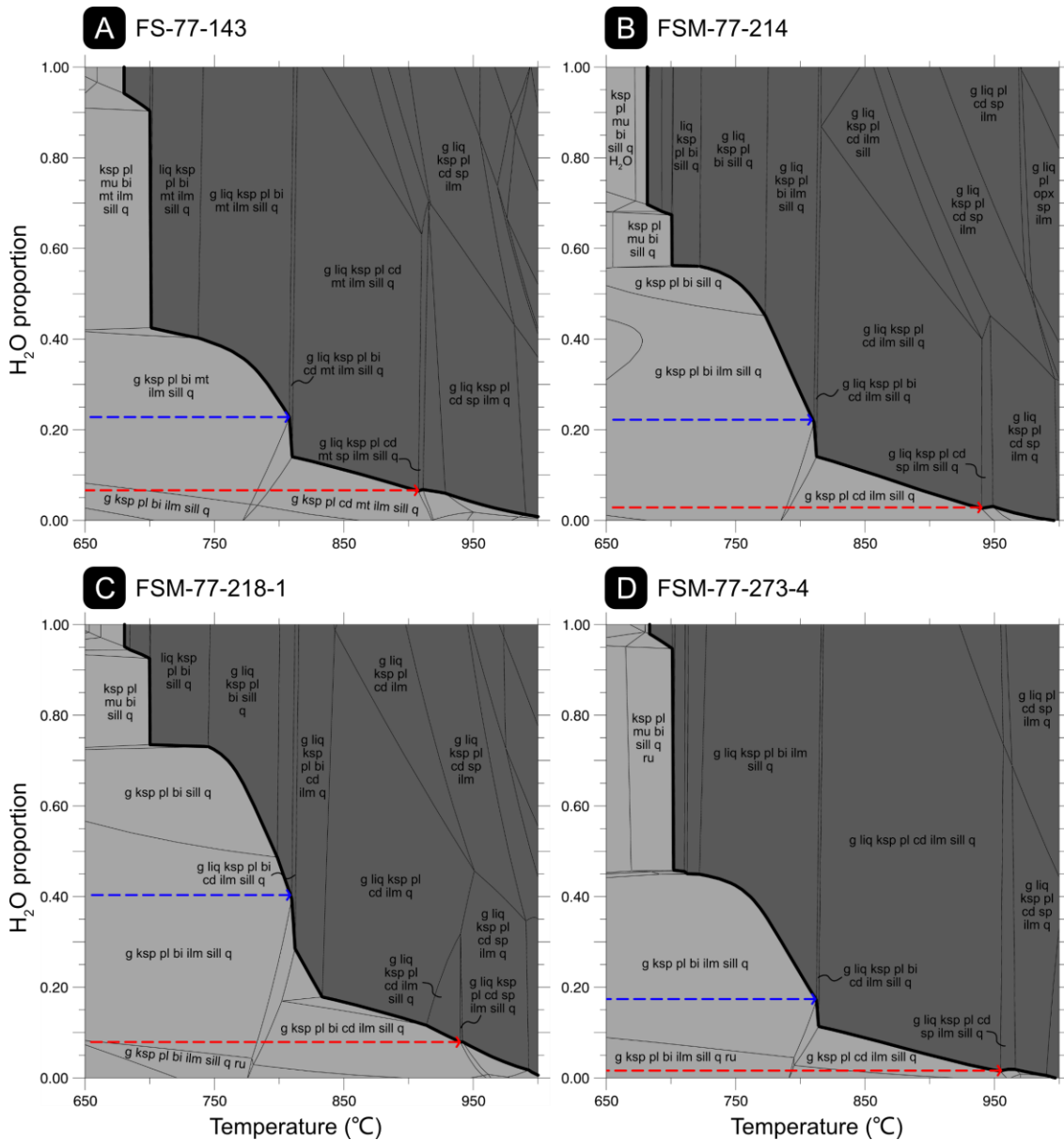
**D** ED-C-2  
bt-opx metabasite



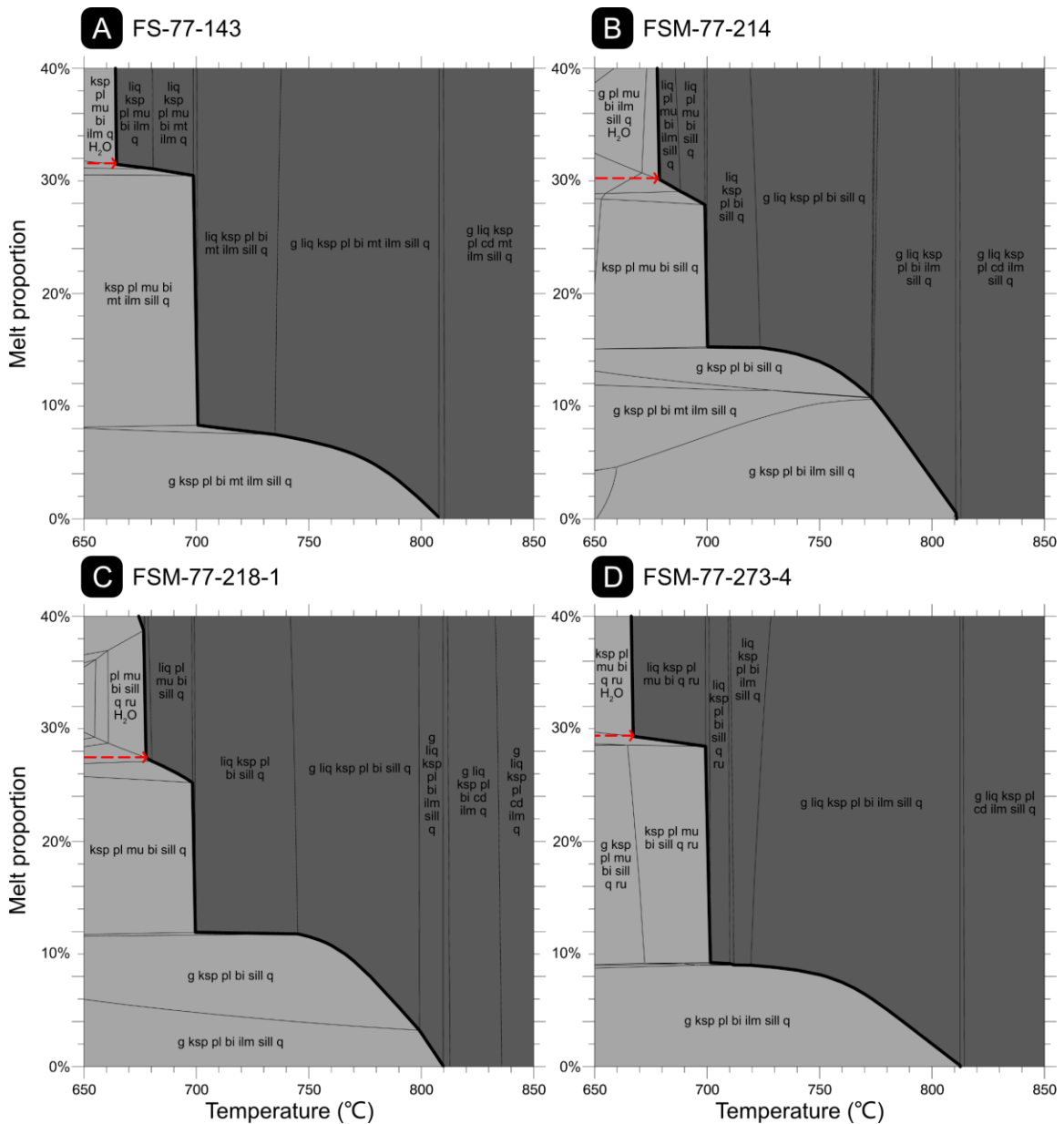
**Appendix 11. Bulk-rock compositions (mol.%) for H<sub>2</sub>O–T and melt–T modelling of migmatitic paragneiss samples from the Ellesmere tectonic zone.  $X_{\text{Fe}^{3+}} = \text{O}(\text{Fe}_2\text{O}_3)/\text{FeO} \cdot 2$ .  $X_{\text{Mg}} = \text{MgO}/(\text{MgO}+\text{FeO})$ .**

Sample	Figure	H <sub>2</sub> O	SiO <sub>2</sub>	Al <sub>2</sub> O <sub>3</sub>	CaO	MgO	FeO <sub>t</sub>	K <sub>2</sub> O	Na <sub>2</sub> O	TiO <sub>2</sub>	MnO	O	$X_{\text{Fe}^{3+}}$	$X_{\text{Mg}}$
FS-77-143	A.12	0.01	66.05	13.75	1.18	4.37	6.86	3.82	2.29	0.65	0.07	0.93	0.27	0.39
FS-77-143	A.12	7.50	61.10	12.72	1.09	4.04	6.35	3.54	2.12	0.60	0.06	0.86	0.27	0.39
FS-77-143	A.13	1.70	64.94	13.52	1.16	4.30	6.75	3.76	2.26	0.64	0.07	0.92	0.27	0.39
FS-77-143	A.13	7.93	65.59	11.43	0.85	2.69	4.27	3.59	2.67	0.39	0.04	0.55	0.26	0.39
FSM-77-214	A.12	0.01	64.02	13.92	1.47	5.85	8.10	3.28	2.18	0.69	0.10	0.38	0.09	0.42
FSM-77-214	A.12	8.00	58.90	12.81	1.35	5.39	7.45	3.02	2.01	0.63	0.09	0.35	0.09	0.42
FSM-77-214	A.13	1.66	62.96	13.69	1.45	5.76	7.97	3.23	2.15	0.67	0.09	0.38	0.09	0.42
FSM-77-214	A.13	7.75	64.51	11.55	1.03	3.58	5.02	3.29	2.58	0.40	0.06	0.23	0.09	0.42
FSM-77-218-1	A.12	0.01	64.32	13.43	1.13	6.78	7.72	3.56	1.96	0.70	0.07	0.34	0.09	0.47
FSM-77-218-1	A.12	6.37	60.23	12.57	1.06	6.35	7.23	3.33	1.83	0.66	0.06	0.32	0.09	0.47
FSM-77-218-1	A.13	2.52	62.70	13.09	1.10	6.61	7.52	3.47	1.91	0.68	0.06	0.33	0.09	0.47
FSM-77-218-1	A.13	8.36	64.28	11.18	0.81	4.09	4.75	3.41	2.48	0.41	0.04	0.20	0.08	0.46
FSM-77-273-4	A.12	0.01	74.53	11.06	1.35	3.21	4.50	2.94	1.71	0.52	0.06	0.12	0.06	0.42
FSM-77-273-4	A.12	5.50	70.44	10.45	1.27	3.03	4.25	2.78	1.62	0.49	0.05	0.12	0.06	0.42
FSM-77-273-4	A.13	0.93	73.84	10.96	1.34	3.18	4.46	2.91	1.70	0.51	0.06	0.12	0.06	0.42
FSM-77-273-4	A.13	2.74	73.07	10.65	1.24	2.85	4.01	2.99	1.84	0.45	0.05	0.11	0.05	0.42

**Appendix 12. H<sub>2</sub>O–T models for migmatitic paragneiss samples from the Ellesmere tectonic zone. The proportion of H<sub>2</sub>O selected for P–T modelling of garnet–sillimanite–cordierite–biotite peak assemblages is shown as a dashed blue line. The proportion of H<sub>2</sub>O selected for P–T modelling of spinel + quartz peak assemblages is shown as a dashed red line. The solidus is bolded and suprasolidus stability fields are shaded in darker grey. Mineral abbreviations follow the a–x models used.**



**Appendix 13. Melt–T models for migmatitic paragneiss samples from the Ellesmere tectonic zone. The proportion of melt selected for melt-reintegrated protolith P–T modelling of is shown as a dashed red line. The solidus is bolded and suprasolidus stability fields are shaded in darker grey. Mineral abbreviations follow the a–x models used.**



## A.7 References

- Droop, G. T. R. (1987). A general equation for estimating Fe<sup>3+</sup> concentrations in ferromagnesian silicates and oxides from microprobe analyses, using stoichiometric criteria. *Mineralogical Magazine*, 51(361), 431–435.
- Lanari, P., Vidal, O., De Andrade, V., Dubacq, B., Lewin, E., Grosch, E. G., & Schwartz, S. (2014). XMapTools: A MATLAB©-based program for electron microprobe X-ray image processing and geothermobarometry. *Computers & Geosciences*, 62, 227–240.

## Curriculum Vitae

**Name:** Joshua Laughton

**Post-secondary  
Education and  
Degrees:** University of Western Ontario  
London, Ontario, Canada  
2017–2023 Ph.D. Geology

University of Western Ontario  
London, Ontario, Canada  
2014–2017 B.Sc. Honours Specialization in Geology

**Related Work  
Experience** Electron Microprobe Research Technician  
University of Western Ontario  
2022–2023

Teaching and Research Assistant  
University of Western Ontario  
2017–2022

Pre-Graduate Research Student  
University of Western Ontario  
2017

Geological Technician  
Ontario Oil, Gas and Salt Resources Library  
2016

**Publications:**

Laughton, J., Osinski, G. R., & Yakymchuk, C. (2022). Late Neoproterozoic HT–UHT metamorphism on southern Devon Island, Canadian Arctic. *Precambrian Research*, 377, 106718. <https://doi.org/10.1016/j.precamres.2022.106718>